DESIGN AND PERFORMANCE ANALYSIS OF A LOW-COST AIDED DEAD RECKONING NAVIGATOR

A DISSERTATION

SUBMITTED TO THE DEPARTMENT OF AERONAUTICS AND

ASTRONAUTICS

AND THE COMMITTEE ON GRADUATE STUDIES

OF STANFORD UNIVERSITY

IN PARTIAL FULFILLMENT OF THE REQUIREMENTS

FOR THE DEGREE OF

DOCTOR OF PHILOSOPHY

Demoz Gebre-Egziabher

February 2004

I certify that I have read this thesis and that in my opinion it is fully adequate, in scope and in quality, as a dissertation for the degree of Doctor of Philosophy.

Professor J. David Powell
(Principal Advisor)

I certify that I have read this thesis and that in my opinion it is fully adequate, in scope and in quality, as a dissertation for the degree of Doctor of Philosophy.

Professor Per K. Enge

I certify that I have read this thesis and that in my opinion it is fully adequate, in scope and in quality, as a dissertation for the degree of Doctor of Philosophy.

Professor Bradford W. Parkinson

Approved for the University Committee on Graduate Studies:

Dean of Graduate Studies

Abstract

The Federal Aviation Administration is leading the National Airspace System modernization effort, in part, by supplanting traditional air traffic services with the Global Positioning System (GPS) aided by the Wide and Local Area Augmentation Systems (WAAS & LAAS). Making GPS the primary-means of navigation will enhance safety, flexibility and efficiency of operations for all aircraft ranging from single engine general aviation aircraft to complex commercial jet-liners. This transformation of the National Airspace System will be gradual and the build-up to a primary-means GPS capability is expected to occur concurrently with the de-commissioning of a significant number of existing ground-based navigational facilities. If an alternate means of navigation is not available during this transition period, temporary interruptions of GPS services due to intentional or unintentional interference could present significant problems for aircraft lacking backup navigation capability.

To successfully deal with such outage scenarios, this thesis outlines an architecture of a skeletal network of existing radio-navigation aids, the Distance Measuring Equipment (DME), that should be left in place to provide a redundant navigation capability alongside GPS/WAAS during this transition period. When the information from the proposed skeletal network of DME is fused with a low cost dead-reckoning system in terminal areas, performance comparable to VOR and LORAN based navigation can be achieved. This navigation scheme allows reduction of the number of operational radio-navigation aids required while still providing adequate coverage for navigation during the transition to a primary-means GPS National Airspace System.

The dead-reckoning navigation system is based on the fusion of a single low-end DME receiver with low cost inertial, air-data and magnetic sensors. These sensors are already part of the newer general aviation aircraft's suite of navigation sensors.

Estimator architectures for fusing the information from the various sensors is presented. The performance of this navigator depends on the calibration and on-line estimation of sensor errors. Accordingly, various algorithms for estimating sensor errors in the low cost inertial sensors and magnetometers were developed. In particular, a novel non-linear estimation algorithm for calibrating the errors in a strapdown magnetometer is presented.

It is shown that a navigator based on airspeed and magnetometer-derived heading information, augmented by intermittent range measurements from a skeletal network of DME, can provide a backup navigation capability with accuracies better than 0.5 nautical miles.

Acknowledgments

I thank my dissertation adviser, Prof. J. David Powell, for his guidance and mentoring. He fostered a research environment which made the Ph.D. process both fruitful and *enjoyable*. He gave me the freedom to direct my research in areas that were more aligned with my interests, shared my enthusiasm for the research and, above all, was always within reach and unselfish with his time when I needed help. I thank Prof. Per Enge whose infectious enthusiasm for GPS related research made the Stanford GPS Laboratory a fun place in which to work. His advice and guidance were indispensable for my research and I also thank him for extending me the opportunity to teach AA272D–an invaluable experience for one aspiring a future academic career. I thank Prof. Bradford Parkinson for his advice on various issues ranging from the finer points of inertial navigation to things to consider when looking for a faculty job. His careful reading of this dissertation and his feedback are greatly appreciated.

Flight testing was an important and rewarding aspect of my thesis work. I thank the members of the flight testing team (Keith Alter, Andy Barrows, Christopher Comp, Rich Fuller, Andrew Hansen, Chad Jennings, Roger Hayward, Sharon Houck and Todd Walter) and the test pilots from Sky Research Inc. (Sky, Ben Hovelman and Kevin McCoy) for their help and hard work which made flight testing a success. I am also grateful for the help and friendship of all my colleagues, past and present, in the GPS laboratory (Dennis Akos, Doug Archdeacon, Frank Bauregger, Dave Bevly, Lee Boyce, Donghai Dai, Gabriel Elkaim, Jennifer Evans, Konstantin Gromov, Andrew Hansen, Roger Hayward, Sharon Houck, James Shau-Shiun Jan, Chad Jennings, Ping-Ya Ko, Sherman Lo, Eric Phelts and Todd Walter). I gratefully acknowledge their assistance, which ranged from building hardware to discussions which were the catalysts for many research ideas. I owe special thanks to Roger Hayward and Gabriel

Elkaim. Roger designed and built the short baseline GPS attitude determination and sensor data collection systems. Without these systems flight testing would have been impossible. Gabriel's collaboration was instrumental in the development of attitude determination and magnetometer calibration algorithms. I thank Dr. Zeev Berman for his help and very informative lectures on inertial navigation given when he was a visiting scholar in the Stanford GPS laboratory.

The work in this thesis was sponsored by a research grant from the Federal Aviation Administration Satellite Program Office and a NASA-Langley technology transfer grant from Seagull Technology Inc. The support of these organizations is gratefully acknowledged.

Finally, I owe a debt of gratitude to my older siblings Sam and Brikti. They have always been a source of inspiration and I was fortunate to have them as role models for my academic career and life in general. I thank my younger sisters, Meaza and Rahwa. I have benefited greatly from their advice and encouragement over the years. Above all, my deepest thanks go to my parents, Semainesh and Ytbarek. Their unending support and encouragement have been invaluable through out my life. Although in comparison it is significantly smaller to all that they have given me, it is to them, with heartfelt thanks, that I dedicate this thesis.

Contents

List of Tables

List of Figures

Chapter 1

Introduction

1.1 Overview

The systems and procedures used for navigation by modern commercial aircraft are reliable and robust. As such, a failure to successfully navigate from point of departure to destination is a rare and news-worthy event. In the rare instances when such navigation errors occur, they are often the result of human error because the redundancy of on board systems makes complete loss of navigation due to a single equipment failure remote. Even more remote, however, is the possibility of losing all navigation capability due to a failure in the ground based systems used for navigation. This is because most aerial navigation systems in current use rely on a *distributed* terrestrial network of *independent* radio beacons. These beacons are in effect "electronic light houses" that emit radio signals used to safely guide aircraft even in times of limited visibility and inclement weather. This method of navigating is called radio-navigation. It was introduced in the late 1940s and became the worldwide standard by the 1960s.

Currently, efforts are underway to replace radio-navigation by a new and advanced navigation system. This new system, which has been developed and operated by the United States Department of Defense, is called the Global Positioning System (GPS). Instead of using terrestrial beacons, it relies on satellites in Earth's orbit that continuously transmit one-way ranging signals. A user on the surface of Earth determines position by multilateration based on these ranging signals. GPS provides an instantaneous and highly accurate position solution for users worldwide. Because

of its superior performance and capabilities, GPS is slated to replace radio-navigation and become the primary means of navigation for all sectors of aviation[2].

In its current implementation, however, GPS has had localized outages from inadvertent electronic interference[24]. A deliberate or unintentional low-power radio transmission in certain frequency bands can render GPS unusable in a large geographical area[27]. To deal with these scenarios of Radio Frequency Interference (RFI), future aircraft must be equipped with redundant navigation systems that do not rely on GPS. These redundant navigation systems will be used to navigate out of large areas of GPS interference.

Certain classes of aircraft already have this redundant navigation capability. In general, these are the newest aircraft in service today and are operated by the commercial carriers or the military. They are equipped with a redundant navigator called an Inertial Navigation System (INS). An INS is a self-contained system equipped with sensors that continuously measure an aircraft's acceleration and rotation, from which its velocity and position vectors are computed. There are a large number of aircraft in service today, however, that lack such a backup capability. Providing a backup navigation capability for these aircraft by using an INS is not practical because an INS with sufficient accuracy to serve as a backup navigation system is prohibitively expensive for these users.

It is apparent that there will be a need for an affordable backup navigation system in the future aviation environment where GPS is the primary means of navigation. The research in this thesis addresses this problem. More specifically, it is about designing a backup navigation system for aviation use that satisfies the following constraints:

1. It is a low-cost system. In the context here, this is a system costing approximately $\$10,000$.

2. It does not rely on the Global Positioning System (GPS).

3. It has a position accuracy of 0.5 nautical after 30 minutes of operation.

The motivation for these design constraints requires an in-depth understanding of the current and future environments for flight operations which will be discussed in the following sections.

1.2 The National Airspace System

In the United States, the enviroment in which aviation operations are conducted is called the National Airspace System (NAS). In simple terms, the National Airspace System is a complex network of ground based and airborne systems that allow safe navigation and traffic separation for aircraft. The Federal Aviation Administration (FAA) is leading an effort to modernize the National Airspace System[2]. The objectives of this modernization effort are enhanced safety, flexibility and efficiency of flight operations for all aircraft ranging from single engine General Aviation aircraft to complex commercial jet-liners. The modernization of the National Airspace System entails, in part, supplanting navigation services currently being provided by ground based facilities with the satellite based Global Positioning System.

1.2.1 Navigation in the Current NAS

There are three primary ground based facilities that provide enroute navigation services in the current National Airspace System. These facilities are Non-Directional Beacons (NDB), Very High Frequency Omni-directional Range (VOR) and Distance Measuring Equipment (DME).

NDBs are ground based low frequency radio transmitters that provide airborne users with bearing information. The information provided by NDBs is the relative bearing between the NDB transmitter and the user. These days in most areas of the National Airspace System, there is less reliance on NDBs for navigation. This is because they are low frequency transmitters which exhibit degraded performance when atmospheric phenomena such as precipitation and lightning are present.

A VOR is also a ground based radio transmitter that provides bearing information. Unlike NDB, however, the information provided by the VOR is the relative bearing (with respect to magnetic north) between the VOR transmitter and the user. The bearing information is not dependent on the aircraft's heading. This system may be visualized as a wheel with spokes extending from the hub outward. Each spoke is a course with a given magnetic heading and is selectable by the pilot. An indicator in the cockpit tells the pilot which one of these spokes the airplane is on.

DME is an internationally standardized pulse-ranging system used in aviation.

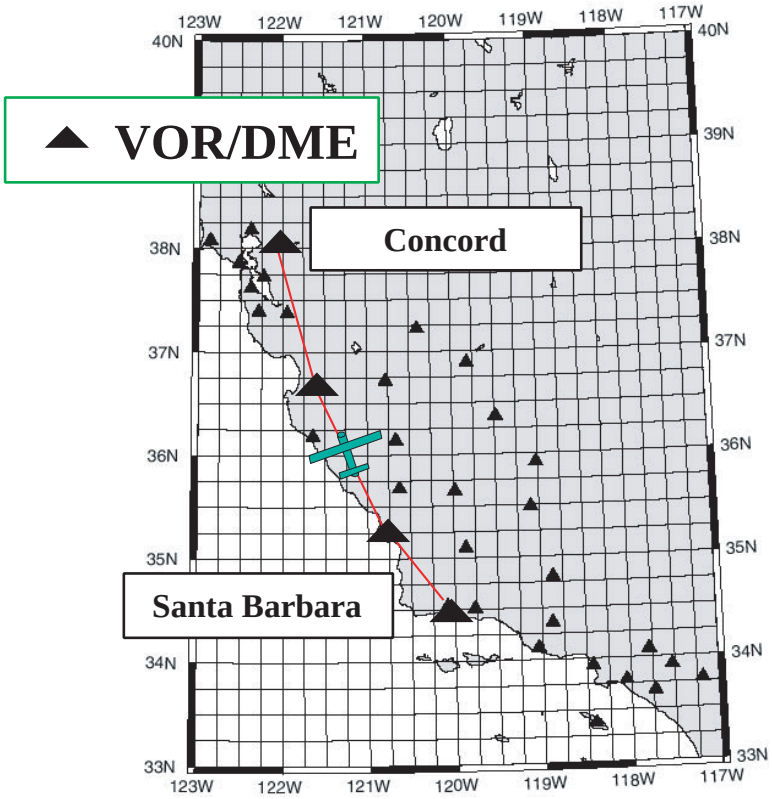

Figure 1.1: Navigation in the Current NAS. (The Larger Triangles Represent the Subset of Available Radionavigation Beacons Used on the Hypothetical Flight from Stanta Barabra to Concord Depicted in the Figure.)

DME is used to determine the range between a user and a ground-based transponder by measuring the round-trip time-of-flight of a pulse train emitted by the airborne user to a ground based transponder. The time-of-flight measurement is converted to a range, normally in nautical miles, and displayed in the cockpit.

With a few exceptions, VOR transmitters are collocated with a DME transponder. Most navigation in the National Airspace System is conducted along VOR radials in a "connect the dots" fashion from one VOR/DME site to the next. For example, a flight from Santa Barbara, CA to Concord, CA would be flown from one VOR/DME to the next as shown in Figure 1.1. This is an inefficient method of navigation.

Flying off VOR radials along complex trajectories is called Random or Area Navigation (R-NAV). R-NAV capability implies that a user can obtain multiple range, multiple bearing, or multiple range *and* bearing measurments and process them in real-time. This requires a navigation computer as well as one of the following:

1. Both a VOR and DME receiver.

2. Two DME receivers or a single scanning-DME. A scanning-DME is a single DME receiver capable of obtaining range information from multiple DME transponders.

3. Two VOR receivers.

It is costly to install all of the above mentioned equipment required for R-NAV capability. This fact is reflected in Table 1.1 which groups current NAS users by their navigation capability with most capable aircraft (Group A) being the first entry and the least capable (Group E) being last. Aircraft in Groups A, B* and C† have the equipment required for R-NAV capability. The less expensive aircraft in Groups D‡ and E normally do not have R-NAV capability. This is why R-NAV capability has traditionally been out of reach for these users. More recently GPS receivers for aviation have brought R-NAV capability to all aircraft. However, the NAS has not been able to fully utilize this capability. This is why the trajectories flown by most aircraft continue to be simple straight lines between VOR/DME sites.

It should be noted that there is another radio-navigation system currently used by some aircraft in the NAS for R-NAV purposes. This system, known as LORAN (short

*Even though military aircraft do not use VOR, they have an equivalent system that provides them with bearing information and is, for all practical purposes, the same as a VOR. This equivalent system is known as TACAN and combines the functionality of both VORs and DMEs.

†Commuter aircraft are turbo-prop aircraft (mostly twin engined) used by air carriers primarily for transporting passengers from major airports to smaller regional airports.

‡General Aviation flying is defined as all aircraft operations except for those performed by the turbine powered business jets, commuters, large commercial carriers and the military. Approximately 60% of all General Aviation operations are personal flights by private individuals [8]. A significant fraction of the remaining General Aviation operations are carried out by businesses and air taxi operators. Very important niche operations such as transportation of critically ill patients to hospitals, law enforcement activities and aerial surveying make up the remaining General Aviation operations.

Group	Installed Navigation Equipment					Type of Aircraft
	Navigation Computer	INS	DME		VOR	
			Normal	Scanning		
A	√	√		√	√	New Commercial Jets. New Business Jets.
B	√	√	√		√	Military Aircraft. Commercial Jets. New Business Jets.
C	√		√		√	Old Commercial Jets. Business Jets. Commuters. New General Aviation.
D			√		√	General Aviation. Commuters.
E					√	General Aviation.

Table 1.1: Users of the NAS Categorized by Navigation Capability.

for LOng RAnge Navigation), is a hyperbolic navigation system [33] operated by the United States Coast Guard and developed primarily for use in marine navigation. Since it relies on low frequency radio transmissions, it has had limited aviation use because it can exhibit degraded performance in the presence of precipitation and lightening. Its aviation applications, therefore, have been limited exclusively to enroute navigation by General Aviation aircraft. However, there has been renewed interest in LORAN and there are research efforts currently underway with the objective of making LORAN robust to precipation static and lightening.

1.2.2 Navigation in the Future NAS

The FAA's National Airspace System modernization effort entails supplanting the navigation services provided by ground based facilities like VOR and DME with GPS. This is motivated, in part, by the desire to eliminate the cost and effort associated with maintaining an expensive ground based infrastructure. Currently, there are 932 VOR and DME facilities operated by the FAA which form the backbone of the National

Airspace System architecture. It is estimated that the yearly cost for maintaining this VOR/DME infrastructure is around $84 Million[2]. The primary motivation for this modernization, however, is the enhanced safety, flexibility and efficiency that will be available with the use of GPS as the primary means of navigation. For example, one of the benefits is that area navigation capability will be accessible and affordable to all aviation users and the inefficient "connect the dots" navigation scheme will be phased out.

1.3 The Need for a Backup Navigation System

The transformation of the NAS will be gradual and the build-up to a primary-means GPS capability is expected to occur concurrently with the de-commissioning of a significant number of existing ground-based navigational facilities. As was noted earlier, however, GPS is susceptible to electronic interference and jamming. In the final state of the NAS–which is an environment where GPS is relied upon as the primary means of navigation–temporary interruptions covering large geographical areas could present operational problems for less capable aircraft that lack backup navigation systems. Such aircraft are those found in Groups C through E of Table 1.1. Since these groups represent a large number of users, *some form of backup navigation capability must be an integral part of the future NAS.*

Until recently, providing a backup navigation capability for NAS users has not been a significant issue. This is because, as shown in Figure 1.2 on page 13, the NAS has had a "built-in" backup navigation capability all along. Figure 1.2 is a time-line that summarizes the transition of the NAS from a radio-navigation based infrastructure to one based on Satellite Navigation (SatNav) systems such as GPS. Prior to 1995, aircraft navigation in the NAS relied on a relatively dense network of ground based radio navigation beacons. Each radio navigation beacon was independent and operated at a different frequency. Therefore, the probability of loosing all navigation capability in a given area was very small. Furthermore, since the distribution of the beacons was dense, a few unusable beacons did not pose a significant problem; there were always enough alternate beacons that could be used.

The transition to the new NAS architecture began when GPS was declared operational in July of 1995. GPS is currently being used in the NAS alongside the radio navigation systems. It is used for enroute navigation and some non-precision approaches. Without some form of augmentation, GPS cannot be relied on as a primary means of navigation because it lacks the accuracy, availability and integrity required for *all* phases of flight[§]. Therefore, as shown in Figure 1.2, the NAS is essentially the same as it was prior to 1995; radio navigation beacons are the primary means of navigation and provide a robust system that has the required redundancy.

The next phase of the NAS transition will occur when the Wide Area Augmentation System (WAAS) and the Local Area Augmentation System (LAAS) become operational. These are two differential systems that are being developed by the FAA to augment GPS and are expected to become operational in the first decade of the 21^{st} century. When these augmentation systems become operational, GPS will have the necessary accuracy and integrity to become the primary means of navigation. However, GPS will still be susceptible to RFI and, as shown in Figure 1.2 on page 13 a backup navigation system will be required. Several alternatives for this backup navigation system have been proposed [55]. One alternative system will consist of a skeletal network of VOR and DME. Another alternative, which is the subject of this thesis and will be discussed in detail later, consists of a skeletal network of DME augmented by a dead reckoning navigation system on board the aircraft.

After WAAS and LAAS are fielded, GPS will undergo more modifications that will make it sufficiently robust to RFI. These GPS modifications involve providing two additional frequencies for civilian users of GPS. Currently, the GPS ranging signals used by civilians are transmitted on a single carrier frequency called L_1 and centered at 1575.42 MHz. The first of the two additional frequencies that will become available to civilian users is the currently military-only L_2 frequency at 1227.60 MHz. The second civil frequency, designated as L_5, will be a new frequency at 1176.45 MHz. The new L_5 frequency is not available on the GPS satellites currently on orbit. It will

[§]Receiver Autonomous Integrity Monitoring (RAIM) is a means of providing GPS integrity without the use of an augmentation system external to the GPS receiver. In simple terms, it is based on a self-consistency check of the available GPS measurements [61]. However, the availability required for all phases of flight (especially precision landing operations) can not be achieved using RAIM alone without augmeting the GPS constellation with additional satellites [62]

be available on the new replacement GPS satellites. These satellites will be launced in the future as the satellites currently on orbit come to the end of their useful lives. Thus, it will take at least a decade for the GPS constellation to achieve the full three frequency capability and become robust to RFI.

Will a backup navigation system be required when GPS achieves a full three frequency capability? It is the judgment of this author that it will be a good idea to retain some form a backup navigation capability even after the three civil frequencies have become operational. This is because even with three civil frequencies, GPS is still a *single* system. Although very remote, there is still the possibility of a single point failure rendering the system unavailable. The consequences of such a failure might affect all aircraft in the NAS.

Figure 1.2 shows that another navigation system called Galileo is expected to become operational in the future. Like GPS, this system is a Global Navigation Satellite System (GNSS) and is planned to be deployed by the European Union. When and if Galileo matures and becomes as robust as the triple frequency GPS, two *independent* GNSS will be available. At that point, it can be argued that the transformation of NAS to a satellite based navigation system with sufficient backup capability is complete. This is because GPS and Galileo will be backups for each other. However, some may argue that a ground-based backup will still be required in order for a country to maintain control over navigation in its airspace system. This may be particularily true outside the United States because GPS is a system operated by the United States Department of Defense. As such, some non-US users may want to retain a backup navigation capability which is not reliant on GPS and over which they can exercise complete sovereignty.

1.4 Research in this Thesis

The research in this thesis concentrated on investigating various designs of a backup navigator for the aircraft in Groups C through E of Table 1.1. The approach taken in this thesis is to design a navigation system that uses, to the maximum extent possible, sensors and systems that will be part of these aircraft in the near future. Specifically, this thesis looked at sensors and systems that would be found in future

generations of Groups D and E aircraft to design the backup navigation system. It follows that, if a navigation system can be mechanized using systems found in aircraft of Groups D and E, then such a system can be implemented, with relative ease, in aircraft in the other categories.

1.5 Previous Research

Many researchers have evaluated navigation systems that do not rely on GPS. For example, the problem of aiding inertial navigation systems with VOR and DME measurements was investigated in [15]. Such navigation systems are in common use today in commercial and military aircraft. In addition, [15] also looked at the problem of aiding air data systems with continuous VOR and DME measurements. The inertial navigation and air data systems explored in [15] were of high quality and are not affordable to the users in Groups C through E of Table 1.1. In [14] navigation using low cost inertial and air data systems in an environment where GPS services have been denied was investigated. The conclusion of the research in [14] was that navigation for periods on the order of 30 minutes is not possible using inertial navigators based on low cost sensors technology that is affordable by users in Groups C through E. The research in [29] proposed an *entirely new* radio-navigation infrastructure that would supplant GPS by providing an area navigation system that is not as susceptible to jamming and interference. A redundant navigation system based on retaining a skeletal network of the existing radio-navigation infrastructure was explored in [55]. The study in [55] presents the distribution of radio-navigation aids that must left in place to retain a usable skeletal network of the existing radio-navigation infrastructure.

As will be shown in later chapters, one of the important components of the backup navigation system described in this thesis is an Attitude Heading Reference System (AHRS). Fusing low cost inertial sensors with a GPS attitude determination system to make an AHRS was first explored in [63]. In that study it was shown that the GPS attitude can be used to calibrate the low cost inertial sensors. A similar fusion algorithm was studied in [57], [38], [43] and [39] where an ultra-short baseline GPS attitude system was used to calibrate the inertial sensors. The conclusion of these

studies was that when GPS input was not available (as would be the case in an interference or jamming scenario) the attitude solution based on low cost inertial sensors alone will have considerable drift.

An essential component of an AHRS based on using low cost inertial sensors that will function in the absence of GPS is a magnetometer for heading determination. Calibration of the magnetometer, therefore, assumes an important role in designing low cost AHRS. Low cost, three-axis magnetometers are a recent invention. Most current heading determination systems use flux-gate compasses to aid a directional gyro or else simply require the pilot to manually update the gyro based on observations of a wet compass. Detailed calibration schemes for the older type of magnetometers are covered in [16] and [46]. Calibration of the more recent magnetometers is discussed in [21]. The calibration scheme in [21] is a 2-dimensional calibration scheme. A 3-D calibration scheme is required for magnetometers that will continue to provide heading information during turns. Such a calibration scheme is developed in this thesis.

1.6 Thesis Contributions

The objectives of this thesis are to research novel architectures for navigators using low cost inertial and dead reckoning sensors that can provide adequate navigation performance during a temporary unavailability of GPS. To this end, the original contributions of this thesis are:

1. Design and quantification of the performance of a DME aided velocity and heading dead reckoning system based on low performance sensor technology.

2. Justification, design and experimental verification of a novel method for calibrating strapdown magnetometers.

3. Design and quantification (analytically and experimentally) of the performance of Attitude Heading Reference Systems (AHRS) that are based on low performance sensors.

4. Design and quantification (analytically and experimentally) of the performance of Inertial Navigation Systems (INS) that are based on low performance sensor

technology.

1.7 Thesis Organization

In Chapter 2, the various components that make up the low cost redundant navigation system will be discussed in detail. The components described include individual sensors such as rate gyros and magnetometers as well as large systems used as sensors such as GPS and the skeletal infrastructure of ground based radio-navigation beacons. In Chapter 3, models describing the output errors of the various sensors used in the navigator are presented. Methods for characterizing the nature of these output errors are presented and applied to experimental data to construct and verify the validity of error models. These error models will be used in analysis and simulation studies in subsequent chapters. A key system that makes the low-cost backup navigator possible is an inexpensive Attitude Heading Reference System. The details of this system are discussed in Chapter 4. In Chapter 5, the mathematics behind inertial navigation and dead reckoning will be presented. A trade-off study on the expected accuracy of such navigation schemes versus sensor cost will also be discussed. In Chapter 6, mechanization details of a DME aided dead-reckoning navigation system will be presented. The discussion in Chapter 6 includes a detailed treatment of observability issues associated with position fixing. In Chapter 7, trade-off studies and experimental results documenting the performance of the backup navigator will be presented. In Chapter 8, concluding remarks and a summary will be presented. Chapter 8 also presents some recommendations for future research.

Figure 1.2: Estimated Time-Line for the Transition to a GNSS Based National Airspace System.

Chapter 2

The DME-Based Navigator

2.1 Introduction

In Chapter 1 the need for an affordable backup navigation system for users in Groups C through E of Table 1.1 was discussed. It was briefly noted that the proposed solution was one that combines dead reckoning information with DME-based position fixing. This chapter provides a detailed description of this navigation system. First a justification for choosing a DME-based system will be discussed. Then a description of when and how the backup navigator is used will be given. This is followed by a description of the various sensors and components of the backup navigator. Since cost is an important aspect of any system that will be used in Groups C through E aircraft, the chapter will close with a brief discussion of the backup navigator's cost and affordability issues.

2.2 Justification of a DME-Based Navigation System

NAS architectures that are based on retaining a small subset of the existing radio-navigation aids as a backup are discussed in [55]. One architecture discussed would retain a skeletal network of DMEs for $\rho - \rho$ navigation capability. The term "$\rho - \rho$" is used to describe an area navigation scheme whereby a user determines position via position fixing based on two or more range measurements. For a discussion of $\rho - \rho$ navigation the reader is referred to Appendix D of this thesis. It is the proposition of

this thesis that this architecture can be the basis for an efficient redundant navigation system because:

1. R-NAV based on DME position fixing combined with inertial navigation is a scheme of navigation that is currently used by Flight Management Systems (FMS) found on complex jet-liners [26]. The availability of inexpensive but high-powered micro-processors along with the recent proliferation of low cost sensors make construction of similar systems for Group C through E users possible. This architecture, therefore, will provide navigation services for all segments of users unlike other proposed alternatives such as LORAN which is used exclusively by General Aviation users.

2. VOR and NDB are systems that provide angular measurements and thus have accuracy that degrades with distance when used as part of a navigation system with area navigation capability. Increased accuracy will require a dense network of VOR or NDB sites. This is counter to the objective of reducing the upkeep cost for the National Airspace System which is predicated on maintaining as few ground based navigation aids as possible.

3. A usable skeletal network of ground based facilities may require relocating some radio-navigation aids. In comparison to a VOR facility, it is easier and less costly to install and maintain a DME facility. It is estimated that the cost of installing a DME facility is approximately 25 percent that of a VOR facility.

The backup navigation system must have the capability of guiding an airplane to the vicinity of an airport in inclement weather in the event GPS services are not available. The minimum navigation performance required to complete such a mission is equivalent to the level of performance provided by the least stringent of currently available non-precision approaches. An example of such a non-precision approach would be a one based on flying from a VOR located 30 nautical miles away to the airport of intended landing [69]. Such an approach is shown schematically in Figure 2.1. VOR bearing measurement errors can be between 1 and 5 degrees [15, 33, 49]. Furthermore, suppose a low performance aircraft traveling at 60 nautical miles per hour would require 30 minutes to fly from the final approach fix to the Minimum

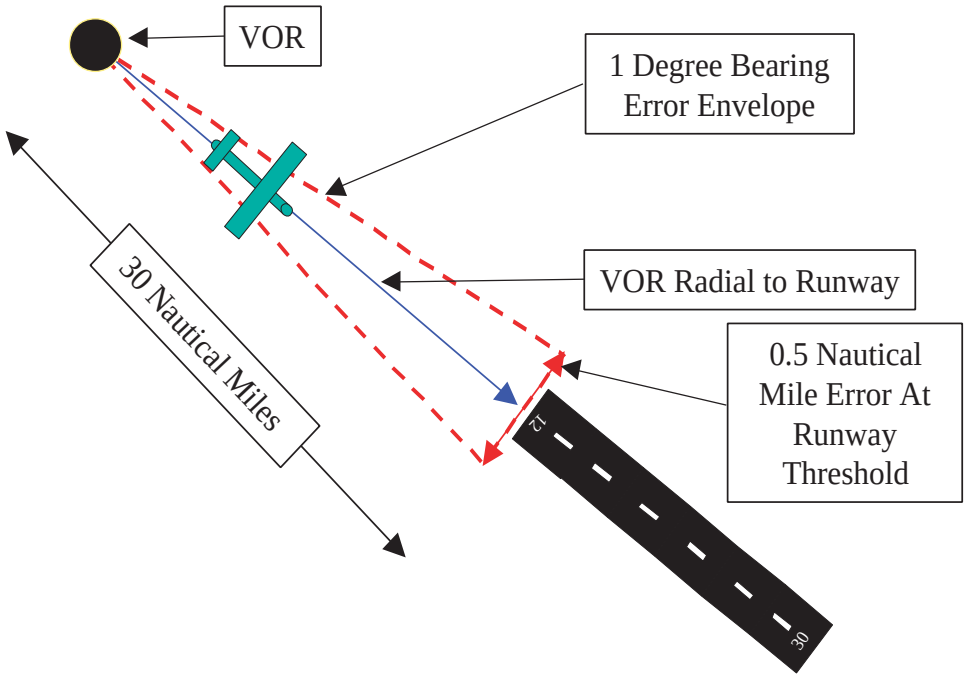

Figure 2.1: A VOR-Based Non-Precision Approach.

Descent Altitude (MDA) of such an approach. This translates into an accuracy requirement between 0.5 and 2.5 nautical miles in position after 30 minutes of flying. Therefore, the design requirement that will be used in this thesis is the more stringent accuracy requirement of 0.5 nautical miles after 30 minutes.

2.3 Operation of the Backup Navigation System

Figure 2.2 presents a flow chart that shows what kind of scenarios would force an aircraft into using a backup navigation system. Essentially, the backup navigator is required when GPS services are not available in a large geographic area due to RFI or a system-wide outage. If it is apparent that GPS services are unavailable in a given area before flight operations commence, the required action is clear and simple; flight operations will cease until GPS is available. If the loss of GPS occurs when the aircraft is in the air, then a landing must be made as soon as practical. It should

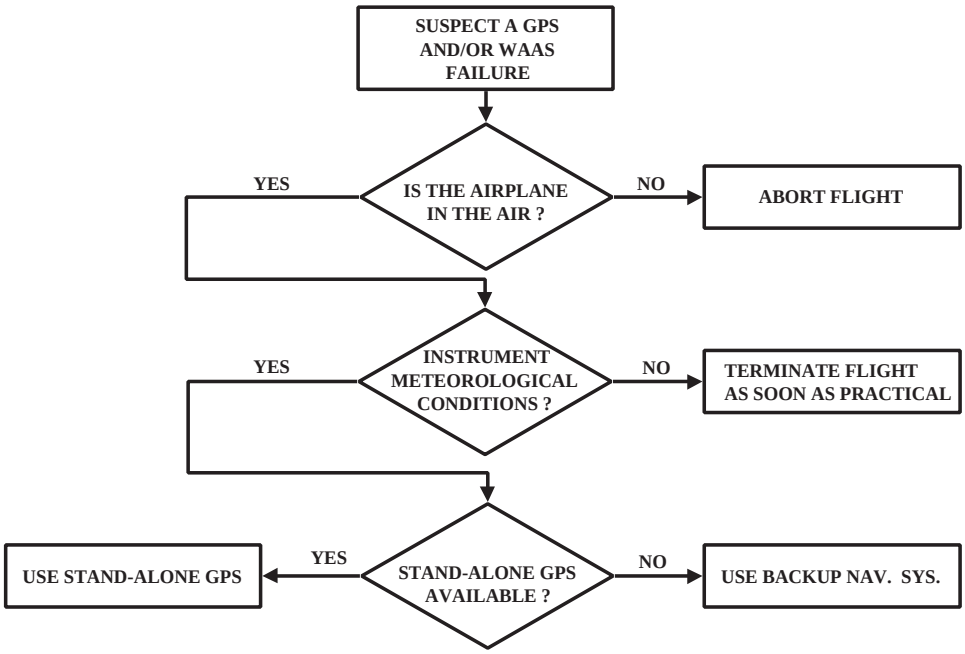

Figure 2.2: Decision Flow-Chart for Switching from GPS to Backup Navigation.

be noted that there is a possibility that only the Wide Area Augmentation System (WAAS) or Local Area Augmentation System (LAAS), which are enhancements to GPS, may be affected by RFI. In such a case, GPS based precision approaches cannot be conducted. Since the backup navigation system is designed to only provide services up to the accuracy of the lowest non-precision approach standard, the loss of WAAS or LAAS does not automatically force the use of the backup navigation system. If the stand-alone GPS level of accuracy is sufficient, it can and should be used. It should be noted that using stand-alone GPS will not provide the same level of integrity afforded by WAAS and LAAS. This is judged to be acceptable, however, in the scenarios where the backup navigator is the *only* means of navigation available for use.

Figure 2.3 is a time-line of a hypothetical flight where the backup system had to be used. The time-line starts on the left side of the schematic. At this point GPS services are available and, therefore, GPS will be used as the primary means of navigation. This phase of flight is called the calibration phase. The term calibration is

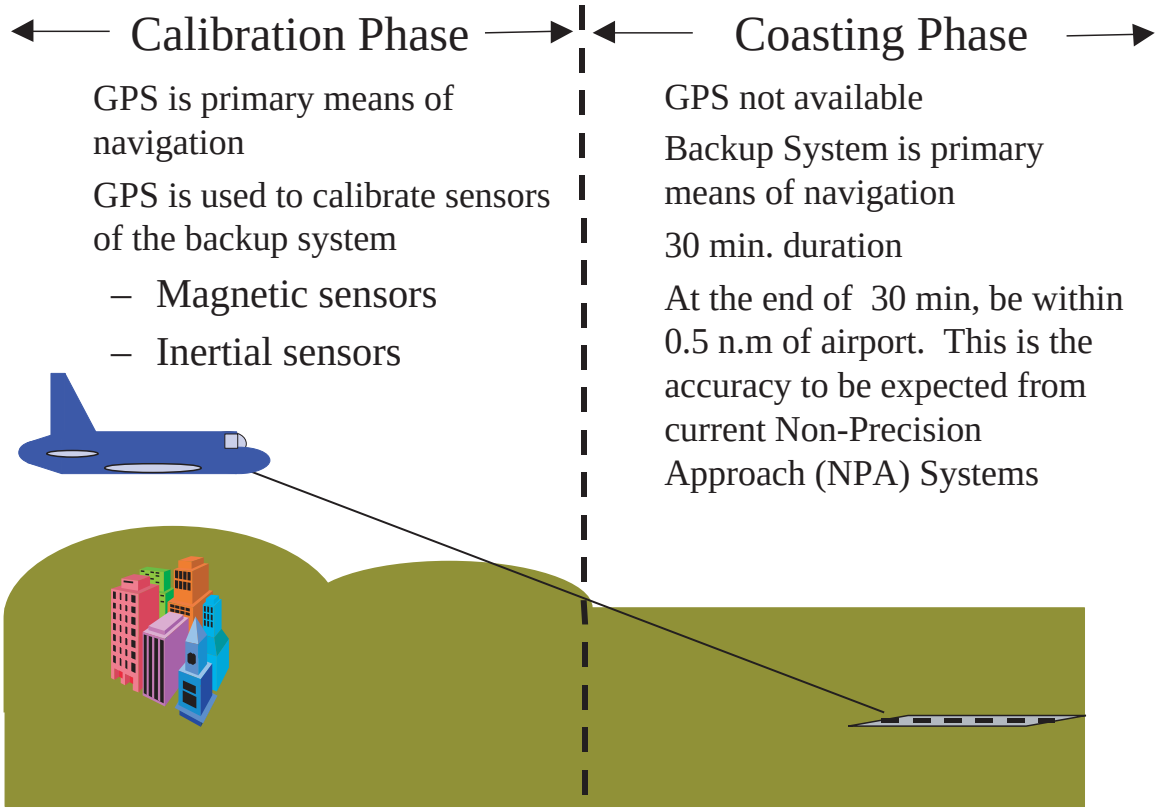

Figure 2.3: Operation of the Backup Navigation System.

used because during this time the backup system algorithms will be using GPS to calibrate the low cost sensors that make up the backup navigation system. Calibration of the magnetic sensor is covered in Chapter 3 while Chapter 4 deals with calibration of the inertial sensors. Midway through this hypothetical flight, GPS services become unavailable. At this point the airplane is relying on the backup navigator and "coasting" through the GPS outage. Hence, this phase of the flight is called the coasting phase. Since the backup system has area navigation capability (i.e., latitude and longitude information are generated by the system), the transition from using GPS to using the backup system should be seamless.

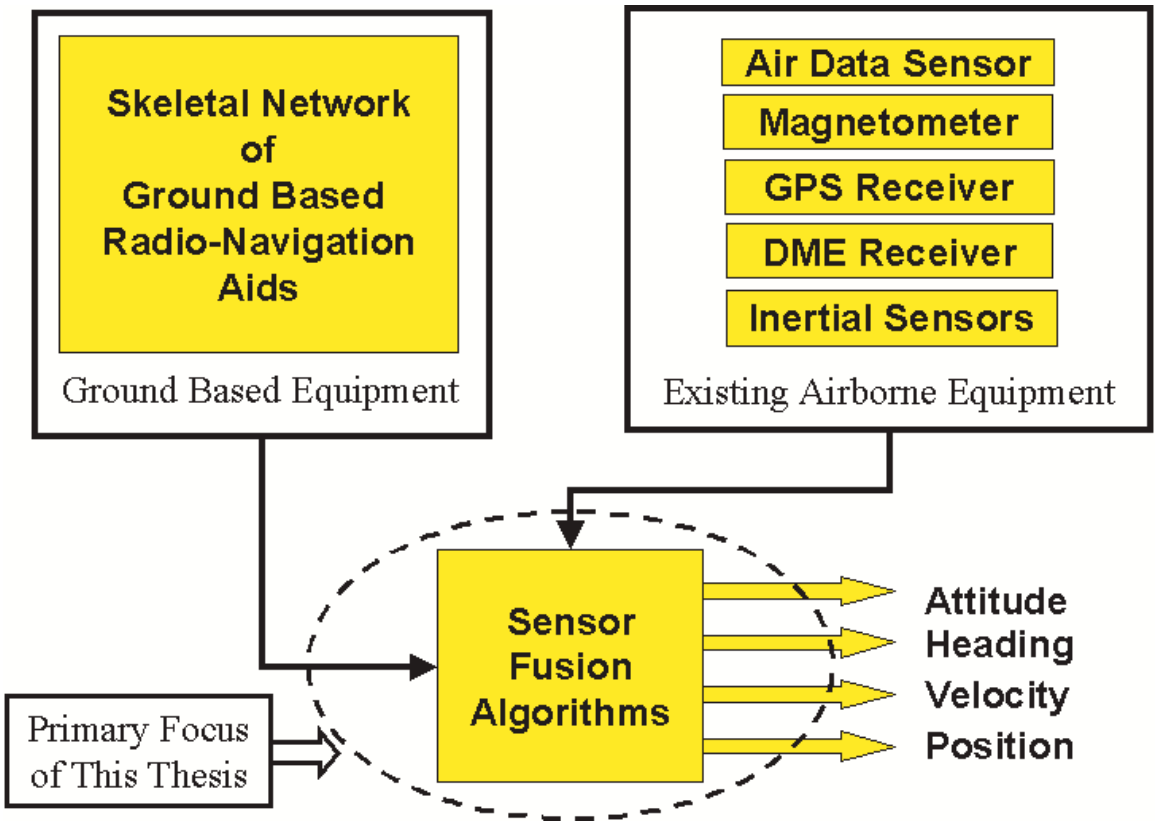

Figure 2.4: Schematic of Backup Navigation System.

2.4 Architecture of the Backup Navigation System

Figure 2.4 shows the three major components (in addition to the GPS constellation) that are required to mechanize the backup navigation system. These components are the equipment on-board the aircraft, the ground based skeletal network of radio-navigation aids and the sensor fusion algorithms. The on-board equipment consists of those sensors required to make a dead reckoning navigator. The ground based skeletal network is composed of a select few DME transponders. The sensor fusion algorithms are the algorithms for blending all the sensor outputs to generate the aircraft navigation state vector which consists of attitude, velocity and position.

When the system is in operation, position updates will come from DME-based

position fixing. Between the DME updates, dead reckoning is used to propagate the position solution. The high bandwidth information needed for guidance and control of the aircraft will be provided by the dead reckoning system. The DME range measurements will be used intermittently to provide position updates thereby bounding the dead reckoning system drift error.

For reasons that will be explained later in the chapter, two simultaneous DME range measurements are not normally available. The position updates have to come intermittently in the form of a single range measurement. In this case, it is obvious that at any instant position is not observable from a single range measurement. Therefore, a means of obtaining a rough position estimate between subsequent range measurements is required. This can be done by:

1. Using inertial sensors combined with barometric altitude information from an air data system or,

2. Dead reckoning using heading information derived from a magnetometer and low-performance inertial sensors combined with air speed and altitude information from an air data system.

All the sensors required to mechanize the inertial navigation or dead reckoning systems discussed above are shown in the upper-right box of Figure 2.4. As will be shown in Chapter 5, however, mechanizing an inertial navigator requires high quality inertial sensors which are unaffordable by users in Groups D and E of Table 1.1. A more practical solution which can be implemented by all users is a heading and air speed dead reckoning navigation system.

From the combined intermittent range measurements, altitude information and dead reckoning, position is observable and hence navigation is possible. This scheme of using a single range measurement combined with dead reckoning is shown graphically in Figure 2.5.

2.5 Equipment Installed on the Aircraft

The backup navigator will require that the following equipment be installed or already available on the aircraft: a WAAS capable GPS receiver, an inertial sensor

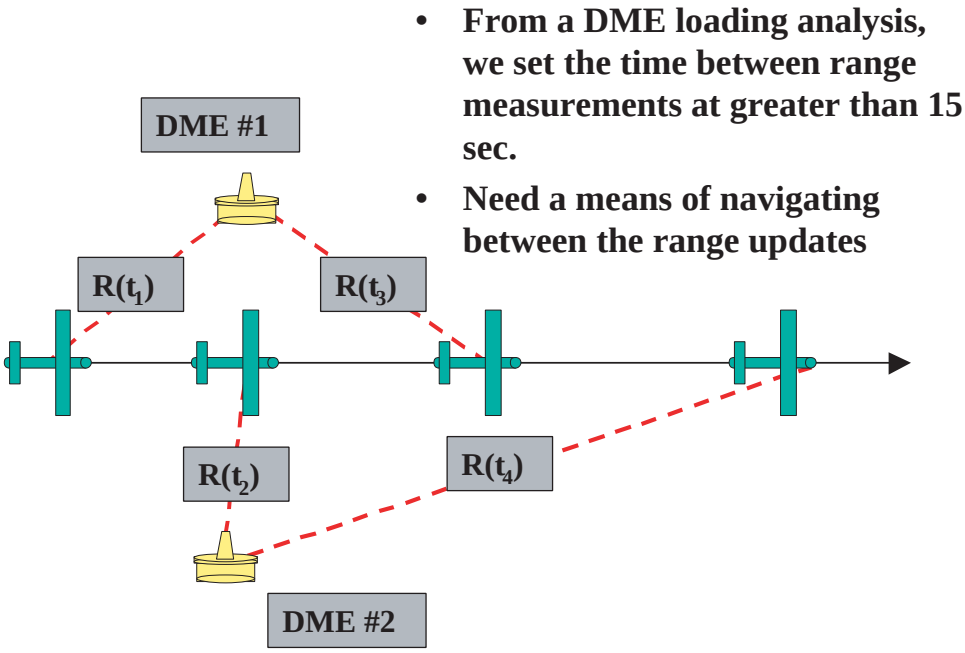

Figure 2.5: Intermittent Ranging Combined with Dead Reckoning.

suite, an air data system, a magnetometer triad and a DME receiver. The inertial sensor suite and the magnetometer triad are used to mechanize an AHRS. The AHRS and the air data system form the core of the dead reckoning system.

2.5.1 GPS/WAAS Receiver

In the absence of RFI, GPS will be the primary means of navigation. So the aircraft will have to be equipped with a GPS receiver. The Global Positioning System (GPS) is a navigation system based nominally on 24 satellites in Earth orbit. A user equipped with a GPS receiver can get ranging information from satellites in view and compute a position solution very accurately. Even though GPS has proven to be an extremely accurate position sensor, in some situations, such as precision approaches, the accuracy and integrity required exceeds that which can be provided by stand-alone GPS. The required levels of accuracy are not achieved with stand-alone GPS because of various unmodeled errors such as satellite ephemeris and clock errors and variations

in ionospheric delays. Furthermore, as noted earlier (see footnote on page 8) RAIM with an unaugmented GPS satellite constellation does not provide the availability required.

The Wide Area Augmentation System (WAAS) is an enhancement to GPS that will become fully operational in the near future and will allow users to conduct precision approaches. The basic idea behind WAAS is the concept of differential GPS. In differential GPS, a receiver is placed at a location with precisely known position coordinates. The precisely known position location is called a reference station. The difference between the GPS generated position solution and the precisely known coordinates of the reference station is the error in the GPS position solution. This error is used to generate a correction vector that is broadcast to users allowing computation of an improved position solution. The correction vector transmitted consists of parameters describing the three-dimensional ephemeris errors, satellite clock offsets, and the ionospheric time delay parameters. The fully operational WAAS is comprised of 25 of these reference stations distributed over the Coterminous United States (CONUS).

2.5.2 Inertial Sensors

Inertial navigation is a method for determining a vehicle's position, velocity and attitude by measuring rotation and acceleration. Rotations and accelerations are derived from rate gyros and accelerometers, respectively. The two sensors as a group are called inertial sensors. The accuracy of the inertial navigation position solution is dependent on the quality of the inertial sensors used. As would be expected, higher quality sensors with characteristically stable outputs give better position accuracy than lower quality sensors with larger time-varying output errors. Figure 2.6 shows that there is a wide spectrum of quality when it comes to inertial sensors and different applications call for different sensor qualities.

The inertial sensors used in the backup navigation system discussed in this thesis are of the quality labeled "automotive grade" or "consumer grade." This term is used to describe these sensors because their primary application is in the automotive industry (active suspensions, skid control, etc.) or consumer hardware (camera stabilization, computer mice, etc.). The individual sensors range in cost from $25 to

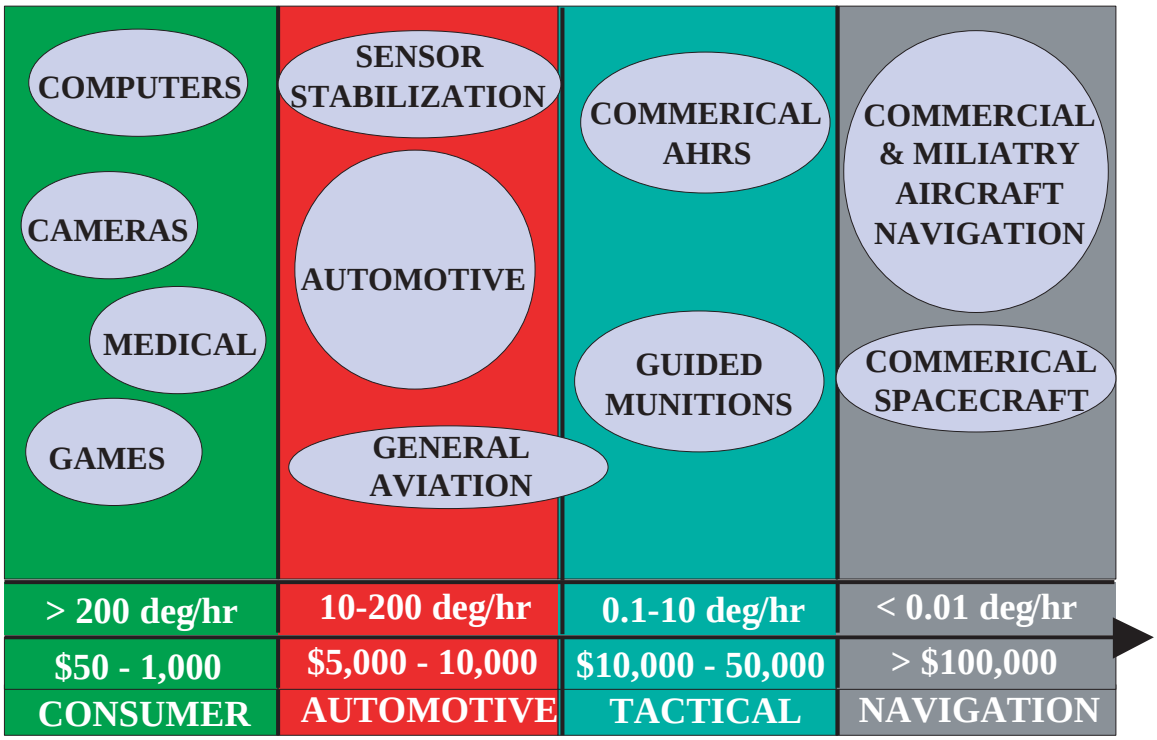

Figure 2.6: Classification of Inertial Sensors and Navigation Systems by Quality.

$1000 and are expected to drop in price in the future. In this thesis, tactical, automotive and consumer grade inertial sensors will collectively be referred to as "low performance" sensors.

The low performance accelerometers used in the backup navigation system are solid state accelerometers. These accelerometers contain a pendulous silicon proof mass. This proof mass deflects when the vehicle is subjected to an acceleration. The deflection is proportional to the vehicle acceleration plus gravity. The deflection is sensed and becomes the accelerometer output. An excellent and detailed treatment of the workings of solid state accelerometers can be found in [52] and [68].

The gyros used in the backup navigation system discussed in this thesis are either solid state vibrating structure gyros or Fiber Optic Gyros (FOG). The vibrating structure gyros have a sensing element that is made to vibrate. When the vibrating structure is subjected to a rotation, a coriolis acceleration will cause the vibrating

element to deflect by an amount proportional to the angular rotation rate. This deflection is sensed and is output as the gyro's reading. The sensing element in a FOG is a coil of fiber-optic material. Two counter-rotating light beams are injected into the coil. When rotation is absent, the two counter-rotating light beams are in phase. When the coil is subjected to a rotation, there will be a phase shift between the two counter-rotating light beams caused by the Sagnac effect. This phase shift is proportional to the rotation rate. The measured phase shift is multiplied by the appropriate proportionality factor and output as the angular rate. A more detailed treatment of the workings of solid state and fiber-optic gyros can be found in [52] and [65].

2.5.3 Air Data Systems

The air data system is a composite of sensors used to measure the aerodynamic and thermodynamic characteristics of the air surrounding an aircraft in flight. From the stand point of navigation, the ultimate objective of determining these characteristics is to be able to determine aircraft speed relative to the air mass in which it is moving and altitude above mean sea level. The system consists of special plumbing called the pitot-static system, pressure transducers and a temperature sensor. A schematic diagram of an air data system is shown in Figure 2.7.

The altitude above mean sea level, also called pressure altitude, is determined by the pressure measurement made at the static port corrected for non-standard atmospheric conditions. The pressure at the static port is sensed by the static port pressure transducer and digitized into information that can be used by the navigation computer. Assuming the aircraft is operating on a day where standard pressure and temperature conditions are present, the relation between measured pressure, p_m, and computed altitude, h_c, is given by [56]:

$$h_c = \frac{T_0}{\lambda}\left[1 - \left(\frac{p_m}{p_0}\right)^{\frac{R\lambda}{g}}\right] \tag{2.1}$$

The variables p_0 and T_0 represent the pressure and temperature respectively at sea level. R is the universal gas constant, g is the magnitude of the local gravitational

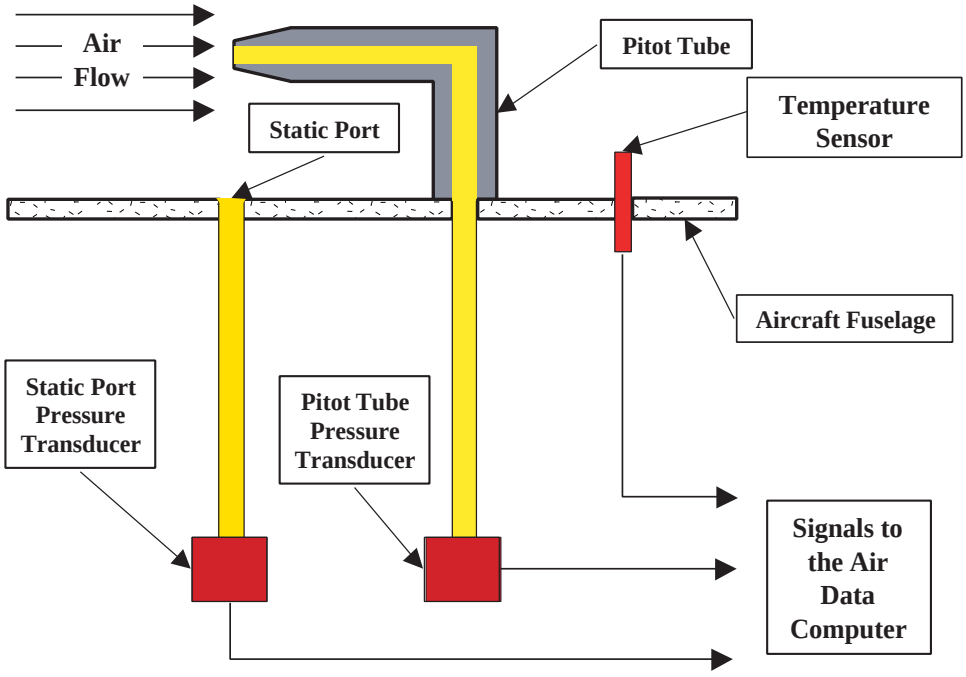

Figure 2.7: Schematic Diagram of an Air Data System.

acceleration vector and λ is the temperature lapse rate. The temperature lapse rate is the rate at which the temperature of the standard atmosphere decreases with increasing altitude.

On a day when the atmospheric conditions are not standard, p_0 and T_0 have to be adjusted to reflect the actual conditions at sea level. Since GPS is part of the navigation system, GPS derived altitude can be used to compute an additive altitude bias to correct Equation 2.1. GPS derived altitude can also be used to back-out the values of p_0 and T_0. However, the information required to compute the altitude bias is readily available at airports with control towers and may be easier to use.

The components of the air data system needed for measuring air speed are the pitot tube and its associated pressure transducers along with an outside air temperature sensor. The pitot tube is normally mounted near the leading edge of a wing or near the front of the fuselage and is used to measure the stagnation or impact pressure of the air stream when the aircraft is in flight. The static port is used to measure

the static pressure of the air stream in which the airplane is flying. The pressure transducers at the end of the pitot tube and the static port convert the stagnation pressure and static pressure measurements into electrical signals that are sent to the air data computer for processing.

The difference between the stagnation and static pressures is the observable quantity used to generate airspeed. The relation between this pressure difference (ΔP) and the calibrated air speed (V_c) is given by:

$$V_c = \sqrt{\frac{2}{\rho}}\sqrt{\Delta P} \tag{2.2}$$

The quantity $\sqrt{\frac{2}{\rho}}$ can be viewed as the sensor scale factor which is a function of air density, ρ. Air density is not constant but changes with altitude and temperature. This is why a temperature sensor is part of an air data system. Air is an ideal gas and given temperature and pressure altitude information, the air density can be computed. In some aircraft (mostly low end General Aviation aircraft), the airspeed sensor is a mechanical device while the air temperature sensor is a separate and independent device. In this case, the compensation for temperature is not made automatically but has to be computed by the pilot and applied to the airspeed reading.

2.5.4 Heading Sensors

Heading is the angle formed between the longitudinal axis of an airplane and the direction to the north pole. For a static user, heading can be determined using high quality rate gyros to measure Earth's rotation rate vector. It's projection onto the locally level horizontal plane yields heading. This process is called gyrocompassing and requires expensive inertial sensors. This is because Earth's rotation rate vector is approximately 15°/hr (0.0042°/sec) in magnitude and determining heading in this fashion requires gyros with a drift stability of better than 0.1°/hr to achieve heading accuracies of 0.5°. Measuring heading with respect to magnetic north, however, requires inexpensive sensors like compasses or magnetometers. Fortunately, the difference between magnetic north and true north is a well known function of location.

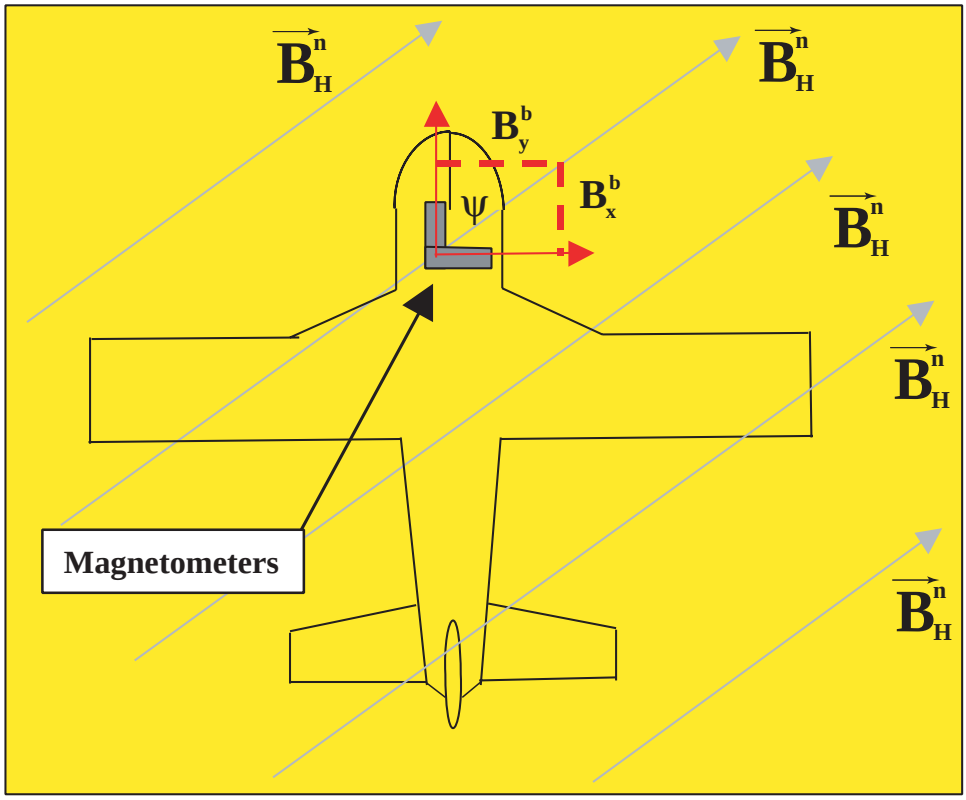

Figure 2.8: Basics of Heading Determination.

This difference is called the magnetic variation or declination. Thus given the latitude, longitude and altitude of a user, true heading is easily obtained by adding magnetic heading to the local magnetic variation.

Since the objective of this research is to construct a navigator that employs low-performance sensors, the heading sensor of choice is a magnetometer. A magnetometer is a device for measuring the strength of magnetic fields. In aviation applications, a single axis magnetometer alone is of very little value. Instead, what is normally used is a pair of magnetometers mounted perpendicular to each other or a triad of magnetometers mounted orthogonally. In this configuration, the magnetometers are used to measure the strength and components of Earth's magnetic field vector from which heading is computed as shown in Figure 2.8. As shown in Figure 2.8, the horizontal component of earth's magnetic field vector, $\vec{B}_H$, points to magnetic north. $\vec{B}_H$

is resolved into its components which are measured by the magnetometers strapped to the aircraft and aligned with its x and y axes. When the aircraft is flying straight and level (zero pitch and roll angles), this information about Earth's magnetic field is used to determine aircraft heading with respect to magnetic north pole using the following formula:

$$\psi = -\tan^{-1}\left(\frac{B_y^b}{B_x^b}\right) \tag{2.3}$$

If the aircraft is not flying with wings level, using Equation 2.3 to compute heading will result in heading errors because now the magnetometers measure a portion of the vertical component of Earth's magnetic field vector. These errors can be very large because the vertical component of Earth's magnetic field vector is typically larger than the horizontal component. If the aircraft is not flying with wings level, then the vector measurements generated by magnetometers strapped to the body axis of the airplane have to be transformed to the locally level navigation frame before using Equation 2.3. This transformation is accomplished by using the pitch and roll attitude information generated by an Attitude Heading Reference System (AHRS).

There are various ways for measuring the strength of magnetic fields. The magnetometers used in the system discussed in this thesis are Anisotropic Magnetoresistive (AMR) sensors. These sensors have a sensing element that is made from a nickel-iron alloy (or Permalloy). The electrical resistance of the Permalloy sensing element changes in the presence of magnetic fields. The Permalloy material is normally deposited on thin silicon wafers which can be bulk manufactured in a form suitable for commercial integrated circuit packages. The sensing element of the magnetometer used in this thesis had dimensions on the order of 10 mm on a side.

2.5.5 Distance Measuring Equipment (DME) Receiver

DME is a pulse-ranging system used in aviation which is based on the radar principle. The airborne DME transceiver is called an interrogator and operates between 960 and 1215 MHz. The airborne interrogator emits a pair of pulses which, when received by the ground transponder, are, after a short delay of 50 μseconds, retransmitted back to the airborne interrogator. The airborne interrogator then measures

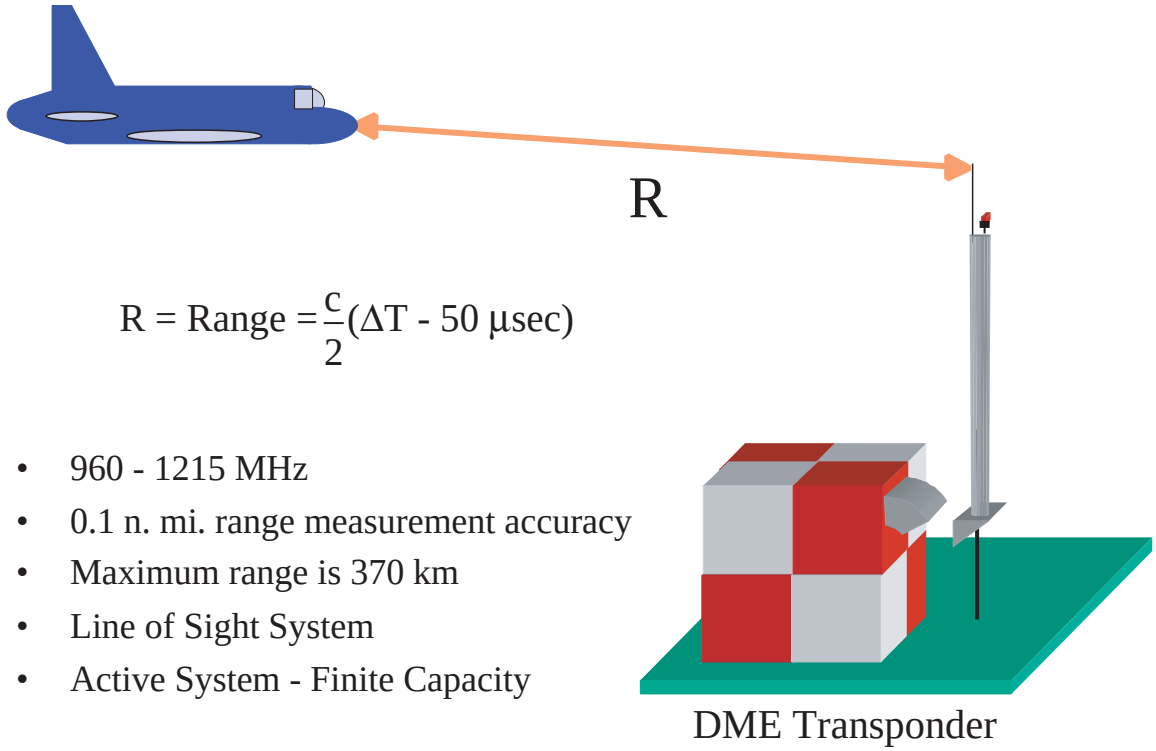

Figure 2.9: Distance Measuring Equipment (DME).

the elapsed time between transmit and receive, subtracts the 50μs delay from the ground based transponder and computes the distance by multiplying the round trip time by the speed of light divided by 2. This is shown schematically in Figure 2.9.

When an airborne transmitter is tuned to a particular ground based transponder frequency for the first time, it emits pulses at an average rate of 135 pulses per second and is said to be in the search mode. Once the airborne interrogator is "locked" on the ground transponder, it reduces its interrogation frequency down to an average of 25 pulse pairs per second and is now in the tracking mode. Each ground transponder is capable of responding to 3000 pulses per second. This translates to roughly 100 airplanes (95 in tracking mode and 5 in search mode).

If high update rate DME range information can be obtained from two or more DME transponders, this information alone can be used for horizontal navigation and other sensors would not be required. However, obtaining continuous or very frequent

range measurements from two or more DME transponders is difficult in practice. Low-end DME receivers are capable of tracking only one DME station at a time. Receivers called scanning DMEs capable of tracking multiple stations at a time exist, but these are high-priced items and used almost exclusively in the newest commercial jet liners. One solution is to carry multiple DME receivers so that two or more simultaneous range measurements from two separate DME ground stations will be available. This is also a costly solution because it requires an additional DME receiver.

Another solution is to use one DME to acquire the range from multiple DME ground stations intermittently. This scheme is problematic because DME is a query and response system and the potential exists for saturating the DME ground transponder if intermittent interrogations are not done carefully. This is because each time an airborne DME receiver switches from tracking one station to tracking another station, it will interrogate at a rate of approximately 135 pulses per second. This is approximately five times greater than the interrogation rate during normal tracking. If this switching is done too frequently, the number of aircraft that can be serviced by a given ground station will be reduced.

This problem can be mitigated by scheduling interrogations in a way that ensures that a given DME ground transponder can handle the expected traffic load. Such an interrogation schedule and supporting calculations are shown in Figure 2.10. In this schedule, a single airborne DME interrogator obtains range measurements from two ground based DME transponders sequentially. In the schedule shown, it is conservatively assumed that it takes a DME receiver four seconds in the tracking mode before it "locks in." Once the airborne unit is tracking a given DME station, it will obtain range measurements for one second. If we match the number of pulses that would be emitted in a minute in this scheme with the number of pulses that would be emitted if the receiver was in tracking mode continuously, then we see that a given DME station can be interrogated only twice a minute. In light of the navigation scheme shown in Figure 2.5, this interrogation schedule can be interpreted as follows: The interval between any measurements adjacent in time shown in Figure 2.10 must be at least 15 seconds apart.

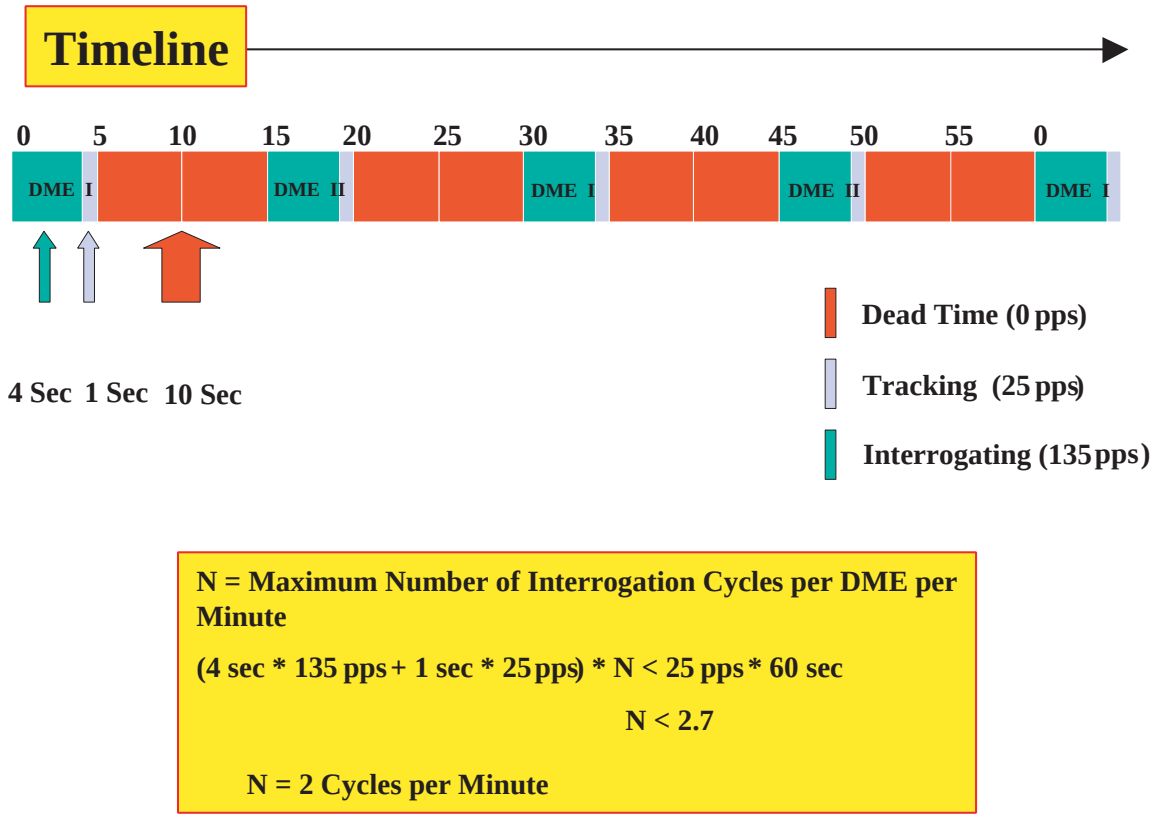

Figure 2.10: DME Interrogation Schedule.

2.6 Ground Based Infrastructure: A Skeletal Network of DME

In [55] various architectures that would reduce the size of the current radio-navigation infrastructure while maintaining emergency navigation capability were investigated. These NAS architectures are intended to assure the safe recovery of aircraft in the event of a GPS/WAAS navigation service failure. One of the architectures looked at would retain enough DME for double or triple ρ-ρ navigation capability using scanning DMEs. Double coverage means that range measurements from two DMEs will be available at all times while triple coverage means range measurements from three DMEs will be available at all times. To support the $\rho - \rho$

navigation scheme, the [55] study looked at four options. The first option provides for double coverage of DME at 200 major airports for altitudes as low as 1500 feet above ground level. The second option provides similar coverage but to altitudes as low as 500 feet. The third option provides triple coverage to 1500 feet. The final option provides triple coverage to 500 feet. The number of DME sites required for these options are:

1. Option I: 318 DME (273 Existing, 25 Additional)
2. Option II: 356 DME (356 Existing, 32 Additional)
3. Option III: 442 DME (366 Existing, 76 Additional)
4. Option IV: 512 DME (393 Existing, 119 Additional)

Figure 2.11 shows the current distribution of DME transponder sites over CONUS. Given two or more DME range measurements and a measurement of barometric altitude, one can derive latitude, longitude and altitude information. DME is a line-of-site system and from Figure 2.11 it is readily apparent that there are places in the CONUS airspace where range measurements from two or more separate DMEs (i.e., multiple DME coverage) will not be available at the same time. The DME coverage density shown in Figure 2.11 does not adequately provide area navigation capabilities everywhere in CONUS airspace; a skeletal network of DME will be even less capable. A solution to this problem is to provide the coverage required in the vicinity of those airports where disruption of GPS navigation services can have a significant effect on the flow of air-traffic in the NAS. Figure 2.12, based on data in [55], shows the locations of the 200 busiest airports in CONUS.

If double DME coverage is provided at these airports, position fixing using DMEs can be accomplished and a redundant means of navigation will have been provided. Figure 2.13 is a summary of data compiled in [55] and shows the number of existing and new DME sites that will be required to provide double and triple coverage down to altitudes of 500 and 1500 feet AGL at the airport locations depicted in Figure 2.12.

Even though triple coverage down to 500 feet AGL may not be necessary at all airport locations, it should be noted that such coverage will only require approximately 1/2 of the total number of DMEs shown in Figure 2.11. These results demonstrate the

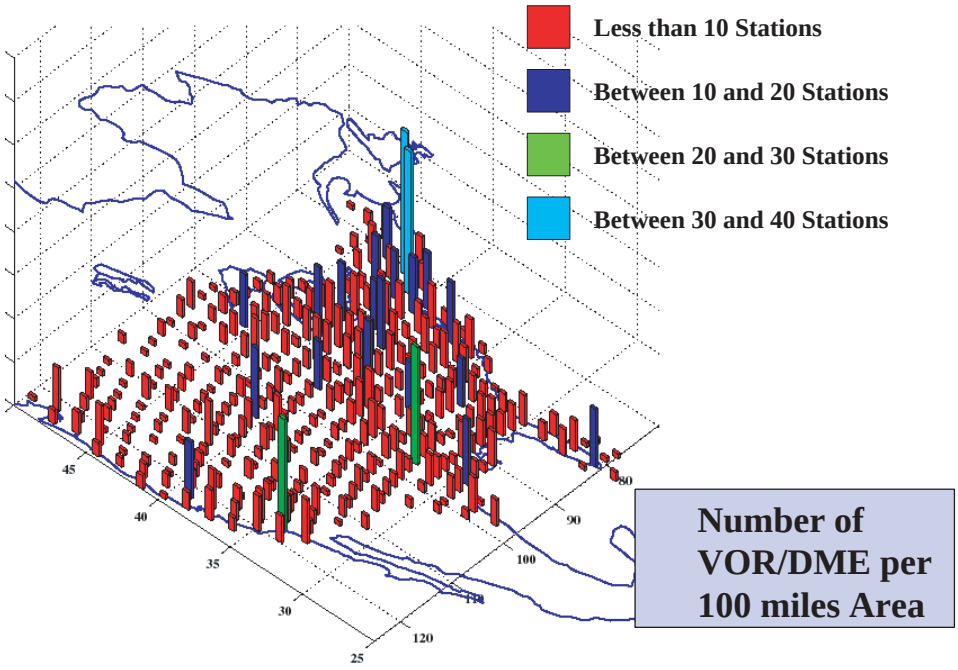

Figure 2.11: VOR/DME Distribution (Bins = 100 miles^2 Area. Total Number of VOR/DME Station Currently = 932.

possible reduction in the existing radio-navigation aid infrastructure while providing a redundant means of navigation in the event that GPS services are disrupted.

There are advantages and disadvantages to the double and triple coverage scenarios. The advantage of the double coverage scenario is that it requires fewer DME and, therefore, results in a smaller total system cost. Its drawback is that there is an ambiguity in the position solution. To illustrate this, suppose a user is located at location A as shown in Figure 2.14. If, in a double coverage scenario, the user processes range measurements from DMEs I and II only, then there will be an ambiguity in the position solution. This is because a user at location B would observe the

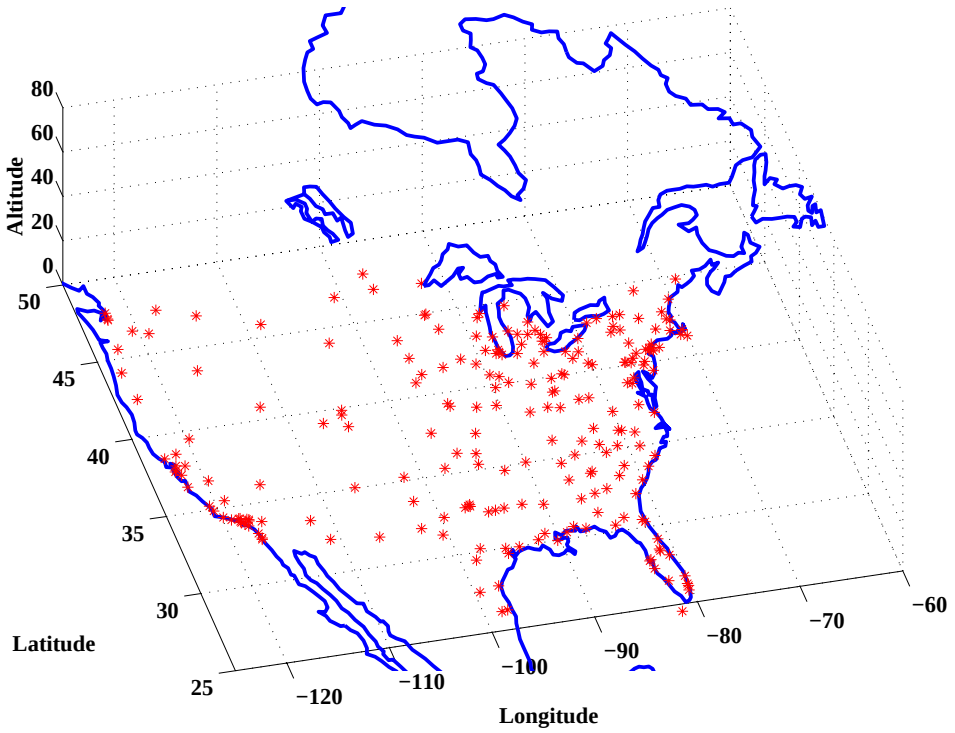

Figure 2.12: Location of 200 Busiest Airports.

same range measurements as the user at location A. As shown in Figure 2.14, a triple coverage scenario whereby range measurements from DME III are also incorporated, eliminates this ambiguity.

A third DME range measurement, however, is not required to eliminate the ambiguity. Heading information in conjunction with prior knowledge of ones position can be used to eliminate the ambiguity. For example, consider an aircraft flying north (i.e., with a heading of $\psi = 0°$) approaching DME I and II from the south. By the time the aircraft is at location A, given the previous range measurements from DMEs I and II and the position history, it is clear that location A would be the correct solution. If the aircraft approaches the DMEs from a point to the west of DME I and is flying with a heading of $\psi = 90°$, then a similar argument can be used to eliminate the position ambiguity. In general, as long as DME I and II are far apart, then the history of the position solution can be used to eliminate the ambiguity. In summary,

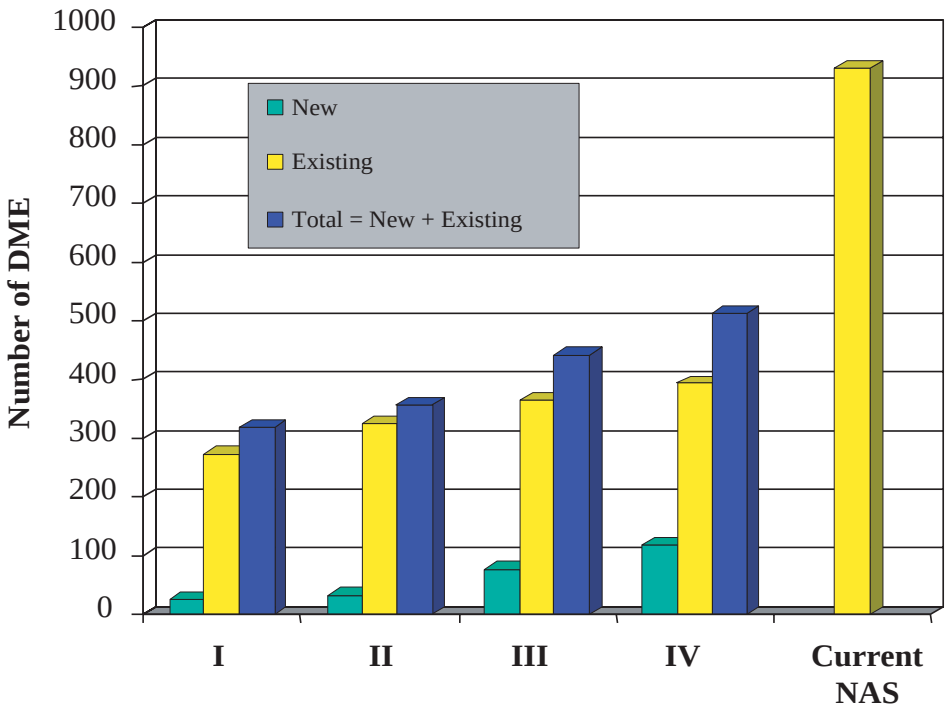

Figure 2.13: Number of DME Required for Triple and Double Coverage Discussed on Page 32. (I) Double Coverage to 1500 AGL, (II) Double Coverage to 500 ft AGL, (III) Triple Coverage to 1500 ft AGL, (IV) Triple Coverage to 500 ft AGL.

if heading information and position history are used and the pair of DMEs providing the range information are far apart, the position ambiguity of a double coverage scenario can be dealt with successfully.

The accuracy of the position fixing solution is affected by geometry of the problem or the relative location of DMEs with respect to the user. Even though triple DME coverage is a superior geometry for the position fixing problem, double coverage can be adequate in certain scenarios. The analysis of DME geometry and its effect on the position fixing solution will be deferred until Chapter 7.

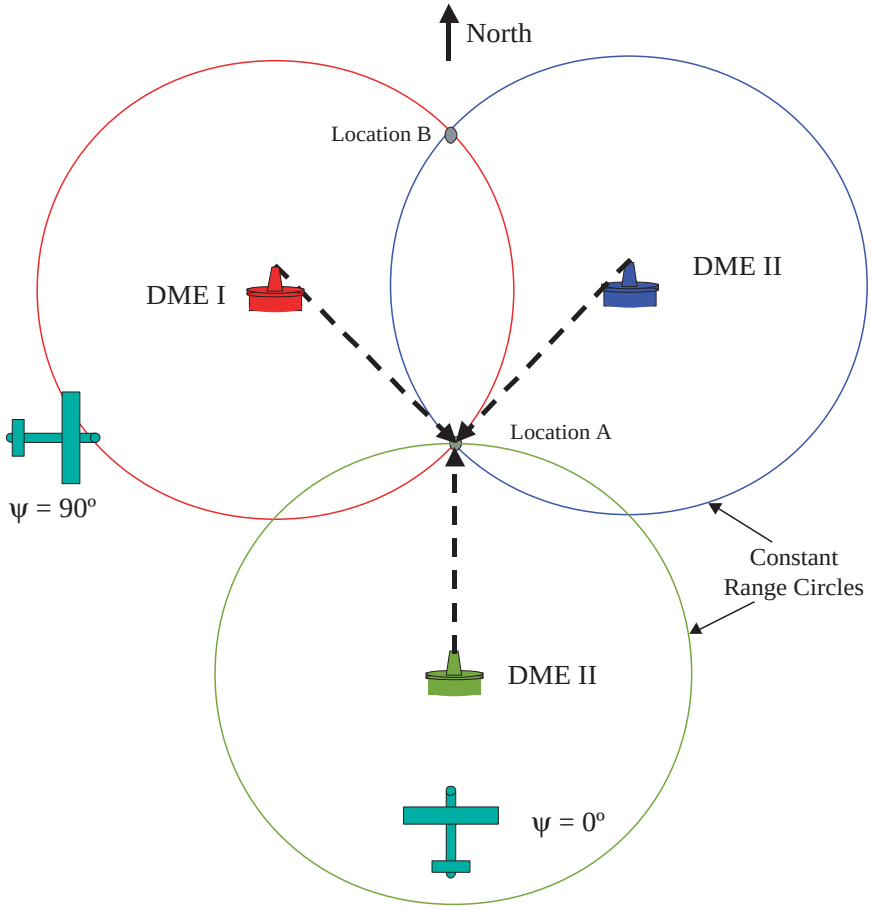

Figure 2.14: Double DME Coverage versus Triple Coverage.

2.7 Cost of the Navigation System

An important constraint in the design of this backup navigator for use by aircraft in Groups C through E is system cost. The approach taken to keep the cost of this system down is, to the maximum extent possible, rely on equipment that already is or will be part of all aircraft in the near future. All the sensors required to mechanize the backup navigator, except for the DME receiver, are also required to mechanize a modern solid state AHRS which can drive a "glass cockpit" type display. These solid state AHRS will be replacing the existing mechanical systems because the mechanical AHRS are unreliable and lack the flexibility that the newer AHRS afford. While such

Sensor or Component.	Is it Existing Equipment?	Estimated Sensor Price.	Estimated Price to Consumer.
GPS Receiver	Yes	$0	$0
DME Receiver	Yes	$0	$0
AHRS based on low-performance sensors	No	$1.5 k	$10k
Microprocessor or Navigation Computer	No	$0.5 k	$3k
Total Cost		**$2.0k**	**$13k**

Table 2.1: Components and Estimated Cost of Sensors Required for Mechanizing a DME-aided Dead Reckoning Navigator In a General Aviation (or Group E) Aircraft.

AHRS are already part of the suite of instruments found in Groups A and B aircraft, it is also reasonable to assume that solid state AHRS are going to be an integral part of the next generation of Groups C through E aircraft. In view of this likely future trend, it is estimated that the sensor cost breakdown for constructing this system will be as shown in Table 2.1. Given this sensor cost breakdown, it is not unreasonable to assume that the cost of the entire system will be on the order of $10,000.

Chapter 3

Sensor Error Models

3.1 Introduction

In the previous chapter a general description of the GPS/WAAS backup navigation system was presented. The sensors that will be part of the proposed system were described. The output of any sensor is, to some degree, corrupted by errors. In this chapter, the nature of these sensor errors and techniques for characterizing them will be discussed. These techniques will be used to identify the source of the sensor errors and develop mathematical models describing them. The chapter will close with a discussion of a three-dimensional magnetometer calibration algorithm.

Before going into the details of developing error models, the objective of this chapter and that of developing error models should be made clear. The primary objective of developing the mathematical error models is so that they can be used in trade-off studies evaluating various configurations of the backup navigator.

3.2 A General Inertial Sensor Error Model

The two inertial sensors used in navigation are gyros and accelerometers. Gyros measure incremental rotation or rotation rate. Gyros that measure incremental rotation are called rate integrating gyros. Gyros that measure rotation rate are called rate gyros. The term "accelerometer" is a misnomer because these devices do not measure acceleration. Instead, accelerometers measure specific force. Specific force,

$\vec{f}$, is the vector quantity defined by the following:

$$\vec{f} = \vec{a} - \vec{g}, \tag{3.1}$$

where $\vec{a}$ is the acceleration of the vehicle containing the accelerometer and $\vec{g}$ is the local gravitational acceleration vector. Since the local gravitational vector, $\vec{g}$, is not a constant but varies with latitude, knowledge of the variation of $\vec{g}$ is required to use an accelerometer in navigation. Furthermore, $\vec{a}$ is measured in a reference frame fixed to the aircraft and $\vec{g}$ is known in the locally level reference frame. Hence, aircraft attitude must be known in order to evaluate Equation 3.1.

In this work, a general sensor output model is used to describe the output of inertial sensors. The sensor output model has the following form:

$$s_m = (1 + s_f)s_t + b(t). \tag{3.2}$$

In Equation 3.2, s_m is the sensor's measured output. s_t is the true value of the quantity that the sensor is measuring. This true value is corrupted by a scale factor error, s_f and a bias, $b(t)$.

The bias term, $b(t)$, has the following form:

$$b(t) = b_0 + b_1(t) + b_w(t). \tag{3.3}$$

The term b_0 represents a constant null-shift. The term $b_1(t)$ represents a time varying component of the bias. The term $b_w(t)$ represents the sampling noise. Constructing sensor error models consists of identifying the value of the variable s_f and the components of $b(t)$.

It is straight forward to obtain the b_0 term. For example, it can be obtained by taking long term data when the sensor is subjected to a zero input; the average of the long term data will be b_0. In can also be computed on-line using an estimator that is part of the very navigation system that employs the sensor. This aspect of determining b_0 for rate gyros will be discussed in Chapter 4. The value of b_0 is sometimes listed on data sheets for inertial sensors and is referred to as the "turn-on to turn-off" bias variation or "null-shift."

The challenge in constructing error models is primarily associated with the process of determining $b_1(t)$. There are two aspects to this process. Firstly, the mathematical form of the error model must be identified. Secondly, the the specific numerical quantities that are part of the mathematical model must be determined. The discipline of system identification provides various techniques that can be used for fitting error models to data. For example, one can use the classical tools such as ARX, ARMA, or Box-Jenkins described in [54] or modern methods like OKID and subspace identification techniques discussed in [48]. These methods will simultaneously identify the mathematical form and determine the numerical quantities to be used in these mathematical models. It has been this authors experience, however, that these tools are not efficient when trying to model low-performance inertial sensors. The reasons for this are:

1. In this work, the approach taken is to construct a *single* model that is descriptive of the characteristics of *all* the inertial sensors in a given class shown in Figure 2.6 on page 23. For a given brand of low-performance inertial sensor, let alone a class, the output error model is different from sensor to sensor. Thus, the classical model identification tools result in models that are specific to a given sensor and not a given class of sensors. This runs counter to the objective of constructing an error model that is uniform across a general class of sensor quality.

2. These tools can result in mathematical models that are of high order. This does not make them suitable for implementation in an estimator running in real time. This is because higher order models have more unknown parameters that must be estimated. All of these parameters may not be observable.

The sampling noise term, $b_w(t)$, is sometimes called "output noise" on sensor specification sheets and can be accurately modeled as band-limited white noise. The band-limit for $b_w(t)$ is very high relative to the frequency content of $b_1(t)$. Thus, a numerical value for $b_w(t)$ can be obtained by looking at the standard deviation of the sensor output when it is subjected to a zero input and sampled at a rate much higher than the maximum frequency content of $b_1(t)$.

In the sections that follow, the method used to generate error models for low-performance rate gyros and accelerometers will be discussed. The method used in this thesis involved two steps. First, the mathematical form of the error model is identified. Then, numerical values for the various parameters in the mathematical model are determined. Before proceeding with determination of these numerical values, however, we note that the general error model given in Equation 3.2 may appear somewhat simplistic. A more complete error model (like ones that would be found in standard inertial navigation texts such as [68]) would include effects such as cross-axis sensitivity errors, non-orthogonality errors, installation misalignment errors and acceleration (or $\vec{g}$) sensitivity errors. These errors are particularly significant when inertial navigation systems are used for very high precision navigation, for long periods of time and without external aiding. In this thesis, our the primary interest is in aided inertial navigation or inertial navigation for short periods of time. Thus, the general error model given in Equation 3.2 is sufficiently complete for the analysis that will be presented in Chapters 4 and 5.

3.3 Rate Gyro Error Models

In this work, solid state rate gyros that operate on two different principles were investigated. The first class consisted of rate gyros with a vibrating structure sensing element. The second class of rate gyros included those with optical sensing elements. These gyros are called Fiber Optic Gyros (FOGs).

3.3.1 Vibrating Structure Rate Gyros

The two specific rate gyros investigated in this class were the Systron Donner "Horizon" and the rate gyros contained in the Crossbow DMU-6X Inertial Measurement Unit (IMU). The Systron Donner "Horizon" has a sensing element that is described as a vibrating tuning fork. The Crossbow DMU-6X IMU is a low performance inertial sensor suite that consists of a triad of rate gyros and accelerometers. For simplicity, in this thesis these third party gyros and accelerometers will simply be referred to as "Crossbow DMU-6X" rate gyros or accelerometers, respectively. The

Crossbow DMU-6X rate gyros also use a vibrating structure sensing element.

In this thesis, these gyros were used in various applications. For example, both the Systron Donner "Horizon" and Crossbow DMU-6X rate gyros were used in mechanizing an Attitude Heading Reference System (AHRS). On the other hand, because the Crossbow DMU-6X rate gyros are part of an IMU, they were considered to be rate gyros one would find in a prototypical automotive grade Inertial Navigation System (INS). As such, the DMU-6X rate gyro error models are also used in the trade-off studies of INS performance that will be discussed in Chapter 5.

The process used for developing the error models for the Systron Donner "Horizon" and Crossbow DMU-6X rate gyros was identical. Therefore, in what follows, a detailed description of the methodology for developing the Systron Donner "Horizon" error model will be presented. Then the results for DMU-6X rate gyros will be presented.

Characterization of Gyro Output Noise, $b_w(t)$

A numerical figure for the wide-band noise, $b_w(t)$, was obtained by looking at the standard deviation of the detrended (i.e., mean removed) gyro output from the Systron Donner "Horizon" when it was subjected to a zero-rate-input. Figure 3.1 shows the output for a "Horizon" that was sampled at a rate above 100 Hz. For clarity in plotting, the data has been decimated down to 1 Hz in Figure 3.1. The data shows that the wide-band noise has a standard deviation, σ_w, of approximately 0.05 deg/sec. This is the numerical value used for $b_w(t)$ in modeling this gyro.

Characterization of Gyro Bias, $b_1(t)$

The $b_1(t)$ term is a time varying bias and can be viewed as having two components. The first component accounts for non-deterministic output errors. The second component accounts for output errors due to external factors such as temperature. It is possible to identify these external factors and develop an accurate model describing their effects on the gyro output. If one compensates for the output errors caused by these external factors, then the only remaining gyro errors would be stochastic. As will be shown shortly, however, it is not easy to compensate for these external factors.

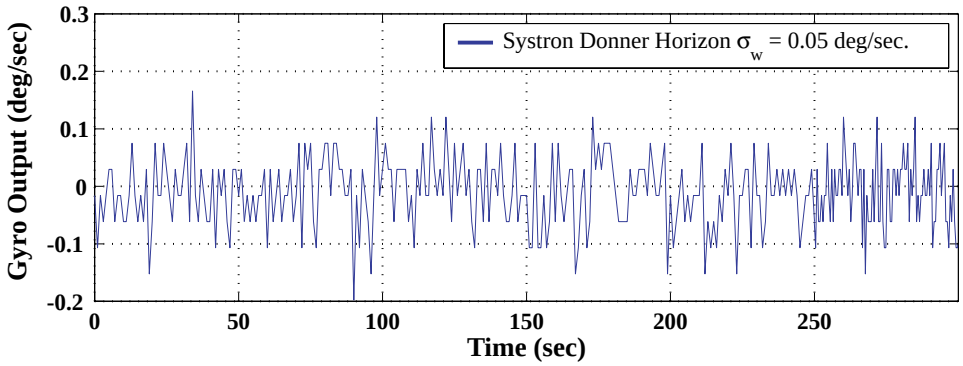

Figure 3.1: Wide Band Noise on the Output of the Systron Donner "Horizon" Rate Gyros.

Thus, for modeling purposes they may sometimes be combined with the stochastic effects.

Characterization of the stochastic component of $b_1(t)$ was accomplished by constructing and analyzing Allan variance charts using long term rate output data collected at constant temperature. The details of how Allan variances are used to construct error models can be found in Appendix C which is a summary of work contained in [5], [59], [66] and [67]. Figure 3.2 shows the Allan variance for the Systron Donner "Horizon" rate gyros. For comparison purposes, the Allan variance for the Crossbow DMU-6X rate gyros are also shown. The Allan variance for the Systron Donner "Horizon" is seen to have a -1/2 slope for roughly the first 300 seconds. This indicates that the error on the rate output is predominately wide-band noise for the first 300 seconds. Therefore, if the rate output from the "Horizon" is integrated to give attitude, for the first 300 seconds the primary *attitude* error would be due to angle random walk. This implies that for at least the first 300 seconds low-pass filtering can be used to minimize the output error.

The gyro exhibits a long term instability, however, which tends to dominate the output error after about 300 seconds. *Immediately* after the initial 300 seconds, the Allan variance has a slope of +1/2. This indicates that the output error for times greater than 300 seconds is a rate random walk or an exponentially correlated process with a time constant much greater than 300 seconds. A random walk is

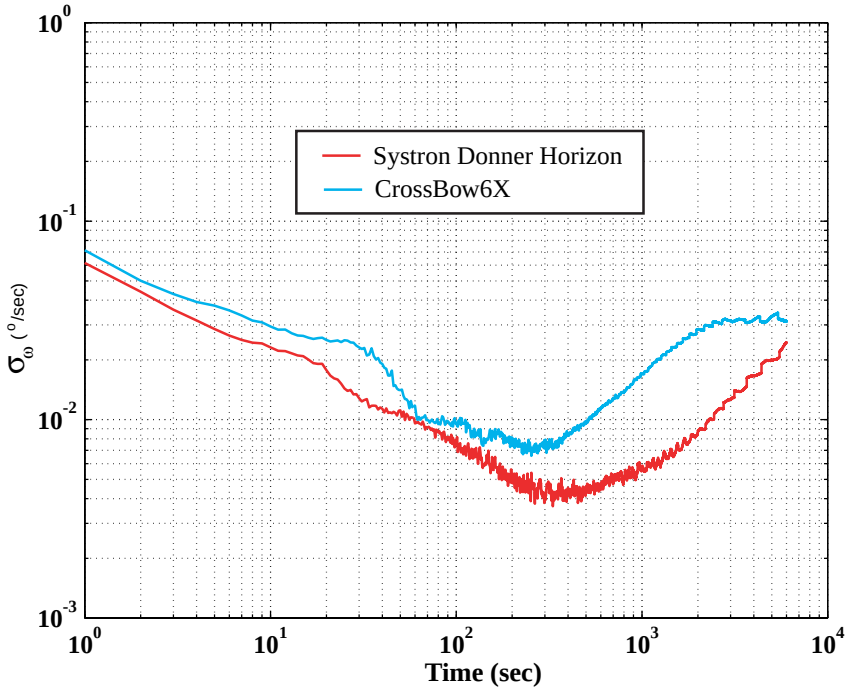

Figure 3.2: Allan Variance Plot for Vibrating Structure Rate Gyros.

a physically unrealistic model for an angular rate bias because it is a process with an ever increasing variance. So, the error model assumed for the rate output from the "Horizon" was an exponentially correlated or a first order Gauss-Markov process with an additive wide-band noise. That is, the $b_1(t)$ term for this gyro is a first order Gauss-Markov process and $b_w(t)$ is wide-band noise with frequency content much higher than $b_1(t)$. Since, in the previous section, a numerical value for $b_w(t)$ was determined, the remainder of this section will focus on characterizing the $b_1(t)$ term.

As noted above, the $b_1(t)$ term for these gyros was modeled as a first order Gauss-Markov process which has the following mathematical form:

$$\dot{b}_1(t) = -\frac{1}{\tau} b_1(t) + w_{b_1}. \tag{3.4}$$

The variable τ is the time constant (or correlation time) and w_{b_1} is the driving process

noise. The process can be described completely by its standard deviation, σ_{b_1}, and time constant, τ, because the power spectral density of the driving process noise, $Q_{w_{b_1}}$, is related to the variance, $\sigma_{b_1}^2 = \mathcal{E}\{b_1^2\}$, and time constant by the following relation [35]:

$$Q_{w_{b_1}} = \frac{2\sigma_{b_1}^2}{\tau}. \tag{3.5}$$

To understand how one can obtain the time constant and standard deviation for such a process from a time-series of rate gyro output data, consider the schematic depicting the behavior of a Gauss-Markov process, $x(t)$, shown in Figure 3.3. The process is described by the standard deviation, σ, and a time constant, τ. In this case, σ is 1 unit and τ is 100 seconds. Assume that at time $t = 0$, the process is perfectly known such that the standard deviation, σ, is equal to zero. As time progress, the uncertainty in process increases until it finally settles at its $1-\sigma$ value as shown in the left-hand plot in Figure 3.3. The right-hand plot of Figure 3.3 shows the autocorrelation function for this process. The right-hand plot shows that the time constant for such a process is the point at which the autocorrelation has dropped to approximately 36.8% (or more precisely, e^{-1}) of its value at zero-lag.

Accordingly, for the Systron Donner "Horizon" rate gyro, numerical values for τ were determined by looking at autocorrelation plots for the detrended rate output. Figure 3.4 shows the autocorrelation plot for the rate output. The autocorrelation has been normalized such that the magnitude at zero-lag is unity. From Figure 3.4, the time constant is seen to be approximately 1000 seconds.

Numerical values for σ_{b_1} were obtained by looking at long term data for the rate output. Figure 3.5 shows detrended (i.e., mean removed) long term output from a Systron Donner "Horizon" rate gyro where each data point represents a one minute average of rate data originally sampled at 1 Hz. The data in Figure 3.5 shows the first five hours of a long data set. The gyro output undergoes an initial transient that lasts for about 3 hours. After 3 hours the output stabilizes and, as shown in Figure 3.6, settles at mean value -0.02 deg/sec. The standard deviation of the stabilized output shown in Figure 3.6 is 0.01 deg/sec. The initial transient is most probably the result of temperature changes caused by self-heating after gyro turn-on as the internal components of the gyro heat up as a result of power being applied to the sensor. A

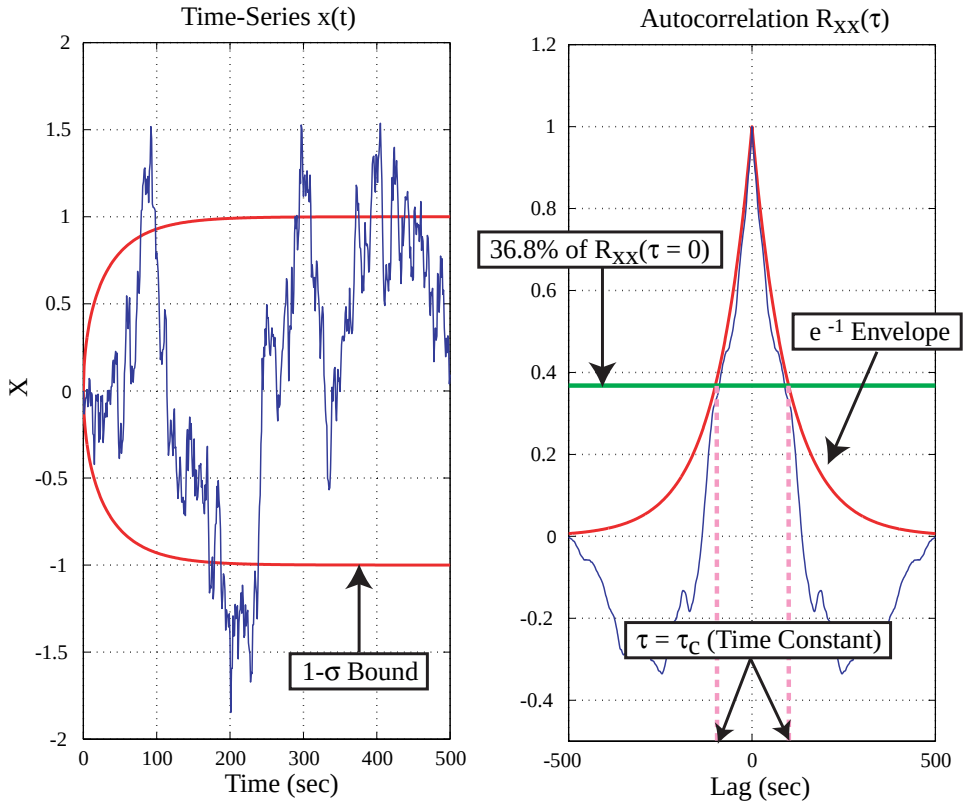

Figure 3.3: Schematic Showing the Standard Deviation and Autocorrelation for a First-Order Gauss-Markov Process.

similar temperature sensitivity for the Systron Donner "Horizon" was reported in [1] and has also been observed by the author in all the other solid state sensors used in this work. If this temperature dependent transient can be modeled easily, then it can be compensated and the remaining output error would be the stochastic component having a standard deviation of 0.01 deg/sec.

Determining the Systron Donner "Horizon" temperature sensitivity required elaborate testing. This was accomplished by placing the gyro in a temperature chamber* and monitoring its output. Since the rate gyros were not rotating, slow changes, if any, in the output would be indicative of bias drift. This was repeated for a number

*Use of the temperature chamber facility was courtesy of the Gyration Corporation of Saratoga, CA.

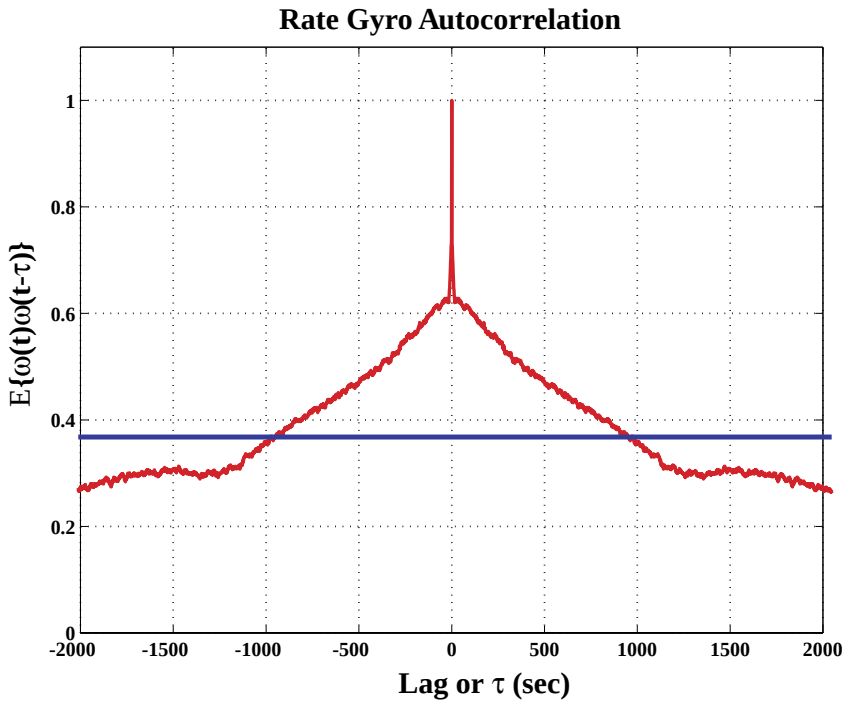

Figure 3.4: Rate Autocorrelation Plot for the Systron Donner "Horizon" Rate Gyro.

of temperatures between 0°C and 60°C. At each new temperature, data collection began only after the temperature chamber reached thermal equilibrium which required approximately 15 minutes. From these tests it was concluded that a short term (15 min) temperature effect was not observable.

It is postulated that the insensitivity of the "Horizon" to short duration temperature changes was due to the fact that the packaging of these gyros is rather bulky. The bulky packaging is believed to give the gyros a large "thermal inertia" that shields the sensing elements of the "Horizon" from outside temperature changes and makes it somewhat insensitive to short term temperature changes. This implies that constructing an error model relating gyro *external* temperature to rate output error is not feasible. Temperature compensation must be accomplished using a temperature measurement inside the gyro packaging.

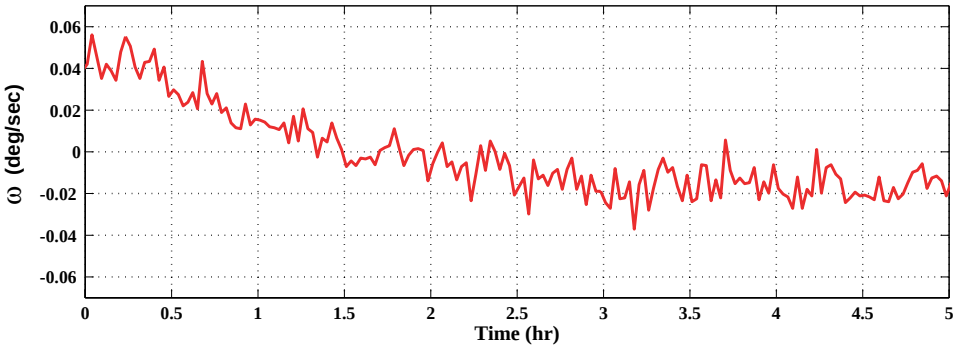

Figure 3.5: Long Term Rate Output for a Systron Donner "Horizon" Rate Gyro.

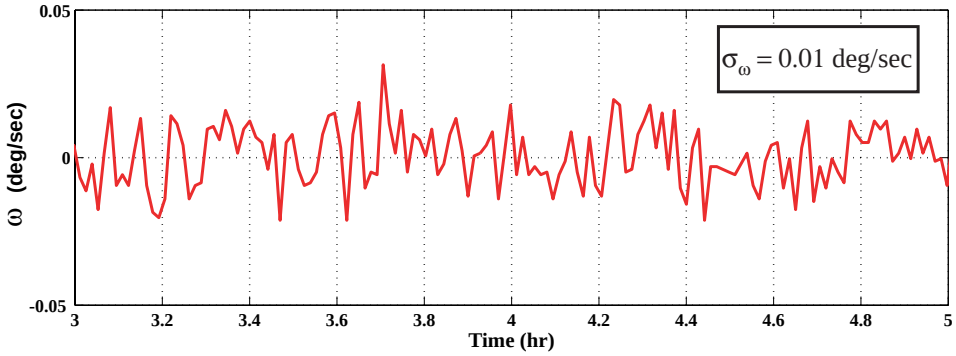

Figure 3.6: Temperature Stabilized and Detrended Output for a Systron Donner "Horizon" Rate Gyro.

Therefore, in the final error model of the Systron Donner "Horizon" the conservative value of 0.05 deg/sec was selected for σ_{b_1}. As can be seen in Figure 3.6, this value covers output errors due to stochastic and temperature effects. A detailed discussion regarding the effect of inflating σ_{b_1} on the appearance of the Allan variance chart is given in Appendix C. The effect of inflating σ_{b_1} is, in part, to move the low point of the Allan variance chart to the left.

Characterization of Scale Factor Errors

The scale factor for gyros was not always as specified on the data sheets. However, once the scale factors were determined experimentally, it was found that they did not change very much in response to outside factors. For example, in the case of the Systron Donner "Horizon" gyros, the temperature sensitivity of the scale factor was explored. This was accomplished by placing the gyros on a single axis rate table that was installed in a temperature chamber. The rate table was rotated at an angular rate of 5 °/sec while the output from the gyros was monitored. From this data the actual scale factor for the gyros was computed. This was repeated for a number of temperatures between 0°C and 60°C. From these tests it was concluded that the effect of temperature on scale factor is minimal (i.e., less than 2.6 % change over the 0°C and 60°C range) and, therefore, excluded from the error model. Figure 3.7 shows the scale factor sensitivity to temperature of one of the rate gyros tested.

In conclusion, the final error model for the bias, $b(t)$, for the Systron Donner "Horizon" rate gyros to be used in subsequent analysis is:

$$
\begin{aligned}
b(t) &= b_0 + b_1(t) + b_w, && (3.6)\\
b_0 &= \text{ Null shift determined on-line by an estimator,} && (3.7)\\
\dot{b}_1(t) &= -\frac{1}{\tau_g} b_1(t) + w_{b_1}, && (3.8)\\
\sigma_{b_1} &= 0.05 \text{ deg/sec} = 180 \text{ deg/hr} , && (3.9)\\
\tau_g &= 1000 \text{ seconds}, && (3.10)\\
\sigma_{b_w} &= 0.05 \text{ deg/sec}. && (3.11)
\end{aligned}
$$

A similar analysis for the rate gyros found in the Crossbow DMU-6X resulted in a very similar error model. As a matter of fact, the only difference between the two error models is the value of the time constant, τ. The DMU-6X error model is given

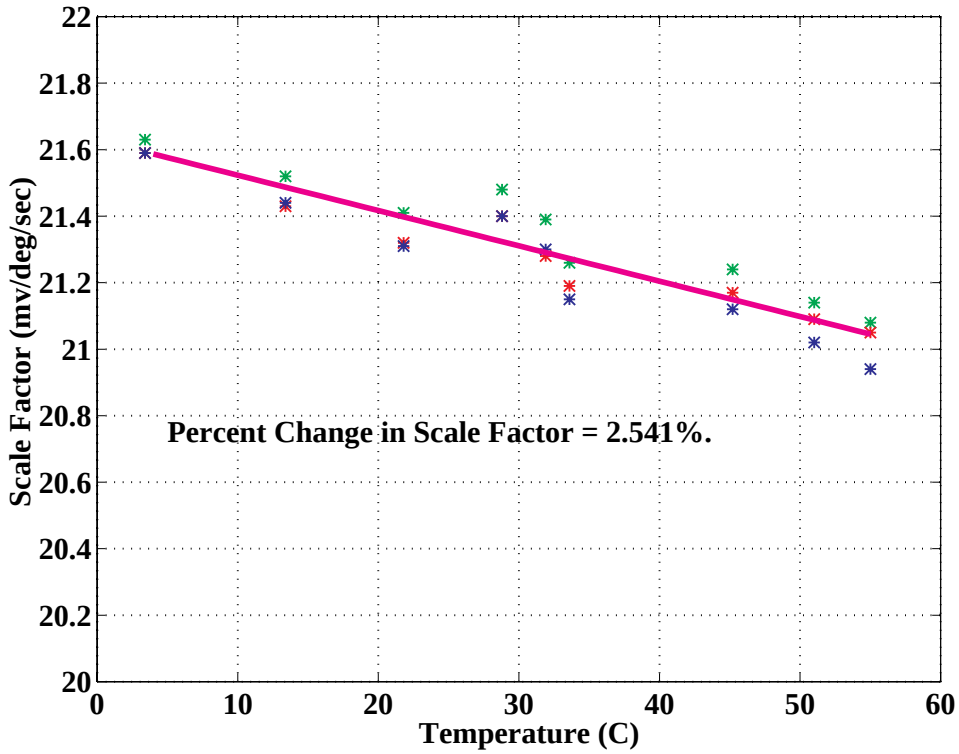

Figure 3.7: Systron Donner "Horizon" Rate Gyro Scale Factor Temperature Sensitivity.

by:

$$b(t) = b_0 + b_1(t) + b_w, \tag{3.12}$$

$$b_0 = \text{ Null shift determined on-line by an estimator,} \tag{3.13}$$

$$\dot{b}_1(t) = -\frac{1}{\tau_g} b_1(t) + w_{b_1}, \tag{3.14}$$

$$\sigma_{b_1} = 0.05 \text{ deg/sec} = 180 \text{ deg/hr}, \tag{3.15}$$

$$\tau_g = 300 \text{ seconds}, \tag{3.16}$$

$$\sigma_{b_w} = 0.05 \text{ deg/sec}. \tag{3.17}$$

It should be noted that the DMU-6X comes with a temperature sensor. It is used

to remove the temperature induced biases from the rate output. Thus, the value of σ_{b_1} in this model accounts for stochastic variation in the rate output only. This implies that, with temperature compensation, the Systron Donner "Horizon" is a higher quality rate gyro than the DMU-6X.

3.3.2 Fiber Optic Rate Gyro Error Models

In this section, the error models for low-performance optical rate gyros are discussed. As noted in Chapter 2, these rate gyros are called Fiber Optic Gyros (FOG). The two specific FOGs investigated as part of this work were the KVH-Autogyro and the rate gyros contained in the Crossbow DMU-FOG IMU. In this thesis, these gyros were only used to mechanize an AHRS. For simplicity, in what follows the third party FOG contained in the Crossbow DMU-FOG will simply be referred to as the "Crossbow FOG."

Figure 3.8 shows the Allan variances for these two low-performance FOGs. The constant $-\frac{1}{2}$ slope suggests that the dominant error source is wide-band noise. Thus, the total error model for the FOGs can be best characterized as constant bias (null-shift) with white sampling noise. Mathematically, this is given as:

$$b(t) = b_0 + b_w(t). \tag{3.18}$$

In this thesis, the b_0 term is estimated on-line using an observer (see Chapter 4) while the $b_w(t)$ is determined using one of two methods. Firstly, referring to the Allan variance plot shown in Figure 3.8, it can be seen that at an averaging time of 1 second the Allan variance is approximately 0.2 deg/sec. This is the standard deviation for the $b_w(t)$ term for these gyros. Secondly, one can use a time-series of FOG outputs as shown in Figure 3.9. Figure 3.9 shows that the standard deviation of the wide-band noise, $b_w(t)$, for the KVH and Crossbow FOGs is 0.21 and 0.18 deg/sec, respectively. This is consistent with what is shown in Figure 3.8; the KVH FOG is slightly noisier than the Crossbow FOG. However, the difference in the standard deviation of $b_w(t)$ for these two FOGs is small. Thus, for purposes of this thesis, these two rate gyros were considered to be identical. As such, taking the average of the two different FOG noise standard deviations and rounding up gives a value of 0.2 deg/sec. This single

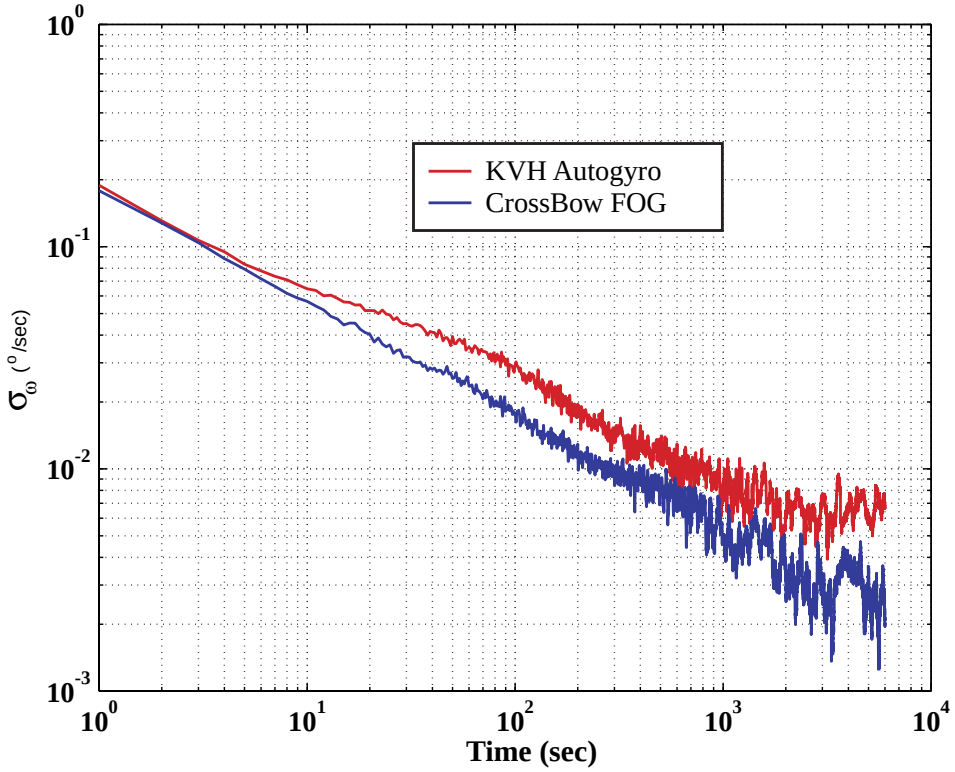

Figure 3.8: Allan-Variance Plot for Fiber Optic Rate Gyros.

value was used to represent the wide-band noise on both low performance FOGs.

Thus, the final error model for the FOG bias, $b(t)$, used in this thesis is:

$$b(t) = b_w \tag{3.19}$$

$$\sigma_{b_w} = 0.2 \text{ deg/sec.} \tag{3.20}$$

It is interesting to note that, although the long term bias stability for the FOGs is superior to that of the solid state vibrating structure gyros, the output noise is greater.

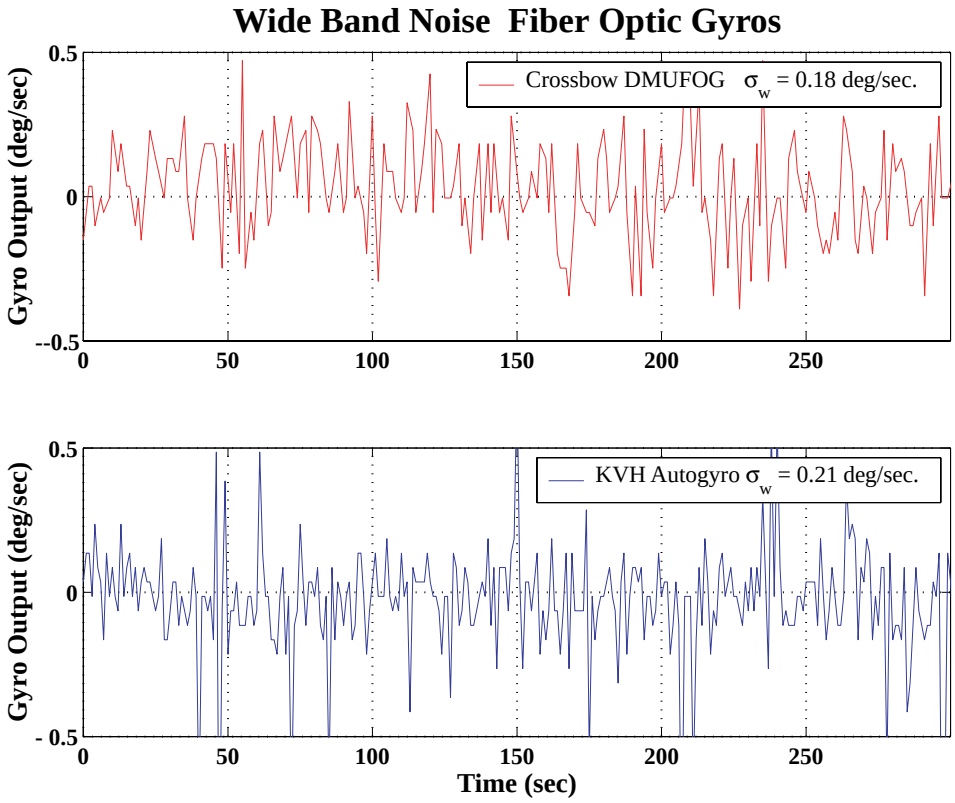

Figure 3.9: Wide-Band Noise on the Output of Fiber Optic Rate Gyros.

3.3.3 Summary of Low-Performance Rate Gyro Error Models

In summary, the low-performance rate gyro error models developed in the previous sections have been consolidated in Table 3.1. The b_0 term is not included in Table 3.1 because it is estimated on-line using an observer as will be discussed in Chapter 4. With exception of the Crossbow DMU-6X rate gyro, all the error models developed were used exclusively in analyzing and mechanizing Attitude Heading Reference Systems (AHRS) which will also be discussed in Chapter 4. The Crossbow DMU-6X rate gyro error models in conjunction with similar accelerometer error models (which will be discussed in Section 3.4) formed the error model for a standard automotive grade INS. This INS error model is discussed in Section 3.5 on page 56.

Rate Gyro	$b_w(t)$ = Wide-Band Noise	$b_1(t) = 1^{st}$ Order Gauss-Markov
Systron Donner "Horizon"	$\sigma_{b_w} = 0.05$ deg/sec	$\sigma_{b_1} = 0.05$ deg/sec $\tau = 1000$ sec
Crossbow DMU-6X	$\sigma_{b_w} = 0.05$ deg/sec	$\sigma_{b_1} = 0.05$ deg/sec $\tau = 300$ sec
FOGs (KVH and Crossbow FOG	$\sigma_w = 0.2$ deg/sec	None

Table 3.1: Summary of Error Model Parameters for Low-Performance Rate Gyros.

3.4 Accelerometer Error Models

There does not appear to be as large a variety in the quality of low-performance accelerometers as there is in rate gyros. For example, all the inertial measurement units of various qualities that are packaged and sold by Crossbow, use the same accelerometers. The lack of variation is perhaps because most low-performance accelerometers are not used in navigation applications but for level sensing. The requirements on output noise and bias stability in leveling applications are not as stringent as those required for navigation.

The accelerometers in the Crossbow inertial measurement units are, therefore, assumed to be the standard low performance accelerometer. Based on the Allan variance chart shown in Figure 3.10, the form of the error model is found to be the same as the error model for the DMU-6X rate gyros. That is, the output error is a combination of wide-band noise, a null shift and a time varying bias. Based on an analysis identical to the one outlined in Section 3.3.1 on page 42, the time varying bias is modeled as a Gauss-Markov process with a correlation time of 100 sec and a standard deviation of 1.2 milli-g. Similarly, the wide-band noise, $b_w(t)$, has a standard

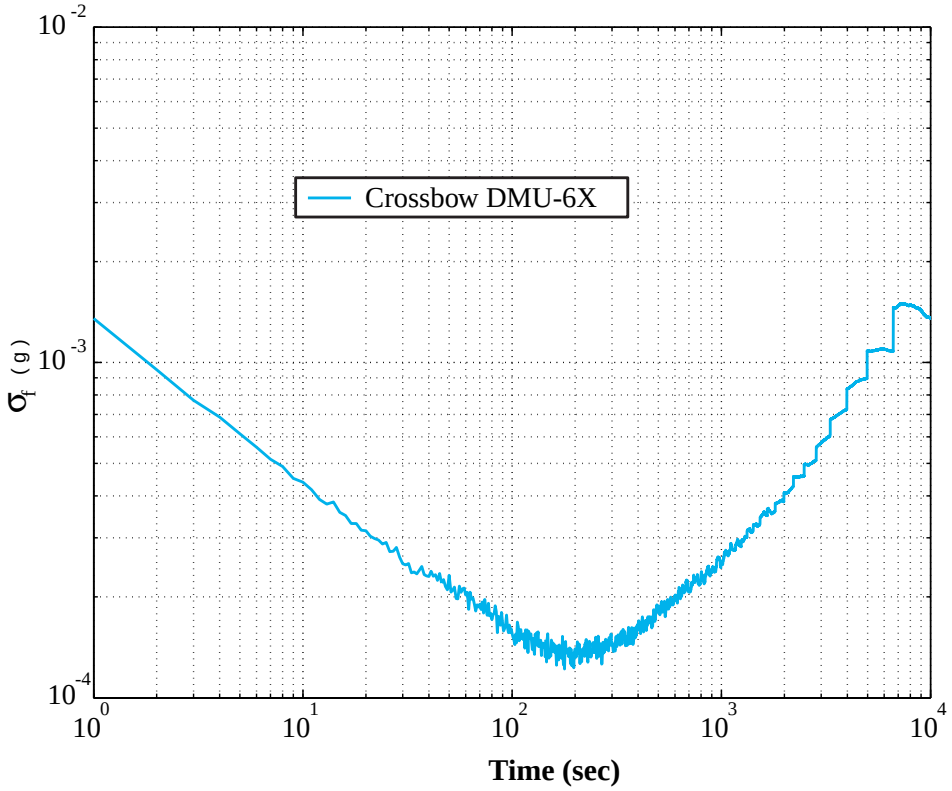

Figure 3.10: Allan-Variance for the Crossbow DMU-6X Accelerometer.

deviation of 1 milli-g. Mathematically, this is given as:

$$b(t) = b_0 + b_1(t) + b_w, \tag{3.21}$$

$$b_0 = \text{Null shift determined on-line by an estimator}, \tag{3.22}$$

$$\dot{b}_1(t) = -\frac{1}{\tau_g} b_1(t) + w_b, \tag{3.23}$$

$$\sigma_{b_1} = 1.2 \text{ milli-g}, \tag{3.24}$$

$$\tau_g = 100 \text{ seconds}, \tag{3.25}$$

$$\sigma_{b_w} = 1 \text{ milli-g}. \tag{3.26}$$

INS Quality	Rate Gyro			Accelerometer		
	σ_ω (deg/hr)	τ (sec)	$Noise$ (deg/sec)	σ_f (g)	τ (sec)	$Noise$ (g)
Tactical	0.35	100	0.0017	50×10^{-6}	60	50×10^{-5}
Automotive	180	300	0.05	1.2×10^{-3}	100	1×10^{-3}
Consumer	360	300	0.05	2.4×10^{-3}	100	1×10^{-3}

Table 3.2: Parameters for Error Models of Inertial Navigation Systems.

3.5 Inertial Navigation System Error Models

Based on the error models developed in the previous section, data contained in [53] and the methodology outlined in [66] a unified error model versus sensor quality table can be constructed. Table 3.2 is such a table. This error model parameterization will be used in Chapter 5 for a trade-off study of dead reckoning systems. It should be noted that all the sensors modeled in the previous sections were what would be considered automotive grade. For the analysis in this thesis, the Crossbow DMU-6X is considered to be the typical automotive grade INS. However, there are sensors of lesser quality in consumer products. Thus, we have generated consumer grade inertial sensor characteristics as shown in the last entry in Table 3.2. It is a somewhat fictitious model because it is simply a sensor package that is two times worse than the automotive grade inertial sensors. More specifically, the colored portion of the gyro and accelerometer biases are double that of the automotive grade sensors. The output noises of the sensors have been kept the same. This model will be used in an INS performance analysis in Chapter 5.

3.6 Magnetometer Error Models

In Chapter 2, it was noted that heading is the angle formed between the longitudinal axis of an airplane and the north pole. It was also noted that the primary sensor for determining heading in this thesis is a magnetometer. If the classical two-magnetometer installation is being used and the aircraft with the magnetometers is level, the output of the magnetometer pair would be the horizontal components of

Earth's magnetic field vector in the vicinity of the aircraft. If the three-magnetometer configuration is being used, the output of the magnetometer triad would be the three components of Earth's magnetic field in the vicinity of the aircraft. Due to sensor imperfections, installation errors and unwanted magnetic fields in the vicinity of the magnetometers, the output from the sensors is corrupted by error. The objective of this section is to develop mathematical models that describe these output errors. Subsequently, these models will be used in estimation algorithms for calibrating magnetometers described in Section 3.11 of this chapter. Before delving into the derivation of the error models, some background concepts and definitions will be discussed.

3.6.1 Background

Derivation of the error models will involve expressing Earth's magnetic field vector in three different coordinate frames. These coordinate frames are defined as follows:

1. Navigation Frame - This is the locally level coordinate frame with its x-y-z axes lined-up with North, East and Down (along the local vertical) directions, respectively. It is sometimes called the North-East-Down, or NED, coordinate frame. In equations, vector quantities expressed in this coordinate frame will have the superscript "n."

2. Body Frame - This is the coordinate frame with the x-axis lined-up with the aircraft's nose, the y-axis out the right wing and the z-axis completing the orthogonal frame. If the aircraft is level and heading north, then the body coordinate frame will be lined-up with the NED frame. In equations, vector quantities expressed in this coordinate frame, will have the superscript "b."

3. Wander-Azimuth Frame - This is the locally level coordinate frame with its x-axis lined-up with the projection of the longitudinal axis of the airplane, it z-axis lined-up with the vertical and the y-axis orthogonal to the x- and z-axes to form a right-handed coordinate system. The angle between the x-axis of this coordinate frame and the x-axis of the NED frame is called the wander angle. In equations, vector quantities expressed in this coordinate frame, will have the superscript "w."

4. Platform Frame - This is the right handed coordinate frame with axes lined-up with the sensitive axes of the magnetometer. In equations, vector quantities expressed in this coordinate frame, will have the superscript "p."

As was noted in Equation 2.3, heading calculations are performed using Earth's magnetic field vector as expressed in wander-azimuth coordinates. In a level aircraft, Earth's magnetic field vector expressed in wander-azimuth coordinates ($\vec{B}^w$) is equal to Earth's magnetic field vector expressed in body coordinates ($\vec{B}^b$). If the aircraft is not flying wings level, however, $\vec{B}^b$ has to be transformed into $\vec{B}^w$ before using Equation 2.3. This transformation is accomplished by using a direction cosine matrix in the following manner:

$$\vec{B}^{\,w} = \overset{b\to w}{C}\ \vec{B}^{\,b}, \tag{3.27}$$

where $\overset{b\to w}{C}$ is the body-to-wander-azimuth frame direction cosine matrix and is computed using pitch and roll information only. This pitch and roll information comes from an AHRS. It should be noted that the mathematical "leveling" scheme, or Equation 3.27 will not work with the two magnetometer system because there will be only two components of the magnetic field vector measured and Equation 2.3 requires three components. This is why the classic two magnetometer system, "wet" compasses or flux-gates, cannot be used in turns. In what follows, a model for this output error will be developed.

3.6.2 General Error Equation

The mathematical model for the output error of a strapdown magnetometer triad is:

$$\hat{\vec{B}}^n = \overset{b\to n}{C}\left[C_m\, C_{sf}\, C_{si}\,\left(\vec{B}^b + \delta\vec{B}^b\right)\right], \tag{3.28}$$

where $\delta\vec{B}^b$ in Equation 3.28 represents the hard iron biases. The matrix C_{si} accounts for the soft iron errors. C_{sf} is a matrix that takes into account scale factor errors. Finally, the matrix C_m represents misalignment errors. Each one of these error terms is discussed in detail below.

3.6.3 Hard Iron Errors: $\delta\vec{B}^b$

The magnetic field that is measured and used in heading determination is Earth's magnetic field. In most practical applications there will be other unwanted magnetic fields in the vicinity of the magnetometer triad. These unwanted fields are normally generated by ferromagnetic materials with permanent magnetic fields (or "hard irons") that are part of the aircraft structure or equipment installed in the vicinity of the magnetometer such as current carrying wires. These unwanted magnetic fields are superimposed on the output of the magnetometers based on Earth's magnetic field. This is shown schematically in Figure 3.11. The effect of this superposition is to bias the magnetometer output. If the unwanted magnetic fields are time invariant then they are called hard iron errors and can be represented by a vector quantity, $\delta\vec{B}^b$. If the strength and direction of these unwanted magnetic fields is known, then their effect can be removed to un-bias the magnetometer readings.

It should be noted that unwanted magnetic fields can also be caused by items external to the aircraft. Since the vehicle is normally moving, however, the effect of such fields will be temporary. Furthermore, the only time that fields due to external sources will be present is when the aircraft is on the ground. Therefore, errors due to fields caused by sources external to the aircraft can be safely neglected.

There can be items inside the aircraft that generate unwanted time varying magnetic fields. An example of such an item would be a current carrying wire. If the current through the wire is time varying, the resulting magnetometer bias will also be time varying and difficult to calibrate. Fortunately, such errors can be easily eliminated by taking care during installation of magnetometers such that there are no sources of time varying magnetic fields in the vicinity of the magnetometers.

3.6.4 Soft Iron Errors: C_{si}

There are materials that generate magnetic fields in response to an externally applied field. The field generated by these materials can vary over a wide range depending on both the magnitude and direction of the applied external magnetic field. Such materials are called soft irons. If such materials are present in the vicinity of a magnetometer, they will generate a magnetic field that will be superimposed on

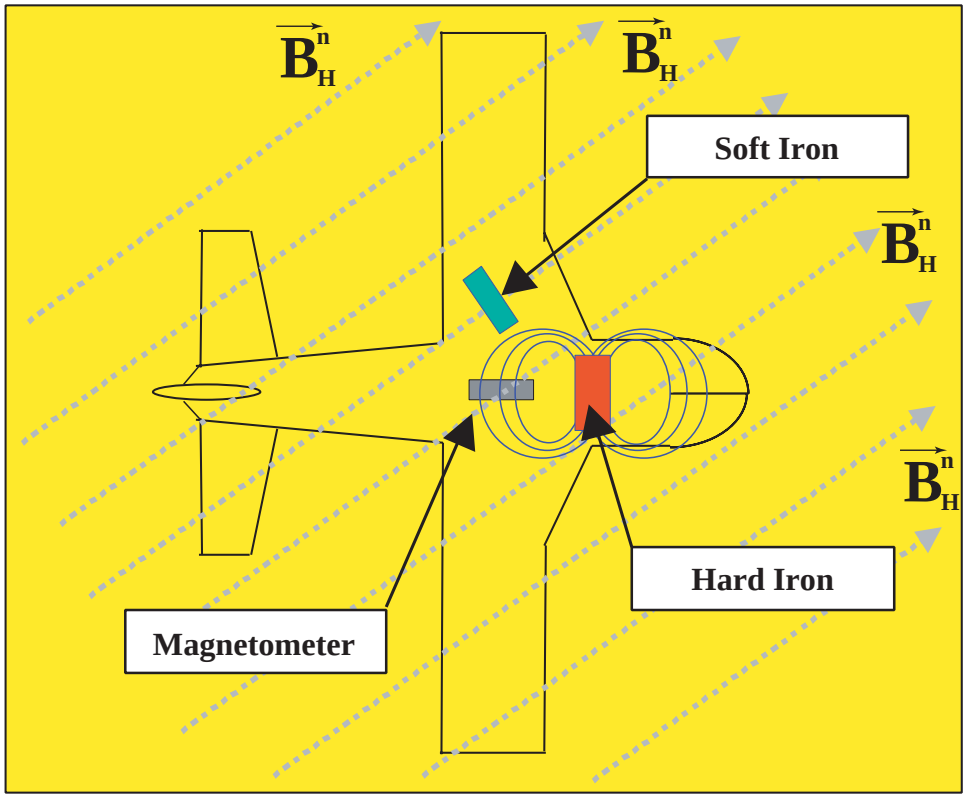

Figure 3.11: Graphical Description of Hard Iron Errors.

the output. The external magnetic field that will cause these soft iron materials to generate their own magnetic field is Earth's magnetic field. Since its orientation with respect to the soft iron changes with aircraft attitude, this gives rise to a varying bias on the magnetometer output.

The effect of soft iron biases can be understood better by looking at the schematics shown in Figures 3.11 and 3.12. In Figure 3.11 a soft iron material is shown. Given the aircraft orientation in Figure 3.11, the horizontal component of Earth's magnetic field is orthogonal to the soft iron material shown. In this instance, the soft iron will not generate a magnetic field. When the aircraft's orientation is changed to that shown in Figure 3.12, the horizontal component of Earth's magnetic field becomes in line with the soft iron material. In this instance the soft iron generates a magnetic field that biases the output of the magnetometer.

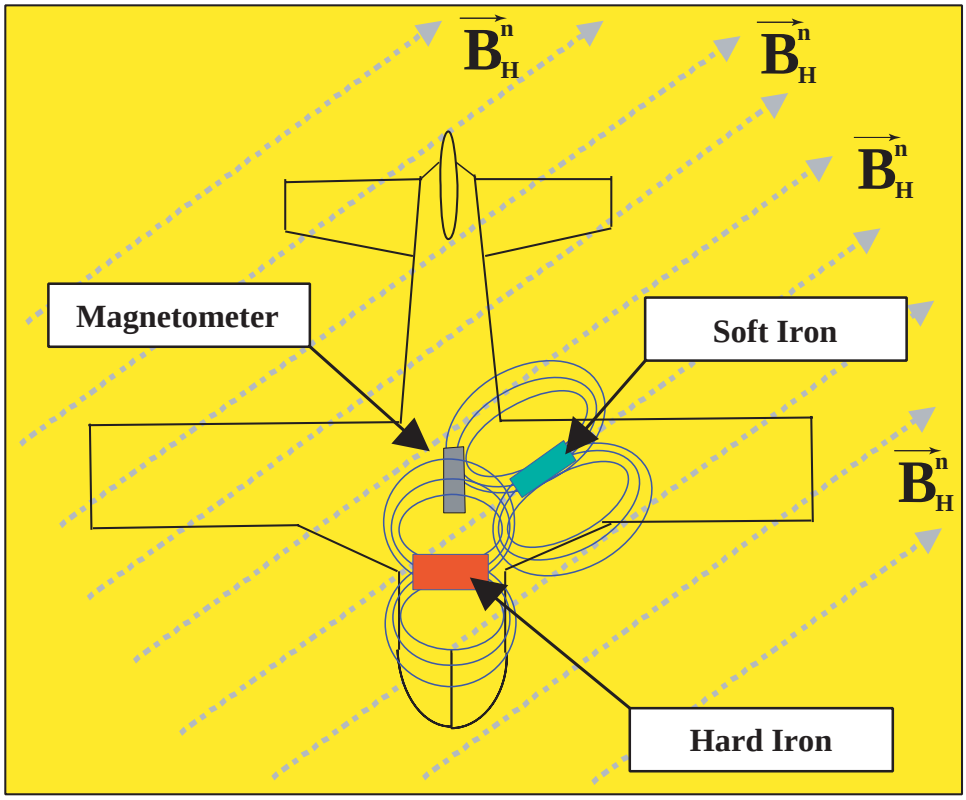

Figure 3.12: Graphical Description of Soft Iron Errors.

In a simple one-dimensional case the magnitude of the magnetic field generated by a soft iron material in response to an external magnetic field is proportional to this external magnetic field. The constant of proportionality is a property of the soft iron material and it is referred to as the material's magnetic susceptibility. In the work in this thesis it will be assumed that this simple linear relationship is sufficient. In reality, however, there can be appreciable hysteresis. In most soft iron materials used in aircraft construction the hysteresis is small enough that the linear model is sufficient. In a hysteresis-free, three-dimensional case, instead of a constant of proportionality, a 3×3 matrix is required. This is the C_{si} matrix in Equation 3.28. A more detailed treatment of the entries in this matrix will be given in a subsequent section on magnetometer calibration.

3.6.5 Scale Factor Errors: C_{sf}

Ideally, the three magnetometers that make up the magnetometer triad are identical sensors. In reality, each magnetometer will have a different sensitivity. That is, when all three magnetometers are subjected to an identical magnetic field, the observed output from each magnetometer will not be the same. This is the result of a scale factor error. Calibrating the scale factor error involves determining the multiplicative factor that has to be applied to each magnetometer output such that the output from each magnetometer will be the same when subjected to an identical magnetic field. In the three-dimensional case, the multiplicative constant is the 3×3 matrix C_{sf}.

3.6.6 Misalignment Errors: C_m

In an ideal installation, the magnetometer triad will be mounted in perfect alignment with the body axis of the aircraft. In actual practice, perfect alignment cannot always be achieved. This misalignment causes errors in the magnetometer's measurement of Earth's magnetic field. To get a better feel for how this error is caused, consider an aircraft that is perfectly level (i.e., roll and pitch angles are zero) and the two vectors $\vec{B}^p$ and $\vec{B}^b$. The vector $\vec{B}^p$ is Earth's magnetic field vector expressed in the platform coordinate frame. Thus, $\vec{B}^p$ is the error-free output of the magnetometer triad. The vector $\vec{B}^b$ is the magnetometer output expressed in the "b" coordinate frame which is fixed to and aligned with the aircraft's body axes. If there are no installation errors such that the platform coordinate frame "p" is aligned with the body frame "b," then the vectors $\vec{B}^p$ and $\vec{B}^b$ would be identical. Otherwise, there will be an error because the wrong vector would be used on the left hand side of Equation 3.27.

If care is taken during the installation process, the misalignment between the triad and the airplane body axes can be minimized. In this case, the small misalignment can be represented by the perturbation direction cosine matrix, $\overset{b\to p}{\delta C}$. In this instance, heading calculations are performed on a modified form of Equation 3.27 which is given as follows:

$$\vec{B}^{\,w} = (\overset{b\to w}{C})(\overset{p\to b}{\delta C})\,\vec{B}^{\,p} \tag{3.29}$$

In this particular instance where the aircraft is level, $\overset{b\to w}{C}$ is an identity matrix because the body and wander-azimuth frames are the same. Furthermore, since the the perturbation direction cosine matrix, $\overset{p\to b}{\delta C}$, represents small angle rotation, it is a skew-symmetric matrix with three independent parameters. These independent parameters are the rotations about the roll, pitch and yaw axes of the airplane, respectively. Determining the misalignment errors, therefore, is reduced to identifying these small angles. Since misalignment errors are installation errors, they are time invariant and only need to be estimated once.

Estimating the various errors modeled in Equation 3.28 involves discussion of magnetometer calibration algorithms which will be the subject of the final section of this chapter.

3.7 Air Data System Errors

The air data system generates air speed and pressure altitude measurements which are used by the backup navigator in generating a position solution. In what follows, error models for the air speed and pressure altitude measurements will be discussed separately.

3.7.1 Airspeed Measurement Errors

The air speed measurement (V_i) from an air data system is corrupted by various errors. This measurement is called "indicated" air speed (hence, the subscript "i") and can be expressed in the following manner:

$$V_i = V_c + \delta V \tag{3.30}$$

$$= V_c + \delta V_a + \delta V_i + \delta V_w. \tag{3.31}$$

In this equation, V_c is the calibrated air speed and is a measurement proportional to the pressure difference sensed by the pitot tube and the static port as shown in Equation 2.2 on page 26. δV is the total air speed measurement error and is composed of three terms.

The error term δV_a is the result of air density changes due to non-standard atmospheric condition. As noted in Equation 2.2 on page 26, the air density is a scale factor of sorts which is a function of temperature. Since a temperature probe is part of the air data system, corrections for variations in the air density can be made. Therefore, for the error analysis in subsequent chapters we assume that corrections for non-standard atmospheric conditions have been made. Therefore, the term δV_a is assumed to be zero.

When the temperature corrections noted above are made, the only remaining time varying air speed errors are δV_i and δV_w. The term δV_i represents errors primarily due to variations in the air flow characteristics in the locations where the pitot tube and static ports are installed. It is a function of flight conditions and an accurate model of this air speed error would require a complicated model involving factors such as angle of attack and side slip angle. Previous researchers have taken various approaches to simplify this model. For example, in the work documented in [15] air speed errors are ignored altogether; it was judged that the magnitude of navigation errors introduced by *all* air speed errors was less than those due to the stochastic variations of wind speed. The work in [14] takes a different approach to modeling this error. The approach taken in [14] is to model all time varying air speed errors as an exponentially correlated process with a 400 sec time constant and a standard deviation of 5 m/s.

In this thesis, the model developed in [14] will be used. That is, the air speed errors are modeled as exponentially correlated processes with a time constant of 400 seconds. However, the standard deviation of 5 m/s is considered to be large and instead it is set equal to 2.6 m/s (5 knots). The justification for this is the fact that for a certified airspeed measuring device used in a General Aviation aircraft (Group E of Table 1.1), this error cannot be larger than 5 knots [4]. Thus, it is judged that this is a reasonable upper bound on the time-varying component of the air speed measurement errors.

The error term δV_w represents the wide-band noise on the airspeed measurement. The work in [14] modeled δV_w as an additive white noise term with a standard deviation equal to 1 m/s. For the air data system used in this research (Shadin ADC-200),

the wide-band noise was less than 1 m/s and also less than the resolution of the sensor. Thus, for the analysis in this thesis, the wide-band noise was set to zero. Setting this term to zero is further justified by the fact that other air speed measurement errors are considerably larger and more persistent and thus will have a larger effect on the resulting navigation error.

Thus, the final model for the total air speed measurement error δV is an exponentially correlated process with a standard deviation, σ_v, of 2.6 m/s and a correlation time, τ_v, of 400 seconds. Mathematically, this model is written as:

$$\begin{aligned} \delta\dot{V} &= -\frac{1}{\tau_v}\delta V + w_v, \\ \sigma_V &= 2.6 \text{ m/s}, \\ \tau_v &= 400 \text{ sec}. \end{aligned} \tag{3.32}$$

The variable w_v is the driving process noise. Once again, since the errors are modeled as an exponentially correlated process the power spectral density, Q_{w_v}, of the driving process noise, w_v, is a function of the variance and time constant[35]. That is,

$$Q_{w_v} = 2\frac{\sigma_v^2}{\tau_v}. \tag{3.33}$$

3.7.2 Altitude Measurement Errors

The baro-altimeter is part of the air data system and is the primary sensor for measuring altitude in the backup navigator. As will be shown in Chapter 5, the contribution of altimeter error to the final lateral position error is very small. For completeness, however, a model for altimeter errors was developed and included in the analysis. A general mathematical model for baro-altimeter errors is given in [65]. The model given in [65] is an exponentially correlated process. However, standard deviations and time constants for the baro-altimeter error model are not given in [65].

In this thesis, the same functional form cited in [65] for the baro-altimeter errors is used. The standard deviation is set to 75 ft (23 m) because, as documented in [3], this is the maximum altitude error considered acceptable (or tolerated) in normal flying.

The time constant was selected based on the author's judgment and was set to 400 seconds. This value was selected because it is the same time constant used for the air speed sensor error model and the physical sensor used for altitude determination (i.e., the static pressure transducer shown in Figure 2.7 on page 25) can be viewed as a subsystem of the sensors used for air speed determination. Even though this may be somewhat arbitrary, once again, as will be shown in Chapter 5, the magnitude or standard deviation of altimeter errors has very little effect on the final lateral position error. The effect of the time constant will even be smaller (if not negligible) for the level of navigation accuracy that is being discussed in this thesis. Thus, the final model for altimeter errors, δh, used is:

$$\begin{aligned} \delta\dot{h} &= -\frac{1}{\tau_h}\delta h + w_h \\ \sigma_h &= 23 \text{ m}, \\ \tau_h &= 400 \text{ sec}. \end{aligned} \tag{3.34}$$

3.8 Wind Error Model

Dead reckoning navigation systems used on aircraft compute a position solution by integrating velocity. The velocity measurement of interest is ground speed which is a measure of the aircraft's speed relative to the ground below. A measurement of ground speed can be obtained by using a Doppler radar. While Doppler radars have been successfully applied in aided-dead reckoning navigation system used by the military [20], they are expensive sensors and, thus, impractical for aircraft such as those in Groups C and E of Table 1.1. Low cost dead reckoning systems for civilian use, therefore, will have to rely on air speed sensors for velocity measurement.

An air speed sensor measures the velocity of an aircraft relative to the air mass in which it is flying. The term wind speed is used to describe the horizontal velocity of this air mass and ground speed is the vector sum of air speed and wind speed. Therefore, successful implementation of an air speed based dead reckoning navigator requires an accurate knowledge of wind speed. An accurate model of wind speed is also useful when performing trade-off studies of air speed based dead reckoning navigation systems. In this thesis, the wind speed model used is the one developed

in [14]. For simplicity, it will be referred to as the Berman-Powell wind model and will be described next.

At any given point and time, the horizontal wind speed is a vector that can be described by specifying the magnitude of its two components; its north-south component, V_{NS}, and its east-west component, V_{EW}. The Berman-Powell wind model provides a description for how the V_{NS} and V_{EW} components of wind speed vary as a function of distance traveled from the observation point and time elapsed from the initial observation. The model was developed using wind data collected by commercial airlines between August 11, 1997 and September 9, 1997. The data collected by these commercial airlines is available from the National Oceanic and Atmospheric Administration (NOAA) Forecast System Laboratory (FSL). The data used for constructing the model was collected at locations between 37° and 42° North latitude; 78° and 118° West longitude; and between 2000 and 10,000 ft altitude.

For a clearer understanding of this model, consider a user located at a point $\vec{p}_k$. At time t_k this user makes measurements of the two wind speed components $V_{NS,k}$ and $V_{EW,k}$. At some later time, t_{k+1}, the user is at location $\vec{p}_{k+1}$ and makes wind speed measurements $V_{NS,k+1}$ and $V_{EW,k+1}$. The change in wind speed between these two observations is a function of both the change in position, $\Delta\vec{p}$, and elapsed time, Δt. This means that wind speed variation will be a function of four variables (i.e., three components of $\Delta\vec{p}$ plus Δt). The Berman-Powell model consolidates the four variables into one variable called traveling time (t_r). The variable t_r is defined as:

$$\begin{aligned} t_r &= \sqrt{t_N^2 + t_E^2 + t_D^2 + \Delta t^2} \\ t_N &= \frac{\Delta p_N}{V_N} \\ t_E &= \frac{\Delta p_E}{V_E} \\ t_D &= \frac{\Delta p_D}{V_D} \end{aligned} \tag{3.35}$$

The variables N, E, and D stand for North, East and Down, respectively. V_N is the users velocity in the north direction, Δp_N is the position change in the north direction, and so on.

For t_r values between 0 and 3600 sec, it was found that the change in wind speed is

stochastic and can be modeled as an exponentially correlated process with a standard deviation of 5 m/s and a correlation time of 400 seconds. The variables δV_{NS} and δV_{EW} are used to denote changes in V_{NS} and V_{EW}, respectively. Given this notation, then the mathematical model for the variation of north-south wind speed can be written as:

$$\begin{aligned} \delta\dot{V}_{NS} &= -\frac{1}{\tau_{NS}}\delta V_{NS} + w_{NS} \\ \sigma_{V_{NS}} &= 5 \text{ m/s}, \\ \tau_{NS} &= 400 \text{ sec}. \end{aligned} \tag{3.36}$$

The variable w_{NS} is the driving process noise and its power spectral density is related to the variance and time constant for δV_{NS}[35]. The model for the east-west wind component is identical to the model for δV_{NS} and is given by:

$$\begin{aligned} \delta\dot{V}_{EW} &= -\frac{1}{\tau_{EW}}\delta V_{EW} + w_{EW} \\ \sigma_{V_{EW}} &= 5 \text{ m/s}, \\ \tau_{EW} &= 400 \text{ sec}. \end{aligned} \tag{3.37}$$

3.9 DME Error Models

The principle of operation for DME was described in Chapter 2. In this section, a DME range measurement error model will be constructed. Analogous to the Figure 2.6 classification of inertial sensors by quality, airborne DME receivers can also be divided into two broad categories. The two categories of DME receivers are:

1. High end receivers used primarily by commercial and turbine business aviation aircraft (i.e., aircraft in Groups A through C). These types of receivers are sometimes referred to as "Gold Crown" by Bendix/King which is the primary manufacturer of DME receivers. Examples of such receivers are the Bendix/King KDM-706 and KDM-441 Scanning DME. The cost of these receivers is in the range of $15,000 to $20,000.

2. Low-end receivers used primarily by General Aviation aircraft. Examples of

this class of airborne DME receivers are the Bendix/King KN-62 and KN-64. This class of receiver is in the cost range of $2000 to $7000 and is standard on a large fraction of General Aviation aircraft[60].

In addition to the two broad classifications of receivers, there are two types of ground based transponders. The first and more common DME ground transponder is what is called the DME-N system. The "N" in this designation stands for "nominal." The second variant of ground based transponders is the so called DME-P[†] system. The "P" in this designation stands for "precise." The error characteristics of DME-P are very similar to DME-N when the user is more than 7 nautical miles away from the ground transponder [17]. Within a seven mile radius of the transponder, the more precise range measurement from the DME-P system becomes functional. An airborne DME-P receiver, therefore, will experience an increase in accuracy as it approaches the DME-P ground transponder. A DME-N receiver obtaining range measurements from a DME-P transponder, however, will not experience a similar change in accuracy. The reader interested in a very comprehensive treatment of DME-N and DME-P systems is referred to [50]. The error characteristics of range measurements obtained from DME, therefore, depend on both the type of airborne receiver and the ground based transponder. Because the aim of this thesis is, in part, to develop a backup navigator using low-performance sensors, the only error models that have to be developed are those for a DME-N receiver and transponder pair.

A general mathematical model for the errors in the range measurement, δR, obtained when using a DME-N receiver and transponder is:

$$\begin{aligned} \delta R &= R - \hat{R} \\ &= \delta R_0 + \delta R_b(t) + \delta R_w \end{aligned} \tag{3.38}$$

[†]DME-P was developed to serve as the precise range measurement portion of the Microwave Landing System (MLS). In the 1980s intense research and development work was undertaken to develop MLS. The objective of this effort was to develop a landing system having the accuracy and reliability of ILS but with enhanced flexibility and capability. Landing systems based on GPS, however, are envisioned to be capable of matching, if not surpassing, the accuracy and flexibility provided by MLS. The wide spread civilian use of GPS preempted the adoption of MLS and, therefore, there are very few DME-P transponder installations.

In this error model R is the actual range from the transponder and $\hat{R}$ is the measurement generated by the DME receiver. The term δR_0 represents a time invariant range bias, δR_b represents a time varying bias and δR_w is wide-band measurement noise.

The constant range bias, δR_0, can be caused by offset in the 50μs delay of the ground transponder or in the timing circuits of the DME receiver. Such biases can be calibrated by using a scheme similar to the one reported in [7]. In this scheme, differentially corrected GPS was used as a precise measurement against which the DME range measurements were compared and used to estimate the constant range bias, δR_0. Therefore, the error model used in this thesis assumes that this constant bias term has been calibrated and is thus set equal to zero.

The time varying bias, δR_b, can be caused by several factors. Causes of this error are time varying drift, induced by phenomena such as temperature changes in the oscillators that control the 50μs ground transponder delay or the timing circuits in the airborne receiver that measure the time of flight of the DME pulses. The ground based transponders have a "zero range" self-check capability. In this self-test, the transponder generates a pulse which is sent though its receiving circuitry. If the range determined by this test is much greater than zero, the DME is taken off-line [31]. Thus, it is more likely for the airborne receiver's oscillator to be the cause of the range error as they are normally inexpensive and low-quality oscillators. Another cause of this time-varying bias was observed by researchers in [7] and was a scale-factor-like error caused by variations in the signal-to-noise ratio of the DME pulses. The signal-to-noise ratio is dependent on the distance between the airborne receiver and the ground transponder. This in turn affects the pulse time-of-arrival at the ground transponder and airborne receiver. Finally, for completeness, it should be noted that multipath is also another contributor to this time varying bias. However, if care is taken when siting the DME, these errors will be minimal.

Based on requirements for DME-N operation in [47], the magnitude of this time varying bias due to all the above noted causes is set to 0.17 nautical miles (315 m). In accordance with [15], it is assumed that this error has a correlation distance of 0.5 nautical miles. Dividing the correlation distance by the aircraft's speed yields a correlation time.

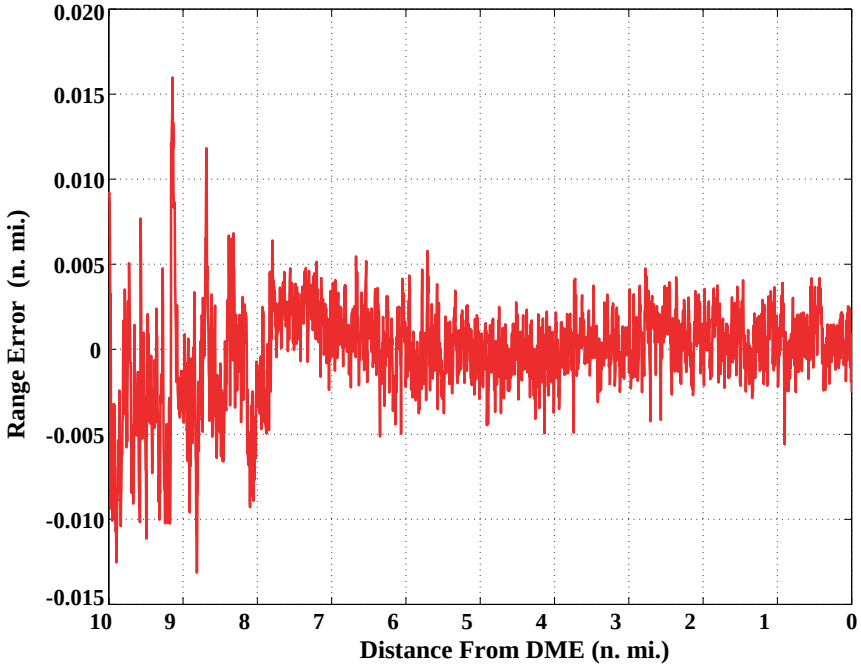

Figure 3.13: Wide Band Noise on DME-N and DME-P Range Errors. (Data Courtesy of Dr. Michael S. Braasch, Ohio University Avionics Engineering Center)

The wide-band noise δR_w can be caused by factors such as thermal noise in both the airborne and ground equipment. Figure 3.13 is a plot of detrended range errors from a DME-P transponder and receiver pair collected during a flight test. The error characteristics are seen to change when the user is within 7 nautical miles of the ground based transponder. Beyond the 7 nautical mile point, the DME-P receiver can be assumed to be the same as a DME-N receiver. The detrended error trace beyond the 7 nautical mile point is seen to have a standard deviation of 0.004 nautical miles. This is the value used as the standard deviation of the wide-band noise δR_w in the DME range error equation.

In summary, the total DME range error δR used in this thesis has the following mathematical model:

$$\begin{aligned} \delta R &= \delta R_b(t) + \delta R_w, \\ \delta \dot{R}_b &= -\frac{1}{\tau_r}\delta R_b + w_r, \\ \sigma_{R_b} &= 0.17 \text{ N.M.}, \\ \tau_r &= \frac{0.5 n.mi}{V} \text{ sec.}, \\ \sigma_{R_w} &= 0.004 \text{ N.M.} \end{aligned} \tag{3.39}$$

3.10 GPS/WAAS Errors

Error characteristics of GPS and GPS augmented by WAAS are well documented. The primary means of navigation in the future NAS is GPS augmented by WAAS for which performance requirements are documented in [25]. For the level of accuracy with which one is concerned when navigating by this backup navigation system, the WAAS position and velocity errors can be assumed to be wide-band noise. Consistent with results documented in [22], the standard deviation for the horizontal position error wide-band noise is *conservatively* set to 2 meters. Similarly, the standard deviation for the vertical position wide-band noise is *conservatively* set to 5 meters. Finally, attitude error from a short baseline GPS attitude system was taken to be wide-band noise with a standard deviation of 0.25 degrees on yaw, pitch and roll [39].

3.11 Magnetometer Calibration

Equation 3.28 presented a mathematical model for the various error sources that corrupt magnetometer measurements. The process of determining the magnitude of these various errors and removing them from the magnetometer measurements is called magnetometer calibration. Three methods for calibrating magnetometers will be presented. The first method, called Calibration in the Heading Domain (CHD), is only applicable to the classical two-magnetometer heading determination systems. The second method, called Two Dimensional Calibration in the Magnetic

Field Domain (CMFD-2), is also only applicable to the classical two-magnetometer heading determination systems. Finally, the third method is an extension of the CMFD-2 method to three dimensions (CMFD-3) and is applicable to two- and three-magnetometer configurations[‡].

3.11.1 Calibration In the Heading Domain

The classical two-magnetometer heading determination systems have been used extensively in General Aviation and marine applications. Traditionally the sensors used in these systems were flux-gate or flux-valve magnetometers. The method of calibration in the heading domain has been known for a long time [16] and was developed to deal with these heading determination systems. The heading determination system used in the dead reckoning navigator discussed in this thesis is based on a three-magnetometer configuration. As such, calibration of this system will require use of the three dimensional calibration method. However, a detailed discussion of the CHD method is judged to be necessary here because:

1. The CHD algorithm will be used as a bench mark against which the two- and three-dimensional CMFD algorithms will be compared.

2. The fundamental equation for the CHD algorithm is an equation relating heading errors to magnetometer measurement errors. This is a convenient equation that will be used to evaluate the expected heading error as a function of magnetometer calibration residuals when dealing with the two- and three-dimensional CMFD algorithms.

In what follows, it will be assumed that the two-magnetometer system is level. Furthermore, for the sake of clarity it will be assumed that the magnetometer installation is such that there are no misalignment errors. The effect of misalignments will be considered later. In this case, an error-free two-magnetometer system will measure the strength of the *horizontal* component of the local Earth magnetic field vector

[‡]The algorithms for two- and three-dimensional calibration in the magnetic field domain were developed in collaboration with Elkaim as documented in [37] and [30].

($\vec{B}_H$). In mathematical terms, an error-free magnetometer having a sensitivity axis aligned with the body x-axis will measure the following component of $\vec{B}_H$:

$$B_x^b = B_H \cos(\psi) \tag{3.40}$$

where

$$B_H = \|\vec{B}_H\|. \tag{3.41}$$

Similarly, a magnetometer with sensitivity axis aligned with the body y-axis will measure the following component of $\vec{B}_H$:

$$B_y^b = -B_H \sin(\psi). \tag{3.42}$$

Since the magnetometer assembly is assumed to be level, the body coordinate system is the same as the wander-azimuth coordinate system and B_x^b and B_y^b can be used in Equation 2.3 for B_x^b and B_y^b to determine heading. If measurement errors are present, the output from the magnetometers in the body frame will not be B_x^b and B_y^b. Instead, the output of the x-magnetometer will be $\hat{B}_x^b$ given by

$$\begin{aligned} \hat{B}_x^b &= B_x^b + \delta B_{x_0} + \alpha_{xx} B_x + \alpha_{xy} B_y \\ &= B_x^b + \delta B_{x_0} + \alpha_{xx} B_H \cos\psi - \alpha_{xy} B_H \sin\psi, \end{aligned} \tag{3.43}$$

and the y-magnetometer output will be $\hat{B}_y^b$ given by:

$$\begin{aligned} \hat{B}_y^b &= B_y^b + \delta B_{y_0} + \alpha_{yx} B_x + \alpha_{yy} B_y \\ &= B_y^b + \delta B_{y_0} + \alpha_{yx} B_H \cos\psi - \alpha_{yy} B_H \sin\psi. \end{aligned} \tag{3.44}$$

The terms δB_{x_0} and δB_{y_0} are the hard iron errors. The terms α_{xx}, α_{xy}, α_{yx} and α_{yy} represent the *effective* soft iron coefficients which are the constants of proportionality between the magnetic field applied to a soft metal and the resulting induced magnetic field. From a notation point of view, α_{xy}, for example, represents the effective coefficient relating the field generated in the x-direction in response to an applied field in the y-direction. The term "effective" is used to describe these coefficients because they represent the effect of *all* soft iron material present that may corrupt

the magnetometer outputs.

To get a better understanding for what these effective soft iron coefficients are, consider a collection of N distinct soft iron materials in the vicinity of the magnetometers. The i^{th} soft iron material will generate an induced magnetic field in the x-direction of magnitude, B^i_{sx}, given by:

$$B^i_{sx} = \alpha^{(i)}_{xx} B_H \cos\psi - \alpha^{(i)}_{xy} B_H \sin\psi. \tag{3.45}$$

From the previous equation it follows that the total field generated by all the soft iron materials will be:

$$B^N_{sx} = \left(\sum_{i=1}^{N} \alpha^{(i)}_{xx}\right) B_H \cos\psi - \left(\sum_{i=1}^{N} \alpha^{(i)}_{xy}\right) B_H \sin\psi. \tag{3.46}$$

Therefore, the effective soft iron coefficient α_{xx} is defined as:

$$\alpha_{xx} = \sum_{i=1}^{N} \alpha^{(i)}_{xx} \tag{3.47}$$

The objective of the CHD algorithm is to evaluate heading errors as function of magnetometer measurement errors. An expression relating heading errors to magnetometer measurement errors can be arrived at by taking a perturbation of Equation 2.3. This leads to:

$$\begin{aligned} \delta\psi &= \left(\frac{\partial\psi}{\partial B_y}\right)\delta B_y + \left(\frac{\partial\psi}{\partial B_x}\right)\delta B_x \\ &= -\frac{1}{B_H}\left(\delta B_x \sin\psi + \delta B_y \cos\psi\right) \end{aligned} \tag{3.48}$$

The perturbation quantities δB_x and δB_y represent magnetometer measurement errors and are given by:

$$\delta B_x = \hat{B}^b_x - B^b_x \tag{3.49}$$

$$\delta B_y = \hat{B}^b_y - B^b_y \tag{3.50}$$

Substituting these values into Equation 3.48 and rearranging leads to the following equation for heading error:

$$\begin{aligned}\delta\psi &= \left(\frac{\alpha_{xy}-\alpha_{yy}}{2}\right) - \frac{\delta B_{x_0}}{B_H}\sin(\psi) - \frac{\delta B_{y_0}}{B_H}\cos(\psi) \\ &\quad + \left(\frac{\alpha_{xx}-\alpha_{yx}}{2}\right)\sin(2\psi)\left(\frac{\alpha_{yy}-\alpha_{xy}}{2}\right)\cos(2\psi) \qquad (3.51)\end{aligned}$$

$$= A + B\sin(\psi) + C\cos(\psi) + D\sin(2\psi) + E\cos(2\psi). \qquad (3.52)$$

Equation 3.51 is effectively a truncated Fourier series where the Fourier coefficients B and C are functions of the hard iron and the D and E coefficients represent the soft iron errors. Estimation of the Fourier coefficients is accomplished by a procedure called swinging. The procedure involves leveling and rotating the vehicle containing the magnetometer through a series of N *known* headings as shown schematically in Figure 3.14. At each known k^{th} heading, the heading error, $\delta\psi_k$, is computed and then used to form the system of Equations 3.53. A batch least squares solution of Equation 3.53 yield estimates for the coefficients A through E.

$$\begin{bmatrix} \delta\psi_1 \\ \delta\psi_2 \\ \vdots \\ \delta\psi_N \end{bmatrix} = \begin{bmatrix} 1 & \sin(\psi_1) & \cos(\psi_1) & \sin(2\psi_1) & \cos(2\psi_1) \\ 1 & \sin(\psi_2) & \cos(\psi_2) & \sin(2\psi_2) & \cos(2\psi_2) \\ \vdots & & \ddots & & \vdots \\ 1 & \sin(\psi_N) & \cos(\psi_N) & \sin(2\psi_N) & \cos(2\psi_N) \end{bmatrix} \begin{bmatrix} A \\ B \\ C \\ D \\ E \end{bmatrix} \qquad (3.53)$$

One of the important facts that becomes apparent when examining Equation 3.51 is that the coefficients A through E are either linear combinations of the α_{ij} soft iron coupling terms or are functions of the local earth magnetic field strength. This implies that the calibration is location dependent and is one of the disadvantages of the CHD algorithm. That is, if the vehicle with the magnetometer based heading determination system is expected to travel over a large geographic area such that large variations in the magnitude of the local Earth magnetic field vector are expected, then multiple calibrations must be performed. Each calibration will yield a location dependent coefficient set A through E that can be scheduled as needed. Marine vehicles avoided

this complication by using *hardware* to accomplish this calibration: hard and soft iron metals were installed in the vicinity of the compass or magnetometer to negate the hard and soft iron effects of the ships structure.

Another shortcoming of the CHD method which becomes apparent when examining Equation 3.51 is that heading is an input to the algorithm. Since heading errors due to hard and soft iron errors are not constant but heading dependent, the heading input into the algorithm will be corrupted by a non-constant bias. Therefore, another independent measurement of heading is required when calibrating magnetometers using this method. When performing this calibration for magnetometers installed in aircraft, the standard practice is to use a compass rose painted on the tarmac, as shown in Figure 3.14 on page 78, as the secondary independent heading measurement.

Up to this point, misalignments were ignored. For the two-magnetometer system, misalignment errors can be classified into two categories. The first category is the case of pitch and roll misalignment. Pitch and roll misalignments are installation errors that result in the magnetometers not being level when the vehicle is level. The two dimensional CHD algorithm cannot deal with with pitch and roll misalignments because the errors introduced by such misalignments are time varying. The second category is a yaw misalignment. This is the case where installation errors result in the magnetometer assembly being installed with an azimuth bias. Mathematically, a constant azimuth bias, $\delta\psi_0$, due to installation errors modifies Equation 3.51 in the following manner:

$$\delta\psi = A + B\sin(\psi+\delta\psi_0) + C\cos(\psi+\delta\psi_0) + D\sin(2\psi+2\delta\psi_0) + E\cos(2\psi+2\delta\psi_0). \quad (3.54)$$

When this equation is expanded using trigonometric identities and rearranged, one gets

$$\delta\psi = \bar{A} + \bar{B}\sin(\psi) + \bar{C}\cos(\psi) + \bar{D}\sin(2\psi) + \bar{E}\cos(2\psi). \quad (3.55)$$

All that has happened is that the Fourier coefficients are now modified. Thus, the CHD algorithm can deal with yaw misalignments. This also implies that a compass rose is not really required when using the CHD algorithm. All that is required is to swing the magnetometer assembly through equally spaced headings around the

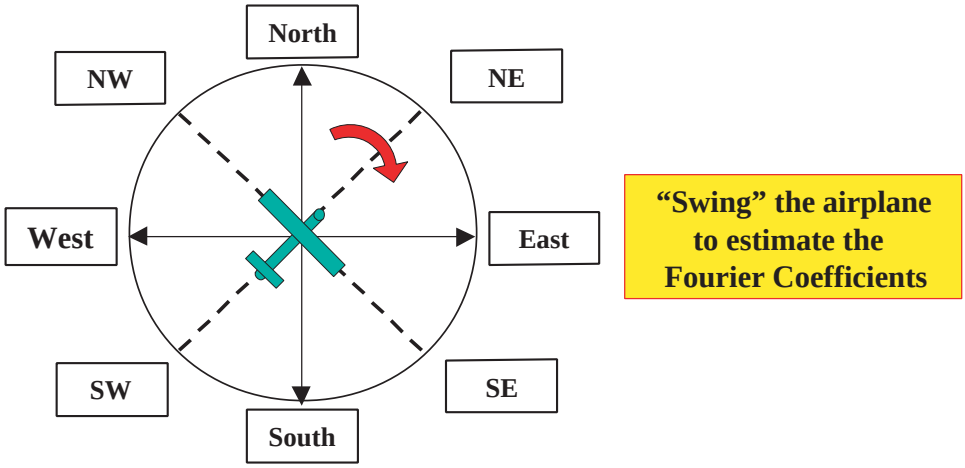

Figure 3.14: Graphical Description of Swinging.

compass rose followed by one final known heading. In this instance, the offset term, $\delta\psi_0$, will be the sum of the installation error and the constant heading error introduced by the fact that a compass rose was not used. Thus, the final known heading is used to separate the two individual components of $\delta\psi_0$.

3.11.2 2-D Calibration in the Magnetic Field Domain

This section presents the two-dimensional Calibration in the Magnetic Field Domain (CMFD-2) algorithm. Unlike the CHD algorithm, the CMFD-2 algorithm is not location dependent. The fundamental idea behind this calibration method is that the locus of error-free measurements from a two-magnetometer heading system is a circle. It is easy to show that this is indeed the case just by examining Equations 3.40 and 3.42. If Equation 3.40 is squared and added to the square of Equation 3.42, the following expression results:

$$B_x^{b\,2} + B_y^{b\,2} = B_H^2 \cos^2\psi + B_H^2 \sin^2\psi = B_H^2 \tag{3.56}$$

This is the equation of a circle with its center at the origin. The radius of the circle is equal to the magnitude of the horizontal component of the local Earth magnetic

field vector. The magnitude of the radius varies with latitude, longitude and altitude because Earth's magnetic field vector varies with location. This variation of Earth's magnetic field vector is well known and modeled. In this work, the magnitude of Earth's local magnetic field vector was determined using the 1999 International Geomagnetic Reference Field model [13].

The effect of the various magnetometer errors described in Equation 3.28 is to alter the shape of the locus of measurements described in Equation 3.56. Hard iron errors, for example, shift the origin of the basic locus. This can be shown mathematically by considering a hard iron bias vector with components δB_{x_0} and δB_{y_0}. If the x and y field measurements in the platform axes are biased by δB_{x_0} and δB_{y_0}, respectively, the equation for the locus of the magnetometer measurements becomes:

$$\left(\hat{B}_x^b - \delta B_{x_0}\right)^2 + \left(\hat{B}_y^b - \delta B_y\right)^2 = B_H^2. \tag{3.57}$$

This is still the equation of a circle but instead of having its center located at the origin, its center is at $(\delta B_{x_0}, \delta B_{y_0})$.

In the absence of other forms of errors, scale factor errors cause the body x and y magnetometer measurements to be different when both magnetometers are subjected to a magnetic field of the same strength. This can be expressed mathematically by modifying Equations 3.40 and 3.42 as follows:

$$\hat{B}_x^b = (1 + s_{fx})\, B_H \cos\psi \tag{3.58}$$

$$\hat{B}_y^b = -(1 + s_{fy})\, B_H \sin\psi \tag{3.59}$$

Carrying out a similar squaring and adding as was done in the derivation of Equation 3.56 leads to

$$\left(\frac{B_x}{1 + s_{fx}}\right)^2 + \left(\frac{B_y}{1 + s_{fy}}\right)^2 = {B_H}^2, \tag{3.60}$$

which is the equation of an ellipse centered at the origin. The major and minor axes' magnitudes are determined by the scale factor errors, s_{fx} and s_{fy}. When the magnetometer output is corrupted by scale factor errors as well as hard iron error biases δB_{x_0} and δB_{y_0} the resulting locus is an ellipse with its center at δB_{x_0} and δB_{y_0}.

In comparison to hard iron and scale factor errors, the effect of soft iron errors

on the locus of magnetometer measurements is more complicated. This is due to the fact that in the absence of hard iron and scale factor errors, soft iron errors have two separate effects on the locus of magnetometer readings. Soft iron errors will modify the error-free circular locus into an ellipse as well as rotate the major and minor axes of the ellipse. To show this mathematically, Equations 3.43 and 3.44 are rearranged as follows:

$$\hat{B}_x^b = B_H \cos\psi(1+\alpha_{xx}) - \alpha_{xy} B_H \sin\psi \tag{3.61}$$

$$\hat{B}_y^b = -B_H \sin\psi(1+\alpha_{yy}) - \alpha_{yx} B_H \cos\psi. \tag{3.62}$$

In matrix form these equations become:

$$\begin{bmatrix} \hat{B}_x^b \\ \hat{B}_y^b \end{bmatrix} = \begin{bmatrix} (1+\alpha_{xx}) & \alpha_{xy} \\ \alpha_{yx} & (1+\alpha_{yy}) \end{bmatrix} \begin{bmatrix} B_H \cos\psi \\ -B_H \sin\psi \end{bmatrix} \tag{3.63}$$

Inverting this matrix equation leads to the following:

$$\begin{bmatrix} B_x^b \\ B_y^b \end{bmatrix} = \frac{1}{(1+\alpha_{xx})(1+\alpha_{yy}) - \alpha_{xy}\alpha_{yx}} \begin{bmatrix} (1+\alpha_{yy}) & -\alpha_{xy} \\ -\alpha_{yx} & (1+\alpha_{xx}) \end{bmatrix} \begin{bmatrix} \hat{B}_x^b \\ \hat{B}_y^b \end{bmatrix} \tag{3.64}$$

If the two equations represented by this matrix are squared and added, it is clear that the resulting locus of magnetometer measurements will describe an ellipse with rotated major and minor axes. If, in addition to soft iron errors, hard iron errors are present, the locus will still be a rotated ellipse but will have its center displaced from the origin. Figure 3.15 is a graphical summary of the effect of the various errors on the locus of magnetometer measurements.

At this point a discussion regarding the observability of scale factor, misalignment and soft iron errors is in order. From the previous discussion on the CHD algorithm it is apparent that yaw misalignments are not observable from the magnetometer measurement locus. In the presence of soft iron induced fields, it is difficult to distinguish between the effects due to scale factors and those due to the soft iron. A similar lack of observability occurs when misalignment and soft iron error effects are present. Fortunately, in aviation applications, soft iron materials are rare in the locations where magnetometers are normally mounted. If care is taken during installation

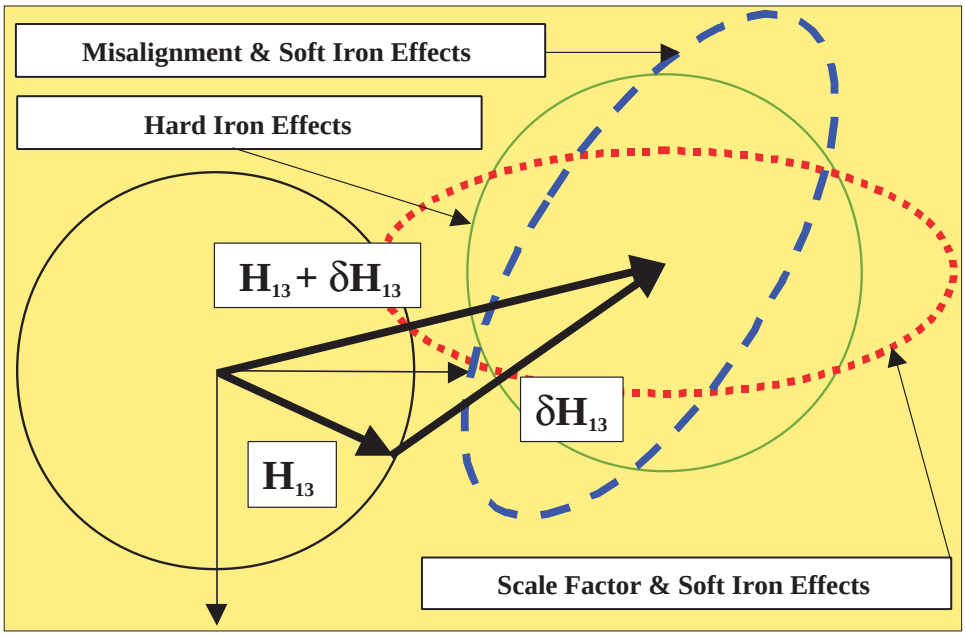

Figure 3.15: Effect of Errors on Magnetic Field Measurement Locus in 2-D.

misalignments will also be small. Thus, in most aviation applications the two errors that magnetometer calibration algorithms encounter are hard iron biases and scale factor errors.

The CMFD-2 algorithm is a nothing more than a parameter estimation problem. If an aircraft with a magnetometer is rotated through 360° about its yaw axis, the locus of magnetometer measurements will be an ellipse. The algorithm is an attempt to fit the best ellipse (in the least squares sense) to the measured magnetometer data. If the above assumptions of installation misalignments and soft iron errors are made, then the parameter estimation problem is one where the only unknowns are the hard iron errors and scale factor errors. In terms of the mathematics of the estimation process, the hard iron errors correspond to the center of the ellipse and the scale factor errors correspond to the size of the major and minor axes of the ellipse.

3.11.3 3-D Calibration in the Magnetic Field Domain

There are cases where the two-dimensional calibration schemes are inadequate. For example, it was noted earlier that the two-magnetometer heading determination system will not give accurate heading information when the magnetometer assembly is not level. Figure 3.16 shows the relationship between heading error and roll angle when using a two-magnetometer heading determination system. In Figure 3.16, the aircraft is on a true heading of 45° and heading errors are induced when the aircraft pitches or rolls. This is because in non-level flight, the vertical component of Earth's magnetic field is measured and induces heading errors. Getting accurate heading information when the magnetometer is not level (e.g., in turns) requires a three-magnetometer system. Calibrating the third magnetometer of this three-magnetometer heading determination requires a three-dimensional calibration system. There are other non-heading determination applications where a three-magnetometer system is required. One such case is an attitude determination system that will be discussed in Chapter 4. This is a vector matching system that requires accurate measurement of all three components of Earth's magnetic field vector.

The 3-D calibration algorithm in the magnetic field domain is an extension of the 2-D calibration algorithm presented previously. In the 3-D case, the locus of outputs for an error-free magnetometer triad measuring Earth's magnetic field vector in a given geographical location is a sphere. This sphere will be centered at the origin with a radius equal to the magnitude of Earth's magnetic field vector. To visualize this, note that Earth's magnetic field vector is a constant vector fixed in the locally level navigation frame. If an aircraft instrumented with a magnetometer triad strapped to its body frame is located at a given geographic area and rotates through all combinations of Euler angles, the constant Earth magnetic field vector will trace out a sphere. For example, in the San Francisco Bay area (approximately $N37°$ Latitude and $W122°$ Longitude) where Earth's magnetic field vector has a magnitude of approximately 0.5 Gauss, the locus of outputs for an error free magnetometer will look like the upper left plot of Figure 3.17.

In the presence of the various magnetometer errors described in Equation 3.28, the shape of this measurement locus is altered. If the scale factor for each magnetometer is not the same (i.e., a scale factor error is present), then the sphere representing

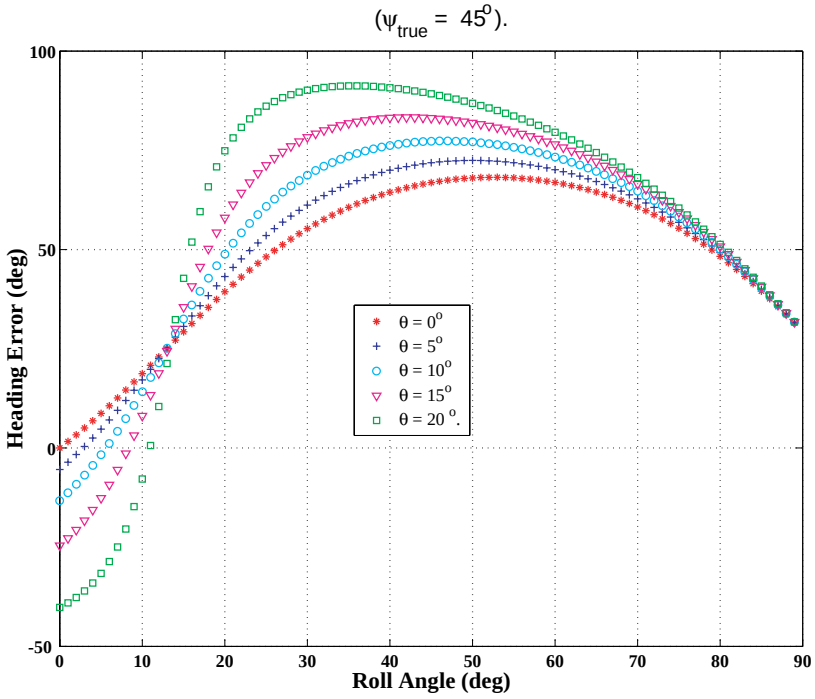

Figure 3.16: Heading Errors Induced by Roll and Pitch In a Two-Magnetometer Heading Determination System.

the locus of outputs will be reshaped into an ellipsoid centered at the origin. This is shown in the upper right of Figure 3.17. Hard iron errors are equivalent to a constant bias. The effect of hard iron errors, therefore, is to shift the ellipsoid away from the origin as shown in the lower left of Figure 3.17. Now assume that the output of the magnetometer is corrupted by wide-band noise. The effect of the wide-band noise is to alter the shape of the locus as shown in the lower right of Figure 3.17.

Estimation of the scale factor errors and hard iron is nothing more than a parameter estimation problem. That is, it is the problem of determining the parameters of an ellipsoid that best fit the data collected from a magnetometer triad. As discussed earlier, misalignment errors will have been removed before this estimation. Thus, cross-axis terms are absent and the parameters that need to be estimated are the six parameters that define an ellipsoid having axes aligned with the coordinate axes.

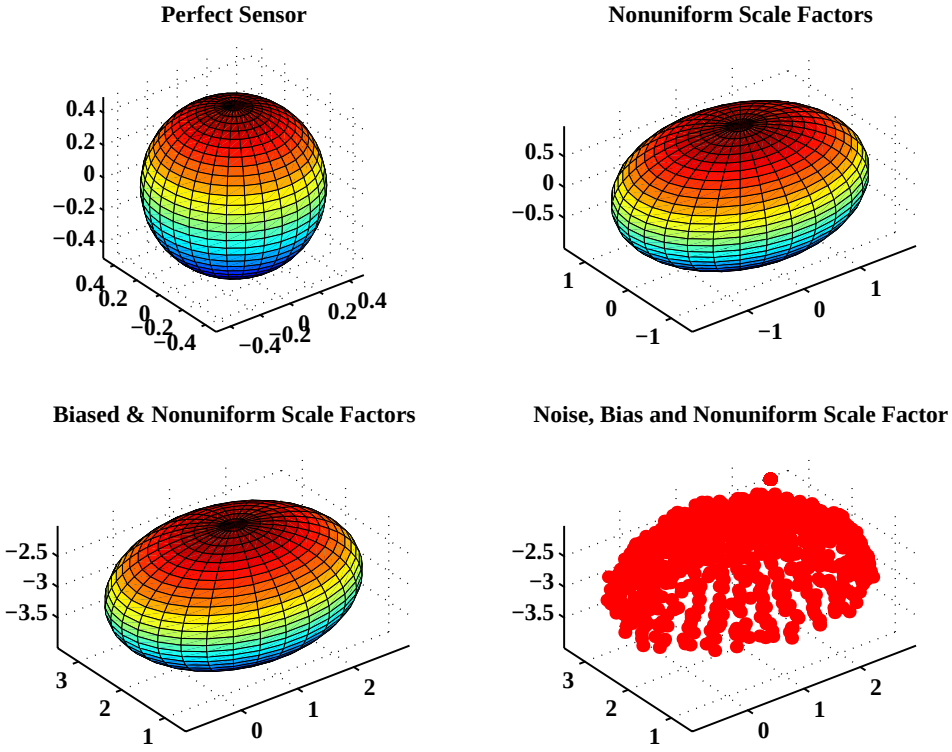

Figure 3.17: 3 Dimensional Locus of Magnetic Field Measurements.

These parameters define the magnitude of the axes and the coordinates of the center. Mathematically, the parameter estimation problem becomes:

$$R^2 = \left(\frac{\hat{B}_x^b - \delta B_{x_0}}{1 + s_{fx}} \right)^2 + \left(\frac{\hat{B}_y^b - \delta B_{y_0}}{1 + s_{fy}} \right)^2 + \left(\frac{\hat{B}_z^b - \delta B_{z_0}}{1 + s_{fz}} \right)^2 \tag{3.65}$$

In terms of Equation 3.65, it is a matter of estimating the scale factors, s_{fx}, s_{fy}, and s_{fz}, along with the hard iron biases, δB_{x_0}, δB_{y_0} and δB_{z_0}, given the magnetometer measured outputs, $\hat{B}_x^b$, $\hat{B}_y^b$, and $\hat{B}_z^b$, and the magnitude of Earth's magnetic field vector, R, in a given geographic location.

Two separate algorithms for estimating these parameters are presented next. The first method is a Linearized Batch Least Squares method and the second method is a Non-Linear 2-Step Estimation method.

Linearized Batch Least Squares (LBLS) Estimation

The Linearized Batch Least Squares (LBLS) estimation algorithm takes the classic approach to non-linear estimation problems. The governing non-linear equations are linearized such that the perturbations of the parameter of interest are estimated. The estimated perturbations are added to non-perturbed variables and the estimation is repeated until convergence is achieved. It is an iterative procedure and requires an initial guess of the scale factors and hard iron biases to start-off the algorithm.

Development of the algorithm begins by taking a perturbation of the ellipsoid relation given in Equation 3.65. A perturbation of Equation 3.65 results in the following:

$$\begin{aligned} 2\,R\delta R = &-2\left(\frac{\hat{B}_x^b - \delta B_{x_0}}{\left(1+s_{fx}\right)^2}\right)\delta\left(\delta B_{x_0}\right) - 2\left(\frac{\left(\hat{B}_x^b - \delta B_{x_0}\right)^2}{\left(1+s_{fx}\right)^3}\right)\delta\left(1+s_{fx}\right) \\ &-2\left(\frac{\hat{B}_y^b - \delta B_{y_0}}{\left(1+s_{fy}\right)^2}\right)\delta\left(\delta B_{y_0}\right) - 2\left(\frac{\left(\hat{B}_y^b - \delta B_{y_0}\right)^2}{\left(1+s_{fy}\right)^3}\right)\delta\left(1+s_{fy}\right) \\ &-2\left(\frac{\hat{B}_z^b - \delta B_{z_0}}{\left(1+s_{fz}\right)^2}\right)\delta\left(\delta B_{z_0}\right) - 2\left(\frac{\left(\hat{B}_z^b - \delta B_{z_0}\right)^2}{\left(1+s_{fz}\right)^3}\right)\delta\left(1+s_{fz}\right). \end{aligned} \tag{3.66}$$

The equation above is linear in the perturbation of the hard iron biases and the scale factors. When multiple measurements are available, this perturbation equation can be simplified and cast into a standard linear measurement equation form of $\delta\vec{z} = H\delta\vec{x}$. In this case, the state vector, $\delta\vec{x}$, to be estimated is a vector of the perturbations given by the following:

$$\delta\vec{x} = \begin{bmatrix} \delta(\delta B_x^b) & \delta(\delta B_y^b) & \delta(\delta B_z^b) & \delta(1+s_{fx}) & \delta(1+s_{fy}) & \delta(1+s_{fz}) \end{bmatrix}^T \tag{3.67}$$

In the case where N measurements are available, the measurement vector, $\delta\vec{z}$, becomes:

$$\begin{bmatrix} \delta R_1 \\ \delta R_2 \\ \vdots \\ \delta R_N \end{bmatrix} = \begin{bmatrix} R_1 - \hat{R}_1 \\ R_1 - \hat{R}_2 \\ \vdots \\ R_N - \hat{R}_N \end{bmatrix} \tag{3.68}$$

Given an initial guess for the biases and the scale-factors, an estimate for the perturbation can be obtained. This is used to update the estimate for the scale factors and biases and the process is repeated until convergence is achieved.

Non-Linear, 2-Step Estimation

The Non-Linear, 2-Step estimator discussed here is an adaptation of an estimator presented in [42] and breaks the parameter identification problem given by Equation 3.65 into two steps. In the first step, a state vector called the "first step state" is formed. The elements of this state vector are algebraic combinations of the elements of the "second step state" vector. The elements of the second step state vector, on the other hand, are the scale factors and hard iron biases. The estimation problem is linear in the first step state and, therefore, retains the desirable properties of a linear system. In particular, the least squares estimate of the first step state is guaranteed to be unbiased. Following estimation of the first step state, elements of the second step state vector are extracted through algebraic manipulation.

Derivation of the equations for the Non-Linear 2-step estimator begin by expanding Equation 3.65 as follows:

$$\begin{aligned} R^2 &= \frac{(\hat{B}_x^b)^2 - 2(\hat{B}_x^b)(\delta B_{x0}) + (\delta B_{x0})^2}{(1+s_{fx})^2} \\ &+ \frac{(\hat{B}_y^b)^2 - 2(\hat{B}_y^b)(\delta B_{y0}) + (\delta B_{y0})^2}{(1+s_{fy})^2} \\ &+ \frac{(\hat{B}_z^b)^2 - 2(\hat{B}_z^b)(\delta B_{z0}) + (\delta B_{z0})^2}{(1+s_{fz})^2} \end{aligned} \tag{3.69}$$

Equation 3.69 can be rearranged and put into matrix notation in the following manner:

$$-(\hat{B}_x^b)^2 = \begin{bmatrix} -2\hat{B}_x^b & (\hat{B}_y^b)^2 & -2\hat{B}_y^b & (\hat{B}_z^b)^2 & -2\hat{B}_z^b & 1 \end{bmatrix} \begin{bmatrix} \delta B_{x0} \\ k_2 \\ k_2(\delta B_{y0}) \\ k_3 \\ k_3(\delta B_{z0}) \\ k_4 \end{bmatrix} \tag{3.70}$$

Given multiple measurements, Equation 3.70 can be written in the form of $\vec{z} = H\vec{x}$. The vector $\vec{x}$ is the first step state and is the right-most vector in Equation 3.70. It consists of the variables k_1 through k_4 which are defined as follows:

$$k_1 = R^2(1+s_{fx})^2 \tag{3.71}$$
$$k_2 = \frac{(1+s_{fx})^2}{(1+s_{fy})^2} \tag{3.72}$$
$$k_3 = \frac{(1+s_{fx})^2}{(1+s_{fz})^2} \tag{3.73}$$
$$k_4 = (\delta B_{x0})^2 + k_2(\delta B_{y0})^2 + k_3(\delta B_{z0})^2 - k_1 \tag{3.74}$$

Once the first step state vector is estimated, the scale factors and hard iron biases are extracted algebraically by the following inverse relations:

$$\delta B_{x0} = \vec{x}(1) \tag{3.75}$$
$$\delta B_{y0} = \frac{\vec{x}(3)}{\vec{x}(2)} \tag{3.76}$$
$$\delta B_{z0} = \frac{\vec{x}(5)}{\vec{x}(4)} \tag{3.77}$$
$$(1+s_{fx}) = \sqrt{\frac{k_1}{R^2}} \tag{3.78}$$
$$(1+s_{fy}) = \sqrt{\frac{k_1}{k_2 R^2}} \tag{3.79}$$
$$(1+s_{fx}) = \sqrt{\frac{k_1}{k_3 R^2}} \tag{3.80}$$

Simulation Studies

Simulation studies were performed to assess the performance of the two algorithms developed and discussed above. The simulations showed that the LBLS algorithm is primarily sensitive to three factors. Firstly, it requires a reasonably close guess of the scale factors and hard iron biases. Initial guesses of scale factors and hard iron biases that are not close to the actual values lead to divergence of the algorithms. Secondly, large amounts of sampling noise tended to cause the algorithm to diverge. However, the amount of noise that can be tolerated was a function of the third factor; the portion of a complete ellipsoid available for estimation purposes. If a smaller portion of the ellipsoid is present in the data, only small amounts of noise are tolerated by the algorithm. If large amounts of the ellipsoid are present, large amounts of noise can be handled.

The sensitivity of these algorithms to the amount of data present (or shape of the measurement locus) has a very important practical implication. When discussing the methods for calibrating a two-magnetometer system, it was noted that the parameter estimation problem is one where the best circle (in the least squares sense) is fit to the noisy magnetometer measurement data. A simple 360° turn on the tarmac yielded the required measurement locus. In extending this method to the three-dimensional case, a tacit assumption is that the entire sphere would be available for the parameter estimation problem. Unfortunately this is not the case. Getting the entire sphere requires spanning the entire Euler angle space. Unless the magnetometer triad is installed in an aerobatic airplane, spanning the entire Euler angle space is not possible. So the three dimensional calibration algorithms must be able to work with data that comprises only a portion of the entire sphere. Actual data collected from a flight test is shown in Figure 3.18. It is clear from this figure that an entire ellipsoid can not be obtained in a non-aerobatic aircraft.

The results of the simulation studies which will be discussed next considered the case where the output from a triad of magnetometers was corrupted by hard iron biases and wide-band noise. Furthermore, two loci of magnetometer measurements were considered. Figure 3.19 is a schematic that illustrates the loci considered. If the entire Euler angle space can be spanned, the locus of magnetometer measurements obtained would be as shown in Figure 3.19(a). For purposes of the simulation, only a

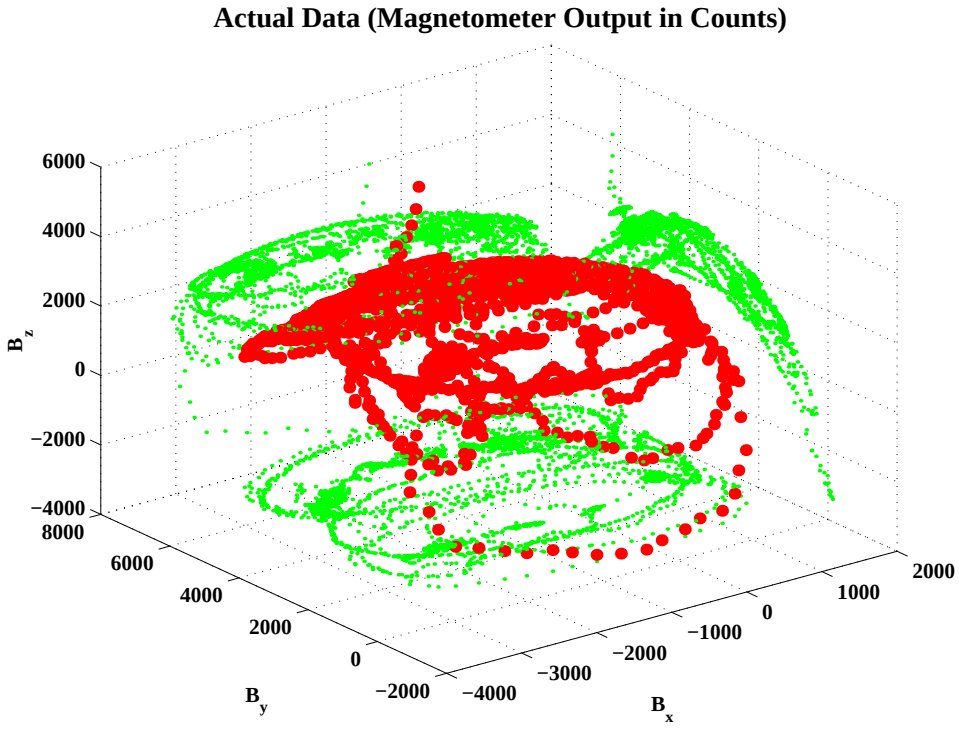

Figure 3.18: Portion of the Ellipsoid Representing the Locus of Magnetometer Measurements from Actual Flight Test Data (The Red Data is the 3-D Measurement Locus. The Green Data is the Projection of the 3-D Data on the x-y, x-z and y-z Coordinate Planes).

small portion of the ellipsoid was assumed to be present. This portion of the ellipsoid is shown in Figure 3.19(b). In this case, one metric for quantifying how much of the measurement locus is available for the estimation is the central angle spanned by the strip of the ellipsoid, Φ, as shown in Figure 3.19(c).

Table 3.3 shows the four cases evaluated in this simulation study. Basically, these simulation studies evaluated estimation accuracy as a function of magnetometer measurement noise and size of the measurement locus. It will be recalled that the LBLS algorithm needs an initial guess of hard iron and scale factor errors. To ensure various initial conditions were tested, for each simulation run, initial guesses for these parameters were selected randomly. The initial guesses for the hard iron biases were picked

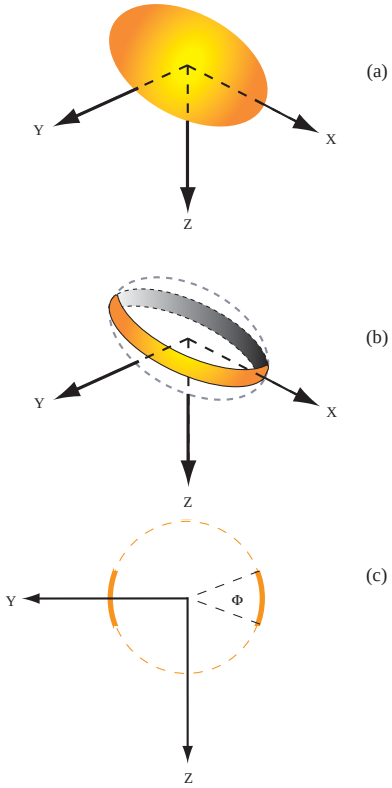

Figure 3.19: Quantifying the Size of the Magnetometer Measurement Locus Available For Estimation.

from a normal distribution centered at (or having a mean equal to) the actual hard iron biases with a standard deviation of 0.5 Gauss. Similarly, the initial guesses for the scale factor errors were picked from a normal distribution centered at the actual scale factor errors with a standard deviation 0.5.

The results of these trade-off studies are shown in Figures 3.20 through 3.25. Figures 3.20 and 3.21 show the performance of the LBLS algorithm in the presence of a 1 milli-Gauss wide-band noise on the magnetometer measurements and when 10° and 20° strips of measurement locus are available. The LBLS algorithm is seen to converge in both cases. When the measurement noise is increased to 5 milli-Gauss, the results shown in Figures 3.22 and 3.23 are obtained. Figure 3.22 shows that the LBLS algorithm diverges when only a 10° strip of the measurement locus is available.

Case & Strip Size	Hard Iron Bias		Scale Factor & Soft Iron		Wide-Band Noise
I, 10°	δB_{x_0}	1 Gauss	$(1 + s_{fx})$	4	1 milli-Gauss
	δB_{y_0}	2 Gauss	$(1 + s_{fy})$	3	
	δB_{z_0}	-3 Gauss	$(1 + s_{fz})$	2	
II, 20°	δB_{x_0}	1 Gauss	$(1 + s_{fx})$	4	1 milli-Gauss
	δB_{y_0}	2 Gauss	$(1 + s_{fy})$	3	
	δB_{z_0}	-3 Gauss	$(1 + s_{fz})$	2	
III, 10°	δB_{x_0}	1 Gauss	$(1 + s_{fx})$	4	5 milli-Gauss
	δB_{y_0}	2 Gauss	$(1 + s_{fy})$	3	
	δB_{z_0}	-3 Gauss	$(1 + s_{fz})$	2	
IV, 20°	δB_{x_0}	1 Gauss	$(1 + s_{fx})$	4	5 milli-Gauss
	δB_{y_0}	2 Gauss	$(1 + s_{fy})$	3	
	δB_{z_0}	-3 Gauss	$(1 + s_{fz})$	2	

Table 3.3: Parameters for Magnetometer Calibration Simulations.

In Figures 3.22 and 3.23 the initial conditions are not the same. This is because, as noted earlier, the initial conditions were varied randomly from one try to the next. The difference in initial conditions, however, is not the cause of the divergence because these plots show the results for just one simulation run out of many. The algorithm diverged repeatedly when only a 10° strip of the locus was used while, as shown in Figure 3.23, the algorithm almost always converged when a 20° strip of the measurement locus was available.

The measurement noise on low performance magnetometers can be as high as the 5 milli-Gauss figure used in these simulations. Therefore, it is concluded that for relatively low performance magnetometers with relatively large magnitude output noise, this algorithm is not suitable unless a large portion of the ellipsoid is available.

The simulation results for using the Non-Linear, 2-Step estimator are shown in Figures 3.24 and 3.25. These figures are histograms for the hard iron bias and scale factor estimation errors for 1000 simulation runs. For each run, simulated magnetometer outputs were corrupted with hard iron, scale factor and wide-band noise. The hard iron bias and scale factor errors were held constant for all 1000 simulation runs and had the values given in Table 3.3. The wide-band noise, however, was

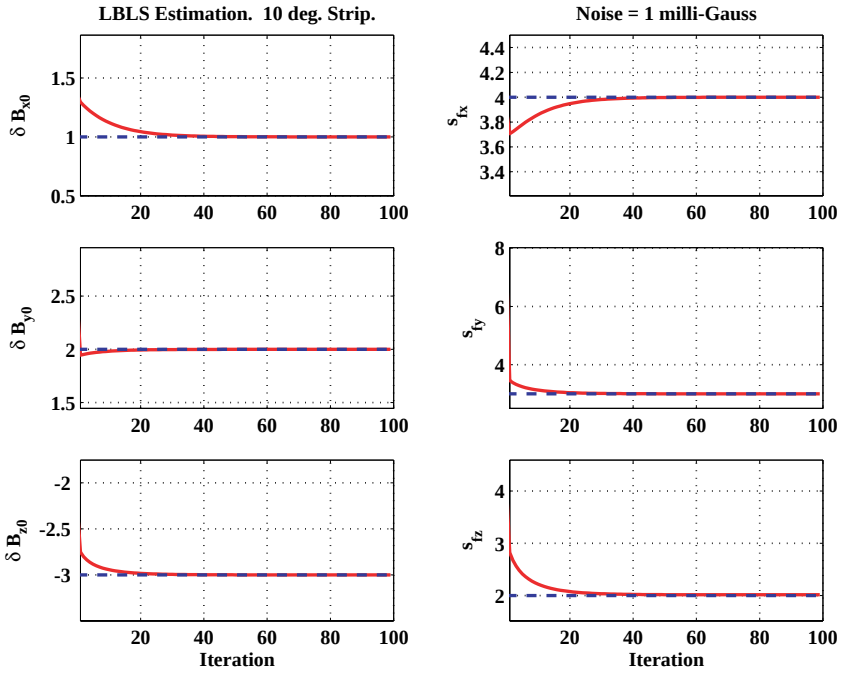

Figure 3.20: LBLS Estimation for a 10° Strip and 1 milli-Gauss Measurement Noise.

varied for each run. It was a random sequence with a standard deviation of 1 or 5 milli-Gauss.

Figure 3.24 shows the bias estimation errors. In none of the cases did the solution diverge. Furthermore, for the x- and y-axes hard iron biases, the estimation errors are seen to be less than ± 0.5 milli-Gauss. In comparison to the x- and y-axes, the z-axis estimation errors are slightly larger. However, this error is smaller when the locus of magnetometer measurements is larger. A similar trend is seen in Figure 3.25 which shows the scale factor estimation errors. The fact that the estimation errors for both the z-axis hard iron biases and scale factor errors are larger in comparison to the x- and y-axes errors is not surprising because even in the 20° locus case the data spans only a small amount of space in the z-direction.

In conclusion, the Non-Linear, 2-Step Estimator is seen to be superior to the LBLS estimator. It does not diverge even in the case when the wide-band noise on

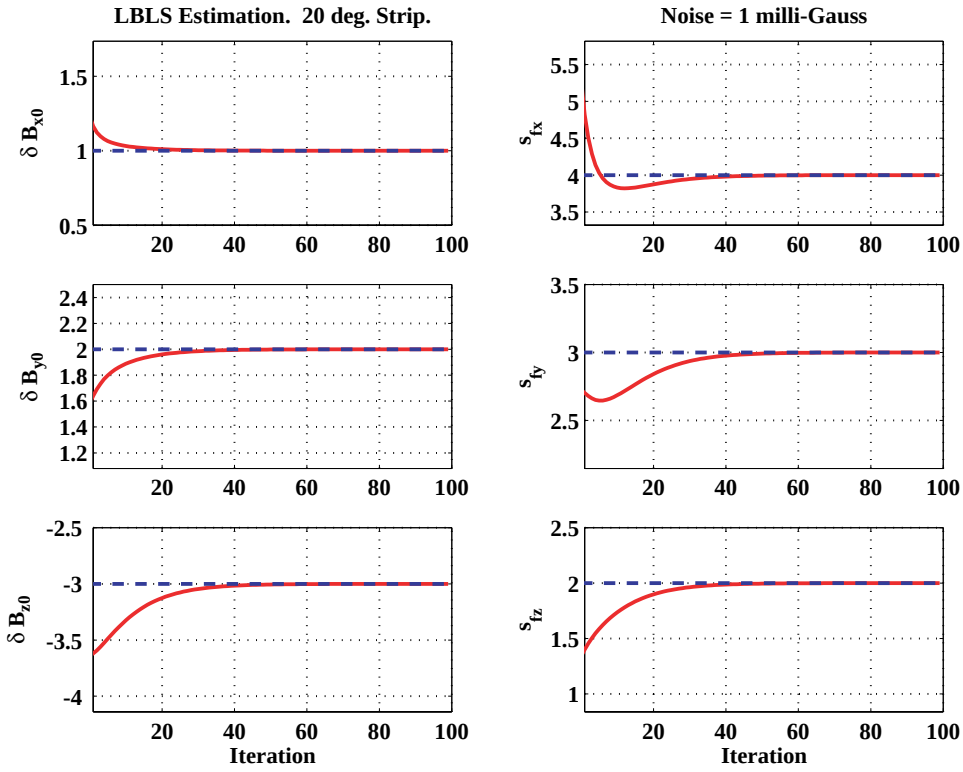

Figure 3.21: LBLS Estimation for a 20° Strip and 1 milli-Gauss Measurement Noise.

the magnetometer measurements is large. Furthermore, it requires a smaller portion of the measurement locus than the LBLS algorithm.

Experimental Verification

As a final verification, a triad of low performance magnetometers was calibrated using the Non-Linear, 2-Step Estimator algorithm. The data was collected from an experimental set up where a set of low performance magnetometers were strapped on to a long wooden boom as shown in Figure 3.26. The wooden boom was used in order to isolate the magnetometers from magnetic field generating electronics in the data collecting computer and associated hardware. The determination as to whether the magnetometers were calibrated correctly was to be done by comparing the heading

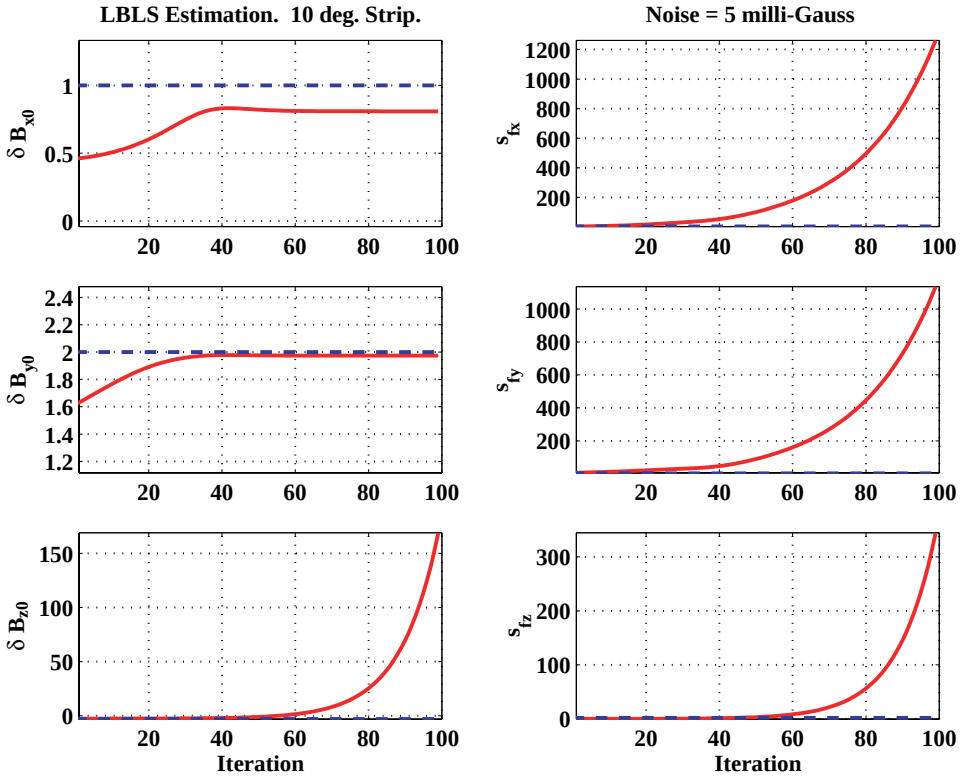

Figure 3.22: LBLS Estimation for a 10° Strip and 5 milli-Gauss Measurement Noise.

solution generated by the magnetometers with the heading solution from an expensive navigation grade INS (Honeywell YG1851 IRU). The INS and the experimental set up are shown in Figure 3.26. Figure 3.27 shows a histogram of the residual in the magnetic field domain after the calibration is complete. These residuals were computed by resolving the known magnetic field vector in the area where this calibration took place (i.e., the San Francisco Bay Area) and resolving it into the axes of the magnetometer triad using the precise INS attitude information. The largest residual, which is on the x-axis magnetometer, has a mean of -0.007 Gauss and a standard deviation of 0.004 Gauss.

Figure 3.28 shows a one-minute trace comparing the heading solution computed using the magnetometers with the heading solution generated by the INS. The heading residuals for this one-minute trace are less than 3° RMS. Figure 3.29 is a histogram

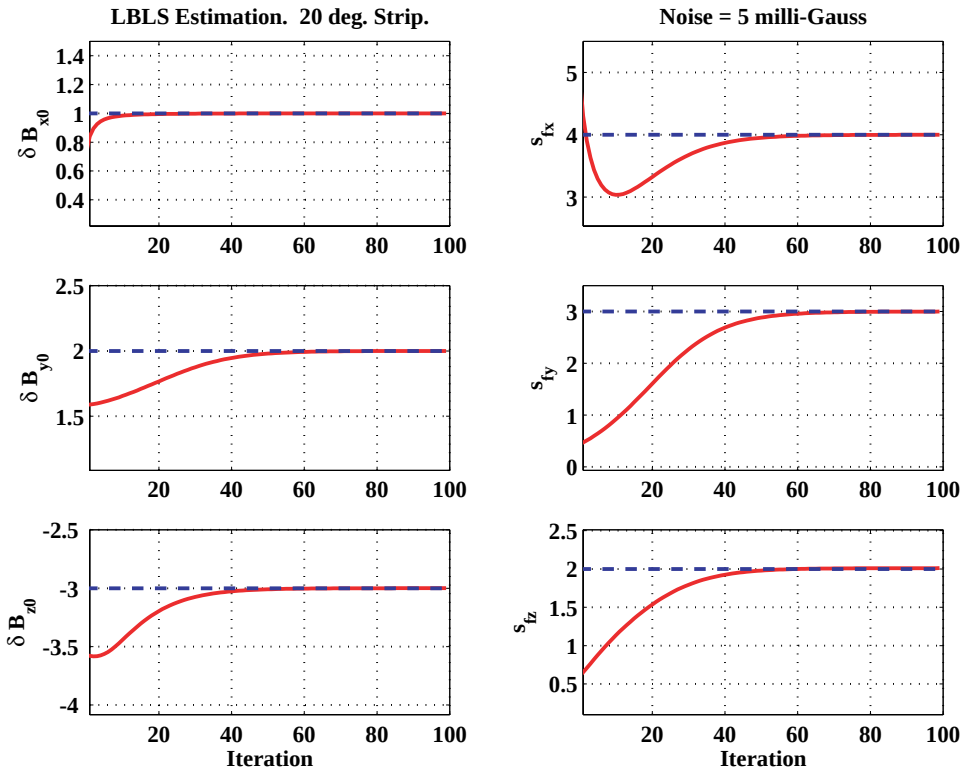

Figure 3.23: LBLS Estimation for a 20° Strip and 5 milli-Gauss Measurement Noise.

of the heading errors for the entire experiment. It is seen that the heading error has a standard deviation of 3.6° and a mean of 1.2°. The largest heading error observed was 18° and was the result of the wooden boom flexing relative the the INS (i.e., the truth reference) during the data collection maneuvers. Once the mean is removed, the remaining heading error is, to a large extent, in the form of wide-band noise which can be easily filtered using a rate gyro or a low-pass filter.

3.12 Heading Error Model

At this point most of the information needed to construct a mathematical model for heading error is available. This model will be used in Chapter 5 to analyze the performance of a dead reckoning navigation system. The general mathematical form

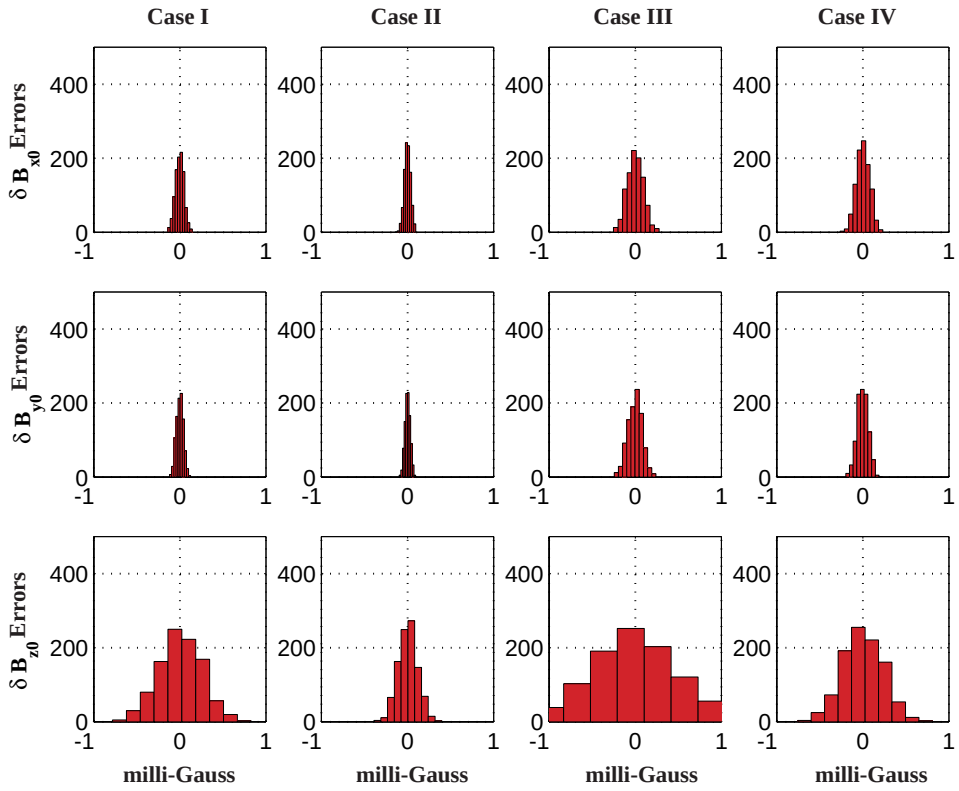

Figure 3.24: Hard Iron Bias Estimation Errors for the Non-Linear, Two-Step Estimator.

for this error model is consistent with all the other sensor error models developed up to this point and can be written as:

$$\delta\psi = \delta\psi_0 + \delta\psi(t) + \delta\psi_w \tag{3.81}$$

The term $\delta\psi_0$ represents a constant offset or bias. Such a bias was discussed in Section 3.11.1 (page 78) and is caused by a misalignment of the magnetometer triad. This is an installation error that can be minimized if care is taken during the installation process. Thus, for the error model here, it is assumed that care was taken during the installation of the magnetometers such that this error is zero. This is justified because, as will be shown next, the $\delta\psi(t)$ term in Equation 3.81 is the dominant error

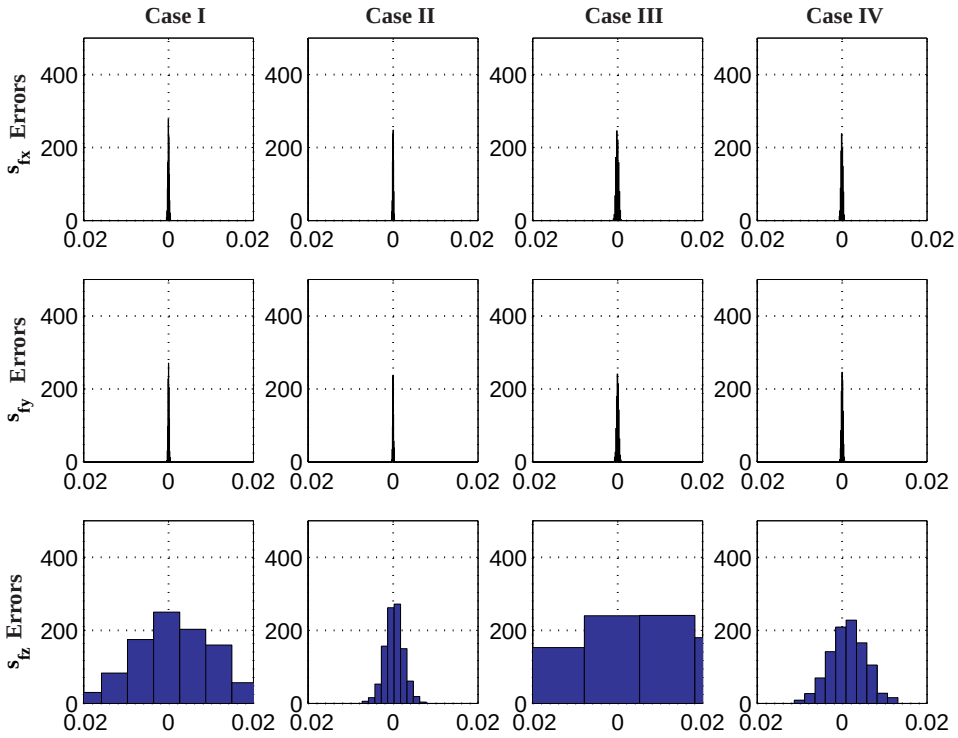

Figure 3.25: Scale Factor Estimation Errors for the Non-Linear, Two-Step Estimator. (Note: The Errors Are Unitless).

term and can be very large in comparison to $\delta\psi_0$.

For the analysis in Chapter 5, what is needed is a $\delta\psi(t)$ error model that can be easily cast into state-space form and represents the error behavior relatively accurately. In [14], a heading error model is given which is a first order Gauss-Markov process. Even though the model in [14] was given without justification, it is the author's judgment that this is a reasonable error model for the following reason: The $\delta\psi(t)$ term is a time varying error. It is caused by residual errors from the magnetometer calibration. Quantifying the contribution of the magnetometer calibration residuals to $\delta\psi(t)$ is relatively straight forward. This is done by using Figure 3.27 and Equation 3.48. Figure 3.27 shows that the mean of the post calibration residual errors on all three magnetometers is between 4 and 7 milli-Gauss. When this residual error

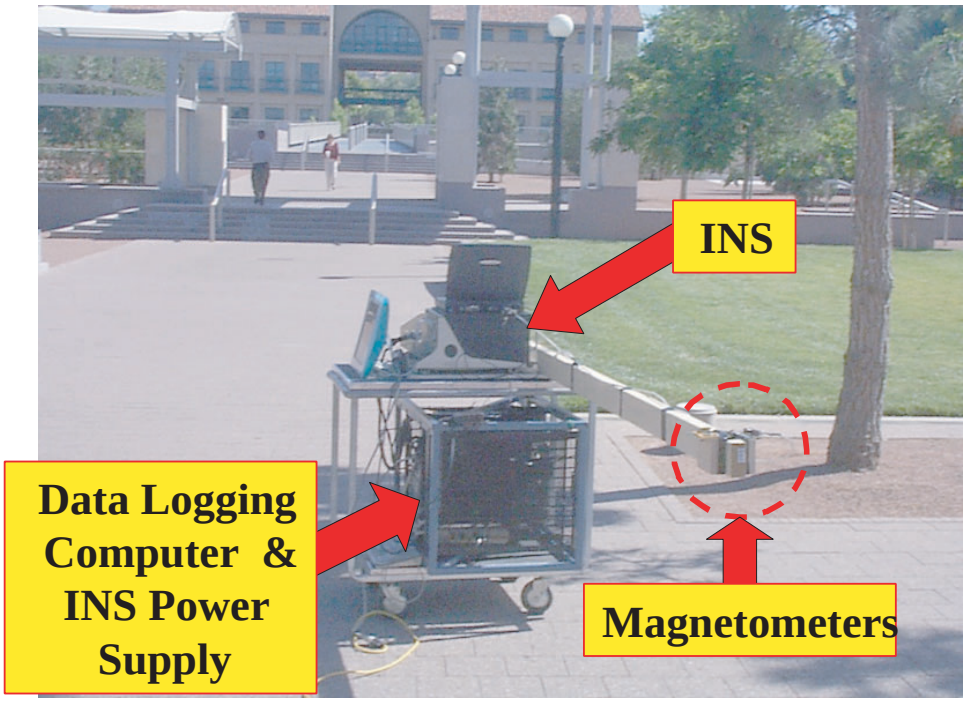

Figure 3.26: Experimental Setup for Ground Test.

is substituted into Equation 3.48, it results in the heading errors shown in Figure 3.30. These errors are heading dependent and have a maximum magnitude of 2.5°.

The dead reckoning navigator will rely on heading generated primarily from a magnetometer triad after GPS services are lost. Prior to that, as will be discussed in Chapter 4, GPS aided by inertial sensors will be the primary sensor for heading. When GPS is available, the errors in heading for such an Attitude Heading Reference System will be less than 2.5°. Once GPS services are lost, the heading errors will ramp up to the maximum 2.5°. The speed at which the errors ramp up (or time constant of the error model) is a function of the attitude estimator poles. The time constant used in [14] was five minutes (300 seconds). Five minutes appears to be a long time constant and, thus, other time constants were investigated. The time constants evaluated were between 120 seconds and 300 seconds. It was found that the dead reckoning navigator's performance was relatively insensitive to the magnitude of this time constant. So the conservative lower bound of 120 seconds was used for the time

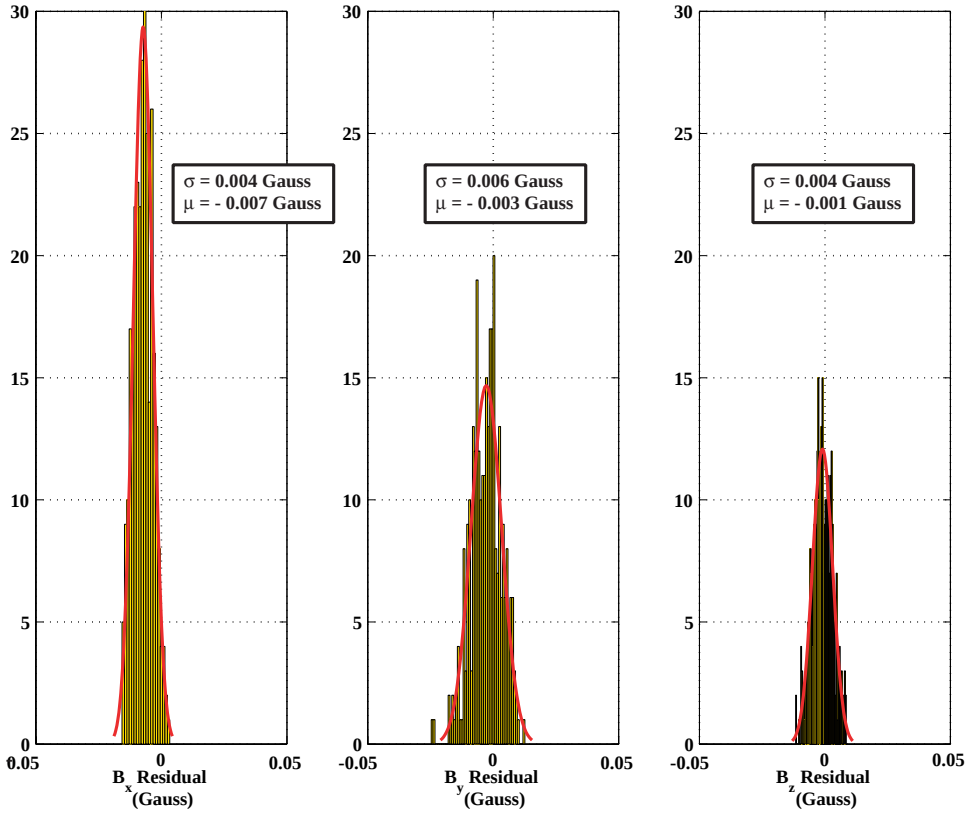

Figure 3.27: Magnetometer Calibration Residuals.

constant.

The final component of the heading error is the wide-band noise ψ_w. The magnitude of this error is shown in Figure 3.29. This wide-band noise has a magnitude of 3.5°. When used as part of the dead reckoning navigator, the magnetometer derived heading will be filtered using rate gyros. The effect of the filter is to reduce the root mean square value of the wide-band noise. The data shown in Figure 3.29 was collected at 20 Hz. As will be discussed in Chapters 6 and 7, the magnetometer derived heading information used by the dead reckoning navigator is only computed at a rate of 1 Hz. Thus, the 3.5° RMS wide-band noise will be reduced by a factor of $\sqrt{20}$ to a value of 0.8° RMS.

In conclusion, the final heading error model used is a first order Gauss Markov

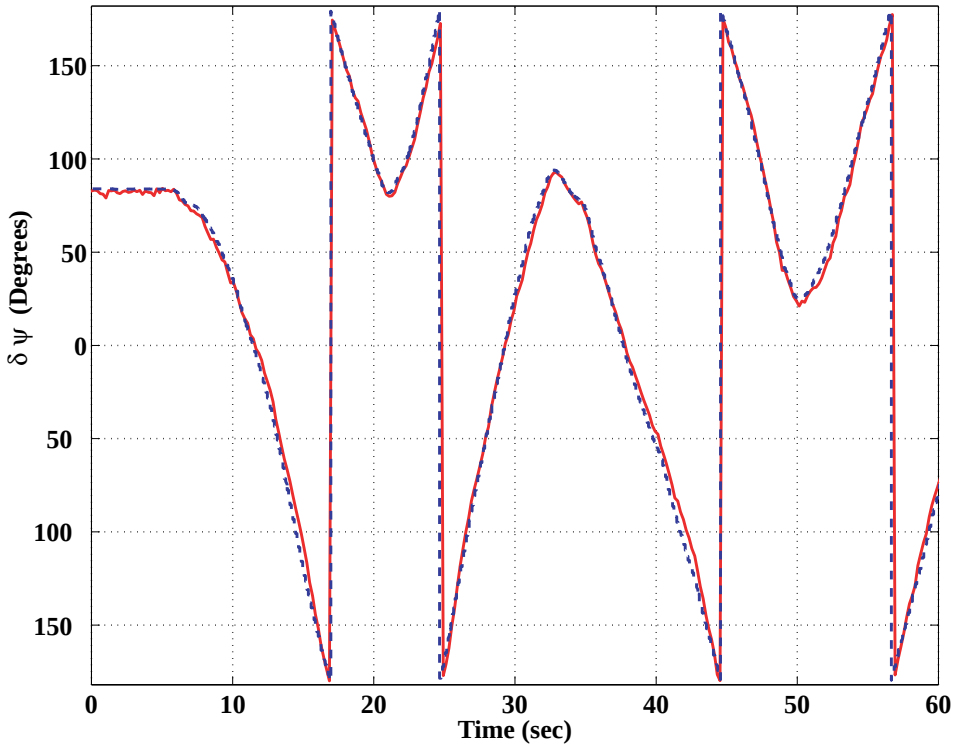

Figure 3.28: Comparison of INS Heading and Magnetometer Heading After Calibration.

process with additive white noise. Mathematically, this error model is written as:

$$\delta\psi = \delta\psi(t) + \delta\psi_w \tag{3.82}$$

$$\delta\dot{\psi}(t) = -\frac{1}{\tau_\psi}\delta\psi + w_\psi \tag{3.83}$$

$$\sigma_{\delta\psi(t)} = 2.5^\circ \tag{3.84}$$

$$\tau_\psi = 120 \text{ seconds} \tag{3.85}$$

$$\sigma_{\delta\psi_w} = 0.8^\circ. \tag{3.86}$$

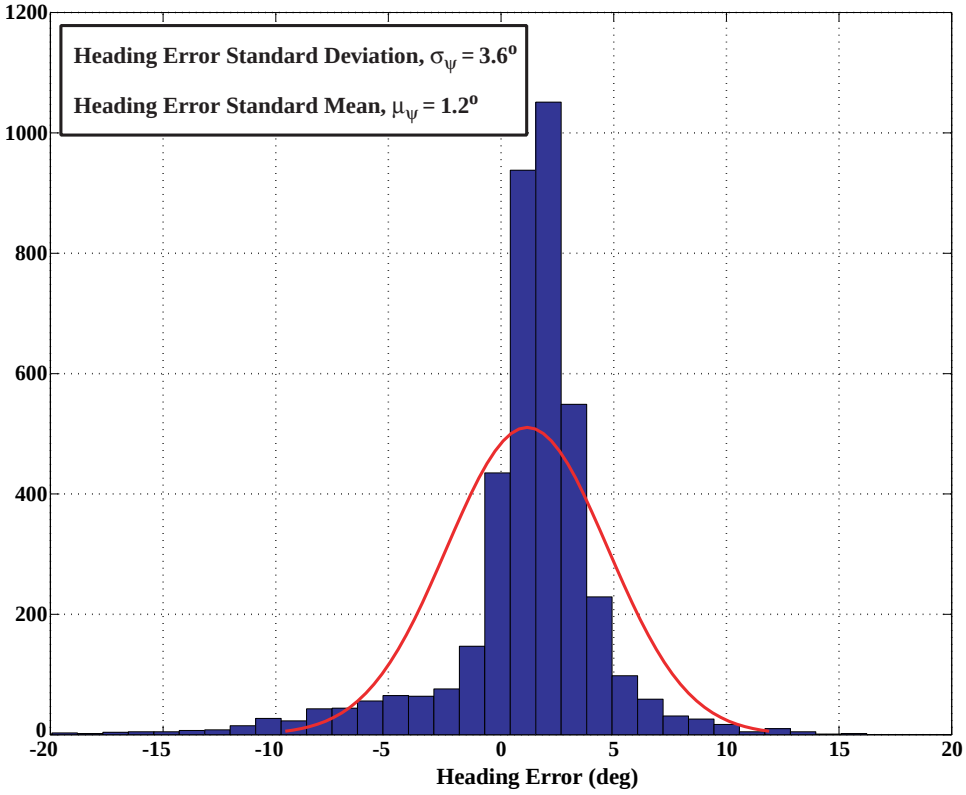

Figure 3.29: Histogram of Post Calibration Heading Errors.

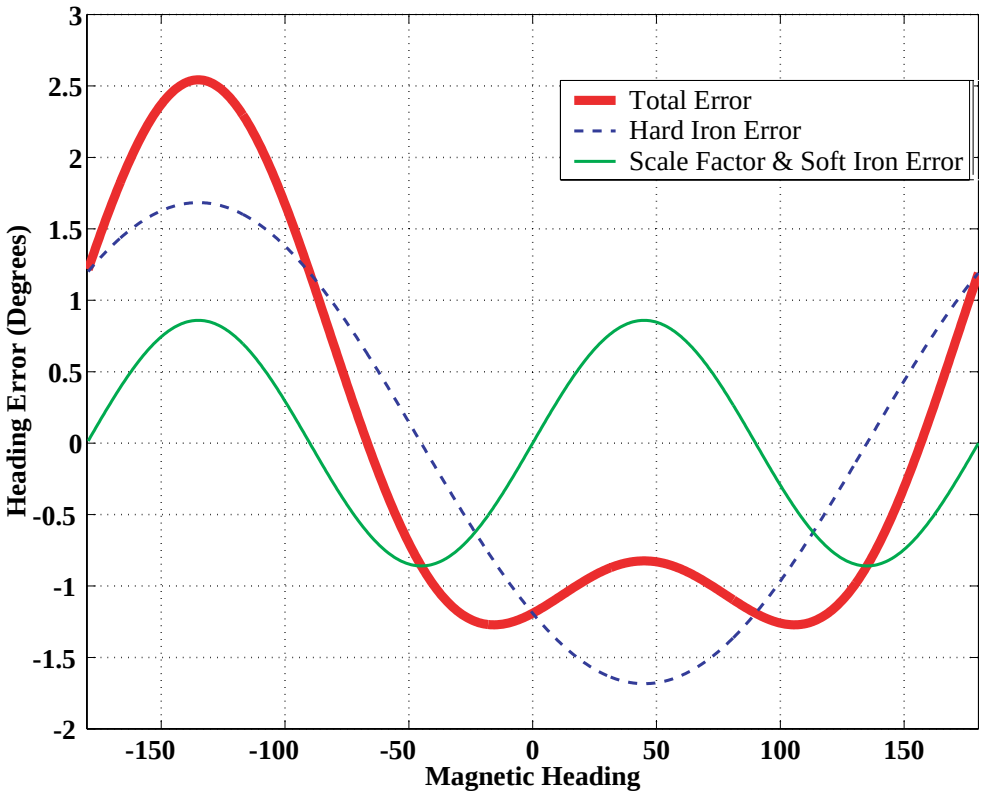

Figure 3.30: Heading Errors Due to Magnetic Field Calibration Residuals.

Chapter 4

Attitude Heading Reference Systems

4.1 Introduction

Traditionally, Attitude Heading Reference Systems (AHRS) have been used for pilot-in-the-loop control of aircraft attitude and heading. They have also been used to provide the attitude information required by automatic pilots. In Chapters 1 and 2, it was also noted that an AHRS is an integral part of the backup navigator discussed in this thesis. This chapter discusses the design details of an AHRS mechanized using low performance inertial sensors. The discussion begins with a definition of the attitude determination problem. This will be followed by a discussion of various methods for describing the attitude of an aircraft. A brief discussion of the classical methods for determining aircraft attitude and heading will follow. A similar discussion for newer and modern attitude determination systems is then presented. Finally, the mechanization details of various AHRSs based on the fusion of GPS, magnetometers and low-performance inertial sensors will be discussed.

4.2 The Attitude Determination Problem

The information presented by an AHRS is an aircraft's attitude. An aircraft's attitude is defined to be its orientation in space. For a clearer understanding of this, consider two coordinate frames. The first coordinate frame is called the reference

coordinate frame and is normally the navigation frame described in Chapter 3 coordinatized in NED axes. The second coordinate frame is rigidly attached to and moves with the aircraft's body. This coordinate frame is called the body frame. Even though both coordinate frames may be aligned initially, as the aircraft moves the orientation of the body frame with respect to the reference frame will change. Determining the relative orientation of two coordinate frames is the attitude determination problem that is solved by an AHRS. Before delving into the details of constructing an AHRS that uses low-performance inertial sensors, the following point should be emphasized: From the viewpoint of this thesis, the ultimate purpose of an AHRS is to generate heading information that will be used to mechanize an aided dead reckoning navigation system.

4.3 Attitude Parameterization

There are various ways of describing or parameterizing the relative orientation of two coordinate frames. In what follows, the two attitude parameterizations that were used in the AHRS implementations explored in this thesis are discussed. These two parameterizations are interchangeable. They both describe the relative orientation of the reference frame with respect to the body coordinate frame.

4.3.1 Euler Angle Parameterization

Euler angles are a set of three angles that describe the orientation of an aircraft with respect to some pre-defined reference frame. The three Euler angles are called yaw, pitch and roll. These angles are shown in Figure 4.1. To take an airplane from one attitude state to another, the aircraft is rotated through the three angles, yaw, pitch and roll–in that order. Euler angles have the advantage of being very intuitive. As a matter fact, any AHRS that is used for pilot-in-the-loop control of attitude will display the attitude information in terms of Euler angles.

The disadvantages of the Euler angle formulation are two fold. Firstly, the differential equations that describe the time evolution of the angles are non-linear in the Euler angles and contain transcendental functions. This requires extra processing

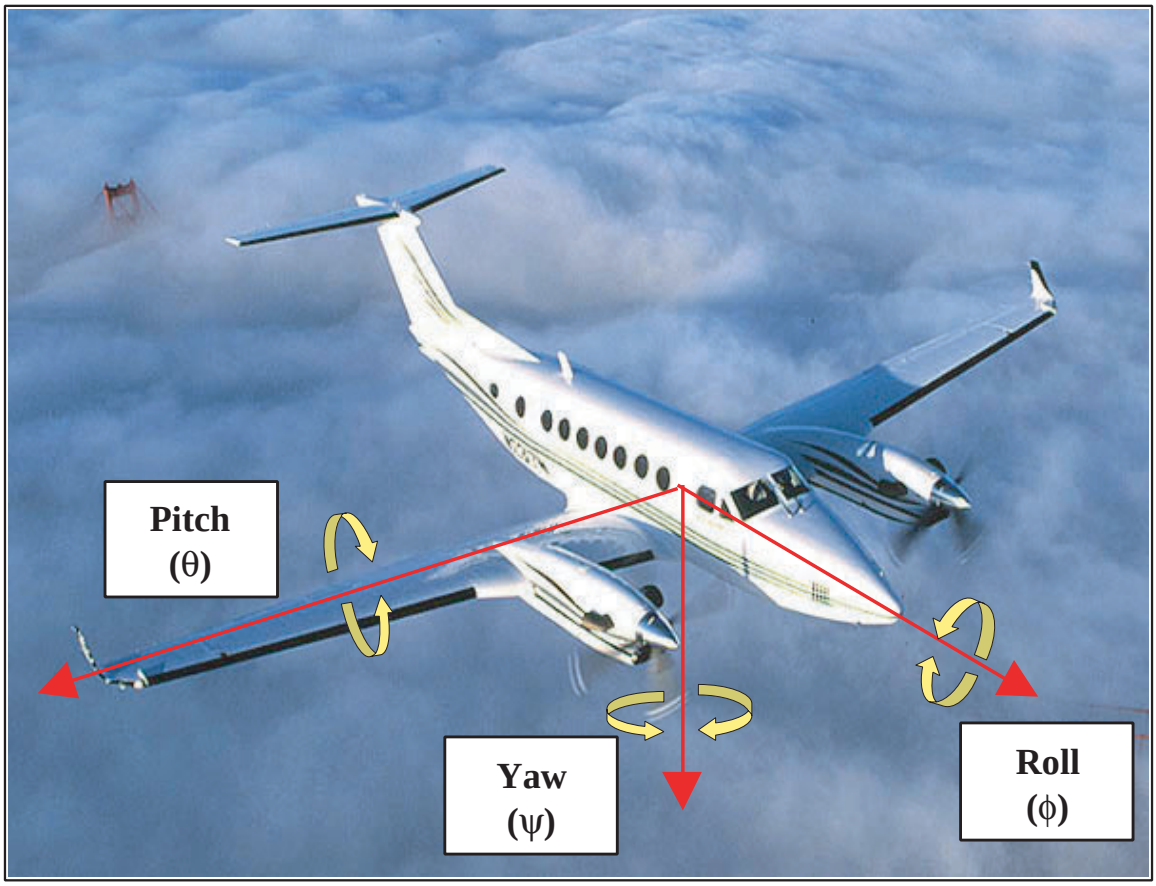

Figure 4.1: Definition of Euler Angles (Photograph Courtesy of Raytheon Aerospace).

power in computers used to determine attitude in real-time. Secondly, the Euler angle space has a singularity; there are certain points in the attitude space that cannot be uniquely represented by Euler angles. These points correspond to cases where the pitch angle is $\pm 90^o$. At this point, yaw and roll are interchangeable.

4.3.2 Quaternion Parameterization

Quaternions are a four element description of attitude. To get a physical insight into what quaternions are one has to understand Euler's theorem of rotation. This theorem states that the orientation of one coordinate frame with respect to another,

after a series of rotations, can be described by a single rotation of magnitude Φ about a single axis whose orientation in space is defined by the unit vector $\hat{e}$. If the orientation of this axis of rotation and the magnitude of the rotation about it are known, then the relative orientation of the coordinate frames of interest is completely specified. A quaternion describing the attitude of an aircraft is normally written as:

$$\mathbf{q} = \begin{bmatrix} q_0 \\ \vec{q} \end{bmatrix}. \tag{4.1}$$

It is composed of a scalar component, q_0, defined as

$$q_0 = \cos(\Phi), \tag{4.2}$$

and a vector component given by

$$\vec{q} = \Phi\,\hat{e} = \begin{bmatrix} q_1 \\ q_2 \\ q_3 \end{bmatrix}. \tag{4.3}$$

Loosely, the first element of a quaternion describes the amount of rotation about the axis defined in the Euler rotation theorem. The vector part of the quaternion describes the orientation of the angle of rotation. A more precise mathematical definition and detailed treatment of attitude quaternions can be found in specialized books such as [51] or most advanced dynamics texts.

4.4 Classical Attitude Determination Methods

The information presented by AHRS used in aircraft without modern glass cockpits is generated by mechanical gyros. The mechanical gyros used for indicating pitch and roll attitude consist of a spinning rotor that is mounted on a two axis gimbal. A separate rotor is used for heading. The aircraft vacuum or electrical system provides the power needed to spin the rotors in these gyros. A drawback of these mechanical systems is that they have too many moving parts and, thus, lack reliability. In aircraft with glass cockpits, the attitude information is generated by an AHRS that uses

relatively accurate solid state rate gyros. While systems based on these solid state rate gyros are reliable they can be costly and out of reach of some low-end users such as General Aviation aircraft.

4.5 Modern Attitude Determination Methods

Since an AHRS is an integral part of the dead reckoning navigator, the research in this thesis is, in part, aimed at providing reliable, accurate and affordable attitude information. This is accomplished by taking advantage of the improved sensor and display technology available today which entails the use of GPS, solid state inertial, air data and magnetic sensors linked through intelligent sensor fusion algorithms. The attitude information from these sensors can be displayed on computer generated "glass cockpit" type displays. Such systems are finding their way into modern aircraft and are expected to be standard equipment on all aircraft. A case in point is the prototype Lanceair Columbia-400 (a General Aviation, or Group E, aircraft) which has an AHRS driven by a sensor suite which includes low-performance solid state inertial, air data and magnetic sensors.

In this thesis, five basic ways of implementing modern attitude determination systems are explored. These systems are based on solid-state (or non-mechanical) sensors and have a digital output that can be easily integrated into a modern navigation system. These five basic methods are:

1. Multiple-antenna GPS attitude determination systems.
2. Gyro-based attitude determination systems.
3. Accelerometer and magnetometer-based attitude determination systems.
4. Vector matching attitude determination systems.
5. Systems based on the fusion of two or more of the above methods.

Each of these methods is discussed in detail in the sections that follow.

4.6 GPS Attitude Determination

What follows is a brief description of GPS attitude determination. It is given here for completeness. For a more detailed treatment of the subject the reader is referred to [23] and [39]. The basic idea behind GPS attitude determination is the mathematical fact that three non-collinear points in space define a plane. If the location of these three points with respect to some predefined reference frame is known, then the orientation of the plane containing the three points can be computed. In practical terms, if three non-collinear GPS antennas are mounted on a rigid plane (e.g., the fuselage of an airplane) and the relative location of the antennas with respect to each other on the rigid plane is known, then the attitude of the rigid plane containing these antennas can be determined. The relative location of the three antennas can be measured using Carrier Phase Differential GPS techniques. This is the basis of multiple-antenna GPS attitude determination.

Multiple-antenna GPS attitude determination systems can provide accurate and drift free attitude information. The accuracy of the attitude information generated by these systems is dependent on many factors which are discussed in detail in [43] and [39]. One of the factors affecting accuracy is the spacing between the GPS antennas. The farther apart the antennas are, the more accurate and less noisy the attitude solution becomes. Installing multiple GPS antennas far apart, however, has several drawbacks. Firstly, the speed at which the attitude determination algorithm can be initialized is inversely proportional to the spacing between the antennas; the larger the spacing the more time is required to initialize the attitude determination algorithm after the receiver has acquired lock on the signal from the GPS satellites. This is problematic because GPS receivers can sometimes lose momentary lock on the signals from the satellites and during the long initialization times attitude information will not be available. Secondly, there is not enough surface area on the fuselage of most aircraft to provide the antenna spacing required for accurate attitude determination. While antennas can be spaced far apart by installing them on each wing tip and the vertical tail, the spacing between the antennas will not be a constant because of structural flexing during flight. This adds complexity to the attitude determination algorithm. Robust and efficient GPS attitude determination

systems, therefore, require small spacing between the antennas [43, 44]. This means that the attitude solution generated by such a GPS attitude determination system will be noisy.

There are other drawbacks of a GPS attitude determination system. One of these drawbacks is that that the rate at which the attitude solution is generated is a function of how often a GPS measurement is available from a GPS receiver. Normally, the maximum data output rate from currently available GPS receivers is on the order of 10 Hz. Most AHRS applications require update rates higher than 10 Hz. Finally, another drawback of multiple-antenna GPS attitude determination is that it requires complex GPS receivers that can be expensive. These are receivers capable of processing the data from three or more GPS antennas simultaneously. As will be shown in later sections, all these drawbacks can be mitigated by fusing the output from a GPS attitude determination system with information derived from inertial sensors.

4.7 Rate Gyro-Based Attitude Determination

In rate gyro-based attitude determination systems, three orthogonal rate gyros are affixed to the body reference frame with their sensitive axes aligned with each of the body axes of the aircraft. The angular rate measurements from the gyros form the inputs to a set of kinematic differential equations that describes the time evolution of attitude. Thus, determination of the aircraft's attitude is a simple matter of integrating the output of the gyros.

If the Euler angle parameterization is being used, the system of differential equations that have to be integrated to determine attitude are:

$$\begin{bmatrix} \dot{\psi} \\ \dot{\theta} \\ \dot{\phi} \end{bmatrix} = \left(\frac{1}{\cos(\theta)} \right) \begin{bmatrix} 0 & \sin(\phi) & \cos(\phi) \\ 0 & \cos(\phi)\cos(\theta) & -\sin(\phi)\cos(\theta) \\ 1 & \sin(\phi)\sin(\theta) & \cos(\phi)\sin(\theta) \end{bmatrix} \begin{bmatrix} p \\ q \\ r \end{bmatrix}. \tag{4.4}$$

The variables ψ, θ and ϕ represent yaw, pitch and roll, respectively. The variables p, q and r represent the angular rate output from the three orthogonal rate gyros. More specifically, p is the output of the rate gyro with its sensing axis aligned with the roll

axis (see Figure 4.1 on page 105). Similarly, q is the pitch axis rate gyro output and r is the yaw axis gyro output. If quaternions are used to parameterize the attitude, the governing differential equation becomes:

$$\dot{\mathbf{q}} = \frac{1}{2}\Omega \begin{bmatrix} q_0 \\ \vec{q} \end{bmatrix}. \tag{4.5}$$

The matrix Ω is given by:

$$\Omega = \begin{bmatrix} 0 & -p & -q & -r \\ p & 0 & r & -q \\ q & -r & 0 & p \\ r & q & -p & 0 \end{bmatrix} \tag{4.6}$$

In an AHRS that uses high quality inertial sensors, once the rate gyro null-shifts have been estimated, any change will be slowly time-varying and very small. Thus, the attitude solution can be derived by simply integrating any one of the above differential equations after accounting for the gyro null-shifts. If low-performance sensors are being used, simple integration will not work for two reasons. The first reason is that the output from such rate gyros is normally corrupted by a null-shift as well as a large time varying bias. As will be shown later, it is possible to design an observer to estimate and compensate for the null-shift. Since time varying output biases for low-performance rate gyros have short time constants, unless they are estimated continuously they will cause errors in the attitude solution obtained by simple integration. Secondly, low-performance rate gyros tend to have outputs that are corrupted by wide-band noise. Thus, even in the absence of any appreciable bias instability (as would be the case when using a low-cost FOG), angle random walk resulting from the integration of the gyro output noise will result in a drift in the attitude estimate.

The random walk error growth is a function of the spectral density of the wide band output noise ($\sigma_{\dot{\theta}}$), the sampling frequency (f_s), and the duration of integration (T). Mathematically, the standard deviation of the angular error due to random walk

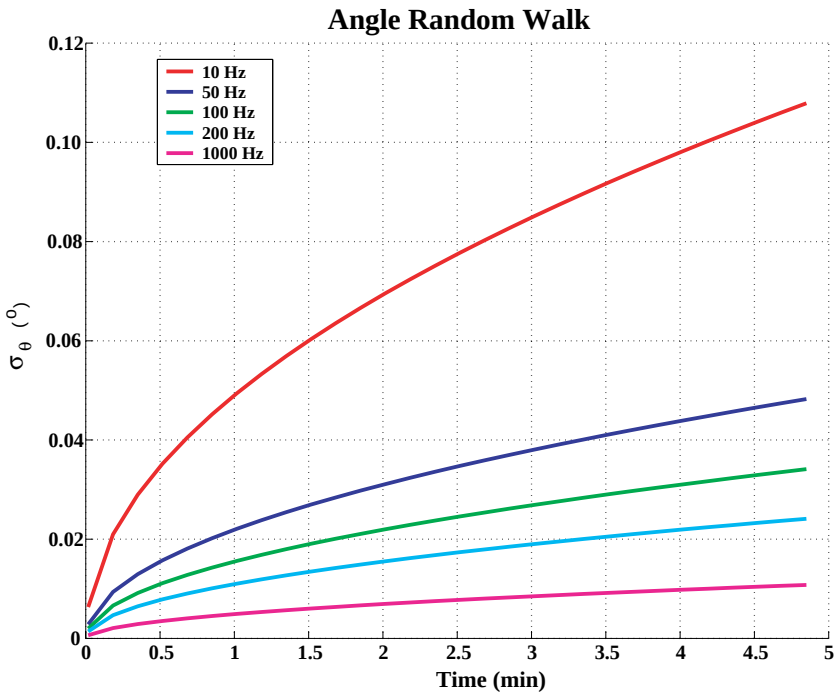

Figure 4.2: Angular Error Growth Due to Random Walk.

is given by:

$$\sigma_\theta = \sigma_{\dot{\theta}} \sqrt{\frac{T}{f_s}} \tag{4.7}$$

A more detailed discussion and derivation of this relation is contained in Appendix B. Figure 4.2 shows the angle random walk error growth. The important fact that is apparent from Figure 4.2 is that higher sampling frequency will result in smaller errors. Since processing equations that contain transcendental functions in real-time requires considerable computer processing power, it is advantageous to use quaternions instead of Euler angles in systems with higher sampling rates.

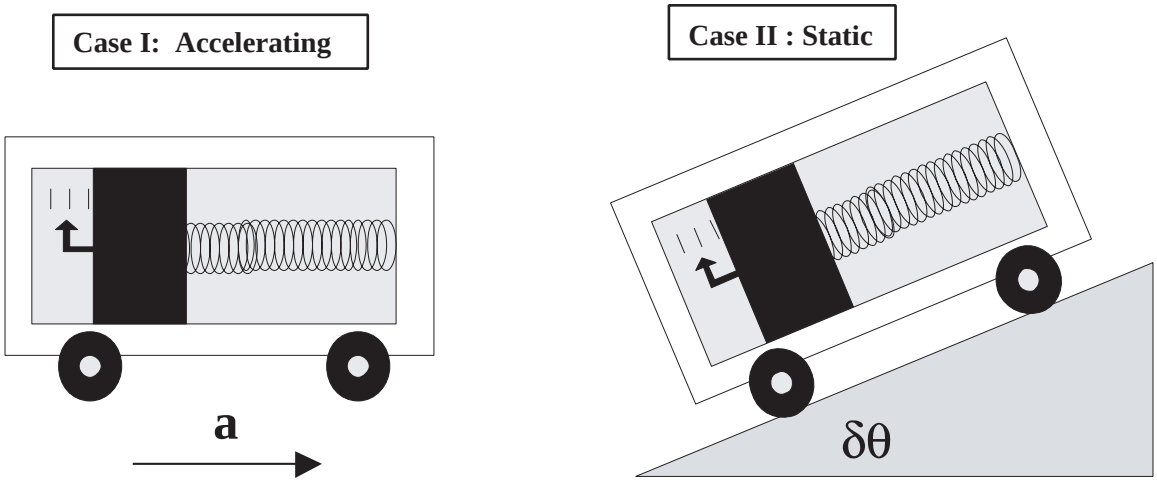

Figure 4.3: Ambiguity of Attitude and Acceleration.

4.8 Accelerometer and Magnetometer Attitude Determination

In a magnetometer and accelerometer attitude determination system, pitch and roll information are determined by using the accelerometers. Heading or yaw information is determined by using the magnetometer readings leveled by the accelerometer derived pitch and roll information. More specifically, given the pitch accelerometer reading, f_x, and the roll accelerometer reading, f_y, the following expressions are used to determine pitch and roll attitudes:

$$\theta = -\sin^{-1}(f_x) \tag{4.8}$$

$$\phi = \sin^{-1}(f_y) \tag{4.9}$$

Heading or yaw is determined using Equation 2.3.

During maneuvers where the aircraft is accelerating, there will be an error in the accelerometer derived attitude for pitch and roll. This is because, as shown in Figure 4.3, a bias-free accelerometer can not distinguish the difference between tilt and

acceleration. This is due to the fact that the sensing element of an accelerometer is a pendulous mass. If the acceleration is of a short duration, then an attitude solution can be generated using low-performance rate-gyros until the acceleration stops.

4.9 Vector Matching Attitude Determination Systems

Since attitude determination by integrating the output of low-cost rate gyros in an open loop fashion results in attitude errors that are unbounded in time, a vector matching attitude determination method is presented.* Unlike rate gyro open loop integration, this method results in attitude errors that are bounded with respect to time. The idea behind this method is that given any two non-collinear vectors, a unique plane containing the two vectors can be defined. If the components of these two vectors can be measured in two non-aligned coordinate frames, then the rotation needed to align the two coordinate frames can be determined.

Vector matching methods are a solution to the classic Wahba's problem. First published in 1966[70], Wahba proposed an attitude solution by matching two non-zero, non-collinear vectors that are known in one coordinate frame, and measured in another. Several solutions to this method of attitude determination have been proposed and implemented [9, 10, 11], usually on satellites with star-tracker sensors. All vector matching attitude determination algorithms solve for the rotation that aligns two or more vectors into the base coordinate frame. The use of only one vector, or collinear vectors, results in an ambiguity of rotation about that vector.

The equations for attitude determination using only two vectors will now be derived. Let the two coordinate frames in which the measurements of vector components are made be designated the "body frame" (denoted by superscript b and fixed to the vehicle's body) and the "navigation frame" (denoted by superscript n and attached to the locally level plane). Furthermore, let the two vectors defining the plane which will be used for the attitude determination be designated $\vec{u}$ and $\vec{v}$. First, the relations involving the vector $\vec{u}$ will be derived. The relations involving $\vec{v}$ will be a repeat of

*Developed in collaboration with Elkaim as documented in [36] and [30].

those derived for $\vec{u}$. The transformation between the vector $\vec{u}$ as expressed in the body frame and the navigation frame is:

$$\vec{u}^b = \overset{n\rightarrow b}{C}(\mathbf{q})\vec{u}^n. \tag{4.10}$$

The Direction Cosine Matrix (DCM), $\overset{n\rightarrow b}{C}(\mathbf{q})$, for the transformation from navigation to body frame is a function of the attitude quaternion, $\mathbf{q}$. In terms of the attitude quaternion, the DCM is expressed as:

$$\overset{n\rightarrow b}{C}(\mathbf{q}) = \begin{bmatrix} 1-2({q_2}^2+{q_3}^2) & 2(q_1q_2+q_3q_0) & 2(q_1q_3-q_2q_0) \\ 2(q_1q_2-q_3q_0) & 1-2({q_1}^2+{q_3}^2) & 2(q_2q_3+q_0q_1) \\ 2(q_1q_3+q_2q_0) & 2(q_2q_3-q_1q_0) & 1-2({q_1}^2+{q_2}^2) \end{bmatrix}. \tag{4.11}$$

The quaternion, $\mathbf{q}$, is defined in Equation 4.1 and is

$$\mathbf{q} = \begin{bmatrix} q_0 \\ \vec{q} \end{bmatrix}. \tag{4.12}$$

It is composed of a scalar component, q_0, and a vector component given by:

$$\vec{q} = [q_1\ q_2\ q_3]^T. \tag{4.13}$$

Equation 4.10 can be written in terms of quaternions as follows:

$$\vec{u}^b = \mathbf{q}^* \otimes \vec{u}^n \otimes \mathbf{q}, \tag{4.14}$$

where $\otimes$ represents quaternion multiplication which, for any two arbitrary quaternions $\mathbf{r}$ and $\mathbf{s}$, is defined as follows:

$$\mathbf{r} \otimes \mathbf{s} = \begin{bmatrix} s_0r_0 - \vec{r}^T\vec{s} \\ \vec{r}\times\vec{s} + r_3\vec{s} + s_3\vec{r} \end{bmatrix}. \tag{4.15}$$

$\mathbf{q}^*$ is the complementary rotation of the quaternion, $\mathbf{q}$, and is defined as:

$$\mathbf{q}^* = [q_0\ -\vec{q}]^T. \tag{4.16}$$

Let $\hat{\mathbf{q}}$ be an estimate of the true attitude quaternion, $\mathbf{q}$. The small rotation from the estimated attitude, $\hat{\mathbf{q}}$, to the true attitude is defined as $\mathbf{q}_e$. This is the error quaternion which is small but non-zero. It is non-zero because errors in the various sensors result in attitude errors. The relationship is expressed in terms of quaternion multiplication as follows:

$$\mathbf{q} = \hat{\mathbf{q}} \otimes \mathbf{q}_e, \tag{4.17}$$

The error quaternion, $\mathbf{q}_e$, is assumed to represent a small rotation, and thus $\mathbf{q}_e$ can be approximated as [65]:

$$\mathbf{q}_e = \begin{bmatrix} 1 \\ \vec{q}_e \end{bmatrix}. \tag{4.18}$$

The error quaternion, $\mathbf{q}_e$, is nothing more than a perturbation to the direction cosine matrix $\overset{n\to b}{C}(\mathbf{q})$. That is,

$$\overset{n\to b}{\delta C}(\mathbf{q}) \triangleq \overset{n\to b}{C}(\mathbf{q}_e). \tag{4.19}$$

Noting that the vector components of $\mathbf{q}_e$ are small, the perturbation to the DCM in Equation 4.11 can be written as:

$$\overset{n\to b}{C}(\mathbf{q}_e) = \begin{bmatrix} 1 & 2q_3 & -2q_2 \\ -2q_3 & 1 & 2q_1 \\ 2q_2 & -2q_1 & 1 \end{bmatrix}. \tag{4.20}$$

In a more compact form, Equation 4.20 can be written as

$$\overset{n\to b}{C}(\mathbf{q}_e) = I_{3\times 3} - 2[\vec{q}_e]^{\times} \tag{4.21}$$

where $[\vec{q}_e]^{\times}$ is a skew symmetric matrix whose entries are the components of $\vec{q}_e$. Equation 4.17 relating $\hat{\mathbf{q}}$ and $\mathbf{q}$ can be written in terms of DCMs as

$$\overset{n\to b}{C} = \overset{n\to b}{\delta C}\ \hat{\overset{n\to b}{C}}. \tag{4.22}$$

$\hat{\overset{n\to b}{C}}$ is the estimate of the direction cosine matrix or the equivalent of $\hat{\mathbf{q}}$. Transposing both sides of the above equation to recast the equation in terms of body to navigation

frame direction cosine matrices results in:

$$\overset{b\to n}{C} = \overset{\hat{}}{\overset{b\to n}{C}} \left[I_{3\times 3} + 2[\vec{q}_e]^{\times} \right]. \tag{4.23}$$

If this is substituted into Equation 4.10, the following relation is obtained:

$$\begin{aligned} \vec{u}^n &= \overset{\hat{}}{\overset{b\to n}{C}} \left[I_{3\times 3} + 2[\vec{q}_e]^{\times} \right] \vec{u}^b & (4.24)\\ &= \hat{\vec{u}}^n + 2[\vec{q}_e]^{\times}\vec{u}^b & (4.25)\\ &= \hat{\vec{u}}^n - 2[\vec{u}^b]^{\times}\vec{q}_e & (4.26) \end{aligned}$$

Let the following definition be made:

$$\delta\vec{u}^n \triangleq \vec{u}^n - \hat{\vec{u}}^n. \tag{4.27}$$

If a similar argument is carried out for the second vector, $\vec{v}$, then the following linear measurement equation (standard form) is obtained for the vector portion of quaternion error:

$$\begin{bmatrix} \delta\vec{u}^n \\ \delta\vec{v}^n \end{bmatrix} = \begin{bmatrix} -2[\vec{u}^n]^{\times} \\ -2[\vec{v}^n]^{\times} \end{bmatrix} \vec{q}_e. \tag{4.28}$$

The highly non-linear attitude determination problem has been recast into a standard form of a linear measurement equation:

$$\vec{z} = H\vec{q}_e. \tag{4.29}$$

The measurement vector $\vec{z}$ is defined as:

$$\vec{z} = \begin{bmatrix} \delta\vec{u}^n \\ \delta\vec{v}^n \end{bmatrix}. \tag{4.30}$$

The observation matrix, H, is defined as:

$$H = \begin{bmatrix} -2[\vec{u}^n]^{\times} \\ -2[\vec{v}^n]^{\times} \end{bmatrix}. \tag{4.31}$$

Note that the observation matrix, H, is unique to each measurement, but this can still be used in linear time-varying solutions.

The physical implementation of this low cost system relies on a three-axis magnetometer to resolve Earth's magnetic field into body coordinates, and three solid state accelerometers to resolve the specific force field into body coordinates. In the case where the vehicle is not accelerating, then specific force measured by the accelerometers is solely due to gravity. The magnitude of Earth's magnetic field and gravitational field are both well known, and well modeled. Thus two non-collinear vectors (of non-zero length) are available to determine attitude in the static case. If the vehicle is accelerating, the accelerometer readings will have to be corrected to take into account the vehicle's acceleration.

An iterated least-squares solution of the measurement equation is formulated as follows: Define $\vec{m}^b$ as the magnetic field vector, as measured in the body frame and $\vec{m}^n$ as the magnetic field vector in the local level frame (navigation frame). Likewise, define $\vec{a}^b$ as the acceleration measured in the body fixed frame, and $\vec{a}^n$ as the acceleration in the local level frame (including gravity).

1. $\hat{\mathbf{q}} = \begin{bmatrix} 1 & 0 & 0 & 0 \end{bmatrix}^T$, and $\mathbf{q}_e = \begin{bmatrix} 1 & 0 & 0 & 0 \end{bmatrix}^T$
2. $\hat{\vec{m}}^n = \hat{\mathbf{q}} \otimes \vec{m}^b \otimes \hat{\mathbf{q}}^*$ and likewise for $\hat{\vec{a}}^n$
3. $\delta\hat{\vec{m}}^n = \vec{m}^n - \hat{\vec{m}}^n$ and likewise for $\delta\hat{\vec{a}}^n$
4. Form H (Equation 4.31), take the pseudo-inverse: $[H^T H]^{-1} H^T$
5. $q_e(+) = \alpha[H^T H]^{-1} H^T \begin{bmatrix} \delta\hat{\vec{m}}^n \\ \delta\hat{\vec{a}}^n \end{bmatrix}$ where α is a tuning parameter or stepwise gain factor discussed below.
6. $\hat{\mathbf{q}}(+) = \hat{\mathbf{q}}(-) \otimes \mathbf{q}_e$.
7. Return to step (2), repeat until converged.

To validate the algorithm, a Monte-Carlo simulation was performed where a random starting attitude was given to the algorithm. For each Monte-Carlo run, the starting Euler angle triad was picked randomly from a uniformly distributed population that spanned normal aircraft attitudes. More specifically, for each run, the stating yaw angle, ψ, came from a uniform population between $\pm 180°$, the pitch angle, θ, from a uniform population between $\pm 20°$, and the roll angle, ϕ, from a uniform

population between ±60°. Once the starting Euler angle triad was picked, the body-fixed sensor measurements that corresponded to this attitude were generated. These body-fixed measurements were corrupted with appropriate levels of sensor wide-band noise. For the magnetometer measurements, the measurement noise was 1 milli-Gauss and for the accelerometer measurements it was 1 milli-g.

The algorithm was allowed 100 iterations to converge with the tuning parameter, α, set to 1/10. Figure 4.4 shows a time history for the attitude quaternion components during a single run in these series of Monte-Carlo simulations. As can be seen, the convergence to the correct attitude is rapid and assured. Furthermore, it can be seen that, although the formulation of this solution methodology assumed a small q_e, the algorithm performs very well even when the initial estimate of the attitude quaternion, $\hat{\mathbf{q}}$, is not close to the final attitude. The range of the tuning parameter (α) was found to be robust, ensuring convergence as long as α was within $[1/N$ to 2] where N is the number of iterations and is the maximum value of the abscissa shown in Figure 4.4. Figure 4.5 shows a histogram of attitude errors for 10,000 Monte-Carlo runs. The largest attitude errors are in yaw. Of the 10,000 runs only 3 had yaw errors in excess of 10°. The largest pitch and roll errors were 1.8° and 2.3°, respectively. The standard deviation for the errors are as shown in Figure 4.5.

4.10 Sensor Fusion-Based Attitude Determination Systems

Table 4.1 summarizes the advantages and disadvantages of the various attitude determination systems discussed thus far. A close examination of Table 4.1 reveals that the various attitude determination methods have complementary characteristics. For example, as was noted in Chapter 3, the output of low-performance rate gyros is always corrupted by errors. This results in unbounded attitude errors when the gyros are used in an open loop fashion. If the error growth is to be bounded, some form of external aiding is required. Any of the other systems listed in Table 4.1 can be used as an aiding system for the rate gyros. That is, the attitude solution from the rate gyros would be fused with the aiding system's solution. This is the basic concept behind the sensor fusion-based attitude determination systems.

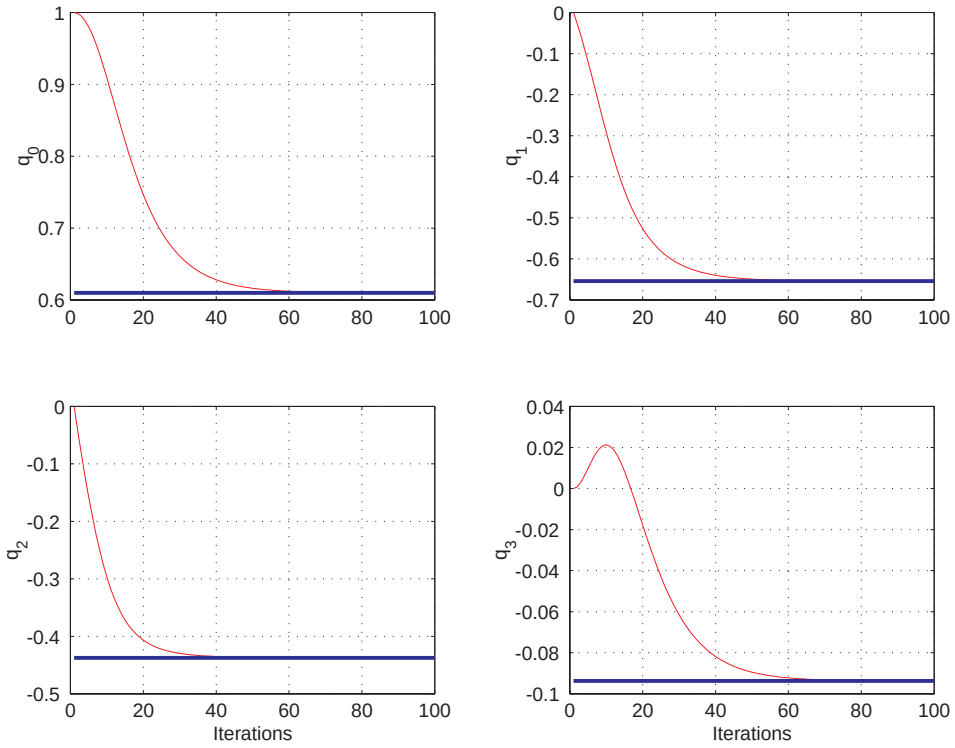

Figure 4.4: Quaternion Convergence History.

The concept of a sensor fusion based attitude determination system is shown schematically in Figure 4.6. The system depicted combines low-performance rate gyros with an aiding system. Even though such rate gyros have good high-bandwidth response over short periods of time, their large bias drifts lead to unbounded attitude errors. An attitude sensor which has good long term stability can be used as an aiding system for the gyros. The aiding system will be used to "reset" the attitude solution derived from the low cost inertial sensors. In the context of this thesis, an AHRS based on the fusion of sensors is one of the sub-systems of the backup navigator and is relied on for heading information when GPS services are not available. Even though this will be discussed in detail in Chapter 6, for clarity, the reader is referred to Figure 6.5 on page 200 at this time. The AHRS discussed in this chapter and shown schematically in Figure 4.6 constitute the backup navigator's sub-system labeled "AHRS" at the

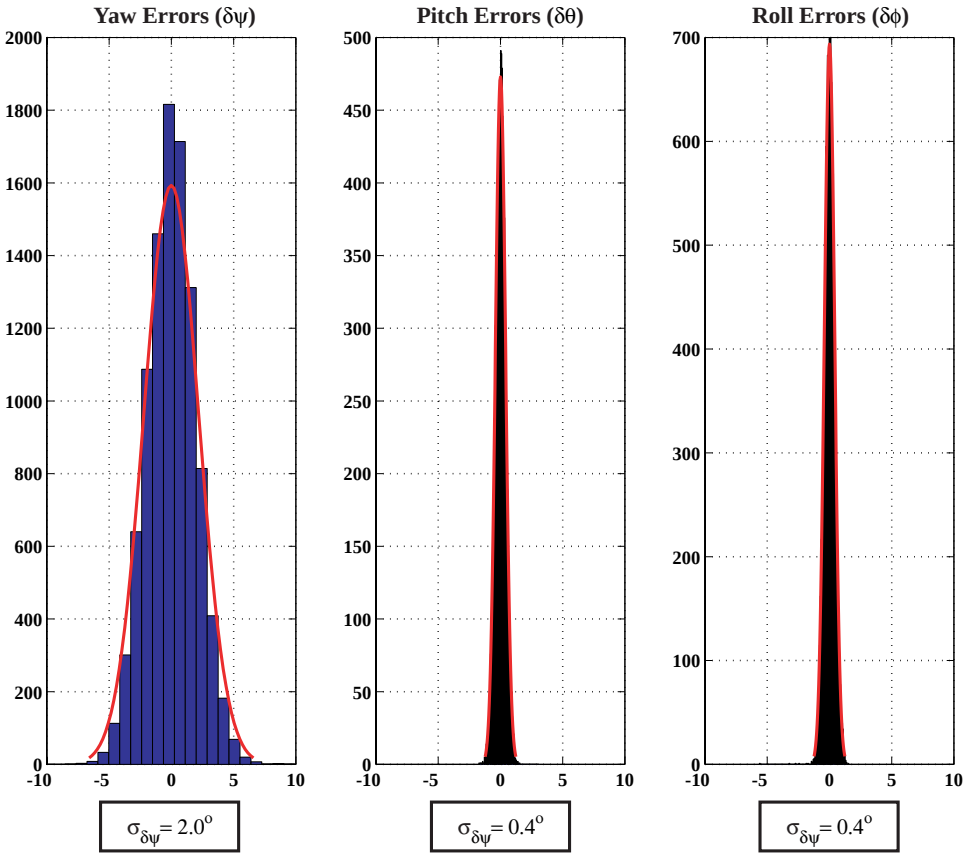

Figure 4.5: Histogram of Attitude Errors for 10,000 Monte-Carlo Runs.

bottom left of Figure 6.5

In this thesis, two aiding systems were investigated. The first aiding system was a GPS based attitude determination system. The second aiding system was composed of a magnetometer and two accelerometers. Both of these systems provide attitude information with errors that are bounded in time. Therefore, their outputs can be blended with the gyro derived attitude to give a combined and filtered drift-free attitude solution. The tool used for blending the two attitude solutions is an estimator (Kalman filter). In the next sections, the algorithms for blending the two solutions using the Euler angle and quaternion parameterization techniques will be discussed.

Regardless of the type of attitude parameterization used, the basic workings of

Attitude Determination System	Advantages	Disadvantages
Multiple GPS Antenna System	Drift-Free Attitude Solution	Potentially Expensive (i.e., Requires Multiple Antennas). Robustness Issues Associated with Integers.
Open Loop Gyro Integration	Inexpensive Sensor Suite	Large Errors Due to Bias Drift
Accelerometer and Magnetometer System	Inexpensive Sensor Suite	Fails in an Accelerating Vehicle
Vector Matching Methods	Inexpensive Sensor Suite	Fails When GPS is Unavailable

Table 4.1: Comparison of Various Attitude Determination Methods.

the attitude estimators discussed are all similar to the one depicted in Figure 4.7. This figure is a time-line of the various events that occur during the operation of an attitude estimator. After the initial conditions for the attitude are established, the rate gyros are integrated to propagate the attitude estimate forward in time. The process of propagating attitude forward in time is called the "time update" and is carried out at a relatively high rate. The time update provides the high bandwidth attitude information that is needed for functions such as pilot-in-the-loop control. Due to gyro drift and noise, however, the errors in the attitude solution derived from the rate gyros will grow with time. This is shown in the top graph of Figure 4.7 and implies that the attitude solution obtained by integrating the rate gyros cannot be propagated too far forward in time without periodic resets. A periodic reset is called the "measurement update." In addition to resetting the attitude solution, the gyro biases are also estimated at the measurement update. After a measurement update, a new time update phase begins and the cycle repeats.

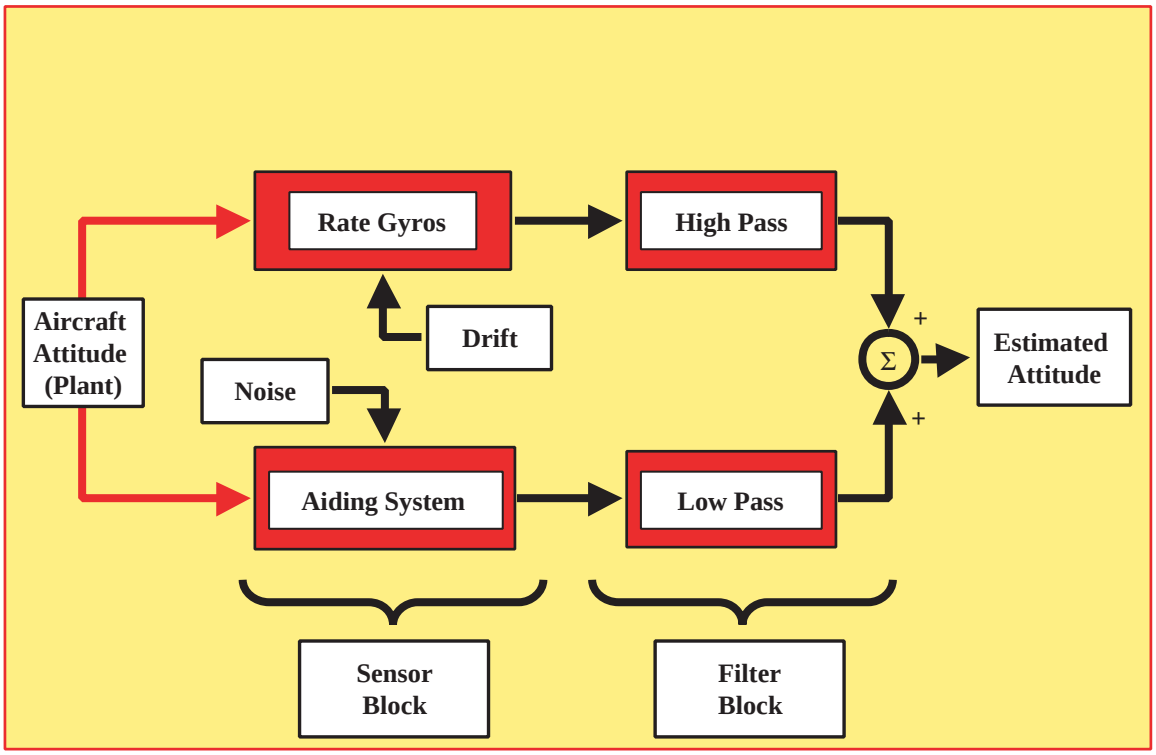

Figure 4.6: Basic Concept of Complementary Filtering.

4.11 GPS/Gyro Attitude System

Combining GPS with inertial sensors is not a new idea. Much work has been done in this area in the recent years. Blending GPS with inertial sensors has several advantages. As noted previously, there is a limit to the attitude accuracy that can be obtained by a GPS alone attitude system. The accuracy of the system can be enhanced by combining GPS with inexpensive inertial sensors. Other benefits that are also realized when GPS is fused with inertial sensors are an increased bandwidth and robustness. That is, inertial sensors can provide attitude information at rates as high as several hundred Hz and can be used in high dynamic environments. They will also provide a degree of immunity against temporary GPS outages. Finally, in the air, the gyros would provide a good attitude estimate for re-initialization of the GPS attitude determination algorithm if a momentary loss of GPS lock occurs.

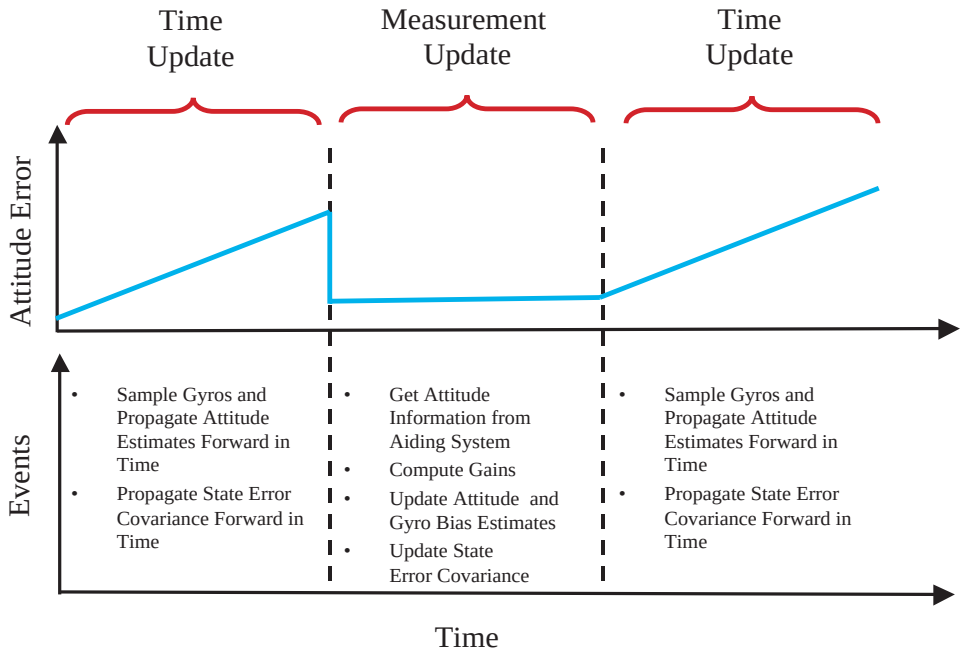

Figure 4.7: Time Line for an Attitude Estimator.

Before proceeding with the mechanization details, once again the role of GPS/Gyro attitude system in the backup navigation system must be clarified. As noted above, in the context of this thesis the AHRS is one of the sub-systems of the backup navigator and will be relied on for heading information when GPS services are not available. This will be during the coasting phase as defined in Figure 2.3 on page 18. However, when GPS services are available during the calibration phase of Figure 2.3, the GPS/Gyro attitude system will be used to calibrate inertial sensors. More specifically, it will be used to estimate the rate gyro null-shift denoted by the b_0 term in the rate gyro error model given by Equation 3.3 on page 39.

4.11.1 Euler Angle Based Filtering

In what follows the design of an estimator for blending GPS derived attitude with the attitude solution obtained from an inexpensive set of rate gyros is discussed. Earlier it was noted that in systems where attitude information is needed at a very high

rate, Euler angle parameterization was not desirable because of the computational burdens it imposes on the real time system. There are instances, however, where Euler angle parameterization is a good choice. An example of such an instance is where attitude information is being generated solely for use in pilot-in-the-loop control of aircraft. In this application generating attitude information at a rate of approximately 20 Hz is acceptable. Euler angle parameterization in this instance allows for sending the attitude solution directly to a display at the same rate without increasing the computational burden on the microprocessor performing the computations.

In the aided attitude determination system where the attitude parameterization is in the form of Euler angles, the state vector is defined as:

$$\hat{\vec{x}} = \begin{bmatrix} \psi & \theta & \phi & \delta p & \delta q & \delta r \end{bmatrix}^T. \tag{4.32}$$

The first three entries in the state vector $\vec{x}$ are the yaw, pitch and roll states, respectively. The remaining three entries are the roll, pitch and yaw axis gyro biases, respectively.

Time Update Equations

The time update equation for the Euler angle based estimator can be written in the standard state-space form as follows:

$$\dot{\hat{x}} = F\hat{\vec{x}} + G\hat{u} + \Gamma\vec{w} \tag{4.33}$$

where the vector $\hat{\vec{x}}$ is an estimate of $\vec{x}$. The F matrix is the system's dynamics matrix which is given by the following:

$$F = \begin{bmatrix} 0_{3\times3} & f(\theta,\phi)_{3\times3} \\ F_{Gyro} & 0_{3\times3} \end{bmatrix} \tag{4.34}$$

where the sub-matrix $f(\theta, \phi)$ is defined to be

$$f(\theta,\phi) = \begin{bmatrix} 0 & \frac{\sin(\phi)}{\cos(\theta)} & \frac{\cos(\phi)}{\cos(\theta)} \\ 0 & \cos(\phi) & -\cos(\phi) \\ 1 & \sin(\phi)\tan(\theta) & \cos(\phi)\tan(\theta) \end{bmatrix}. \tag{4.35}$$

This matrix maps gyro bias drift into Euler angle drift. The matrix F_{gyro} is a 3×3 matrix and describes the gyro error model being used. For example, if the estimator is being mechanized using vibrating structure rate gyros, then, as discussed in Chapter 3, the bias drift is modeled as an exponentially correlated process. Thus, the F_{Gyro} matrix would have the following form:

$$F_{Gyro} = \begin{bmatrix} -\frac{1}{\tau} & 0 & 0 \\ 0 & -\frac{1}{\tau} & 0 \\ 0 & 0 & -\frac{1}{\tau} \end{bmatrix}, \tag{4.36}$$

where τ is the appropriate time constant for the rate gyro being used. If FOGs are being used to mechanize the estimator, then F_{Gyro} would be a 3×3 matrix of zeros.

The input matrix, G, is given by:

$$G = \begin{bmatrix} f(\theta,\phi) \\ 0_{3\times 3} \end{bmatrix}. \tag{4.37}$$

The input vector for this estimator is:

$$\vec{u} = \begin{bmatrix} p & q & r \end{bmatrix}^T. \tag{4.38}$$

The entries for the input vector, $\vec{u}$, are the previously defined roll, pitch and yaw axis rate gyro outputs, respectively.

The matrix, Γ, maps the process noise vector, $\vec{w}$, into the time rate of change of the states and is given by:

$$\Gamma = \begin{bmatrix} \alpha f(\theta,\phi) & 0_{3\times 3} \\ 0_{3\times 3} & \beta I_{3\times 3} \end{bmatrix}. \tag{4.39}$$

The variables α and β are constants that are used as tuning parameters and will be discussed in the next section when the method for scheduling filter gains is described.

The process noise vector, $\vec{w}$, which multiplies the matrix Γ is given by:

$$\vec{w} = \begin{bmatrix} n_p \\ n_q \\ n_r \\ w_p \\ w_q \\ w_r \end{bmatrix}. \tag{4.40}$$

The first three entries of the input vector $\vec{w}$ are the wide band noise on the p, q and r gyros. The last three entries of $\vec{u}$ are the driving noise term in the stochastic model of the gyro bias given by Equation 3.4 of Chapter 3. In the actual implementation of the estimator, however, the process noise vector, $\vec{w}$, itself is not used. Instead, what is used is the process noise covariance matrix ,R_w, and its associated power spectral density matrix, R_{wpsd}. The matrix R_w is defined as:

$$R_w = \mathcal{E}\{\vec{w}\vec{w}^T\}. \tag{4.41}$$

The symbol $\mathcal{E}$ represents the expectation operator. The power spectral density matrix, R_{wpsd}, is defined as:

$$R_{wpsd} = \begin{bmatrix} R_{wn} & 0_{3\times3} \\ 0_{3\times3} & R_{wb} \end{bmatrix}. \tag{4.42}$$

The variables R_{wn} and R_{wb} are the Euler angle and gyro bias process noise matrices respectively. That is, R_{wn} represents the uncertainty in the model for propagating the Euler angles forward in time and R_{wb} represents the uncertainty in the dynamic model of the gyro biases. The matrix R_{wn} is given by:

$$R_{wn} = \begin{bmatrix} \sigma_p^2 & 0 & 0 \\ 0 & \sigma_q^2 & 0 \\ 0 & 0 & \sigma_r^2 \end{bmatrix}. \tag{4.43}$$

The variables σ_p^2, σ_q^2 and σ_r^2 are the variances of the wide-band noise on the three rate gyros. Numerical values for these variables depend on the type of gyro being used to mechanize the AHRS and can be found under the column labeled "Noise" in Table 3.2 of Chapter 3.

When using a vibrating structure rate gyro (e.g., Systron Donner "Horizon"), the matrix R_{wb} is given by:

$$R_{wb} = \frac{2\sigma^2{}_w}{\tau_w} \begin{bmatrix} 1 & 0 & 0 \\ 0 & 1 & 0 \\ 0 & 0 & 1 \end{bmatrix}. \tag{4.44}$$

Numerical values for these entries are taken from the column labeled "σ_w" in Table 3.2 of Chapter 3. In accordance with the error models developed in Chapter 3, when FOGs are being used, the R_{wb} matrix should theoretically be zero. Clearly, this results in filter gains that are zeros and leads to a situation where the rate gyro biases (in this case, null-shifts) are not estimated. To prevent this from happening when FOGs are used, the R_{wb} matrix is set equal to the identity matrix and a very small number is selected for the parameter β from Equation 4.39. The use of a FOG in an AHRS is discussed in Section 4.12 later in this chapter.

When this estimator is implemented as a sampled-data system, a discrete form of Equation 4.33 is used. In the discrete implementation, the rate gyros are sampled at regular intervals. At each sample instant k, the discrete input vector ,$\vec{u}_k$, is constructed. The vector $\vec{u}_k$ is then used as the input to a numerical integration routine for propagating the state vector, $\vec{x}_k$, forward in time.

Even though the dynamic model given in Equation 4.33 includes a mathematical expression for the time rate of change of the rate gyro biases, the model is a stochastic one and cannot be used to deterministically propagate the gyro biases forward in time. It is only used for propagating the state error covariance matrix. Changes in the rate gyro biases are determined using the measurement. This means that only the first three equations in the system given by Equation 4.33 are solved on-line. More specifically, the following system of equations is numerically integrated to propagate

the Euler angles forward in time:

$$\begin{bmatrix} \dot{\psi} \\ \dot{\theta} \\ \dot{\phi} \end{bmatrix} = \begin{bmatrix} 0 & \frac{\sin(\phi)}{\cos(\theta)} & \frac{\cos(\phi)}{\cos(\theta)} \\ 0 & \cos(\phi) & -\cos(\phi) \\ 1 & \sin(\phi)\tan(\theta) & \cos(\phi)\tan(\theta) \end{bmatrix} \begin{bmatrix} p \\ q \\ r \end{bmatrix} \tag{4.45}$$

The matrix, R_w is used in the equations for propagating the state error covariance matrix, P. Propagation of P forward in time is accomplished by using the solution to the discrete Riccati equation[34]. Given the state error covariance matrix, P_k, at time step k, then the covariance at time step $k+1$ is given by:

$$P_{k+1} = \Phi_k P_k \Phi_k^T + C_d \tag{4.46}$$

The variable Φ_k is the discrete equivalent of the matrix F at time step k and C_d is the discrete equivalent of $\Gamma R_w \Gamma^T$. Computation of C_d is accomplished using standard methods discussed in [34] which use R_{wpsd} as an input. As will be discussed in the next section, if estimator gains are scheduled, then Equation 4.46 does not have to be solved on-line.

Measurement Equation

As was noted in the discussion associated with Figure 4.7 the measurement update occurs at a slower rate than the time update. The measurement update equation that is used once at each measurement update is given by:

$$\hat{\vec{x}}_k^{(+)} = \hat{\vec{x}}_k^{(-)} + L_k(\vec{y}_k - H\hat{\vec{x}}_k). \tag{4.47}$$

The "$-$" superscript indicates a quantity *before* the measurement update and "$+$" superscript indicates a quantity *after* the measurement update. The measurement vector ,$\vec{y}_k$, is given by:

$$\vec{y}_k = \begin{bmatrix} \psi_{gps} & \theta_{gps} & \phi_{gps} \end{bmatrix}_k^T. \tag{4.48}$$

The measurement matrix, H, is defined as:

$$H = \begin{bmatrix} I_{3\times 3} & 0_{3\times 3} \end{bmatrix}. \tag{4.49}$$

The estimator gain matrix, L_k, is computed using the standard Kalman gain matrix equation [34]:

$$L_k = P_k^{(-)} H^T (H^T P_k^{(-)} H + R_v)^{-1}. \tag{4.50}$$

The variable R_v is the measurement noise covariance matrix and is defined as follows:

$$R_v = \begin{bmatrix} \sigma_\psi^2 & 0 & 0 \\ 0 & \sigma_\theta^2 & 0 \\ 0 & 0 & \sigma_\phi^2 \end{bmatrix}. \tag{4.51}$$

The diagonal entries in Equation 4.51 are the wide band noise on the measurements of ψ, θ and ϕ from the GPS attitude determination system. Numerical values for these entries are obtained from the GPS attitude determination system error model described in Chapter 3 and are repeated in Table 4.2 which will be discussed in the next section.

There are two methods for determining the estimator gain, L_k. These methods are:

1. Compute a time-varying gain matrix. This involves using Equation 4.46 to propagate the state covariance during the time update and then using Equation 4.50 to compute L_k.

2. The second way of determining gains relies on the fact that the structure of the gain matrix, L_k, is a function of the aircraft's attitude. While the relation between the aircraft's attitude and the structure of L_k will be discussed later, it should be noted that for a given model of rate gyros, the numerical values for the entries in the gain matrix, L_k, are a function of the time between measurement updates and the tuning parameters, α and β, in Equation 4.39. Thus, for a given attitude, model of rate gyros and frequency of measurement updates, the gain matrix, L_k, becomes constant once the estimator covariance reaches a steady state value. Thus, one can compute gain matrices as a function of aircraft attitude. These gains can be scheduled and used in the real-time system thereby obviating the need to solve Equations 4.46 and 4.50 on-line.

Unless otherwise stated, the gain matrices for all the estimators discussed in this

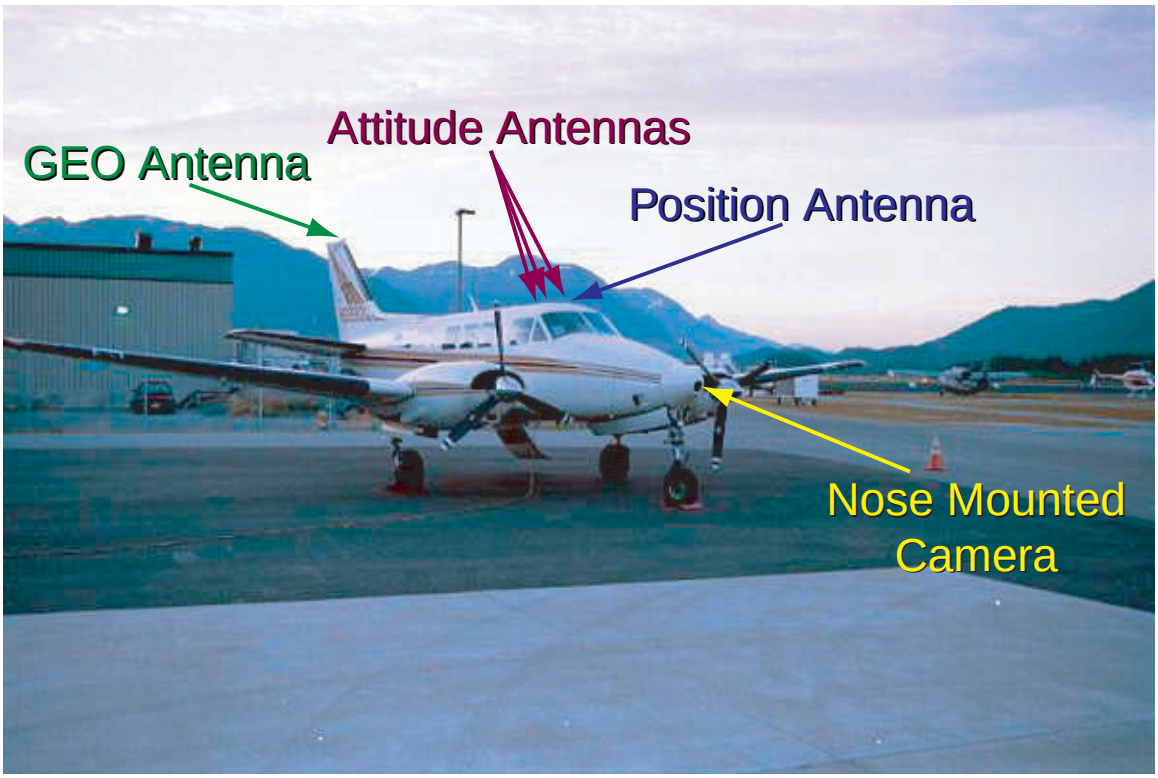

Figure 4.8: A Beechcraft Queen Air Flying Test-bed.

thesis were computed using the second method discussed above.

Estimator Performance

Experimental validation of the Euler angle based filtering algorithms was done on data collected using a Beechcraft Queen Air test aircraft shown in Figure 4.8. This aircraft was modified to be a flying test bed for research work associated with navigation systems and algorithms. The aircraft was equipped with the following sensors:

1. A low cost magnetometer triad (Honeywell HMR2300).

2. Two low cost Inertial Measurement Units (IMUs). One of the IMUs was a DMU-6X made by Crossbow Technology. The sensor suite in the DMU-6X

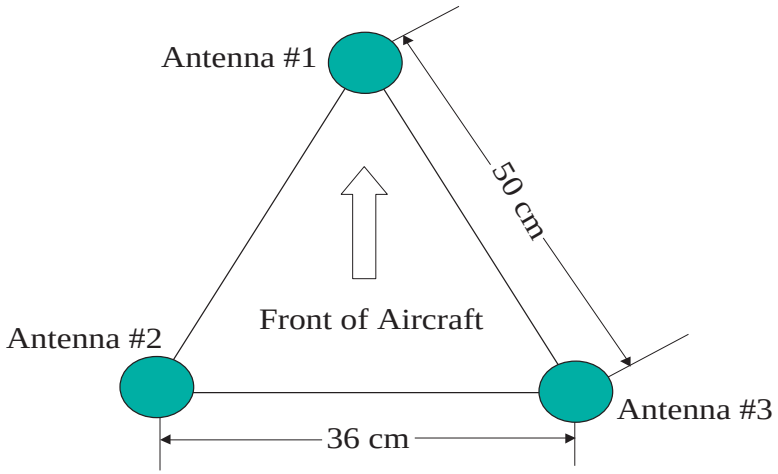

Figure 4.9: Configuration of the GPS Antennas used with the GPS Attitude Determination System.

consisted of a triad of vibrating structure rate gyros and a triad of solid-state accelerometers. The second IMU was a DMU-FOG also made by Crossbow Technology. The DMU-FOG consisted of a triad of fiber optic rate gyros and a triad of solid-state accelerometers.

3. An orthogonally mounted triad of Systron-Donner "Horizon" rate gyros.

4. A navigation grade Inertial Reference Unit (Honeywell YG1851 IRU). This system was used to provide a highly accurate record of the aircraft's yaw, pitch and roll angles.

5. A triple antenna short-baseline GPS Attitude Determination system. The GPS attitude determination system used three antennas that were installed on the top of the aircraft's fuselage as shown in Figure 4.8. The geometry of the antenna configuration is shown in Figure 4.9. The antennas formed the vertices of an isosceles triangle. The shorter of the two baselines was to the rear and was formed by an antenna pair (rear two) that was 36 cm apart. The other baselines were formed by antenna pairs that were 50 cm apart.

In addition to the aforementioned equipment, the aircraft was also equipped with a Differential GPS (DGPS) system which was used for accurate position measurements. The primary antenna for this DGPS system was installed on the fuselage just above the cockpit. This is the antenna marked as "Position Antenna" in Figure 4.8. The DGPS system used was the Stanford University Wide Area Augmentation System (WAAS) prototype. Differential corrections were relayed to the aircraft using a VHF or a geostationary satellite data link. When the geostationary satellite data link was used, differential corrections were received via the GEO Antenna mounted on the vertical tail as shown in Figure 4.8. Other sensors installed in the test airplane included an air-data computer (Shadin ADC200) and a low cost DME receiver (Allied Signal/Bendix-King KN-64)

A real-time implementation of the Euler angle based filter used the Systron-Donner Horizon rate gyros. The filtering algorithm for blending the GPS attitude solution with the inertial attitude solution in real-time sampled the output from the three gyros at 20 Hz. The output from the gyros was numerically integrated to provide an estimate (time update) of the three Euler angles. The triple antenna GPS attitude determination system generated estimates of the three Euler angles at a 2 Hz rate. The GPS determined attitude allowed for correction of the attitude errors resulting from the open loop gyro integration and also provided a means for estimating the gyro drift rates.

To minimize the computational burden, the estimator used constant gains that were computed off-line in accordance with the second method discussed in the previous section. Even though the Euler angle based estimator is non-linear, scheduled constant gains were found to work acceptably. The details of why constant gains work with this non-linear problem are discussed in detail later in Section 4.11.2 where the Euler angle based filter is compared with a quaternion based filter. Table 4.2 lists the numerical values for the various parameters used in mechanizing this filter.

Figure 4.10 on page 134 shows the real-time estimate of the gyro biases after filter start-up. It can be seen that the estimates of gyro biases stabilized after 3 to 4 minutes from power up. On-line estimation of the rate gyro biases allows the AHRS to coast during momentary GPS outages. To demonstrate this coasting capability, the estimator gain, L, was set to zero (in post process) to simulate an extended

Matrix	Matrix Parameter	Numerical Values	Relevant Equation(s), Sections or Pages
R_v	σ_ψ σ_θ σ_ϕ	0.25°	Equation 4.51 and Chapter 3, Section 3.10 Page 72
R_{wn}	α	0.2	Equation 4.39
	σ_p σ_q σ_r	0.05°/sec	Equations 4.43 and 4.42
R_{wb}	β	2.0×10^{-4}	Equation 4.39
	σ_w	0.05°/sec	Equations 4.44 and 4.42

Table 4.2: Summary of Numerical Values for the Parameters in the Euler Angle Filter.

GPS outage. The plots in Figure 4.11 on page 135 show the deviation between the gyro integrated attitude solution and the GPS attitude solution during this simulated outage. At $t = 0$, the estimator gain is set to zero. There is less than a 4 degree error in all axes 5 minutes after the GPS feedback has been removed. Experience has shown that GPS outages in flight are rare and of a short duration lasting at most a few seconds. Figure 4.11 clearly shows that the Systron Donner "Horizon" rate gyros can adequately coast through such short outages.

Using a more expensive set of inertial sensors will extend the allowable coasting time during GPS outages. It also changes the architecture of the attitude estimator. For example, when navigation grade inertial sensors (as defined in Figure 2.6, page 23) are used to mechanize an AHRS, GPS becomes a means of initial alignment and subsequent periodic attitude resets. After the initial alignment, the gyro biases do not have to be estimated on-line because their change from the initial estimate will be very small. The time between GPS updates, therefore, can be increased. Thus, the importance of the GPS measurement update is deemphasized as the quality of the inertial sensors increases.

The attitude solution generated by this estimator was used to drive a display that was used by pilots for control of aircraft attitude. This meant that the attitude solution generated had to have very little jitter (i.e., it had to be smooth) and lag.

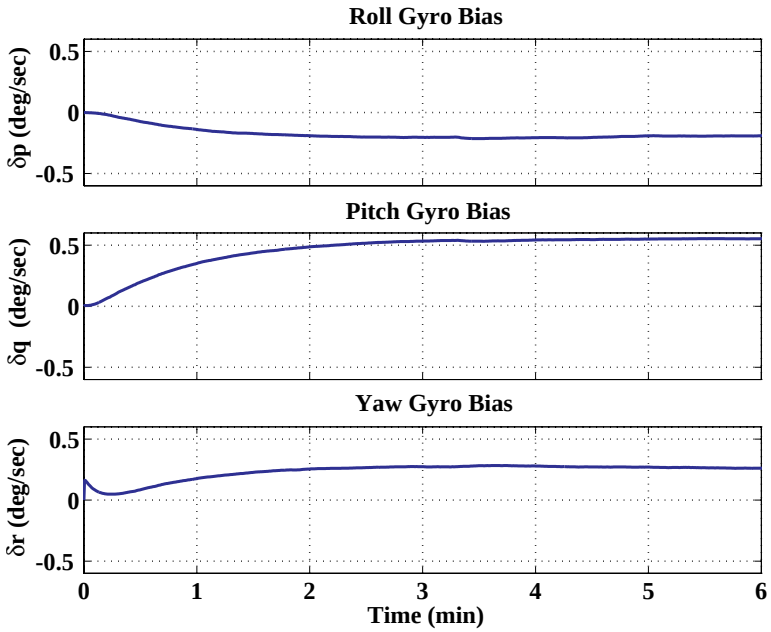

Figure 4.10: Real-Time Estimation of Biases for Inexpensive Rate Gyros (Systron Donner "Horizon" Solid-State Rate Gyro).

Figure 4.12 on page 136, which is a blow-up of the pitch solution generated by the real-time system, shows that the attitude solution is indeed jitter free. This demonstrates that the high bandwidth information from the gyros has eliminated jitter in the attitude solution generated by the triple antenna GPS attitude system.

A method of trial-and-error was used to select the values of the tuning parameters, α and β, defined in Equation 4.39. The values selected were those that, based on the judgment of the author, resulted in the desired estimator performance. The results shown in Figures 4.10, 4.11 and 4.12 highlight the important trade-offs involved in selecting these values. The location of the estimator poles are controlled by the tuning parameters, α and β. Larger values of α and β result in faster the poles. Fast estimator poles result in large gains while slow estimator poles result in small gains. Furthermore, an examination of Equation 4.39 shows that α controls the poles associated with the Euler angle states while β controls the poles associated with the gyro biases.

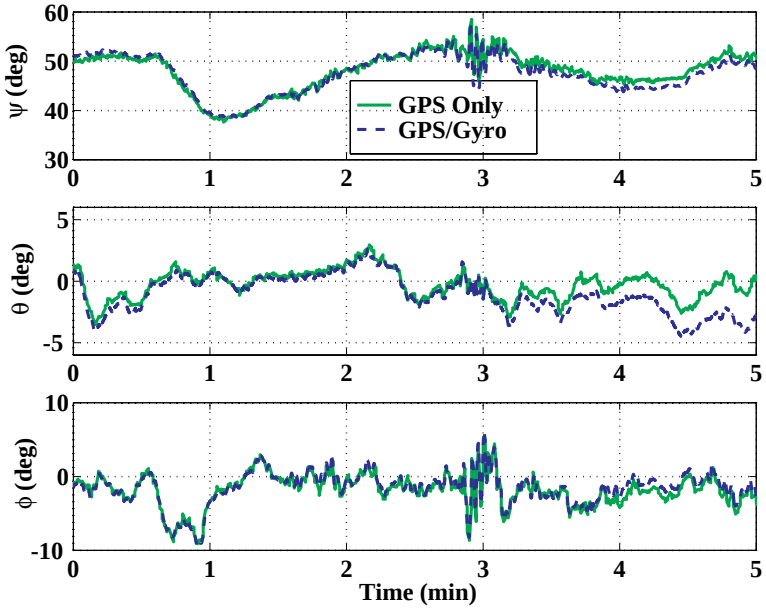

Figure 4.11: Attitude Time History and Gyro Coast Capability (Systron Donner "Horizon" Solid-State Rate Gyro).

Faster estimator poles (larger values of α and β) would have resulted in faster convergence for the gyro biases estimates shown in Figure 4.10. However, increasing the values of α and β to get a faster convergence would have resulted in a noisier attitude solution and the relatively smooth attitude estimates shown in Figure 4.12 would not have been achieved.

It is possible to increase the value of β only and this should speed up the convergence of the gyro bias estimates without magnifying the noise on the Euler angle states. The problem with this approach is that it results in a noisy (or poor) gyro bias estimate which affects the ability of the system to coast through temporary GPS outages.

Figure 4.13 shows the result of a simulation study showing the trade-off involved in choosing the speed of the estimator poles. The values for various estimator parameters are shown in Table 4.3. The red trace in Figure 4.13 is the actual value of the roll gyro bias. The blue trace in the left hand side plot in Figure 4.13 shows the roll gyro bias estimate from an estimator using slow poles. The blue trace in the right hand

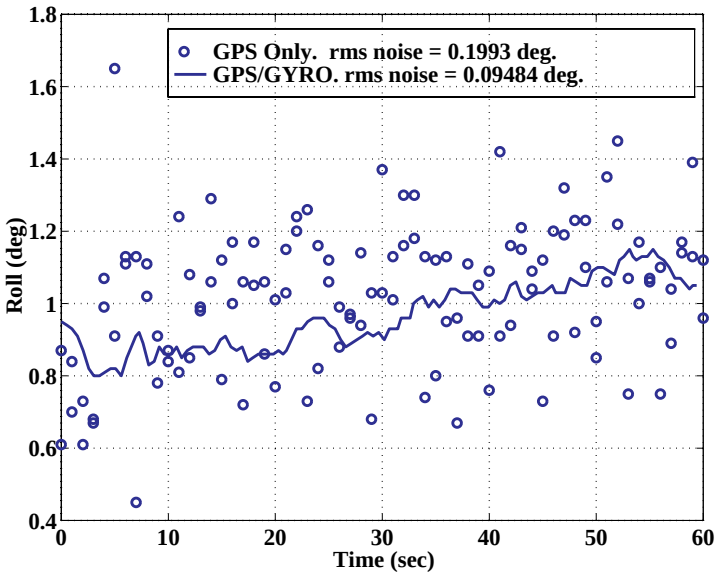

Figure 4.12: Filtering of GPS Attitude Noise by Inexpensive Rate Gyros (Systron Donner "Horizon" Solid-State Rate Gyro).

side figure shows an estimate of the same state using an estimator with faster poles. As would be expected, the use of faster poles speeds up the convergence of the bias state estimate but leads to a much noisier solution.

4.11.2 Quaternion Based Filtering

In the aided attitude determination system where the attitude parameterization is in the form of quaternions, the state vector is as follows:

$$\vec{x} = \begin{bmatrix} \vec{q}_e \\ \delta p \\ \delta q \\ \delta r \end{bmatrix}. \tag{4.52}$$

The first entry is a quaternion error vector which was defined in Equations 4.17 and 4.18. The remaining three entries are the roll, pitch and yaw axis gyro biases,

Matrix	Matrix Parameter	Numerical Values		Relevant Equation(s), Sections or Pages
		Slow Poles	Fast Poles	
R_v	σ_ψ σ_θ σ_ϕ	0.25°	0.25°	Equation 4.51, Chapter 3, Section 3.10 Page 72
R_{wn}	α	10	10	Equation 4.39
	σ_p σ_q σ_r	0.05°/sec	0.05°/sec	Equations 4.43 and 4.42
R_{wb}	β	1	10	Equation 4.39
	σ_w	0.05°/sec	0.05°/sec	Equations 4.44 and 4.42

Table 4.3: Estimator Pole Trade-Off Study. Numerical Values for an Euler Angle Filter.

respectively.

Time Update Equations

The time update equation used with the quaternion mechanization of an AHRS is written in the standard state-space form as follows:

$$\dot{\hat{x}} = F\hat{\vec{x}} + \Gamma\vec{w}. \tag{4.53}$$

The system dynamics matrix, F, is given by:

$$F = \begin{bmatrix} -[\vec{\omega}]^\times & \frac{1}{2}I_{3\times3} \\ F_{Gyro} & 0_{3\times3} \end{bmatrix}. \tag{4.54}$$

The interested reader can refer to [28] for a discussion of how this dynamic model is derived. In what follows, however, only the results of the discussion found in [28] will be presented.

The vector $\vec{\omega}$ in the definition of the dynamic matrix, F, is the total angular rate and is given by:

$$\vec{\omega} = \begin{bmatrix} p & q & r \end{bmatrix}^T. \tag{4.55}$$

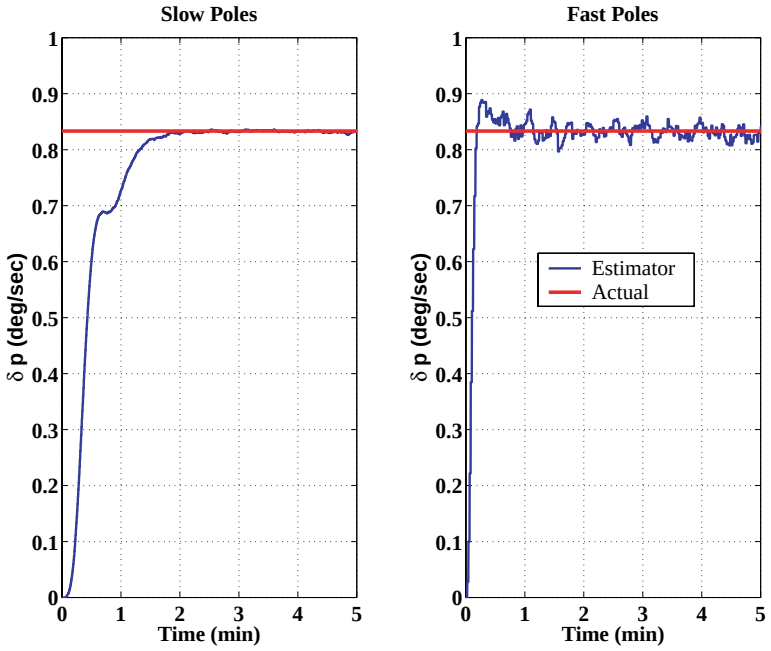

Figure 4.13: Effect of Pole Speed on Rate Gyro Bias Estimation.

The matrix F_{Gyro} was defined in Equation 4.36. The matrix Γ maps the process noise vector, $\vec{w}$, into the time rate of change of the states and is given by:

$$\Gamma = \begin{bmatrix} -\frac{1}{2}I_{3\times 3} & 0_{3\times 3} \\ 0_{3\times 3} & I_{3\times 3} \end{bmatrix}. \tag{4.56}$$

The process noise vector, $\vec{w}$, is given by

$$\vec{w} = \begin{bmatrix} n_p \\ n_q \\ n_r \\ w_p \\ w_q \\ w_r \end{bmatrix}. \tag{4.57}$$

The process noise vector, $\vec{w}$, is identical to the one used in the Euler angle mechanization and is given by Equation 4.40. Thus, the process noise matrix, R_w, for the quaternion implementation is identical to the one used with the Euler angle implementation given by Equation 4.42. This also implies that the method for forming the matrix R_w and obtaining the numerical values needed to populate the two submatrices R_{wn} and R_{wb} is identical to that described previously for the Euler angle based estimator. Therefore, R_w is used to propagate the state covariance matrix, P, in the same manner as was done for the Euler angle mechanization described earlier.

Measurement Equation

The measurement equation is given by:

$$\hat{\vec{x}}^{(+)} = L(\vec{y} - H\hat{\vec{x}}^{(-)}). \tag{4.58}$$

There are two options available for the measurement matrix H. The first option is applicable when a multiple GPS antenna system is used as the aiding system. In this case, the measurement matrix H is identical to one defined in Equation 4.49 for the Euler angle based estimator but the associated measurement vector $\vec{y}$ is different. The measurement vector is the quaternion error $\mathbf{q}_{e_{GPS}}$ which is defined as:

$$\mathbf{q}_{e_{GPS}} = \mathbf{q}_{GPS} \otimes \hat{\mathbf{q}} = \vec{y}. \tag{4.59}$$

That is, $\mathbf{q}_{e_{GPS}}$ is the difference (in the quaternion sense) between the GPS computed and filter estimated attitude.

The second option for H is applicable when a vector matching attitude determination system is used as the aiding system. As noted earlier in Section 4.9, this aiding system requires only one GPS antenna and a triad of magnetometers. The H matrix in this instance is defined as follows:

$$H = \begin{bmatrix} -2[\vec{u}^n]^\times & 0_{3\times3} \\ -2[\vec{v}^n]^\times & 0_{3\times3} \end{bmatrix} \tag{4.60}$$

This matrix is very similar to the measurement matrix defined in Equation 4.31 with

the only difference being the added last three columns of zeros to account for the fact that the state vector now includes rate gyro biases. The measurement vector, $\vec{y}$, is defined in Equation 4.30. From this point on, the implementation proceeds in the same way described earlier for the Euler angle estimator.

For attitude determination systems mechanized using low-performance sensors, the accuracy of the system is ultimately a function of the aiding system's accuracy. Thus, there is no difference in accuracy whether the implementation is done using Euler angles or quaternions.

4.11.3 Comparison of Euler Angle and Quaternion Based Estimators

At this point the obvious question is what advantage does the quaternion mechanization have over the Euler angle mechanization? To answer this question, consider an aided AHRS where the aiding system is a triple antenna GPS attitude determination system.

The first advantage of the quaternion mechanization is that the well known problem of "gimbal lock" is eliminated. That is, the Euler angle singularity at a pitch angle, θ, of $\pm 90^\circ$ does not exist when quaternions are used. Unless one is dealing with aerobatic flight, this is usually not a problem because extreme attitudes where θ is $\pm 90^\circ$ are not common in normal aircraft operations.

The second advantage is that the filter implementation is simplified when using quaternions. More specifically, scheduling gains is an easier task when using quaternions. To see why this is the case, we will write out the Kalman filter gain equation as follows:

$$\begin{aligned} \hat{\vec{x}}^{(+)} - \hat{\vec{x}}^{(-)} &= \delta\vec{x} \\ &= L(\vec{y} - H\hat{\vec{x}}) \\ &= L\delta\vec{y} \end{aligned} \tag{4.61}$$

The vector $\delta\vec{x}$ represents the state estimation error and $\delta\vec{y}$ is the innovations process or measurement residuals. In an optimal filter, the innovations process is a white

noise process [40]. Otherwise, there will be information left in $\delta\vec{y}$ that is mapped into the state error vector. The state error vector, in turn, is used to update the estimate of the state vector, $\vec{x}$, such that it becomes optimal. From Equation 4.61 it can be seen that the gain matrix is the "constant of proportionality" (or more appropriately a matrix of Jacobians) for the mapping of the innovations process into the state error vector.

In the Euler angle mechanization, the state error vector, $\delta\vec{x}$, consists of the errors in the estimate of the three Euler angles and the gyro biases. That is, it is the difference in the state vector estimate before and after a measurement update. Using the "$\wedge$" notation above variables to indicate *estimated* quantities, superscripts "$-$" and "$+$" to denote quantities *before* and *after* a measurement update, respectively, then the vector $\delta\vec{x}$ can be written as:

$$\delta\vec{x} = \begin{bmatrix} \hat{\psi}^{(+)} - \hat{\psi}^{(-)} \\ \hat{\theta}^{(+)} - \hat{\theta}^{(-)} \\ \hat{\phi}^{(+)} - \hat{\phi}^{(-)} \\ \delta\hat{p}^{(+)} - \delta\hat{p}^{(-)} \\ \delta\hat{q}^{(+)} - \delta\hat{q}^{(-)} \\ \delta\hat{r}^{(+)} - \delta\hat{r}^{(-)} \end{bmatrix}. \tag{4.62}$$

In the Euler angle mechanization, the three elements of the innovations process, $\delta\vec{y}$, are the differences between the GPS derived attitude solution and the filter's estimate of the attitude before a measurement update. The first entry in the innovations process is the difference between GPS derived yaw and the filter's estimate of yaw. Similarly, the remaining two entries are the pitch and roll differences respectively. Mathematically, $\delta\vec{y}$ is given by:

$$\delta\vec{y} = \begin{bmatrix} \psi_{GPS} - \hat{\psi}^{(-)} \\ \theta_{GPS} - \hat{\theta}^{(-)} \\ \phi_{GPS} - \hat{\phi}^{(-)} \end{bmatrix} = \begin{bmatrix} \Delta\psi \\ \Delta\theta \\ \Delta\phi \end{bmatrix}. \tag{4.63}$$

Given these definitions for $\delta\vec{y}$ and $\delta\vec{x}$, it is clear to see that the estimator gain matrix

must have the following form:

$$L = \begin{bmatrix} L_{(\psi,\Delta\psi)} & L_{(\psi,\Delta\theta)} & L_{(\psi,\Delta\phi)} \\ L_{(\theta,\Delta\psi)} & L_{(\theta,\Delta\theta)} & L_{(\theta,\Delta\phi)} \\ L_{(\phi,\Delta\psi)} & L_{(\phi,\Delta\theta)} & L_{(\phi,\Delta\phi)} \\ L_{(\delta p,\Delta\psi)} & L_{(\delta p,\Delta\theta)} & L_{(\delta p,\Delta\phi)} \\ L_{(\delta q,\Delta\psi)} & L_{(\delta q,\Delta\theta)} & L_{(\delta q,\Delta\phi)} \\ L_{(\delta r,\Delta\psi)} & L_{(\delta r,\Delta\theta)} & L_{(\delta r,\Delta\phi)} \end{bmatrix}. \tag{4.64}$$

In the matrix above, the notation $L_{(\delta p,\Delta\psi)}$, for example, means that this is the element of the gain matrix, L, that maps the yaw innovations, $\Delta\psi$, into the roll gyro bias estimate, δp. Another way to look at this is that $L_{(\delta p,\Delta\psi)}$ is a measure of how much of the yaw error is a result of the roll gyro bias. The interpretation is similar for the remaining entries of the estimator gain matrix, L.

Now it is clear to see that in the Euler angle mechanization the mapping of the innovations process into the first three entries of the state error vector should be one to one. That is, yaw innovations should map into yaw state errors, and the same for pitch and roll. More importantly, this mapping is independent of attitude. This situation is different for the mapping of the innovations process into the gyro bias estimate errors. This mapping is a function of the current attitude estimate. For example, if the AHRS is level, then the yaw innovations map into yaw gyro biases, pitch innovations map into pitch gyro biases and roll innovations map into roll gyro biases.

To understand this better, consider the scenario shown in Figure 4.14. In Figure 4.14, a level aircraft at a yaw angle of ψ is shown. Because of gyro drift, the yaw angle computed by the attitude estimator is off by an amount $\Delta\psi$ and is depicted by the grey silhouette. That is, the estimator "thinks" the aircraft is at a yaw angle of $\psi + \Delta\psi$ when, in fact, the airplane is at a yaw angle of ψ. Because the aircraft is perfectly level, this difference can only be due to an error in the estimate of the yaw gyro bias. Thus, the yaw difference, $\Delta\psi$, between the GPS measured and the estimator computed yaw angle estimate has to be proportional to the yaw gyro drift. The constant of proportionality is the $L_{6,1}$ element of the gain matrix or $L_{(\delta r,\Delta\psi)}$.

Instead of being level, if the AHRS is now at a roll angle of 90°, the mapping

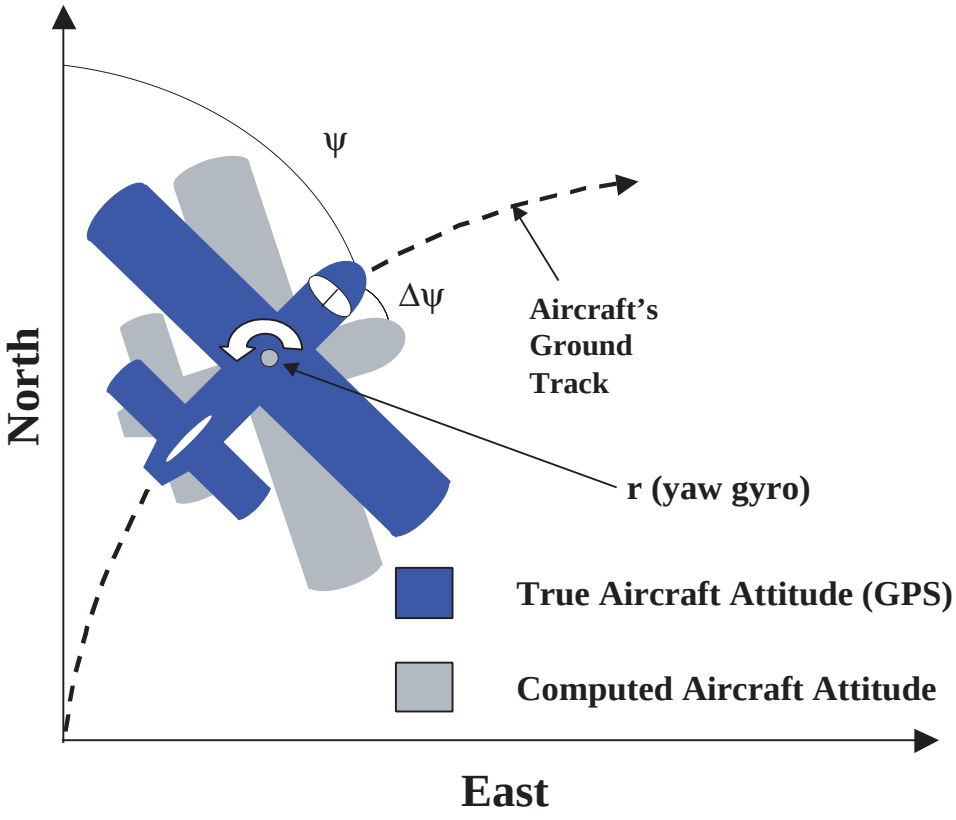

Figure 4.14: Mapping of Yaw Innovations into the δr Gyro Biases for a Level AHRS.

from innovations to gyro bias estimate errors is changed. Now pitch innovations map into yaw gyro bias estimate errors and yaw innovations map into pitch gyro bias estimate errors. The mapping between the roll innovations and the roll gyro bias estimate errors remains unaffected. This change in mapping is shown in Figure 4.15 which depicts an aircraft rolled 90° to the right and at a yaw angle of ψ. Once again, because of gyro drift, the yaw angle computed by the estimator is in error by an amount $\Delta\psi$. That is, the estimator "thinks" the aircraft is as shown by the grey silhouette which is at a yaw angle of $\psi + \Delta\psi$ when, in fact, the airplane is at a yaw angle of ψ. Since the aircraft is banked 90° degrees to the right, the yaw error can only be due to errors in the estimate of the pitch gyro bias. Thus, the difference $\Delta\psi$ between the GPS measured and the estimator computed yaw angle estimate has to

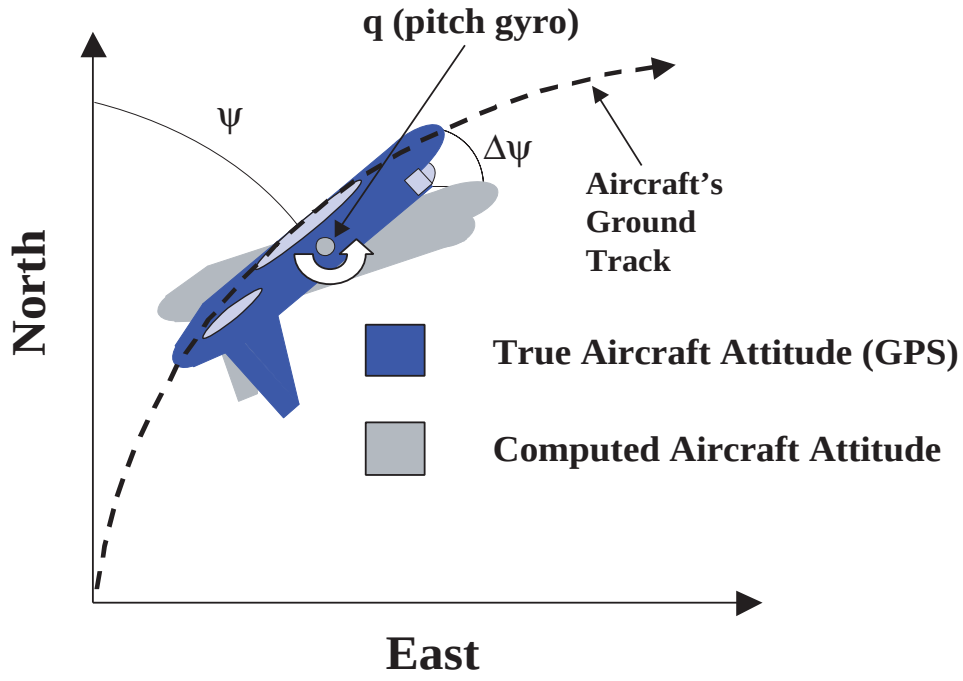

Figure 4.15: Mapping of Yaw Innovations into the δq Gyro Biases for an AHRS at 90° Roll.

be proportional to the pitch gyro drift. The constant of proportionality in this case is the $L_{5,1}$ element of the gain matrix or $L_{(\delta q, \Delta\psi)}$.

The dependence of this mapping can be clearly seen in the results of a simulation study shown in Figure 4.16. The upper left hand figure shows the history of the three Euler angles. Yaw and pitch are zero for the entire history while roll varies sinusoidally between +90° and -90°. The mapping of the innovations process into the roll gyro bias, δp, are shown in the upper right figure. After the initial transient, the only non-zero gain is $L_{(\delta p, \Delta\phi)}$. This is the $L_{4,3}$ element of the gain matrix and maps roll innovations into roll gyro bias estimate errors. The lower left figure shows the mapping of the innovations process into pitch gyro bias estimate errors. In this case it is seen that the gain mapping yaw innovations into the pitch gyro bias estimate is the largest. It is zero when the roll angle is zero. This indicates that at zero roll the mapping is from pitch innovations to pitch gyro bias estimate errors. Similarly, the

bottom right figure shows that mapping of the innovations process, $\delta\vec{y}$, into the yaw gyro bias estimate errors is also a function of roll angle.

Now consider the quaternion mechanization. From the discussions in Section 4.11.2 (Equation 4.59 on page 139) it will be recalled that the measurement vector, $\vec{y}$, consists of the vector part of the error quaternion $\mathbf{q}_{e_{GPS}}$ which is generated by the quaternion multiplication of $\mathbf{q}_{GPS}$ and $\hat{\mathbf{q}}$. Therefore, the innovation process, $\delta\vec{y}$, is given by:

$$\delta\vec{y} = \begin{bmatrix} q_{e_{GPS}}(1) - q_e^{(-)}(1) \\ q_{e_{GPS}}(2) - q_e^{(-)}(2) \\ q_{e_{GPS}}(3) - q_e^{(-)}(3) \end{bmatrix} = \begin{bmatrix} \Delta q_e(1) \\ \Delta q_e(2) \\ \Delta q_e(3) \end{bmatrix}. \tag{4.65}$$

Accordingly, the gain matrix, L, has the following structure:

$$L = \begin{bmatrix} L_{(q_e(1),\Delta q_e(1))} & L_{(q_e(1),\Delta q_e(2))} & L_{(q_e(1),\Delta q_e(3))} \\ L_{(q_e(2),\Delta q_e(1))} & L_{(q_e(2),\Delta q_e(2))} & L_{(q_e(2),\Delta q_e(3))} \\ L_{(q_e(3),\Delta q_e(1))} & L_{(q_e(3),\Delta q_e(2))} & L_{(q_e(3),\Delta q_e(3))} \\ L_{(\delta p,\Delta q_e(1))} & L_{(\delta p,\Delta q_e(2))} & L_{(\delta p,\Delta q_e(3))} \\ L_{(\delta q,\Delta q_e(1))} & L_{(\delta q,\Delta q_e(2))} & L_{(\delta q,\Delta q_e(3))} \\ L_{(\delta r,\Delta q_e(1))} & L_{(\delta r,\Delta q_e(2))} & L_{(\delta r,\Delta q_e(3))} \end{bmatrix}. \tag{4.66}$$

In the equation above, the notation $L_{(\delta p,\Delta q_e(1))}$, for example, means that this is the element of the gain matrix, L, that maps the error in the estimate of the first element of quaternion error vector, $\Delta q_e(1)$, into the roll gyro bias estimate, δp.

The results of a simulation study for the quaternion mechanization are shown in Figure 4.17. In this case it is seen that the gains for the mapping of the innovations process to gyro bias estimate errors is constant and independent of the estimated attitude. This is because in the quaternion mechanization, the innovations process represents errors in the estimate of the quaternion error vector, $\vec{q}_e$. The quaternion error, $\vec{q}_e$, is small and its elements are nothing more than the rotation errors about the roll, pitch and yaw axes of the aircraft respectively. For example, in the upper right figure the gains for mapping the innovations process into roll gyro bias estimate errors are shown. The only non-zero element here is $L_{(\delta p,\Delta q_e(1))}$. This is the $L_{4,1}$ element of the gain matrix and maps roll axis rotation error (i.e., the first element of $\vec{q}_e$) into the roll gyro bias estimate.

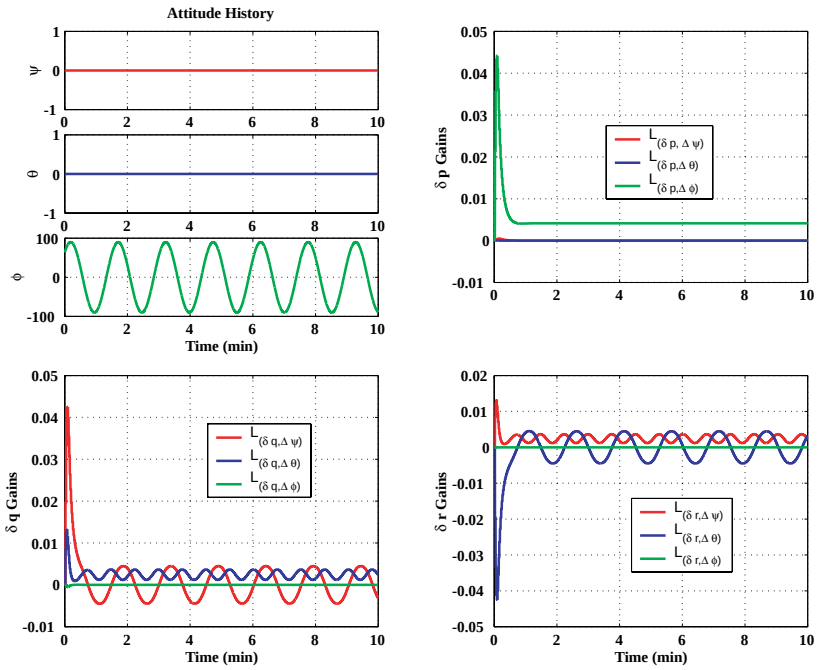

Figure 4.16: Filter Gain History for an Euler Angle Mechanization.

In the case where the aiding system is based on the vector matching algorithm, the gains are a mapping from the errors in the lengths of the components of the two vectors used for the vector matching to the quaternion errors and gyro biases. From Equation 4.60 it can be seen that the measurement matrix, H, is time varying. Therefore, scheduling of gains in this case is more complicated.

4.12 Gyro/Accelerometer and Magnetometer Attitude System

Aiding low performance rate gyros using an accelerometer-magnetometer attitude system is essentially the same as aiding using a multiple GPS antenna attitude system. The accelerometers provide measurement of pitch and roll while the magnetometer

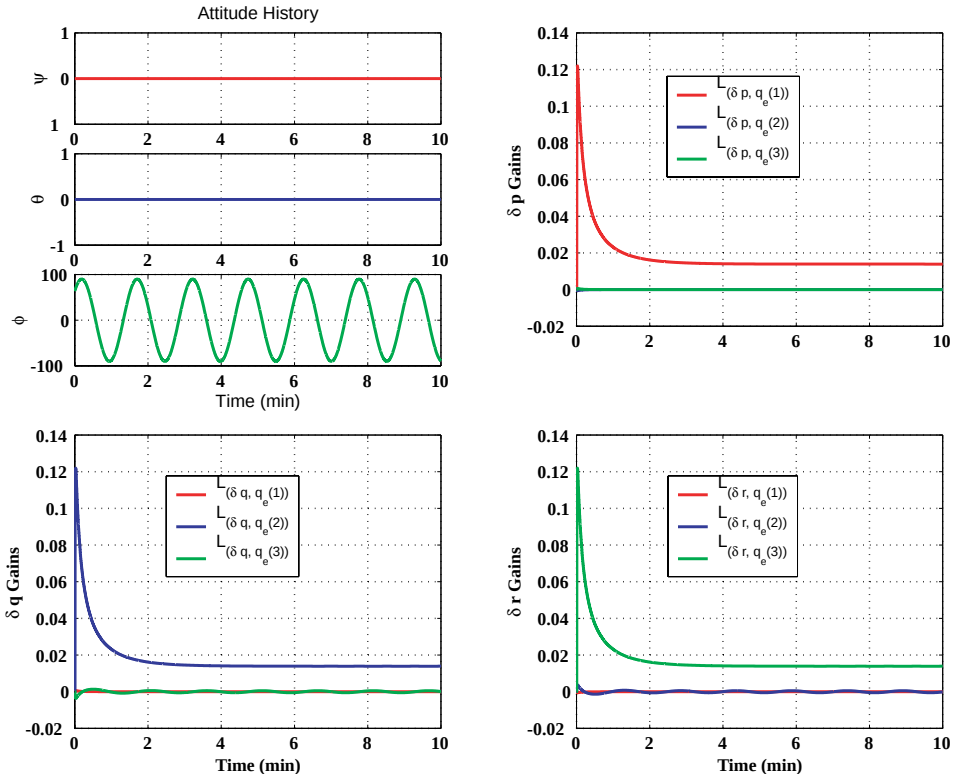

Figure 4.17: Filter Gain History for a Quaternion Mechanization.

provides the yaw measurement. These estimates of yaw, pitch and roll are blended with the gyro derived attitude solution using a Kalman filter.

The filter architecture is essentially the same as that of the GPS attitude aided systems described earlier. There is, however, one major difference. As was noted earlier, the accelerometer and magnetometer attitude system does not provide an accurate attitude estimate when the aircraft is accelerating. When the acceleration is of a short duration, the effect of the acceleration can be minimal. However, in prolonged accelerations such as would occur in turns, the blended attitude solution will diverge if the feedback from the accelerometers and magnetometer is not turned off. This is the fundamental difference between the GPS aided attitude system and the accelerometer and magnetometer aided system: the measurement updates must be turned off occasionally in the accelerometer and magnetometer aiding system.

What should be the trigger used to determine when the measurement updates should be turned off? It was found that using a computed yaw rate, $\dot{\psi}_c$, works well as a "switch." That is, the computed yaw rate, $\dot{\psi}_c$, defined as the difference between the yaw solution at the current time step, ψ_k, and the previous time step, ψ_{k-1}, divided by the elapsed time, Δt, is used as the trigger to turn-on and off the filter. Mathematically, this is given by:

$$\dot{\psi}_c = \frac{\psi_k - \psi_{k-1}}{\Delta t}. \tag{4.67}$$

For the rate gyros used in this thesis, it was found that a $\dot{\psi}_c$ threshold value of 0.5 $^\circ$/sec was acceptable. Whenever the value of $\dot{\psi}_c$ exceeded 0.5°/sec, the filter assumed the aircraft was in a turn and hence, accelerometer feedback was turned off.

In addition, for the cases where the acceleration is not induced by turning, the magnitude of the accelerometer outputs is checked. If it is less than a certain threshold, the feedback is kept on. The threshold was set to 1.05g for the AHRS developed and used in this thesis. That is, if the magnitude of the accelerometer readings is in excess of 1.05g, then feedback from the accelerometers is turned off.

To assess the performance of this filter, experimental data was collected from a Crossbow vibrating structure rate gyro that was flown in the test aircraft described earlier. Table 4.4 is a summary of the numerical values for the parameters used in this filter. Once again, the numerical values listed in Table 4.4 were used to compute the steady state gains off-line. In turn, the computed steady state gains were scheduled. Note that the measurement noise on pitch and roll were obtained by converting the accelerometer wide-band noise into an angular measurement using Equations 4.8 and 4.9.

The results from this flight test are shown in Figure 4.18. The top most plot in the figure shows a comparison of the attitude solution from a Navigation grade INS, a low performance solid state gyro aided by an accelerometer and magnetometer and open loop integration of the same gyro. The attitude solution from the INS is used as a truth reference. The null-shift of the rate gyros has been estimated using a triple antenna GPS attitude system prior to the 105 second mark. Clearly the open loop solution is seen to diverge. This is not surprising because the bias instability

Matrix	Matrix Parameter	Numerical Values	Relevant Equation(s)
R_v	σ_ψ	0.80°	Equation 3.86, Page 100
	σ_θ	0.06°	Equation 3.26, Page 55
	σ_ϕ		Equation 4.51
R_{wn}	α	10	Equation 4.56
	σ_p	0.05°/sec	Equations 4.43 and 4.42
	σ_q		
	σ_r		
R_{wb}	β	1.0×10^{-5}	Equation 4.39
	σ_w	0.05°/sec	Equations 4.44 and 4.42

Table 4.4: Numerical Values for the Filter Parameters in the Accelerometer/Magnetometer AHRS.

of these low performance gyros is high. Even after estimation of the bias using a GPS attitude system the bias changes shortly thereafter. As would be expected, the attitude solution when the system is aided by accelerometers and magnetometers is seen to be much better than the open loop case. The second plot in Figure 4.18 shows the filter state. The filter state indicates whether the accelerometer and magnetometer feedback is on or off. The last plot shows the computed yaw rate that is used to trigger the filter on or off. What is clear from these three plots is that the filter turns itself off when in turns or during accelerations. Accelerations where the aircraft is not turning are of very limited duration. The long accelerations occur in turns. Thus, if turns are limited to short duration this aiding scheme will work acceptably. However, if turns are of a long duration, the gyros will be open loop and the integrated attitude solution will drift.

One possible solution in this instance is to use gyros with good bias stability. For example, the use of a FOG will allow for coasting through very long turns without aiding. Figure 4.19 shows the comparison between the roll attitude solution from a Navigation grade INS (Honeywell YG1851), a low performance FOG (Crossbow DMU-FOG) being integrated open loop and the same FOG being aided by a magnetometer and accelerometer. Once again the INS attitude solution is being used as

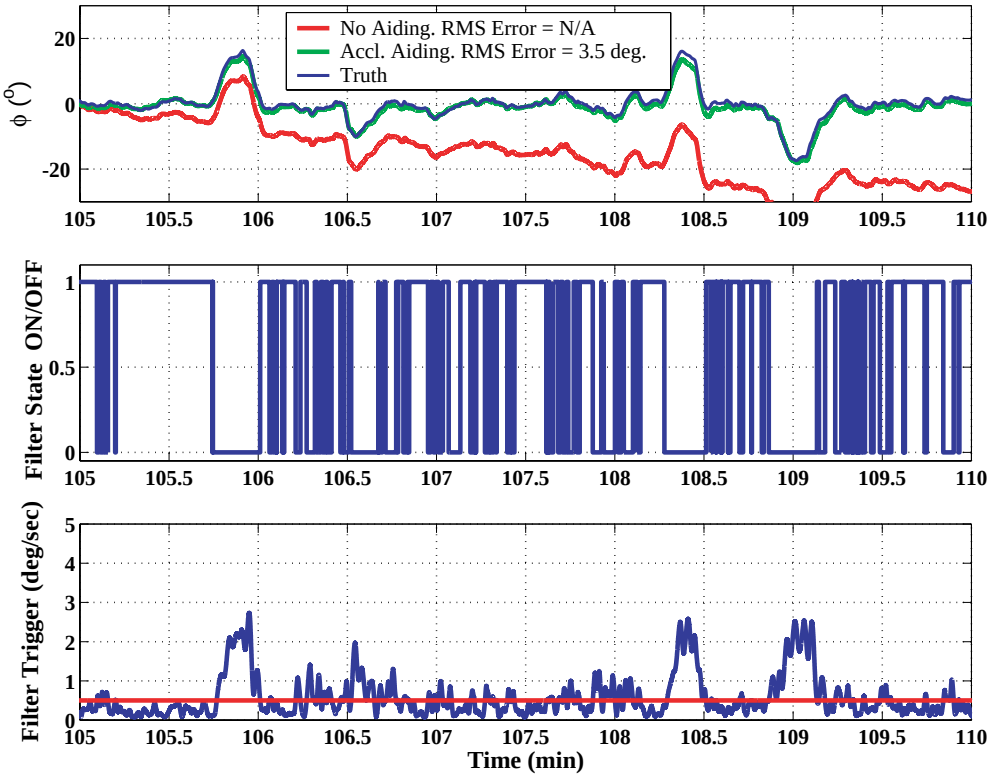

Figure 4.18: Roll Solution-Vibrating Structure Gyro aided by Accelerometer and Magnetometer.

truth. That data shown comprises a 20 minute section of a flight test that lasted 65 minutes. Clearly, the attitude solution with the FOG being aided by the accelerometers and magnetometers is superior to the case where no aiding is being performed. In view of the Allan variances for the Crossbow FOG shown in Figure 3.8 one may wonder why any aiding of the FOG is required. The answer to this question is provided by Figure 4.2. Wide band noise on the FOG will get integrated into angular errors. As a matter of fact, inspection of Figure 4.19 shows the effect of random walk.

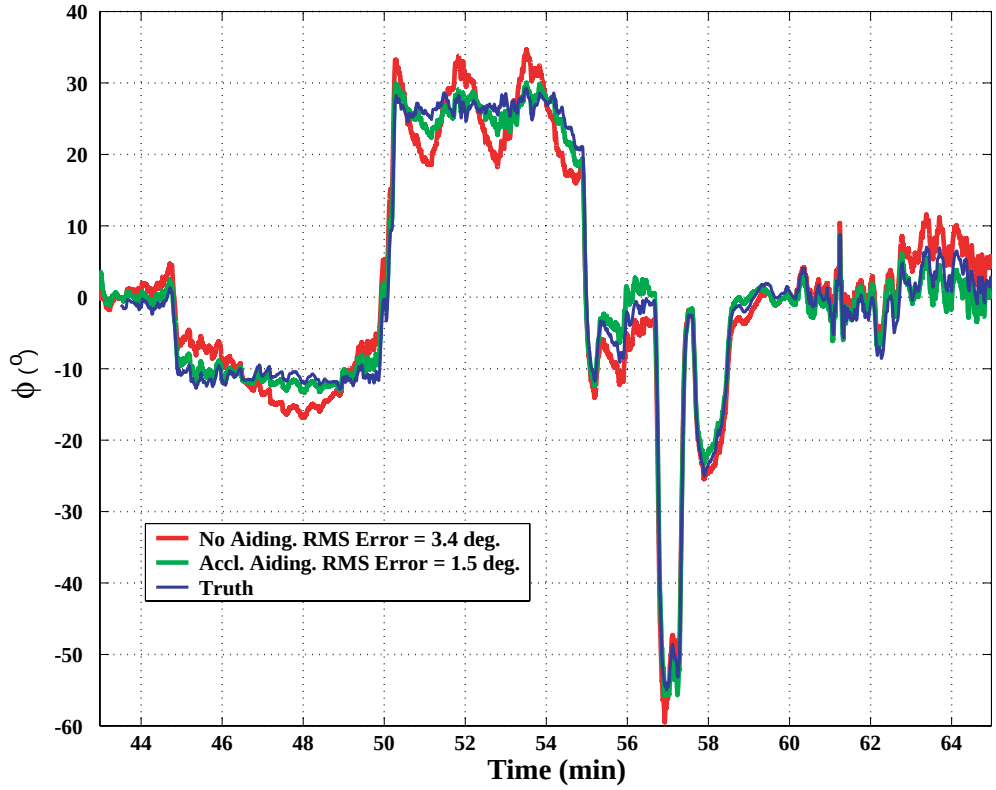

Figure 4.19: Roll Solution-FOG with Accelerometer and Magnetometer Aiding.

Chapter 5

Dead Reckoning and Inertial Navigation

5.1 Introduction

In Chapter 2, the general architecture of a backup navigator was described. The system described combined dead reckoning with intermittent position fixing. This chapter deals with the dead reckoning aspects of the navigator. The discussion begins with a general overview of dead reckoning which will be followed by a detailed discussion of the dead reckoning error equations. Next, a similar discussion for inertial navigation is presented. The chapter will close with the results of a trade-off study evaluating the expected navigation accuracy of dead reckoning and inertial navigation systems as a function of sensor quality.

5.2 Overview of Dead Reckoning and Inertial Navigation

Dead reckoning is a form of navigation where the current position of a moving vehicle is deduced by knowing speed and direction of travel since the last known position. The origin of the term dead reckoning is not clear. One of the popular explanations for the term is that it is a shortened version of the word "deduced reckoning"[45]. Another explanation is that it originated from the nautical practice of "reckoning" (or reasoning) one's position by observing motion with respect to something "dead"

in the water. Regardless of the origins of the term "dead reckoning," the technique has been used in navigation for centuries. The primary advantage of dead reckoning is that it relies on sensors contained within the vehicle.

Inertial navigation is a method whereby the current position of a vehicle is determined from a history of acceleration measurements. This is accomplished by using the well known kinematic relationships between acceleration, velocity and position. That is, acceleration measurements are integrated once to yield velocity and the computed velocity is integrated once again to yield position. One of the important advantages of inertial navigation systems is that they require no interaction with the world outside of the vehicle. A self-contained navigator such as this is desirable especially to military users where outside aiding cannot be relied upon or for oceanic navigation where aiding sources are scarce.

All navigation techniques can be viewed as processes in which the mathematical operation of integration is performed on the sensor outputs to yield position. This view of navigation is summarized in Figure 5.1. In position fixing systems, such as GPS, VOR and DME, there are no (or zero) integrations required to convert sensor measurements into a position solution. In dead reckoning, only a single integration of sensor outputs is required. In inertial navigation systems, two to three integrations are required to get from sensor outputs to a position solution. This is the major disadvantage of dead reckoning and inertial navigation; the fact that one or more integrations are required to convert sensor outputs to a position solution means that errors in sensor outputs lead to position errors that grow with time. In the following sections, dead reckoning and inertial navigation systems will be discussed. This discussion will include mechanization and error growth characteristics of these navigation systems.

5.3 Dead Reckoning

The oldest and simplest way of implementing a dead reckoning navigator is by using speed and heading measurements. The idea of dead reckoning using speed and heading measurements is simply this: Given a measurement of heading and speed, use the heading measurement to resolve speed into north-south and east-west velocity

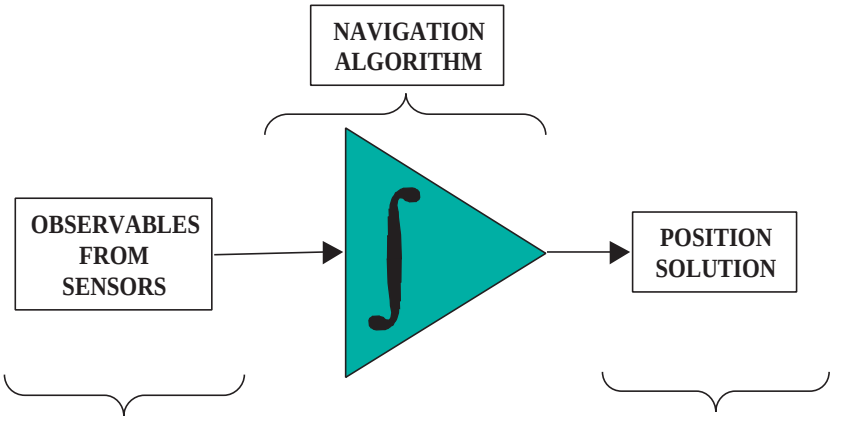

System	Integrations	Error Growth
GPS, VOR, DME	0	None
Heading & Velocity Dead-Reckoning	1	t
Inertial Navigation	2 & 3	t^2 & t^3

Figure 5.1: Navigation Systems as Integration Processes.

components. By integrating the resolved velocity components once, north-south and east-west positions are obtained. This idea is shown graphically in Figure 5.2 on page 155. In aviation applications the speed measurements are obtained from an air speed sensor or a Doppler radar. Heading information is obtained from an Attitude Heading Reference System (AHRS) or a compass while altitude information is obtained from a barometric altimeter.

5.3.1 Basic Navigation Equations

The basic navigation equation used in dead reckoning systems is the following:

$$\vec{p}(t) = \int_0^t \vec{v}(\tau)\, d\tau. \tag{5.1}$$

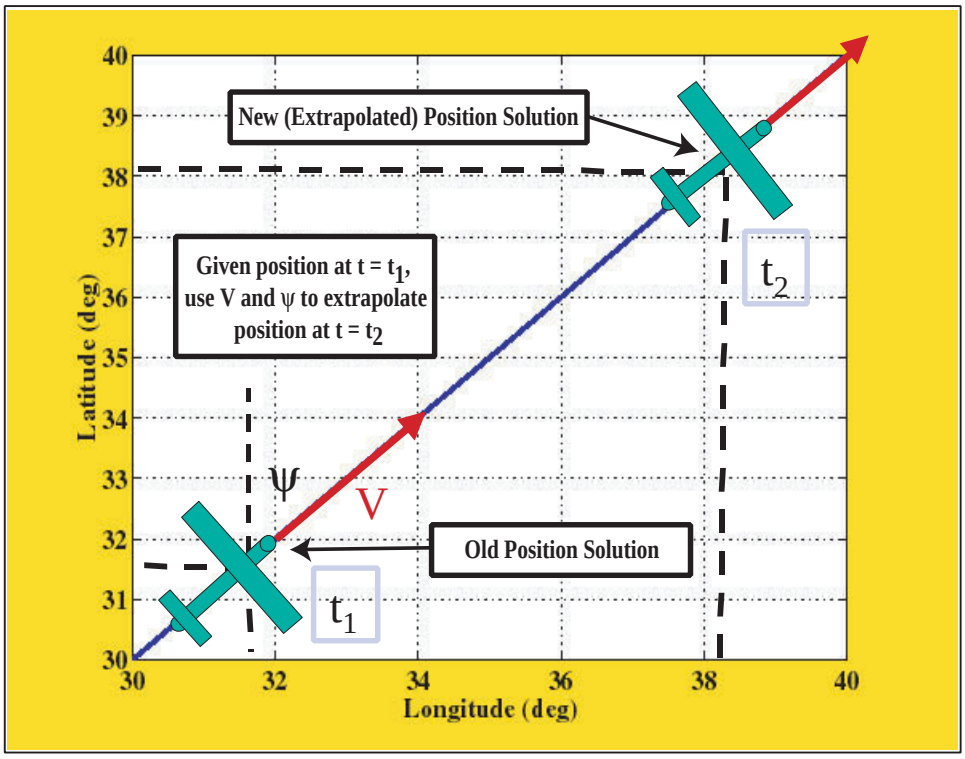

Figure 5.2: Dead Reckoning Based on Speed and Heading Measurements.

This is a vector equation which has as an input velocity vector, $\vec{v}(t)$. The entries of this vector are the north, east and down velocity components. That is,

$$\vec{v} = \begin{bmatrix} V_N \\ V_E \\ V_D \end{bmatrix}. \tag{5.2}$$

The output is position vector, $\vec{p}$. In NED coordinates, $\vec{p}$ is written as:

$$\vec{p} = \begin{bmatrix} p_n \\ p_e \\ h \end{bmatrix}. \tag{5.3}$$

The variables p_n, p_e and h are the north, east and altitude coordinates, respectively. If the geodetic coordinates of latitude (Λ), longitude (λ) and altitude (h) are being used, the position vector, $\vec{p}$, becomes:

$$\vec{p} = \begin{bmatrix} \Lambda \\ \lambda \\ h \end{bmatrix}. \tag{5.4}$$

It is easier to mechanize the navigation equations in NED coordinates. However, position in the form of the geodetic coordinates is more meaningful to a user. Therefore, these two position coordinates are used interchangeably in dead reckoning.

A dead reckoning system can be mechanized in the NED coordinate frame where the variables computed by the system are the horizontal position and velocity while vertical position (altitude) and vertical speed are measured directly using other sensors. In this case, the navigation equations that have to be solved are those describing the time evolution of the horizontal position coordinates only. Accordingly, the velocity vector is resolved into its two horizontal components in NED coordinates where the north component of velocity becomes:

$$V_{North}(t) = V_N = V\cos(\psi). \tag{5.5}$$

The variable, V, is the speed measurement and ψ is heading. Similarly, the east component is given by:

$$V_{East}(t) = V_E = V\sin(\psi). \tag{5.6}$$

Thus, with an initial position estimate, these two components of velocity can be integrated to yield latitude and longitude. Specifically, given the north-south component of velocity, latitude (Λ) is obtained from the following integral equation [65]:

$$\Lambda(t) = \int_{t1}^{t2} \left(\frac{\partial \Lambda}{\partial t}\right) dt = \int_{t1}^{t2} \left(\frac{V_{North}}{R_{NS} - h}\right) dt. \tag{5.7}$$

Similarly, the longitude (λ) is given by:

$$\lambda(t) = \int_{t1}^{t2} \left(\frac{\partial \lambda}{\partial t} \right) dt = \int_{t1}^{t2} \left(\frac{V_{East}}{(R_{EW} - h)\cos(\Lambda)} \right) dt. \tag{5.8}$$

In the above equations, h is altitude. Since a North-East-Down coordinate system is being used, h is negative for altitudes above the reference ellipsoid. Furthermore, since an ellipsoid Earth model is assumed, the north-south and east-west radii of curvature for Earth will not be the same. That is why in the equations above, two variables are used to describe Earth's radius of curvature. The variable, R_{NS}, is the radius of curvature in the north-south direction and a relatively accurate mathematical model for it is given by the following [65]:

$$R_{NS} = R_0(1 + f(3\sin^2(\Lambda) - 2)). \tag{5.9}$$

The variable, R_{EW}, is Earth's radius of curvature in the north-south direction given by:

$$R_{EW} = R_0(1 + f\sin^2(\Lambda)). \tag{5.10}$$

The variable f in the above equations is the flattening of Earth. The variable R_0 is the equatorial radius of Earth. The values for these variables are obtained from [58] and are:

$$\begin{aligned} f &= 1/298.257223563 \\ R_0 &= 6378137.0 \text{ metres.} \end{aligned}$$

5.3.2 Dead Reckoning Error Equations

Mechanizing a dead reckoning navigation system yielded navigation equations that are non-linear. There are instances where these non-linear equations have to be linearized. A case in point is the implementation of a Kalman Filter for aiding a dead reckoning navigator. Another instance is when performing a covariance analysis to assess the performance of a dead reckoning system. A covariance analysis is the basis for the trade-off study at the end of this chapter evaluating the position solution errors

of a dead reckoning navigator as a function of sensor and initial condition errors.

Linearizing the dead reckoning equations yields a dynamic system with the following error state vector, $\delta\vec{x}_{DR}$:

$$\delta\vec{x}_{DR} = \begin{bmatrix} \delta p_n & \delta p_e & \delta h & \delta V_{NS} & \delta V_{EW} & \delta\psi & \delta V \end{bmatrix}^T. \tag{5.11}$$

The first two entries of the state vector, $\delta\vec{x}_{DR}$, are the north and east position errors, respectively. The third entry, δh, is the altitude error. The entries δV_{NS} and δV_{EW} are the north-south and east-west wind errors. The sixth entry in the state vector is $\delta\psi$, which represents the heading error. The final entry in the state vector is δV and is the speed sensor error.

The dynamic system for propagating the error state vector, $\delta\vec{x}_{DR}$, is written as:

$$\delta\dot{\vec{x}}_{DR} = F_{DR}\delta\vec{x}_{DR} + \Gamma\vec{w}_{DR}. \tag{5.12}$$

The variable F_{DR} represents the dynamic matrix, $\vec{w}_{DR}$ is the process noise vector and Γ is the process noise input matrix which maps the process noise vector into the time rate of change of the the state vector. In the following sections, each of these variables will be described in detail.

The Dynamic Matrix, F_{DR}

The matrix F_{DR} describes the dynamics of the navigation state errors in $\delta\vec{x}_{DR}$ and is given by:

$$F_{DR} = \begin{bmatrix} 0 & 0 & 0 & 1 & 0 & -V\sin(\psi) & \cos(\psi) \\ 0 & 0 & 0 & 0 & 1 & V\cos(\psi) & \sin(\psi) \\ 0 & 0 & -\frac{1}{\tau_h} & 0 & 0 & 0 & 0 \\ 0 & 0 & 0 & -\frac{1}{\tau_{NS}} & 0 & 0 & 0 \\ 0 & 0 & 0 & 0 & -\frac{1}{\tau_{NS}} & 0 & 0 \\ 0 & 0 & 0 & 0 & 0 & -\frac{1}{\tau_\psi} & 0 \\ 0 & 0 & 0 & 0 & 0 & 0 & -\frac{1}{\tau_V} \end{bmatrix}. \tag{5.13}$$

Error State	Model Parameters		
	σ_{markov}	τ	White Noise
Altitude (δh)	23 m	400 sec	None
Wind (δV_{NS}, δV_{EW})	5 m/s	400 sec	None
Heading ($\delta\psi$)	2.5 deg	120 sec	0.8 deg
Air Speed (δV)	2.6 m/s (5 knots)	400	None

Table 5.1: Sensor Error Models Used in Dead Reckoning System Covariance Analysis.

Except for the first two rows (which describe the dynamic model for δp_n and δp_e), all the entries in F_{DR} are seen to be the sensor error models derived in Chapter 3 and restated in Table 5.1. It will be remembered that, in Chapter 3, these sensor errors were modeled as Gauss-Markov processes with an additive white noise component. That is, the i^{th} error state (excluding δp_n and δp_e) is mathematically modeled as

$$\delta x_i = \delta x_{i,\,white} + \delta x_{i,\,markov} \tag{5.14}$$

$$\delta \dot{x}_{i,\,markov} = -\frac{1}{\tau_i}\delta x_{i,\,markov} + w_{i-3}, \tag{5.15}$$

where the index i has values between 3 and 7 and w_{i-1} is the appropriate entry from the process noise vector which is described in detail below. Once again it should be noted that σ_i and τ_i provide a complete description of these error models because the power spectral density of w_{i-1} is related to the standard deviation, σ_i, and time-constant, τ_i, of δx_i. Thus, in order to complete the description of F_{DR}, the error equations for the remaining two variables, δp_n and δp_e, will be derived.

Error equations for δp_n and δp_e are obtained by performing a perturbation analysis on the dead reckoning equations derived in Section 5.3.1. A perturbation of the north velocity expression (Equation 5.5) results in the following:

$$\delta V_N = \delta V \cos(\psi) - V \sin(\psi)\delta\psi. \tag{5.16}$$

A similar perturbation of the east velocity expression given by Equation 5.6 results in the following:

$$\delta V_E = \delta V \sin(\psi) + V \cos(\psi)\delta\psi \tag{5.17}$$

Up till this point it has been assumed that V represented the speed of the vehicle with respect to the ground. These equations have to be slightly modified in the case where the vehicle is an airplane and the speed measurement, V, is derived from an air speed sensor. The air speed sensor measures the airplane's speed relative to the air mass in which it is flying. If the air mass is also moving with respect to the ground below it, then the speed at which it is moving must be included into Equations 5.5 and 5.6. When wind motion is accounted for, the following equations are obtained:

$$V_{North} = V\cos(\psi) + V_{NS} \tag{5.18}$$

$$V_{East} = V\sin(\psi) + V_{EW} \tag{5.19}$$

In the above equations wind motion has been accounted for by decomposing the movement of the air mass into its north-south component, V_{NS}, and east-west component, V_{EW}. Carrying out a perturbation and using the notation of δV_{NS} and δV_{EW} for the north-south and east-west wind velocity errors, respectively, results in the following modified form of Equations 5.16 and 5.17:

$$\delta\dot{p}_n = -V\sin(\psi)\delta\psi + \cos(\psi)\delta V + \delta V_{NS} \tag{5.20}$$

$$\delta\dot{p}_e = V\cos(\psi)\delta\psi + \sin(\psi)\delta V + \delta V_{EW} \tag{5.21}$$

This completes the derivation of the dynamic equations for δp_n and δp_e and the description of the dynamic matrix, F_{DR}.

If F_{DR} is to be constructed using latitude and longitude errors, $\delta\Lambda$ and $\delta\lambda$, instead of δp_n and δp_e, then the necessary error equations are derived by a perturbation of Equations 5.7 and 5.8. When the latitude rate equation is perturbed, it yields:

$$\delta\dot{\Lambda} = \frac{\delta V_N}{(R_{NS} - h)} + \frac{V_N\delta h}{(R_{NS} - h)^2}. \tag{5.22}$$

A similar perturbation of the longitude rate equation gives:

$$\delta\dot{\lambda} = \frac{\delta V_E}{(R_{EW} - h)\cos(\Lambda)} + \frac{V_E\delta h}{(R_{EW} - h)^2\cos^2(\Lambda)} + \frac{V_E\sin(\Lambda)\delta L}{(R_{EW} - h)\cos^2(\Lambda)}. \tag{5.23}$$

When Equations 5.16 and 5.17 are substituted into the perturbation equations for

the latitude and longitude rates, respectively, the latitude rate perturbation becomes:

$$\delta\dot{\Lambda} = \frac{\cos(\psi)\delta V}{(R_{NS}-h)} - \frac{V\sin(\psi)\delta\psi}{(R_{NS}-h)} + \frac{V\cos(L)\delta h}{(R_{NS}-h)^2}. \tag{5.24}$$

Similarly, the longitude rate perturbation becomes:

$$\begin{aligned}\delta\dot{\lambda} = &\frac{\sin(\psi)\delta V}{(R_{EW}-h)\cos(\Lambda)} - \frac{V\cos(\psi)\delta\psi}{(R_{EW}-h)\cos(\Lambda)} \\ &+\frac{V\sin(L)\delta h}{(R_{EW}-h)^2\cos(\Lambda)} + \frac{V\sin(\psi)\sin(L)\delta L}{(R_{EW}-h)\cos^2(\Lambda)}.\end{aligned} \tag{5.25}$$

The latitude error, $\delta\Lambda$, is related to the north-south position error, δp_n, while longitude error, $\delta\lambda$, is related to the east-west position error, δp_e. The relationship between the position error variables is given by the following relations:

$$\delta p_n = (\delta L)\, R_{NS}. \tag{5.26}$$

$$\delta p_e = (\delta\lambda)\, R_{EW}\cos(\Lambda). \tag{5.27}$$

These relationships will be used when mechanizing an estimator that blends the dead reckoning position solution with DME based position fixing.

The Process Noise Vector, $\vec{w}_{DR}$

The disturbances that drive the navigation error states are the errors in the baro-altitude, heading and air speed measurements which are the result of stochastic variations in the output of sensors (i.e., sensor output instabilities). An additional driving noise is the stochastic variation of the air mass velocity. Thus, the driving process noise vector is:

$$\vec{w}_{DR} = \begin{bmatrix} n_\psi & w_h & w_{NS} & w_{EW} & w_\psi & w_V \end{bmatrix}^T. \tag{5.28}$$

The first entry in $\vec{w}_{DR}$ is n_ψ and is the wide band noise on the heading measurement. The remaining entries are the process noise entries that drive the sensor and wind error models. In actual implementation or performance analysis of a navigator, the covariance of $\vec{w}_{DR}$ and its associated power spectral density matrix are used. This

matrix is defined as:

$$R_w = \mathcal{E}\{\vec{w}_{DR}\vec{w}_{DR}\}. \tag{5.29}$$

The symbol $\mathcal{E}$ is the expectation operator. The power spectral density matrix of R_w is denoted R_{wpsd} and is defined as:

$$R_{wpsd} = \begin{bmatrix} \sigma^2_{n_\psi} & 0 & 0 & 0 & 0 & 0 \\ 0 & 2\frac{\sigma^2_h}{\tau_h} & 0 & 0 & 0 & 0 \\ 0 & 0 & 2\frac{\sigma^2_{V_{NS}}}{\tau_{NS}} & 0 & 0 & 0 \\ 0 & 0 & 0 & 2\frac{\sigma^2_{V_{EW}}}{\tau_{EW}} & 0 & 0 \\ 0 & 0 & 0 & 0 & 2\frac{\sigma^2_\psi}{\tau_\psi} & 0 \\ 0 & 0 & 0 & 0 & 0 & 2\frac{\sigma^2_V}{\tau_V} \end{bmatrix}. \tag{5.30}$$

$\sigma_{\psi w}$ is the standard deviation of the wide-band noise on the heading measurement and is listed in Table 5.1. The remaining σ entries are the standard deviations of the Gauss-Markov components of the error models and are also listed in Table 5.1 under the column "σ_{markov}." Since the sensor and wind errors are modeled as Gauss-Markov processes, the power spectral density, Q_i, of the i^{th} component of $\vec{w}_{DR}$ is related to the variance and time constant of its respective Gauss-Markov process. This relationship is derived in [35] and is given by:

$$Q_i = 2\frac{{\sigma^2}_i}{\tau_i}. \tag{5.31}$$

The Process Noise Mapping Matrix, Γ

The matrix Γ that maps the process noise vector, $\vec{w}$, into the dead reckoning system error state, δx_{DR}, is given by:

$$\Gamma = \begin{bmatrix} 0 & 0 & 0 & 0 & 0 & 0 \\ 0 & 0 & 0 & 0 & 0 & 0 \\ 0 & 1 & 0 & 0 & 0 & 0 \\ 0 & 0 & 1 & 0 & 0 & 0 \\ 0 & 0 & 0 & 1 & 0 & 0 \\ 1 & 0 & 0 & 0 & 1 & 0 \\ 0 & 0 & 0 & 0 & 0 & 1 \end{bmatrix}. \tag{5.32}$$

From Γ it is seen that the driving noises on heading include both a wide-band and a correlated noise component (i.e., 1s in the first and fifth columns). All the other error states are driven by an exponentially correlated noise.

5.4 Inertial Navigation

The fundamental principle behind inertial navigation is that of determining the position of a vehicle from a time history of acceleration measurements. In mathematical terms this can be expressed simply as:

$$\vec{p}(t) = \int_0^t \int_0^\tau \vec{a}\,(\tau) d\tau\, dt. \tag{5.33}$$

The acceleration history is measured by accelerometers fixed or strapped in the body of the vehicle in conjunction with gyros to yield orientation of the accelerometers. In Chapter 3 it was shown that the output of accelerometers is not error free. This fact and Equation 5.33 point out the greatest short-coming of inertial navigation; position errors are a function of time, t, and become larger the longer the inertial navigator operates. In particular, small accelerometer errors will be integrated twice and lead to position errors that grow as a function of t^2.

This t^2 drift would be the primary time dependent error if the exact orientation of

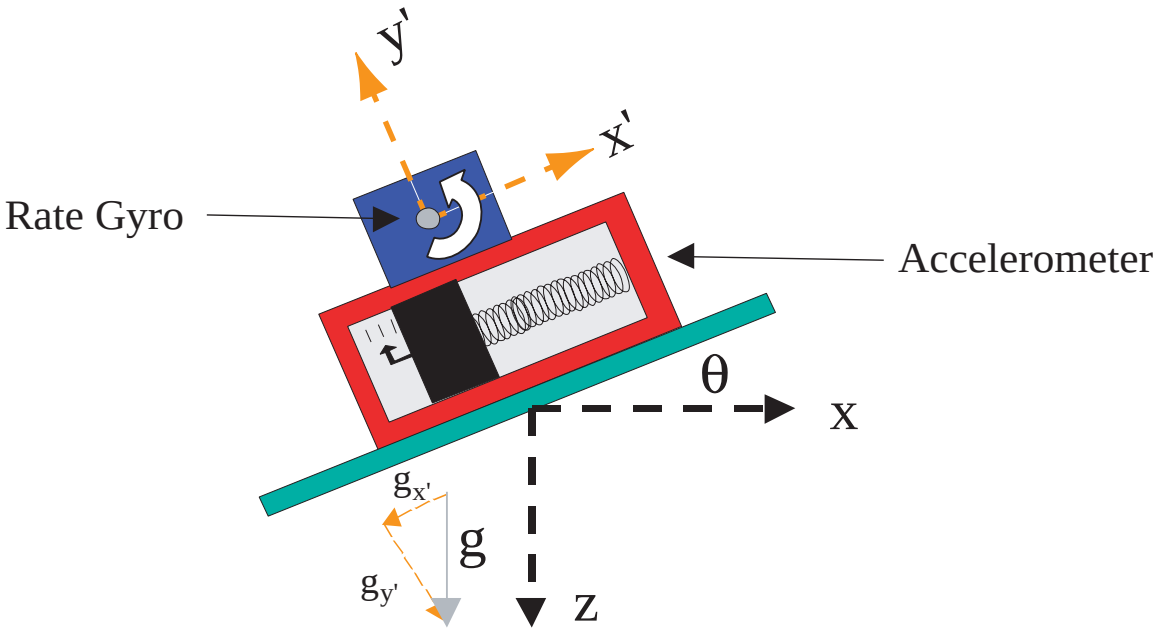

Figure 5.3: A One Dimensional Inertial Navigator.

the accelerometers' sensing axes with respect to the navigation frame were known at all times. Because of rate gyro drift, however, this orientation is not known precisely and leads to position errors that grow in proportion to t^3. This can be shown by considering the simple, one-dimensional example shown in Figure 5.3. In this instance an inertial navigator is mechanized using a single accelerometer and rate gyro. The navigator is used to determine displacement along the x-axis. θ is the navigator's attitude which is the orientation of the accelerometer's sensing axis with respect to the x-axis. It is determined by integrating the rate gyro output ω.

Assume that the accelerometer is initially perfectly level (i.e., $\theta = 0$) and error free. In the presence of a constant uncompensated gyro drift, $\delta\omega$, the attitude error, $\delta\theta$, after a period of time, t, would be given by:

$$\delta\theta = \delta\omega\, t. \tag{5.34}$$

The discussion associated with Equation 3.1 in Chapter 3 indicated that an accelerometer is actually a specific force measuring device. It cannot distinguish the difference between actual acceleration and gravitational mass attraction. Thus, the attitude error, $\delta\theta$, will lead to a portion of the local gravitational acceleration, g, being sensed by the accelerometer. This is an acceleration error, δa, given by:

$$\begin{aligned} \delta a &= g \sin(\delta\theta) \\ &= g \sin(\delta\omega\, t) \approx g\delta\omega\, t. \end{aligned} \tag{5.35}$$

This is an acceleration error which will be integrated twice and lead to a position error proportional to t^3.

Another source of error in inertial navigation is associated with the computation of the local gravitational acceleration vector, $\vec{g}$. This error, denoted $\delta\vec{g}$ (see page 236 in Appendix A) is a function of latitude and altitude errors. As noted earlier (Chapter 3, page 39) an accurate value of $\vec{g}$ at the current location of the INS is an important input into the inertial navigation equations. Errors in the the knowledge of the current location of the inertial navigator lead to errors in $\vec{g}$ which, in turn, lead to acceleration errors. In particular, errors in the knowledge of the altitude are significant in that they lead to the well known vertical channel instability problem. The INS error equations that are derived in Appendix A and will be discussed in subsequent sections will include this effect. However, since the navigators discussed in this thesis derive altitude information from baro-altimeters or, when available, GPS, the INS vertical channel is suppressed and the vertical channel instability is not a problem.

5.4.1 Basics Equations of Inertial Navigation

In the analysis contained in this thesis, the inertial navigation problem is mechanized in NED coordinates. The derivation of the functional relationship between position in NED coordinates and acceleration measured in the body axes can be found in most standard texts on inertial navigation such as [65]. This functional

relationship is:

$$\dot{\vec{p}} = \vec{v} \tag{5.36}$$

$$\dot{\vec{v}} = \overset{b\to n}{C}\,\vec{f} - (2\vec{\Omega}_e + \vec{\rho}) \times \vec{v} + \vec{g} \tag{5.37}$$

The direction cosine matrix, $\overset{b\to n}{C}$, in Equation 5.37 that transforms the specific force measurements from the body coordinate system to the navigation coordinate system must be known to carry out the integral relating velocity to position. The detail of how this matrix is computed from rate gyro and accelerometer measurements was the subject of Chapter 4.

5.4.2 Inertial Navigation Error Equations

The error equations for an Inertial Navigation System (INS) are derived by perturbation of Equations 5.36 and 5.37. This perturbation involves lengthy algebra which will not be derived here. The details of this perturbation analysis can be found in Appendix A and only the results of this analysis are given here. The error state vector for an INS is given by:

$$\delta\vec{x}_{INS} = \left[\begin{array}{ccccc} \delta\vec{p} & \delta\vec{v} & \delta\vec{\epsilon} & \delta\vec{f} & \delta\vec{\omega} \end{array}\right]^T. \tag{5.38}$$

The first entry of the state vector in Equation 5.38 is the position error vector. This vector is composed of the latitude, longitude and altitude errors. The second entry is the velocity error vector in NED coordinates. The third entry includes the attitude or tilt errors. These errors represent the rotation or deviation of the navigation frame from the locally level tangent frame. This rotation or deviation is caused by rate gyro errors. The final two entries are the specific force error and rotation rate error vectors. These are the output errors of the accelerometer triad and the rate gyro triad expressed in body coordinates.

The dynamics of the state vector, $\delta\vec{x}_{INS}$, can be cast in a form similar to that of Equation 5.12. In this case, the dynamic equation becomes:

$$\delta\dot{\vec{x}}_{INS} = F_{INS}\delta\vec{x}_{INS} + \Gamma\vec{w}_{INS}. \tag{5.39}$$

The Dynamics Matrix, F_{INS}

The matrix F_{INS} is a partitioned 15×15 matrix which can be written as:

$$F_{INS} = \begin{bmatrix} P2P & V2P & A2P & S2P & G2P \\ P2V & V2V & A2V & S2V & G2V \\ P2A & V2A & A2A & S2A & G2A \\ P2S & V2S & A2S & S2S & G2S \\ P2G & V2G & A2G & S2G & G2G \end{bmatrix} \tag{5.40}$$

Each entry of this matrix is a 3×3 matrix. The symbols P, V, A, S, and G stand for position, velocity, attitude, specific force and gyro (or angular rate), respectively. The notation P2P means "position to position", V2P means "velocity to position", and so on. Thus, the matrix $V2P$ describes the mapping of velocity errors into position errors. Each 3×3 matrix is a function of the position, velocity and attitude. All the non-zero 3×3 matrices are defined below.

The position-to-position error mapping matrix, $P2P$, is given by the following matrix:

$$P2P = \begin{bmatrix} 1 & 0 & \frac{-V_N}{(R_{NS}-h)^2} \\ \frac{V_E \sin(L)}{(R_{EW}-h)\cos^2(\Lambda)} & 0 & \frac{-V_E}{(R_{EW}-h)^2\cos^2(\Lambda)} \\ 0 & 0 & 1 \end{bmatrix}. \tag{5.41}$$

The velocity-to-position error mapping matrix, $V2P$, is given by:

$$V2P = \begin{bmatrix} \frac{1}{(R_{NS}-h)} & 0 & 0 \\ 0 & \frac{1}{(R_{EW}-h)\cos(\Lambda)} & 0 \\ 0 & 0 & 1 \end{bmatrix}. \tag{5.42}$$

In the $V2P$ matrix definition above, Ω_e is the magnitude of the Earth rate vector (15.046 deg/hr). The variable, g_0, is the magnitude of the local gravitational acceleration which is latitude dependent. R_0 is the equatorial radius of Earth defined in [58] and is equal to 6378.137 km. The position-to-velocity matrix, $P2V$, is given as

follows:

$$P2V = \begin{bmatrix} -2\Omega_e V_E \cos(\Lambda) - \frac{{V_E}^2 \sec^2(\Lambda)}{R_{EW}-h} & 0 & \frac{{V_E}^2 \tan(\Lambda)}{(R_{EW}-h)^2} - \frac{V_D V_N}{(R_{NS}-h)^2} \\ 2\Omega_e(V_N \cos(\Lambda) - V_D \sin(\Lambda)) + \frac{V_E V_N \sec^2(\Lambda)}{R_{EW}-h} & 0 & -\frac{V_E V_N \tan(\Lambda)}{(R_{EW}-h)^2} - \frac{V_D V_E}{(R_{EW}-h)^2} \\ 2V_E \Omega_e \sin(\Lambda) & 0 & \frac{{V_N}^2}{(R_{NS}-h)^2} + \frac{{V_E}^2}{(R_{EW}-h)^2} + 2\frac{g_0}{R_0} \end{bmatrix}. \tag{5.43}$$

The velocity-to-velocity matrix, $V2V$, is given by

$$V2V = \begin{bmatrix} \frac{V_D}{(R_{NS}-h)} & \frac{-2V_E \tan(\Lambda)}{(R_{EW}-h)} - 2\Omega_e \sin(\Lambda) & \frac{V_N}{(R_{NS}-h)} \\ 2\Omega_e \sin(\Lambda) + \frac{V_E \tan(\Lambda)}{(R_{EW}-h)} & \frac{V_N \tan(\Lambda)}{(R_{EW}-h)} + \frac{V_D}{(R_{EW}-h)} & 2\Omega_e \cos(\Lambda) + \frac{V_E}{(R_{EW}-h)} \\ \frac{-2V_N}{(R_{NS}-h)} & \frac{-2V_E}{(R_{EW}-h)} - 2\Omega_e \cos(\Lambda) & 0 \end{bmatrix}. \tag{5.44}$$

The attitude-to-velocity matrix, A2V, is given by:

$$A2V = \begin{bmatrix} 0 & \delta\psi & -\delta\theta \\ \delta\psi & 0 & \delta\phi \\ \delta\theta & -\delta\phi & 0 \end{bmatrix}. \tag{5.45}$$

The variables $\delta\phi$, $\delta\theta$ and $\delta\psi$ are the platform tilt errors described earlier. They represent the small rotation errors of the body frame with respect to the NED navigation frame. The position-to-attitude matrix, $P2A$, is given by:

$$P2A = \begin{bmatrix} \Omega_e \sin(\Lambda) & 0 & \frac{V_E}{(R_{NS}-h)^2} \\ 0 & 0 & -\frac{V_N}{(R_{NS}-h)^2} \\ \Omega_e \cos(\Lambda) + \frac{V_E}{(R_{EW}-h)\cos(\Lambda)^2} & 0 & -\frac{V_E \tan(\Lambda)}{(R_{EW}-h)^2} \end{bmatrix}. \tag{5.46}$$

The velocity-to-attitude matrix, $V2A$ is given by:

$$V2A = \begin{bmatrix} 0 & -\frac{1}{(RNS-h)} & 0 \\ \frac{1}{(R_{NS}-h)} & 0 & 0 \\ 0 & \frac{\tan(\Lambda)}{(R_{NS}-h)} & \end{bmatrix}. \tag{5.47}$$

The specific force-to-velocity matrix, $S2V$, is nothing more than the direction cosine matrix that transforms accelerometer readings from the body coordinate to the North,

East and Down coordinate frame. It is the transpose of the matrix, $\overset{n\rightarrow b}{C}(\mathbf{q})$, defined in Equation 4.11 on page 114 of Chapter 4 and is written as:

$$S2V = \begin{bmatrix} 1-2({q_2}^2+{q_3}^2) & 2(q_1q_2+q_3q_0) & 2(q_1q_3-q_2q_0) \\ 2(q_1q_2-q_3q_0) & 1-2({q_1}^2+{q_3}^2) & 2(q_2q_3+q_0q_1) \\ 2(q_1q_3+q_2q_0) & 2(q_2q_3-q_1q_0) & 1-2({q_1}^2-{q_2}^2) \end{bmatrix}. \tag{5.48}$$

In the definition of $S2V$ above, the variables q_0 through q_3 are the attitude quaternions. The attitude-to-attitude, $A2A$, matrix is defined as:

$$A2A = -\left[\vec{\Omega}_e + \vec{\rho}\right]^{\times} = \begin{bmatrix} 0 & \Omega_{ez}+\rho_z & -(\Omega_{ey}+\rho_y) \\ -(\Omega_{ez}+\rho_z) & 0 & \Omega_{ex}+\rho_x \\ \Omega_{ey}+\rho_y & -(\Omega_{ex}+\rho_x) & 0 \end{bmatrix}. \tag{5.49}$$

The variables ρ_x, ρ_y and ρ_z are the entries of the transport rate vector in NED coordinates, $\vec{\rho}$, while the variables Ω_{ex}, Ω_{ey} and Ω_{ez} are the entries of the earth rate vector, $\vec{\Omega}_e$. That is:

$$\vec{\Omega}_e + \vec{\rho} = \begin{bmatrix} \Omega_{ex} \\ \Omega_{ey} \\ \Omega_{ez} \end{bmatrix} + \begin{bmatrix} \rho_x \\ \rho_y \\ \rho_z \end{bmatrix} = \Omega_e \begin{bmatrix} \cos(\Lambda) \\ 0 \\ -\sin(\Lambda) \end{bmatrix} + \begin{bmatrix} \dot{\lambda}\cos(\Lambda) \\ -\dot{\Lambda} \\ -\dot{\lambda}\sin(\Lambda) \end{bmatrix}. \tag{5.50}$$

The gyro-to-attitude matrix is given by $G2A$ and is identical to S2A which is nothing more than the direction cosine matrix that transforms gyro readings from the body coordinate to the North, East and Down coordinate frame. Thus, $G2A$ is written as:

$$G2A = \begin{bmatrix} 1-2({q_2}^2+{q_3}^2) & 2(q_1q_2+q_3q_0) & 2(q_1q_3-q_2q_0) \\ 2(q_1q_2-q_3q_0) & 1-2({q_1}^2+{q_3}^2) & 2(q_2q_3+q_0q_1) \\ 2(q_1q_3+q_2q_0) & 2(q_2q_3-q_1q_0) & 1-2({q_1}^2-{q_2}^2) \end{bmatrix}. \tag{5.51}$$

The specific force-to-specific force and gyro-to-gyro matrices are based on the error models derived in Chapter 3. They describe the time rate of change of the time varying portion of the sensor bias. For the accelerometers, the $S2S$ matrix is given

INS Quality	Rate Gyro			Accelerometer		
	σ_ω (deg/hr)	τ_g (sec)	$Noise$ (deg/sec)	σ_f (g)	τ_f (sec)	$Noise$ (g)
Tactical	0.35	100	0.0017	50×10^{-6}	60	50×10^{-5}
Automotive	180	300	0.05	1.2×10^{-3}	100	1×10^{-3}
Consumer	360	300	0.05	2.4×10^{-3}	100	1×10^{-3}

Table 5.2: Sensor Error Model Parameters Used in INS Covariance Analysis.

by:

$$S2S = -\frac{1}{\tau_f}\begin{bmatrix} 1 & 0 & 0 \\ 0 & 1 & 0 \\ 0 & 0 & 1 \end{bmatrix}. \tag{5.52}$$

For the gyros, the $G2G$ matrix is given by:

$$G2G = -\frac{1}{\tau_g}\begin{bmatrix} 1 & 0 & 0 \\ 0 & 1 & 0 \\ 0 & 0 & 1 \end{bmatrix}. \tag{5.53}$$

The variables τ_f and τ_g are the time constants for the time varying bias of the accelerometers and rate gyros, respectively. For clarity, they are repeated in Table 5.2.

The Process Noise Vector, $\vec{w}_{INS}$

The process noises that drive the INS error state are the rate gyro and accelerometer stochastic errors. Accordingly, the process noise vector, $\vec{w}_{INS}$, is defined as:

$$\vec{w}_{INS} = \begin{bmatrix} n_{fx} & n_{fy} & n_{fz} & n_p & n_q & n_r & w_{fx} & w_{fy} & w_{fz} & w_p & w_q & w_r \end{bmatrix}^T. \tag{5.54}$$

Consistent with the notation used in the dead reckoning error models, the "n"s in $\vec{w}_{INS}$ represent wide-band noise and the "w"s represent correlated noise. The first three entries in $\vec{w}_{INS}$, therefore, are the wide-band noise on the accelerometer specific force measurement and the following three entries are the wide-band noise on the rate

gyro outputs. Numerical values for these are obtained from the error models developed in Chapter 3. For clarity, the parameters of these error models are repeated in Table 5.2 and the wide-band noise figures are listed under the column labeled "Noise." The remaining entries are the exponentially correlated noise on the accelerometer and rate gyro outputs. They are found under the columns labeled "σ_f" and "σ_ω" in Table 5.2.

Assuming that identical accelerometers and rate gyros are used on all axes, the associated power spectral density, R_{wpsd}, can be written as a block matrix as:

$$R_{wpsd} = \begin{bmatrix} \sigma_{nf}^2 I_{3\times3} & 0_{3\times3} & 0_{3\times3} & 0_{3\times3} \\ 0_{3\times3} & \sigma_{n\omega}^2 I_{3\times3} & 0_{3\times3} & 0_{3\times3} \\ 0_{3\times3} & 0_{3\times3} & 2\frac{\sigma_f^2}{\tau_f} I_{3\times3} & 0_{3\times3} \\ 0_{3\times3} & 0_{3\times3} & 0_{3\times3} & 2\frac{\sigma_\omega^2}{\tau_\omega} I_{3\times3} \end{bmatrix}. \tag{5.55}$$

The Process Noise Mapping Matrix, Γ

The matrix Γ maps the process noise vector (which includes the accelerometer and rate gyro wide-band and exponentially correlated noises) into the the time rate of change of the state vector, $\delta\vec{x}_{INS}$. It can be written as a block matrix as follows:

$$\Gamma = \begin{bmatrix} 0_{3\times3} & 0_{3\times3} & 0_{3\times3} & 0_{3\times3} \\ S2V & 0_{3\times3} & 0_{3\times3} & 0_{3\times3} \\ 0_{3\times3} & G2A & 0_{3\times3} & 0_{3\times3} \\ 0_{3\times3} & 0_{3\times3} & S2V & 0_{3\times3} \\ 0_{3\times3} & 0_{3\times3} & 0_{3\times3} & G2A \end{bmatrix}. \tag{5.56}$$

Since the position, velocity and attitude errors that are part of $\delta\vec{x}_{INS}$ are expressed relative to the NED coordinate frame, the sensor noises have to be transformed from the body to the NED coordinate frame. The process noise mapping matrix Γ is essentially a matrix of direction cosine matrices which perform this mapping of the sensor noises.

5.5 Dead Reckoning and INS Performance Studies

The simulation studies that follow will show that unaided dead reckoning and inertial navigation systems mechanized using low performance sensors cannot be relied on as a backup navigator because they are incapable of generating an acceptably accurate position solution for an extended period of time. The simulation results also show the position errors that develop between DME range measurement updates when a DME aided dead reckoning navigator is mechanized. The analysis will be conducted using a range of sensor qualities. The results will, therefore, be a trade-off study of dead reckoning accuracy as a function of sensor quality. The sensor output errors as a function of quality were developed in Chapter 3 and for clarity are repeated in Tables 5.1 and 5.2.

5.5.1 Simulation Details

The tool that will be used for the trade-off study is a covariance analysis. For the dead reckoning system, the covariance matrix, P_{DR}, of the error state vector, $\delta\vec{x}_{DR}$, is defined as:

$$P_{DR} = \mathcal{E}\{\delta\vec{x}_{DR}\delta\vec{x}_{DR}^{T}\}. \tag{5.57}$$

The symbol $\mathcal{E}$ is the expectation operator and the diagonal elements of the matrix P_{DR} are the variances of the components of the error state vector, $\delta\vec{x}_{DR}$. With the dynamics as defined in Equation 5.12, the state error covariance can be propagated using the solution to the discrete Riccati equation [34]. Similarly, for the INS, the state error covariance matrix, P_{INS}, is defined as:

$$P_{INS} = \mathcal{E}\{\delta\vec{x}_{INS}\delta\vec{x}_{INS}^{T}\}. \tag{5.58}$$

Given the INS error dynamic model in Equation 5.39, P_{INS} is also propagated forward in time using the solution to the discrete Riccati equation.

5.5.2 Simulation Initial Conditions

For this covariance analysis, the aircraft modeled was a small General Aviation airplane (typical of an aircraft in Group E of Table 1.1). The trajectory for these simulations assumes that an aircraft is flying north ($\psi = 0°$). It is cruising wings level at a typical approach speed of 90 knots (46.3 m/s). It is at a constant altitude of 2000 feet and follows the contour of the surface of Earth which is modeled in accordance with the WGS-84 reference ellipsoid [58]. The altitude of 2000 feet was selected because it is the minimum altitude for which the wind model developed in Chapter 3 is valid.

With regard to the initial conditions for P_{DR}, the approach taken in this analysis was as follows: Given the error models developed in Chapter 3, what is the *best* performance that can be achieved when using dead reckoning and inertial navigation systems that are based on low performance sensors? Accordingly, for the dead reckoning it was assumed that all sensors were *perfectly* calibrated at the start of the covariance analysis. Furthermore, the initial wind field velocities were also assumed to be known. Thus, the resulting position errors in the dead reckoning system will be due to sensor error and stochastic changes in wind velocity only. In mathematical terms, these initial condition imply that the covariance matrix at time $t = 0$ is given by:

$$P_{DR}(t = 0) = 0_{9\times 9}. \tag{5.59}$$

Once again, the wind field was modeled using the Berman-Powell model from [14]. As was noted earlier, in this wind model, the east-west and north-south wind field velocity uncertainties are modeled as a first order Gauss-Markov process with a standard deviation of 5 m/s and a time constant of 400 seconds.

Similarly for P_{INS}, all initial sensor biases were set equal to zero. Furthermore, it was assumed that the navigator had *perfect* knowledge of initial position, velocity and attitude. Thus, the errors in position that arise from sensor instabilities only and not initial condition errors. In mathematical terms, these initial condition imply that the covariance matrix at time $t = 0$ is given by:

$$P_{INS}(t = 0) = 0_{15\times 15}. \tag{5.60}$$

It is a well known fact that, the vertical channel (i.e., V_D and h) of an unaided INS is unstable. Therefore, in these simulations the vertical channel instability is suppressed by forcing the altitude, h, to a constant and the vertical velocity, V_D, equal to zero.

5.5.3 Trade Off Study Results

Using the error models of Chapter 3 and the covariance analysis equations above, the graph shown in Figure 5.4 is generated. This figure shows the growth in the horizontal position error as function of time for inertial navigation systems made from low performance inertial sensors of varying quality. This horizontal position error is the Root Sum Square (RSS) of the P_{11} and P_{22} terms of the covariance matrix. Mathematically that is:

$$\text{Horizontal Position Error} = \sqrt{P_{11} + P_{22}} \tag{5.61}$$

In the expression above, P is either the dead reckoning error covariance matrix, P_{DR}, or the INS error covariance matrix, P_{INS}.

It is apparent from Figure 5.4 that the position error growth rate for all the classes of low cost inertial sensors is very large. From Figure 5.4 we see that the position error growth of a tactical grade inertial navigator exceeds the one half nautical mile bound (i.e, 700 m) after approximately 550 seconds. However, it continues to exceed the performance of all the other dead reckoning systems until approximately 1200 seconds. At this point the errors in the inertial navigation system begin to exceed the error of the dead reckoning system. For times beyond 1200 seconds, the heading and speed dead reckoning system is superior to all the low performance inertial navigation systems. This is because of the t^1 error growth characteristics of the heading and speed dead reckoning scheme.

Figure 5.5 is a closer look at the initial error growth rate of the various dead reckoning systems. It is important to note that the speed and heading dead reckoning scheme has a non-linear error growth rate initially. This is because the heading errors are initially those that would be available from an AHRS that is aided by GPS. When GPS services are no longer available, the heading errors grow with time for a short period. This error is integrated once to arrive at position which leads to the initial,

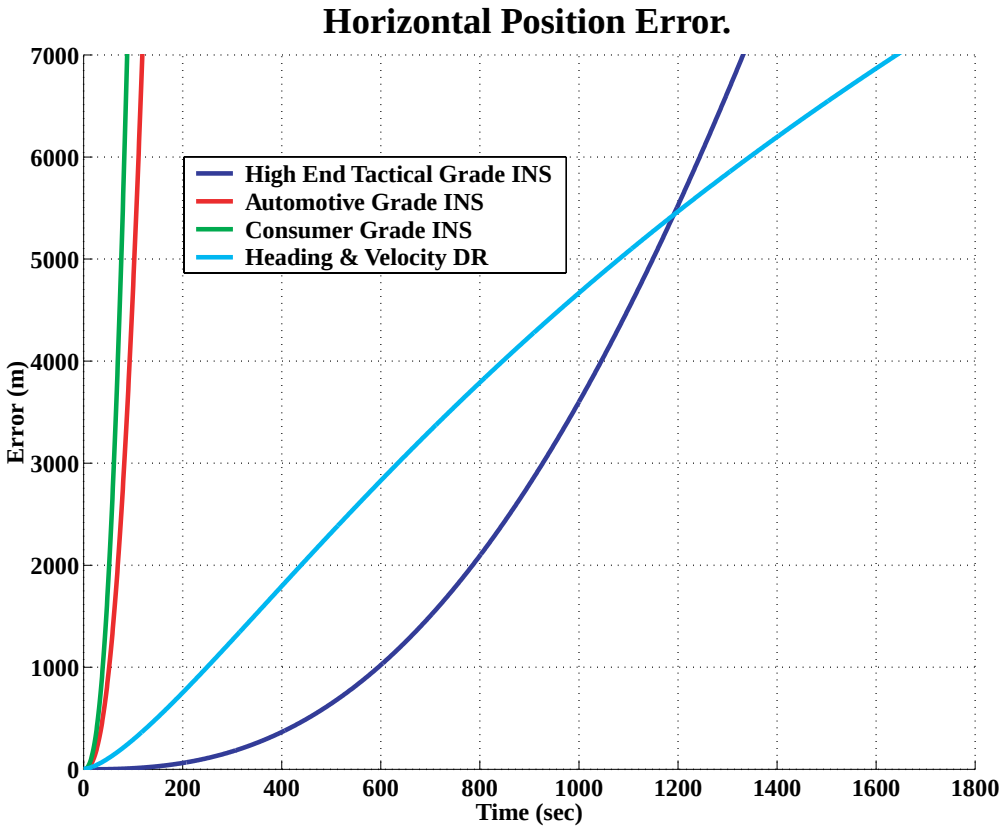

Figure 5.4: Open Loop Performance of Dead Reckoning Systems.

t-dependent, non-linear growth in position errors.

Figure 5.6 shows the contribution of the various error sources to the horizontal position errors in a speed and heading dead reckoning system. From this figure it is seen that the primary contributor to position errors is the error due to neglecting the air mass movement. If this parameter can be estimated, then the errors in a dead reckoning system can be reduced dramatically. This is the reason for integrating some form of position fixing with the dead reckoning.

Another important conclusion of this analysis is that if a tactical grade INS is affordable, it would yield better performance than a dead reckoning system for short

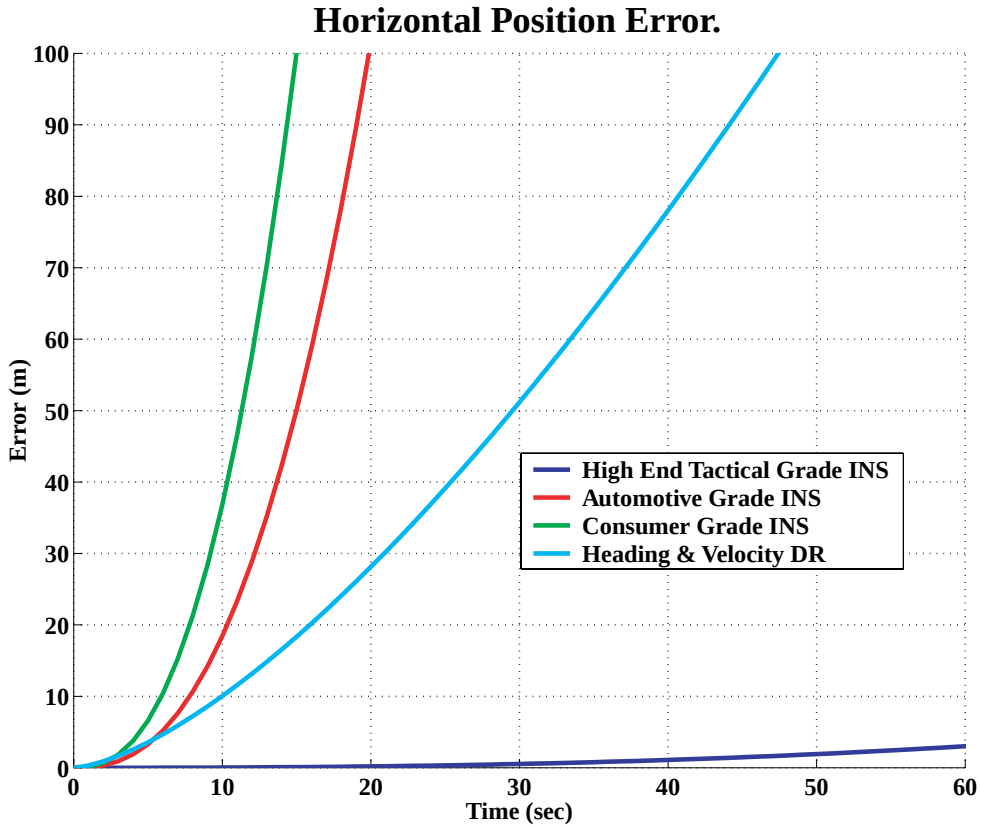

Figure 5.5: Initial Error Growth for Dead Reckoning Systems.

periods of time. However, if using the much more affordable automotive grade inertial sensors, the dead reckoning system yields a substantially superior performance. However, when operating unaided, none of the inertial navigation systems nor the dead reckoning system will provide the navigation accuracy required for the backup navigator. Furthermore, note that an aircraft traveling at the speed of 90 knots assumed in this covariance analysis will cover a distance of approximately 14 nautical miles in 550 seconds (or 9.2 minutes). Therefore, a tactical grade INS would be useful only if the area where GPS services were unavailable was within a 15 nautical mile radius of the airport of intended landing.

In closing, we note that the performance of low cost inertial sensors is constantly

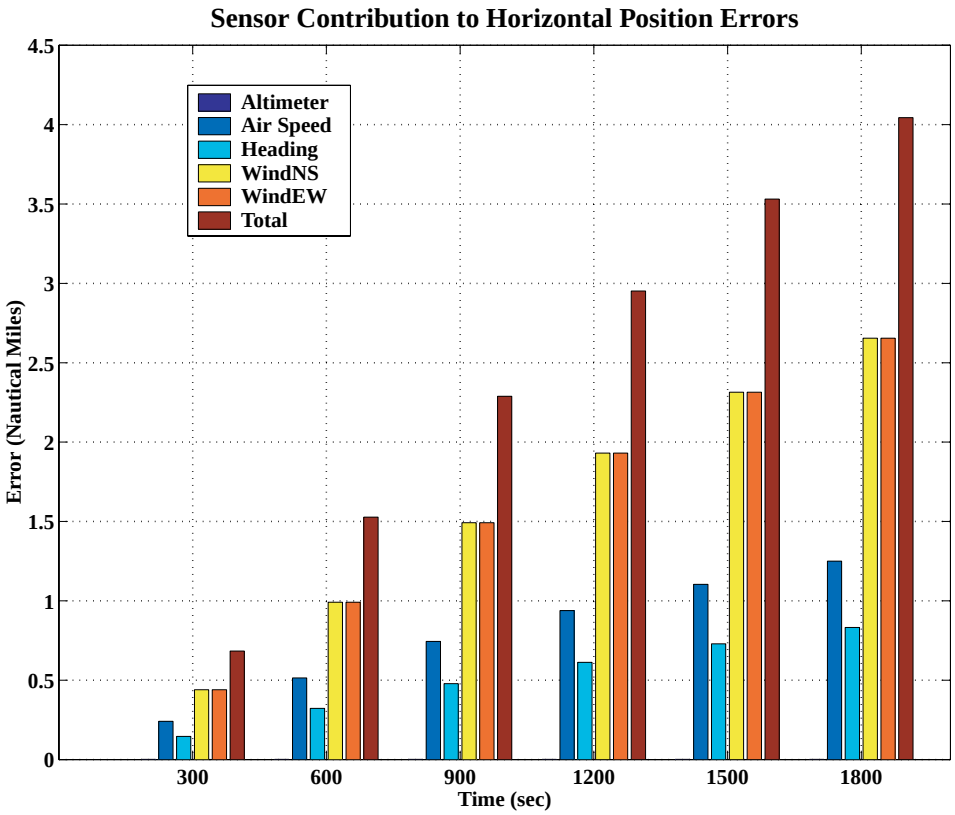

Figure 5.6: Sensor Error Budget.

improving. It is expected that inertial systems that match, if not exceed, the performance of tactical grade INSs will be readily available and affordable in the near future. At that time, the relative merits of using dead reckoning versus inertial navigation when mechanizing a low cost backup navigator will have to be reevaluated.

Chapter 6

Aided Dead Reckoning

6.1 Introduction

This chapter discusses the mechanization details of the GPS backup navigation system. As noted in Chapter 2, the proposed backup is a dead reckoning navigator aided by intermittent DME range measurements. The accuracy of an aided dead reckoning navigation system is ultimately governed by the accuracy of the aiding system. It is also a function of the method by which the aiding system's measurements are incorporated into the total navigation solution. Accordingly, a detailed discussion of position fixing based on intermittent DME range measurements will be presented. The discussion will include a detailed analysis of some observability issues associated with this method of position fixing. The chapter will close by presenting the algorithmic details for mechanizing the DME aided dead reckoning navigation system.

6.2 Dead Reckoning Aided by DME

When used alone, dead reckoning or inertial navigation systems based on low-performance sensors develop position errors in excess of the required 1/2 nautical mile in less than 30 minutes. As a matter of fact, Figure 5.4 shows that a dead reckoning system develops position errors in excess of 1/2 nautical mile in less than 7 minutes. Thus, to keep position errors bounded, dead reckoning or inertial navigation systems based on low-performance sensors have to be coupled with an aiding system.

Even though GPS has been used successfully to aid dead reckoning systems [20], it cannot be considered here because this thesis is concerned with designing a backup system for dealing with GPS outages. As was discussed in Chapter 2, in this context, DME is the logical aiding system.

Inertial navigation systems that are affordable by users in Group E of Table 1.1, will be based on either automotive or consumer grade sensors because tactical grade inertial sensors are too expensive for these users. As part of this work, a backup INS based on these low-performance sensors and DME aiding was explored. The performance of this system was found to be unsatisfactory. One of the reasons for this poor performance is the fact that reconstructing the entire fifteen-dimensional INS error state vector from intermittent DME range measurements is problematic; all the elements of the INS state vector that contribute to the position solution error are not readily observable from sporadic DME range measurements. While a backup INS using higher performance sensors coupled with frequent DME range measurements can be mechanized successfully [15], the cost and DME saturation constraints discussed earlier makes such a system impractical for Group E users.

In view of the discussion above, the logical solution for a backup navigator is a DME aided dead reckoning system. In this system, a high bandwidth navigation solution will be generated by the dead reckoning system while DME aiding will allow estimating and compensating for sensor and wind errors that would otherwise cause the dead reckoning system's lateral position solution to drift. The vertical or altitude information that can be obtained from DME position fixing is very poor. This is because DMEs are always located below an aircraft in flight and this is a poor geometry for altitude determination. This is not a problem, however, because it is highly likely that aircraft will continue to be equipped with barometric altimeters. Therefore, in the event of a GPS outage, a means for continued vertical navigation will still be available.

6.3 Observability Analysis of Intermittent Position Fixing

All that is required for lateral position fixing is range measurements from two suitably located DME transmitters. The position solution is obtained by solving Equation D.2 in Appendix D given two range measurements, R_1 and R_2. However, obtaining two simultaneous range measurements continuously in an environment where only a sparse network of DMEs exists, can lead to DME saturation. This limits the user to obtaining infrequent and sequential DME range measurements.

Using infrequent and sequential DME range measurements degrades the observability of the position fixing problem. Therefore, the main focus of this section is to identify the conditions under which this observability is lost. More precisely, the following two questions regarding the observability of the intermittent position fixing problem will be answered:

1. Firstly, under what conditions are the NED position errors, δp_n and δp_e, observable from intermittent DME range measurements? This is important because, if δp_n and δp_e are observable, then the position errors for the DME aided dead reckoning navigator are bounded.

2. Secondly, under what conditions are the sensor and wind errors observable? In Chapter 5 (Equations 5.20 and 5.21 on page 160), it was shown that the NED position error variables, δp_n and δp_e, are functions of heading error, $\delta\psi$, air speed measurement error, δV, and wind errors, δV_{NS} and δV_{EW}. The ability to estimate these sensor and wind errors will result in a navigator that provides a relatively jitter-free position solution. That is, the measurement updates from the DME will be used to correct the underlying source of the dead reckoning system's position error and not simply reset the resulting position errors periodically.

6.3.1 Observability of δp_n and δp_e

To begin this analysis, consider the position fixing problem where two simultaneous range measurements are available. For clarity and ease of notation (i.e., to

minimize the clutter with too many subscripts), for the time being the position variables p_n and p_e will be replaced by x and y respectively. Making this substitution and linearizing the fundamental position fixing relation given in Equation D.1 of Appendix D leads to:

$$\begin{bmatrix} \delta R_{1,k} \\ \delta R_{2,k} \end{bmatrix} = \begin{bmatrix} \frac{(\hat{x}_k - x_1)}{R_{1,k}} & \frac{(\hat{y}_k - y_1)}{R_{1,k}} \\ \frac{(\hat{x}_k - x_2)}{R_{2,k}} & \frac{(\hat{y}_k - y_2)}{R_{2,k}} \end{bmatrix} \begin{bmatrix} \delta x_k \\ \delta y_k \end{bmatrix} \tag{6.1}$$

$\hat{x}_k$ and $\hat{y}_k$ are the estimates (or initial guesses) of the user's lateral position coordinates at time step k; x_i and y_i where $i = 1$ or 2 are the horizontal position coordinates of the i^{th} DME; δx_k and δy_k are the differences between the actual and estimated x and y position coordinates at time step k; $R_{i,k}$ is the range to DME i at time step k; and $\delta R_{i,k}$ is the difference between the estimated and measured ranges to DME i at time step k. In a more compact matrix notation this equation can be written as:

$$\delta \vec{r}_k = H_k \delta \vec{p}_k \tag{6.2}$$

where $\delta \vec{r}_k$ is the vector of differences between the measured and estimated range to the two DME transmitters at time step k, H_k is the measurement geometry matrix at time step k, and $\delta \vec{p}_k$ is a vector of the position errors at time step k.

If the two DMEs providing the range measurements are suitably located, Equation 6.2 can be solved for the two unknown horizontal position errors. The least-squares solution for $\delta \vec{p}_k$ would be:

$$\delta \vec{p}_k = \left(H_k^T H_k\right)^{-1} H_k^T \delta \vec{r}_k. \tag{6.3}$$

An assumption built into Equation 6.2 and its solution given by Equation 6.3 is that both range measurements are obtained simultaneously at each measurement epoch. If this assumption is not valid, solving for the unknown position errors at each epoch is not possible. Instead, their value can be deduced only after measurements from both DMEs have been received. To see why this is true, consider the most basic case of this problem as shown in Figure 6.1. In this case, the position NED errors, δx and δy, are constant. Such a scenario would be present if the dead reckoning sensors were error-free and there were no winds aloft. The position error would be the result

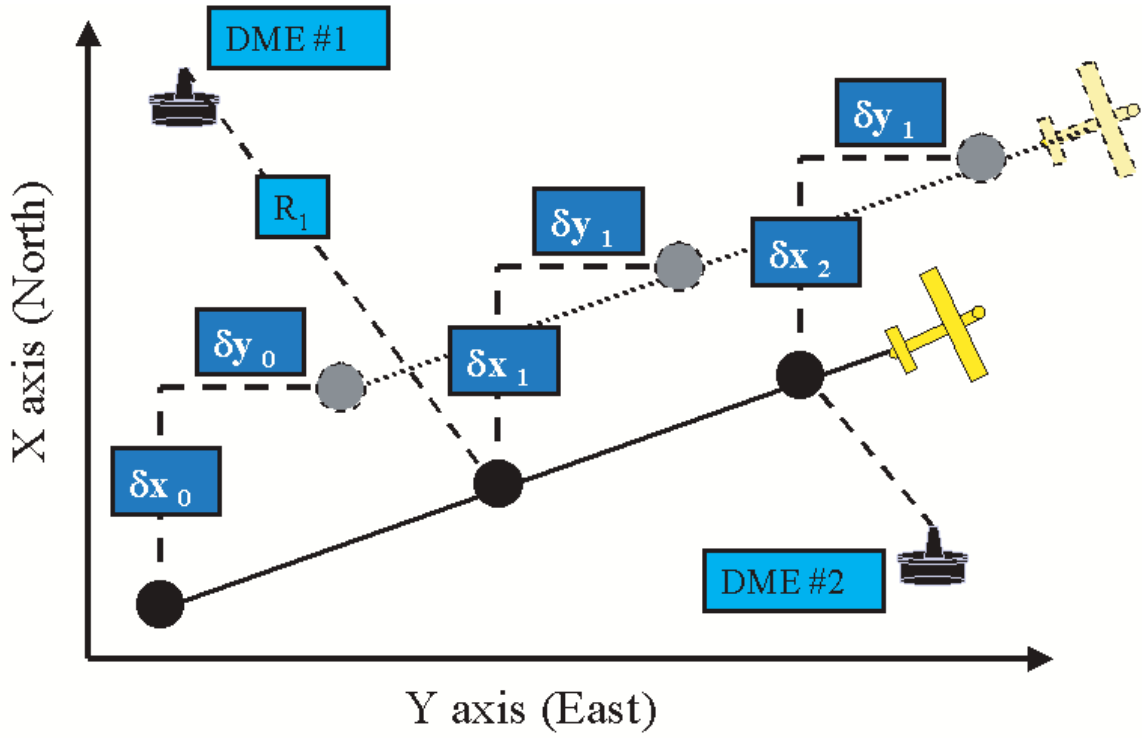

Figure 6.1: DME Position Fixing with Constant Position Errors.

of initial position errors. Mathematically, this is written as:

$$\delta x_1 = \delta x_2 = \cdots = \delta x_n = \delta x, \tag{6.4}$$

$$\delta y_1 = \delta y_2 = \cdots = \delta y_n = \delta y. \tag{6.5}$$

Since the position errors are not time varying, sufficient range measurements reduce the problem down to a simple batch least squares problem as shown in the equation below:

$$\begin{bmatrix} \delta R_{1,k} \\ \delta R_{2,k+1} \\ \vdots \\ \delta R_{i,n} \end{bmatrix} = \begin{bmatrix} \frac{(\hat{x}_k - x_1)}{R_{1,k}} & \frac{(\hat{y}_k - y_1)}{R_{1,k}} \\ \frac{(\hat{x}_{k+1} - x_2)}{R_{2,k+1}} & \frac{(\hat{y}_{k+1} - y_2)}{R_{2,k+1}} \\ \vdots & \vdots \\ \frac{(\hat{x}_n - x_i)}{R_{i,n}} & \frac{(\hat{y}_n - y_i)}{R_{i,n}} \end{bmatrix} \begin{bmatrix} \delta x \\ \delta y \end{bmatrix} \tag{6.6}$$

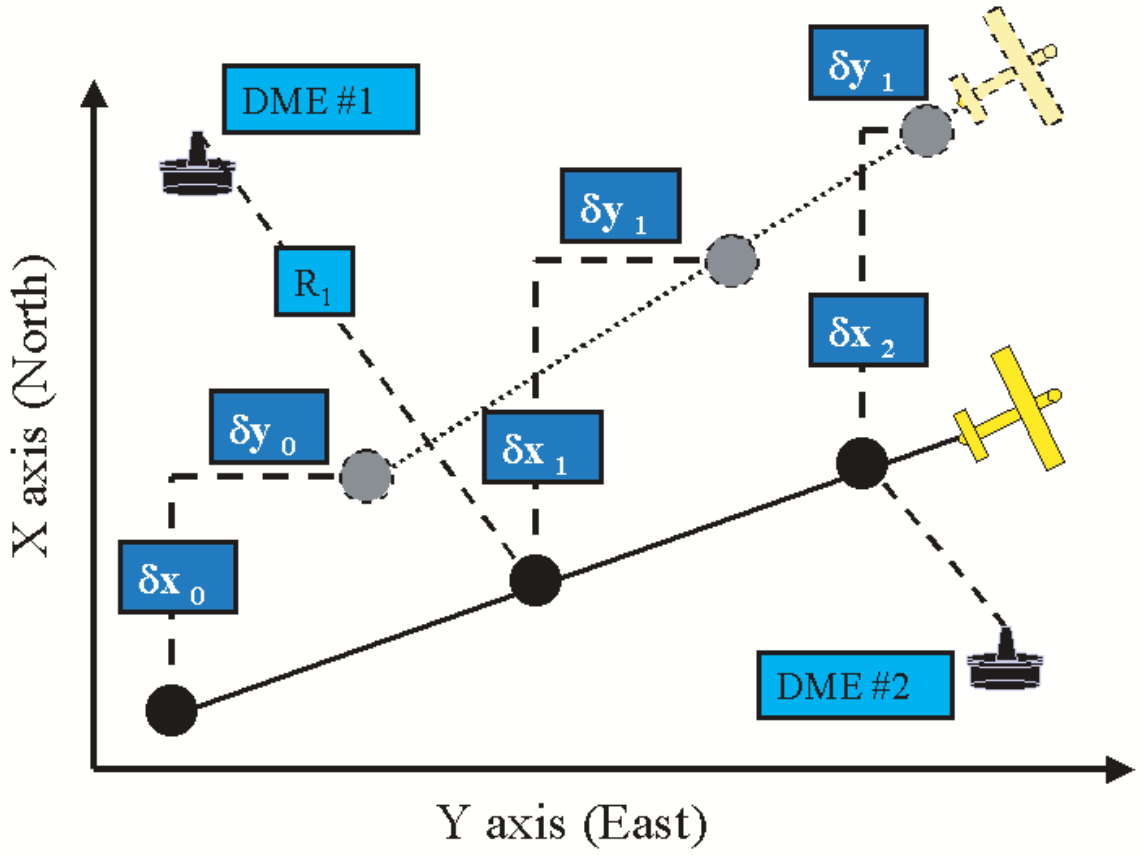

Figure 6.2: DME Position Fixing and Time Varying Position Errors.

In a real-time system, this solution can be implemented using a recursive least squares formulation as well.

This simple batch or recursive least squares solution starts falling apart when the position errors are time varying and the measurement updates are spaced far apart in time. This example arises when, in addition to initial position errors, the sensors being used for dead reckoning contain errors and wind is present. This situation of the position fixing problem is depicted in Figure 6.2. Suppose in this case the position error is modeled as a constant plus a time varying bias. The constant represents the initial position error and the time varying position bias would be due to sensor errors or wind. More specifically, if at time step k the initial x position error is δx_k, then n

time steps later the x position error can be written as:

$$\delta x_{k+n} = \delta x_k + \Delta_x(k+n) \tag{6.7}$$

where the term $\Delta_x(t)$ is a time varying error that accounts for the fact that at each measurement epoch the position error is not constant. A similar expression can be written for the y position errors. Let us define a new vector $\vec{\Delta}_p(t_k) = [\Delta_x(k)\ \Delta_y(k)]^T$. When these expressions are substituted into Equation 6.6, the batch least squares equation can be written as:

$$\begin{bmatrix} \delta R_{1,k} \\ \delta R_{2,k+1} \\ \delta R_{1,k+2} \\ \vdots \\ \delta R_{1,k+n-1} \\ \delta R_{2,k+n} \end{bmatrix} = \begin{bmatrix} H_{1,k} & 0 & 0 & \cdots & 0 & 0 \\ H_{2,k+1} & H_{2,k+1} & 0 & \cdots & 0 & 0 \\ H_{1,k+2} & 0 & H_{1,k+2} & \cdots & 0 & 0 \\ \vdots & \vdots & \vdots & \ddots & 0 & 0 \\ H_{1,k+n-1} & 0 & 0 & \cdots & H_{1,k+n-1} & 0 \\ H_{2,k+n} & 0 & 0 & \cdots & 0 & H_{2,k+n} \end{bmatrix} \begin{bmatrix} \delta\vec{p}_k \\ \vec{\Delta}_p(k+1) \\ \vec{\Delta}_p(k+2) \\ \vdots \\ \vec{\Delta}_p(k+n-1) \\ \vec{\Delta}_p(k+n) \end{bmatrix}. \tag{6.8}$$

The sub-matrices $H_{i,n}$ are the measurement geometry matrices for the i^{th} DME at time step n. We will use the notation $H_{(k)\rightarrow(k+n)}$ to denote the first column of the matrix containing the $H_{i,n}$ sub-matrices, $\tilde{H}_{(k)\rightarrow(k+n)}$ to denote the remaining columns of the matrix containing the $H_{i,n}$ sub-matrices, and $\delta R_{(k)\rightarrow(k+n)}$ to denote the right hand side of Equation 6.8. This then allows us to recast Equation 6.8 as follows:

$$\delta R_{(k)\rightarrow(k+n)} = H_{(k)\rightarrow(k+n)}\delta\vec{p}_k + \tilde{H}_{(k)\rightarrow(k+n)}\vec{\Delta}_{p_{(k)\rightarrow(k+n)}} \tag{6.9}$$

From Equation 6.9 above, some important observations about the position fixing problem can be made. Firstly, the time varying position errors behave as time varying range measurement biases. This can be seen clearly if Equation 6.9 is recast as follows:

$$\delta R_{(k)\rightarrow(k+n)} - \tilde{H}_{(k)\rightarrow(k+n)}\vec{\Delta}_{p_{(k)\rightarrow(k+n)}} = H_{(k)\rightarrow(k+n)}\delta\vec{p}_k \tag{6.10}$$

The term $\tilde{H}_{(k)\rightarrow(k+n)}\vec{\Delta}_{p_{(k)\rightarrow(k+n)}}$ is effectively a range measurement bias. If the position updating is done rapidly, $\Delta_x(k)$ and $\Delta_y(k)$ will not have a chance to grow significantly

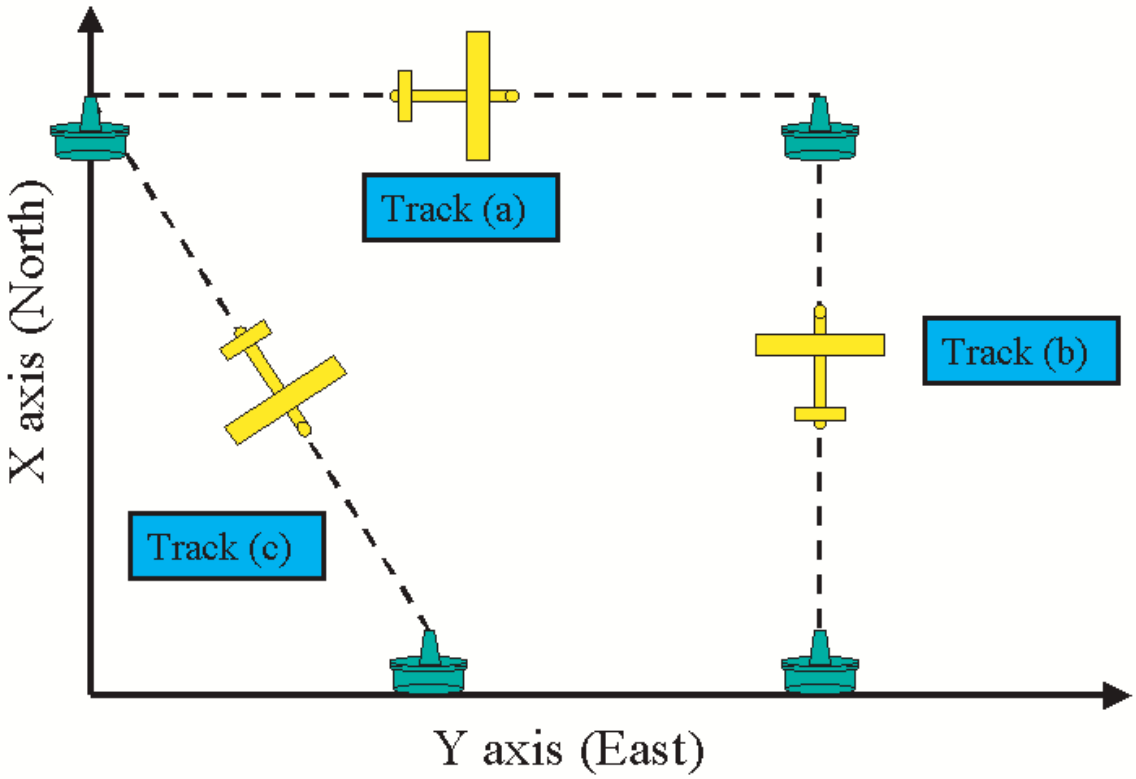

Figure 6.3: Tracks for which the Geometry Matrix is Rank Deficient.

between measurement updates and bias the range measurements. Thus, in this instance the problem has effectively become equivalent to obtaining simultaneous range measurements from two DMEs and is the case that is being solved when a scanning DME is supplying the range measurements. If the measurement update window is opened, however, it is clear that this estimation technique will fall apart.

Secondly, in most instances, the sub-matrix formed by the first two columns of the matrix $H_{(k)\rightarrow(k+n)}$ will be a full rank matrix. A quick inspection reveals the cases where $H_{(k)\rightarrow(k+n)}$ is rank deficient. These situations arise when the two DMEs being used are collinear with the track flown from time step k to $k+n$. Figure 6.3 shows the general instances where the matrix $H_{(k)\rightarrow(k+n)}$ becomes rank deficient. In the track (a) and (b) scenarios where DMEs are located in-line with the ground track flown by the airplane, $H_{(k)\rightarrow(k+n)}$ loses rank because the first or second column becomes a

column of zeros. In the track (c) scenario, again a case where the DMEs are in-line with the ground track, $H_{(k)\rightarrow(k+n)}$ loses rank because the first two columns of the matrix become linearly dependent. That is,

$$H_{(k)\rightarrow(k+n)}(:,1:2) = \begin{bmatrix} \frac{(\hat{x}_k - x_1)}{R_{1,k}} & m\frac{(\hat{x}_k - x_1)}{R_{1,k}} \\ \frac{(\hat{x}_{k+1} - x_2)}{R_{2,k+1}} & m\frac{(\hat{x}_{k+1} - x_2)}{R_{2,k+1}} \\ \vdots & \vdots \\ \frac{(\hat{x}_{k+n} - x_1)}{R_{1,k+n-1}} & m\frac{(\hat{x}_{k+n} - x_1)}{R_{1,k+n-1}} \\ \frac{(\hat{x}_{k+n} - x_2)}{R_{2,n}} & m\frac{(\hat{x}_{k+n} - x_2)}{R_{2,n}} \end{bmatrix} \tag{6.11}$$

where m is the slope of the track.

The third observation is that, as written, Equation 6.8 is under-determined. It is a system of n equations with $2n$ unknowns. If the number of unknowns in Equation 6.8 can be reduced to n or less, then it is possible to implement a batch or recursive least squares algorithm to solve for the unknowns. The number of unknowns can be reduced down to n or less by including a dynamic model for $\delta\vec{p}_k$. Perhaps one of the simplest dynamic models for $\delta\vec{p}_k$ can be constructed by noting that the time varying nature of the position errors are due to wind speed errors. Thus, the model for position error given in Equation 6.7 can be modified as:

$$\delta x_k = \delta x_0 + (\Delta T_k)(\delta V_{NS}) \tag{6.12}$$

$$\delta y_k = \delta y_0 + (\Delta T_k)(\delta V_{EW}) \tag{6.13}$$

In the above equation a simple Euler integration is assumed and ΔT_k is defined to be the integration interval. Furthermore, δV_x and δV_y are assumed to be constants (or slowly varying) over the integration interval. While air speed and heading errors also give rise to the time-varying component of $\delta\vec{p}_k$, Figure 5.6 shows that wind speed error is the largest contributor. Thus, for the time being, ignoring heading and air speed errors in this simple dynamic model is justified. When the δx_k and δy_k entries of $\delta\vec{p}_k$ in Equation 6.8 are replaced with the definitions in Equations 6.12 and 6.13, a

matrix equation of the standard linear form $\vec{y} = H\vec{x}$ results given by the following:

$$\begin{bmatrix} \delta R_{1,k} \\ \delta R_{2,k+1} \\ \delta R_{1,k+2} \\ \vdots \\ \delta R_{1,k+n-1} \\ \delta R_{2,k+n} \end{bmatrix} = \begin{bmatrix} H_{1,k} & 0 \\ H_{2,k+1} & \Delta T_{k+1} H_{2,k+1} \\ H_{1,k+2} & \Delta T_{k+2} H_{1,k+2} \\ \vdots & \vdots \\ H_{1,k+n-1} & \Delta T_{k+n-1} H_{1,k+n-1} \\ H_{2,k+n} & \Delta T_{k+n} H_{2,k+n} 0 \end{bmatrix} \begin{bmatrix} \delta x_0 \\ \delta y_0 \\ \delta V_{NS} \\ \delta V_{EW} \end{bmatrix} \tag{6.14}$$

Therefore, provided we have four independent measurements and the track and DME location geometry does not fall in any of the categories shown in Figure 6.3, the unknowns δx_0, δy_0, δV_x and δV_y are observable from Equation 6.14. The variables δx_k and δy_k are equal to δp_n and δp_e respectively. Thus, it has been demonstrated that δp_n and δp_e can be observable from intermittent DME range measurements. This, in turn, implies that the dead reckoning position errors can be bounded with intermittent range measurements.

6.3.2 Observability of Sensor Errors

For completeness, not only wind but all the factors that contribute to the position errors, δx_k and δy_k, have to be included into the dynamic models given by Equations 6.12 and 6.13. When this is done, a modified form of Equations 5.20 and 5.21 from Chapter 5 is obtained. Keeping in mind the notation change implemented earlier which substitutes x for p_n and y for p_e, the north-south position error (or δx_k) at time step $k+1$ becomes:

$$\begin{aligned} \delta x_{k+1} &= (\delta p_n)_{k+1} \\ &= \int_{t_0}^{t_{k+1}} \delta \dot{p}_n \, dt \\ &= \delta x_0 - (V \sin(\psi) \Delta T_k) \delta\psi + (\cos(\psi) \Delta T_k) \delta V + (\Delta T_k) \delta V_{NS}. \end{aligned} \tag{6.15}$$

Once again, a simple Euler integration scheme has been used and the substitution $\Delta T_k = t_{k+1} - t_0$ has been made. Similarly, for the east-west position error this

becomes:

$$\delta y_{k+1} = \delta y_0 + (V\cos(\psi)\Delta T_k)\delta\psi + (\sin(\psi)\Delta T_k)\delta V + (\Delta T_k)\delta V_{EW}. \tag{6.16}$$

When these substitutions for δx and δy are made in Equation 6.6, it results in a matrix equation of the standard linear form of $\delta\vec{r} = H\delta\vec{z}$ where the measurement vector $\delta\vec{r}$ is given by:

$$\delta\vec{r} = \begin{bmatrix} \delta R_{1,k} \\ \delta R_{2,k+1} \\ \delta R_{1,k+2} \\ \vdots \\ \delta R_{1,k+n-1} \\ \delta R_{2,k+n} \end{bmatrix}. \tag{6.17}$$

The state vector $\delta\vec{z}$ is given by:

$$\delta\vec{z} = \begin{bmatrix} \delta x_0 \\ \delta y_0 \\ \delta V_{NS} \\ \delta V_{EW} \\ \delta\psi \\ \delta V \end{bmatrix} \tag{6.18}$$

The measurement matrix, H, is of dimension $n \times 6$ where n is equal to the number of DME range measurements available. The first four columns of the measurement matrix, H, are nothing more than the entire measurement matrix given in Equation 6.14. The fifth column of H which will be denoted as H_5 is given as:

$$H_5 = \begin{bmatrix} 0 \\ (\Delta T_k)V\left(\frac{\sin(\psi)(\hat{x}_{k+1}-x_2)}{R_{2,k+1}} + \frac{\cos(\psi)(\hat{y}_{k+1}-y_2)}{R_{2,k+1}}\right) \\ (\Delta T_k)V\left(\frac{\sin(\psi)(\hat{x}_{k+2}-x_1)}{R_{1,k+2}} + \frac{\cos(\psi)(\hat{y}_{k+2}-y_1)}{R_{1,k+1}}\right) \\ \vdots \\ (\Delta T_k)V\left(\frac{\sin(\psi)(\hat{x}_{k+n}-x_1)}{R_{1,k+n}} + \frac{\cos(\psi)(\hat{y}_{k+n}-y_1)}{R_{1,k+n}}\right) \end{bmatrix} \tag{6.19}$$

Similarly, the final and sixth column, denoted by H_6, is given by:

$$H_6 = \begin{bmatrix} 0 \\ (\Delta T_k)\left(\frac{\cos(\psi)(\hat{x}_{k+1}-x_2)}{R_{2,k+1}} + \frac{\sin(\psi)(\hat{y}_{k+1}-y_2)}{R_{2,k+1}}\right) \\ (\Delta T_k)\left(\frac{\cos(\psi)(\hat{x}_{k+2}-x_1)}{R_{1,k+2}} + \frac{\sin(\psi)(\hat{y}_{k+2}-y_1)}{R_{1,k+1}}\right) \\ \vdots \\ (\Delta T_k)\left(\frac{\cos(\psi)(\hat{x}_{k+n}-x_1)}{R_{1,k+n}} + \frac{\sin(\psi)(\hat{y}_{k+n}-y_1)}{R_{1,k+n}}\right) \end{bmatrix} \tag{6.20}$$

An important point regarding the system's observability can now be made by inspecting the entire $n \times 6$ measurement matrix, H. In general, the system is not observable because it is not difficult to visualize cases where the measurement matrix H becomes rank deficient. A case in point is when the aircraft is flying at a constant speed and heading. In this instance, the effect of heading errors are indistinguishable from wind induced errors. More specifically, columns 4 through 6 of the measurement matrix become linearly dependent. For observability, the aircraft will have to maneuver such that there is variety in the headings and speed flown ensuring that the columns of the measurement matrix, H, remain linearly independent.

Figure 6.4 summarizes the results of the observability analysis. The position NED errors δp_n and δp_e, are observable in both Cases I and II shown in Figure 6.4. However, it is not possible to simultaneously observe both sensor and wind errors from Case I. In the case of Trajectory II, if the aircraft is flown at a variety of speeds, then *both* wind and sensor errors *may* be observable.

Unless a guarantee is given that the navigator will be flown with a constantly changing heading trajectory, observability cannot be guaranteed. This has an implication on how a usable navigator can be designed. A usable navigator will require that the dimensions of the state vector, $\delta\vec{z}$, be reduced such that a full rank measurement matrix, H, can be guaranteed. Such a system will be referred to as a "reduced-order" system in the discussions that follow. The performance of a navigator mechanized using the reduced-order formulation will be discussed in Chapter 7. Similarly, the system that retains all the elements of the state vector, $\delta\vec{z}$, will be referred to as a "full-order" system. The full-order system will be used solely in covariance analyses (trade-off studies) which will be discussed in Chapter 7.

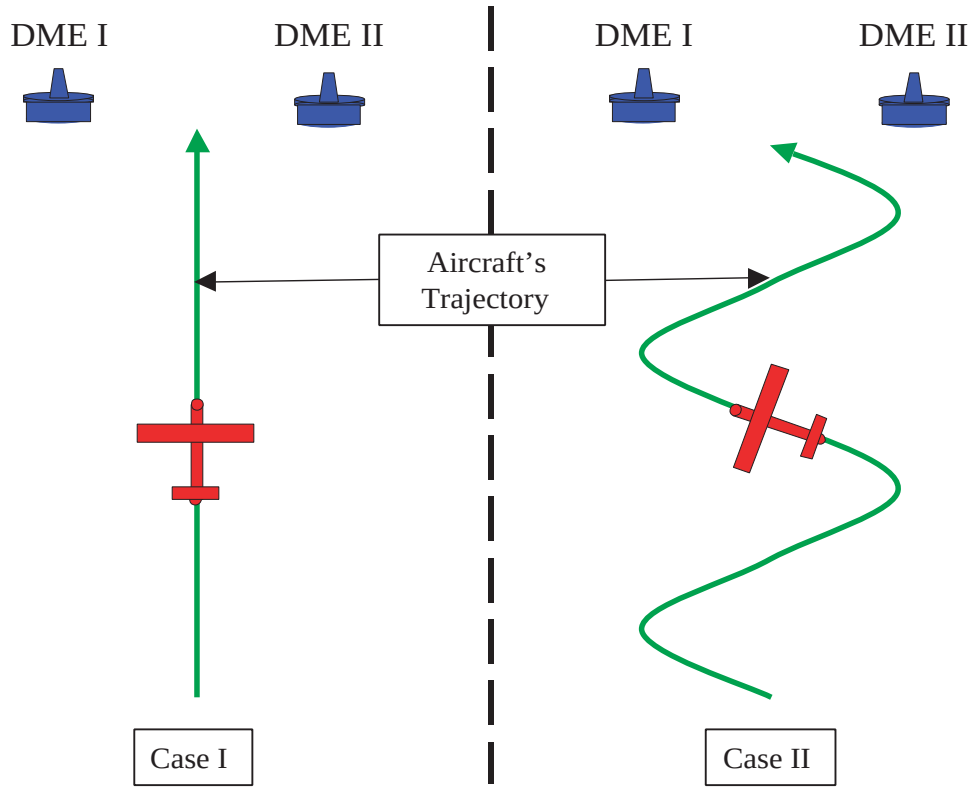

Figure 6.4: Effect of Aircraft Ground Trajectory on Observability. Case I-Position Errors δp_n and δp_e are Observable. Case II-Both Position Errors As Well As Wind and Sensor Errors *may* be Observable.

6.4 Mechanization of the Full-Order System

In the previous section it was shown that, given a dynamic model of the aircraft's motion and the appropriate flight trajectory, initial position, sensor and wind errors are observable from intermittent position fixing. Mechanizing the navigator that combines the DME range measurements with the dead reckoning solution is the objective of this section. First the full-order system described in the previous section will be mechanized. This system will be used to perform trade-off studies which will be discussed in the next chapter. Next, the reduced-order system will be mechanized. As will be discussed in the next chapter, this reduced-order system was implemented and used with data collected from a low-performance sensor suite flown in a test aircraft.

6.4.1 Overview of the Navigation Filter

If it were possible to acquire high bandwidth DME range measurements, position fixing alone could be used for navigation. The concern for DME saturation, however, places an upper limit on the frequency of DME range updates. Therefore, between DME range measurements, an equation for propagating the navigation state vector forward in time is required. The equation for doing this is the time-update equation. The position fixing equation based on DME range measurements is called the measurement-update equation. The tool used for blending the information from the time- and measurement- update equations is an Extended Kalman Filter (EKF). An EKF is used because the equations relating the DME range measurements to the navigation state vector, $\vec{z}$, are non-linear.

During the time-update phase, information in the navigation state vector is propagated forward in time. The navigation state vector, $\vec{z}$, is defined as:

$$\vec{z} = \begin{bmatrix} p_n & p_e & h & V_{NS} & V_{EW} & \psi & V \end{bmatrix}^T \tag{6.21}$$

The two entries p_n and p_e are the north-south and east-west NED position coordinates of the navigator, respectively. h is the navigator's altitude. V_{NS} and V_{EW} are the north-south and east-west wind speeds. V is the airspeed of the navigator and ψ is the true heading.

Given air speed and heading from an AHRS, the velocity vector is obtained by resolving air speed measurement into north-south and east-west components using heading information. The fact that air speed is not always equal to ground speed is accounted for by V_{NS} and V_{EW} which are added to the north-south and east-west velocity components determined from airspeed and heading measurement. This information can be used to propagate p_n and p_e. In practice, it is easier to propagate latitude (Λ) and longitude (λ) of the user. This is accomplished by adding V_{NS} and V_{EW} to the numerator of the latitude and longitude rate differential equations from

Chapter 5 as follows:

$$\dot{\Lambda} = \frac{V\cos(\psi) + V_{NS}}{R_{NS} - h} \tag{6.22}$$

$$\dot{\lambda} = \frac{V\sin(\psi) + V_{EW}}{(R_{EW} - h)\cos(\Lambda)} \tag{6.23}$$

With altitude information (h) from a baro-altimeter, these equations can be integrated to yield the latitude and longitude of the user. The variables h, V and ψ are not propagated forward during the time update as they are measurements obtained from sensors. The two components of wind speed, V_{NS} and V_{EW}, are neither propagated forward nor measured during the time-update. Instead they are estimated during the measurement-update phase.

The measurement update equation relates the state vector, $\vec{z}$, to the measured DME ranges. In addition to estimating the wind components, the measurement update allows for correcting position errors that have accumulated due to less-than perfect estimation of the wind components and sensor noise. Mechanization of the EKF requires linearizing the measurement equation. The state vector for the linearized system, $\delta\vec{z}$, is a perturbation of the navigation state vector, $\vec{z}$. All the EKF equations work with this perturbation vector $\delta\vec{z}$ and not the navigation state vector $\vec{z}$ itself.

This EKF state vector, $\delta\vec{z}$, is essentially the same vector used in the dead reckoning system covariance analysis which was defined in Equation 5.11 in Chapter 5. As noted earlier, however, in this thesis the full-order system is used for covariance analysis *only*. Since DME range measurement errors include both a time varying bias and wide-band noise, the effect of the biases must be included in any realistic covariance analysis. Thus, from this point on the EKF state vector, $\delta\vec{z}$, for the full-order system will be a perturbation of the navigation state vector, $\vec{z}$, given in Equation 6.21 augmented by two more additional states representing the DME range biases. Accordingly, the EKF state vector, $\delta\vec{z}$, is given by:

$$\delta\vec{z} = \begin{bmatrix} \delta p_n & \delta p_e & h & \delta V_{NS} & \delta V_{EW} & \delta\psi & \delta V & \delta R_1 & \delta R_2 \end{bmatrix}^T \tag{6.24}$$

Now the details of the time- and measurement-update equations will be discussed

separately.

6.4.2 EKF Time Update Equation

The time-update equations for the first seven states of $\delta\vec{z}$ were derived and discussed in detail in Section 5.3.2 of Chapter 5 (page 157). The time-update equations for the additional two states–the DME range biases–were derived and discussed in Section 3.9 of Chapter 3 (page 68). Assembling the two set of equations results in the following EKF time-update equation:

$$\delta\dot{\vec{z}} = F\delta\vec{z} + \Gamma\vec{w}. \tag{6.25}$$

The dynamic matrix F is given by:

$$F = \begin{bmatrix} 0 & 0 & 0 & 1 & 0 & -V\sin(\psi) & \cos(\psi) & 0 & 0 \\ 0 & 0 & 0 & 0 & 1 & V\cos(\psi) & \sin(\psi) & 0 & 0 \\ 0 & 0 & -\frac{1}{\tau_h} & 0 & 0 & 0 & 0 & 0 & 0 \\ 0 & 0 & 0 & -\frac{1}{\tau_{NS}} & 0 & 0 & 0 & 0 & 0 \\ 0 & 0 & 0 & 0 & -\frac{1}{\tau_{EW}} & 0 & 0 & 0 & 0 \\ 0 & 0 & 0 & 0 & 0 & -\frac{1}{\tau_\psi} & 0 & 0 & 0 \\ 0 & 0 & 0 & 0 & 0 & 0 & -\frac{1}{\tau_V} & 0 & 0 \\ 0 & 0 & 0 & 0 & 0 & 0 & 0 & -\frac{1}{\tau_r} & 0 \\ 0 & 0 & 0 & 0 & 0 & 0 & 0 & 0 & -\frac{1}{\tau_r} \end{bmatrix}. \tag{6.26}$$

Again, this dynamic matrix is nothing more than the dynamic matrix, F_{DR}, from Section 5.3.2, expanded to include the error model for the DME range biases. Numerical values for the time constants (the various τ above) were derived as part of the error equations in Chapters 3 and 5 which, for clarity, are repeated here in Table

6.1. The process noise input matrix, Γ, is given by:

$$\Gamma = \begin{bmatrix} 0 & 0 & 0 & 0 & 0 & 0 & 0 & 0 \\ 0 & 0 & 0 & 0 & 0 & 0 & 0 & 0 \\ 0 & 1 & 0 & 0 & 0 & 0 & 0 & 0 \\ 0 & 0 & 1 & 0 & 0 & 0 & 0 & 0 \\ 0 & 0 & 0 & 1 & 0 & 0 & 0 & 0 \\ 1 & 0 & 0 & 0 & 1 & 0 & 0 & 0 \\ 0 & 0 & 0 & 0 & 0 & 1 & 0 & 0 \\ 0 & 0 & 0 & 0 & 0 & 0 & 1 & 0 \\ 0 & 0 & 0 & 0 & 0 & 0 & 0 & 1 \end{bmatrix}. \tag{6.27}$$

The process noise vector, $\vec{w}$, is similar to the process noise matrix given by Equation 5.28 but is augmented by the driving noise terms for the DME range biases. That is,

$$\vec{w} = \begin{bmatrix} n_\psi & w_h & w_{NS} & w_{EW} & w_\psi & w_V & w_r & w_r \end{bmatrix}^T. \tag{6.28}$$

In the process noise vector, $\vec{w}$, n_ψ is the wide-band noise on the heading measurement while the remaining entries are the driving noise terms for the state errors modeled as Gauss-Markov processes. A numerical values for n_ψ is given in Table 6.1 under the column labeled "Wide-Band Noise." Numerical values for the remaining entries of $\vec{w}$ can be found under the column labeled "σ_{markov}" in Table 6.1.

During implementation, the value of interest is not the process noise vector itself but its power spectral density matrix, R_{wpsd}, given by:

$$R_{wpsd} = \begin{bmatrix} \sigma_{n_\psi}^2 & 0 & 0 & 0 & 0 & 0 & 0 & 0 \\ 0 & 2\frac{\sigma_h^2}{\tau_h} & 0 & 0 & 0 & 0 & 0 & 0 \\ 0 & 0 & 2\frac{\sigma_{V_{NS}}^2}{\tau_{NS}} & 0 & 0 & 0 & 0 & 0 \\ 0 & 0 & 0 & 2\frac{\sigma_{V_{EW}}^2}{\tau_{EW}} & 0 & 0 & 0 & 0 \\ 0 & 0 & 0 & 0 & 2\frac{\sigma_\psi^2}{\tau_\psi} & 0 & 0 & 0 \\ 0 & 0 & 0 & 0 & 0 & 2\frac{\sigma_V^2}{\tau_V} & 0 & 0 \\ 0 & 0 & 0 & 0 & 0 & 0 & 2\frac{\sigma_r^2}{\tau_r} & 0 \\ 0 & 0 & 0 & 0 & 0 & 0 & 0 & 2\frac{\sigma_r^2}{\tau_r} \end{bmatrix}. \tag{6.29}$$

Error State	Model Parameters		
	σ_{markov}	τ	Wide-Band Noise
Wind Speed(δV_{NS}, δV_{EW})	5 m/s	400 sec	None
Heading ($\delta\psi$)	2.5 deg	120 sec	0.8 deg
Air speed ($\delta\psi$)	2.6 m/s	400 sec	None
DME Range (δR)	0.17 n.mi.	(5 miles)/V	0.004 n.mi.

Table 6.1: Error Model Parameters for Aided Dead Reckoning Navigator.

R_{wpsd} is used for propagating the state error covariance matrix. The state covariance matrix at time step k is P_k and is defined as:

$$P_k = \mathcal{E}\{\delta\vec{x}_k\, \delta\vec{x}_k^T\}. \tag{6.30}$$

The symbol $\mathcal{E}$ represents the expectation operator. Given the state error covariance, P_k, at time step k, then the covariance is propagated forward in time by solving the discrete Riccati equation. That is, at time step $k+1$, the state covariance is given by:

$$P_{k+1} = \Phi_k P_k \Phi_k^T + C_d \tag{6.31}$$

The variable Φ_k is the discrete equivalent of the matrix F_{DR} at time step k and C_d is the discrete equivalent of $\Gamma R_w \Gamma^T$. The state covariance matrix, P_k, is used to compute the time varying gain matrix as described in the next section.

6.4.3 EKF Measurement Update Equation

The measurements needed for position fixing are two DME ranges (R_1 and R_2). Barometric altitude (h) information is obtained from an altimeter. The non-linear measurement equation that relates the navigation state vector $\vec{z}$ to the DME range and barometric altimeter measurements is:

$$\begin{bmatrix} \sqrt{{R_1}^2 - (h - p_{d1})^2} \\ \sqrt{{R_2}^2 - (h - p_{d2})^2} \end{bmatrix} = \begin{bmatrix} \sqrt{(p_n - p_{n1})^2 + (p_e - p_{e1})^2} \\ \sqrt{(p_n - p_{n2})^2 + (p_e - p_{e2})^2} \end{bmatrix}. \tag{6.32}$$

The variables p_n and p_e are the current position of the user in NED coordinates. The variables p_{ni}, p_{ei} and p_{di} are the NED coordinates of the i^{th} DME which is located at a range of R_i from the user. At the kth time step, this measurement equation is of the form:

$$\vec{r}_k = h(\vec{z}_k). \tag{6.33}$$

In order to implement the EKF, it needs to be linearized such that it is in the form of:

$$\delta\vec{r}_k = H_k\,\delta\vec{z}_k + \vec{v}. \tag{6.34}$$

The vector $\vec{v}$ on the left hand side of Equation 6.34 represents the wide-band noise on the DME range measurements. Linearizing Equation 6.32 about the estimated position of the navigator yields a matrix of Jacobians, H_k, with the following form:

$$H_k = \left[\begin{array}{cc} H_{11} & H_{12} \end{array}\right]. \tag{6.35}$$

The sub-matrix H_{12} is a 2×7 matrix of zeros while the sub-matrix H_{11} is given by:

$$H_{11} = \left[\begin{array}{cc} \frac{(\hat{p}_n - p_{n1})}{\hat{R}_{h1}} & \frac{(\hat{p}_e - p_{e1})}{\hat{R}_{h1}} \\ \frac{(\hat{p}_n - p_{n2})}{\hat{R}_{h2}} & \frac{(\hat{p}_e - p_{e2})}{\hat{R}_{h2}} \end{array}\right]. \tag{6.36}$$

Estimated quantities are denoted with a " $\wedge$ " above them. The variables R_{h1} and R_{h2} are the projections of the two range measurements, R_1 and R_2, on the locally level horizontal plane and are the entries in the vector on the left hand side of Equation 6.32. Only these horizontal projections of the range measurements are required because the DME range information is used for obtaining information about the user's lateral position. Accordingly, $\hat{R}_{h1}$ and $\hat{R}_{h2}$ are the *computed* horizontal ranges to the two DMEs and are given by:

$$\hat{R}_{h1} = \sqrt{(\hat{p}_n - p_{n1})^2 + (\hat{p}_e - p_{e1})^2} \tag{6.37}$$

$$\hat{R}_{h1} = \sqrt{(\hat{p}_n - p_{n2})^2 + (\hat{p}_e - p_{e2})^2} \tag{6.38}$$

Thus, at each measurement-update, the matrix H_k is computed based on the current estimate of the user's location.

The matrix H_k is used used to compute the time varying Kalman gain, L_k, using the following relation:

$$L_k = P_k^{(-)} H_k^T (H_k^T P_k^{(-)} H_k + R_v)^{-1} \tag{6.39}$$

The quantity R_v is the measurement noise covariance matrix. It is a diagonal matrix whose non-zero entries are the variance of the wide band noise of the DME range measurement. The matrix R_v is given by:

$$R_v = \mathcal{E}\{\vec{v}\,\vec{v}^T\} = \mathcal{E}\{\delta\vec{R}\,\delta\vec{R}^T\} = \begin{bmatrix} \sigma_{n_r}^2 & 0 \\ 0 & \sigma_{n_r}^2 \end{bmatrix} \tag{6.40}$$

A numerical value for σ_{n_r} is given in Table 6.1 under the column labeled "Wide-Band Noise."

The Kalman gain is now used to update the navigation error state vector, $\delta\vec{z}$, in the following manner:

$$\delta\hat{\vec{z}}_k^{(+)} = L\delta\vec{r}_k \tag{6.41}$$

The state covariance matrix P_k is updated using the following relation:

$$P_k^{(+)} = (I_{9\times 9} - L_k H_k)\, P_k^{(-)} \tag{6.42}$$

After each measurement update, all but the lateral position states are updated in the following manner:

$$\begin{aligned}
\delta h^{(+)} &= \delta h^{(-)} + \delta z_3^{(+)} && (6.43)\\
\delta V_{NS}^{(+)} &= \delta V_{NS}^{(-)} + \delta z_4^{(+)} && (6.44)\\
\delta V_{EW}^{(+)} &= \delta V_{EW}^{(-)} + \delta z_5^{(+)} && (6.45)\\
\delta \psi^{(+)} &= \delta \psi^{(-)} + \delta z_6^{(+)} && (6.46)\\
\delta V^{(+)} &= \delta V^{(-)} + \delta z_7^{(+)} && (6.47)\\
\delta R_1^{(+)} &= \delta R_1^{(-)} + \delta z_8^{(+)} && (6.48)\\
\delta R_2^{(+)} &= \delta R_2^{(-)} + \delta z_9^{(+)} && (6.49)
\end{aligned}$$

Since the variables of interest to the user are position in the form of latitude (Λ) and longitude (λ), after each measurement update, instead of updating δp_n and δp_e, (which are equal to the first δz_1 and δz_2), the latest estimates of δz_1 and δz_2 are blended into latitude and longitude using the following equations:

$$\Lambda_k^{(+)} = \Lambda_k^{(-)} + \frac{\delta z_1^{(+)}}{R_{NS}} \tag{6.50}$$

$$\lambda_k^{(+)} = \lambda_k^{(-)} + \frac{\delta z_2^{(+)}}{R_{EW}\cos(\Lambda^{(-)})} \tag{6.51}$$

As noted in Chapter 5, the variables R_{NS} and R_{EW} are Earth's north-south and east-west radii of curvature and are given by [65]:

$$R_{NS} = R_0(1 + f(3\sin^2(\Lambda) - 2)), \tag{6.52}$$

$$R_{EW} = R_0(1 + f\sin^2(\Lambda)). \tag{6.53}$$

The variable f in the above equations is the flattening of Earth. The variable R_0 is the equatorial radius of Earth. The values for these variables are obtained from [58] and are:

$$f = 1/298.257223563$$

$$R_0 = 6378137.0 \text{ metres.}$$

Finally, since all the information contained in $\delta z_1^{(+)}$ and $\delta z_2^{(+)}$ will have been transferred to Λ and λ after the measurement update, $\delta z_1^{(+)}$ and $\delta z_2^{(+)}$ are set to zero before the next time-update phase begins.

6.5 Mechanization of the Reduced-Order Navigator

As noted earlier, the full-order aided dead reckoning system is, in general, not observable. Observability can only be guaranteed when certain trajectories in relation to the DMEs and specific aircraft maneuvers are flown. It is reasonable to expect

an aircraft to follow certain trajectories in relation to the DMEs. However, it is difficult to ensure certain maneuvers are flown. Thus, for this system to be usable as a navigator, observability must be guaranteed with the only constraint being the one placed on the relation between the trajectory flown and the location of the DME transponders.

A navigation system with the required observability can be designed by reducing the number of states. The logical subset of $\delta\vec{z}$ to use as the state vector, $\delta\vec{z}_{ro}$, for a reduced order system is:

$$\delta\vec{z}_{ro} = \begin{bmatrix} \delta p_n \\ \delta p_e \\ \delta V_{NS} \\ \delta V_{EW} \end{bmatrix} \tag{6.54}$$

That is, the heading, airspeed and DME range bias errors are deleted from $\delta\vec{z}$. Retaining only the states given in Equation 6.54 is justified because heading and air speed errors are small and their contribution to the total lateral position error is, in comparison, smaller than the effect of the wind errors. This fact is clearly demonstrated in Figure 5.6 on page 177. Furthermore, as shown in Figure 3.30 heading error is a function of magnetometer calibration residuals and is dependent on heading. Depending on the maneuvers being flown, this can be rapidly time varying. As such it may be difficult to estimate it using intermittent range measurements. Finally, as shown in Equation 6.10 on page 184, the DME range biases are going to be indistinguishable from position errors. Thus, their effect on the navigator's performance will be to bias the estimate of the various elements of $\delta\vec{z}_{ro}$.

All the matrices required to mechanize the reduced-order system were given in the previous section. That is, they are the same as the full-order system except that the rows and columns associated with the air speed, heading and DME range bias states are deleted. A block diagram of the architecture of this reduced-order estimator is shown in Figure 6.5. This will be an estimator that is suboptimal but, as will be shown in the next chapter, functions acceptably as a backup mode of navigation.

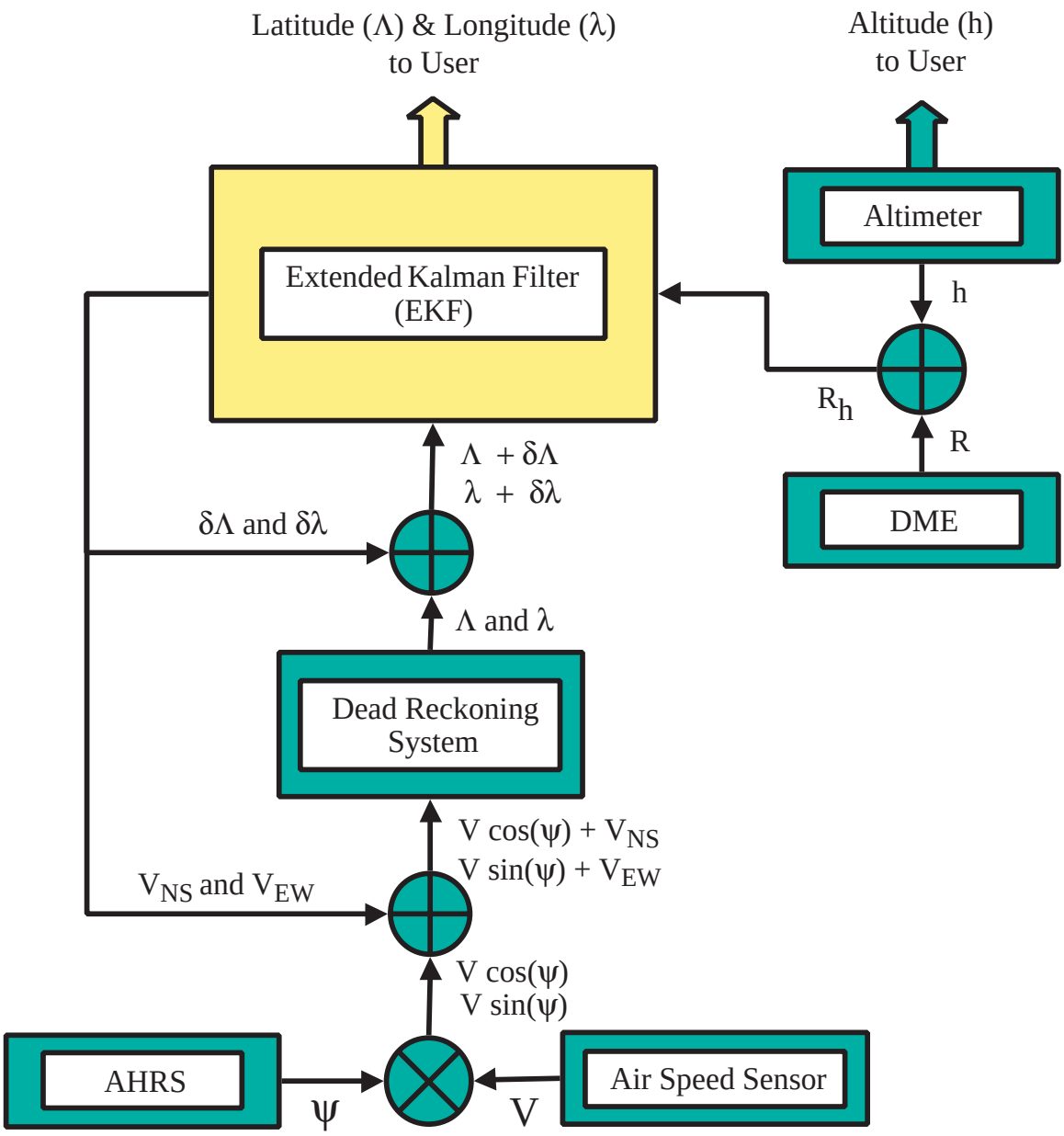

Figure 6.5: Estimator Architecture for the DME Aided Dead Reckoning Navigator.

Chapter 7

Performance of the Backup Navigator

In Chapter 6, the equations for mechanizing the DME aided navigator were presented. In this chapter, these equations are used to evaluate the performance of the navigator. These evaluations will be based on simulated and experimentally collected sensor data. First, results of analyses examining the effect of DME geometry on the accuracy of the position solution will be presented. Next, the results of a trade-off study quantifying the effect of various estimator architectures as well as sensor and modeling errors on the navigator's performance will be presented. The chapter will close with experimental results showing the performance of a DME-aided dead reckoning navigator mechanized using low-performance sensors.

7.1 DME Siting and Navigation Accuracy

Chapter 2 and [55] discuss future NAS architectures consisting of a skeletal network of ground based navigation aids intended to serve as a backup for GPS. The proposed architectures that relied on DMEs as the only ground based navigation aids provided for double or triple coverage at selected airports in CONUS. Double coverage means that two DMEs will be available in the vicinity of the airport. Triple coverage means that three DMEs will be available.

When compared to double coverage, triple coverage is a superior geometry because it provides position accuracies that are less sensitive to user location. For example,

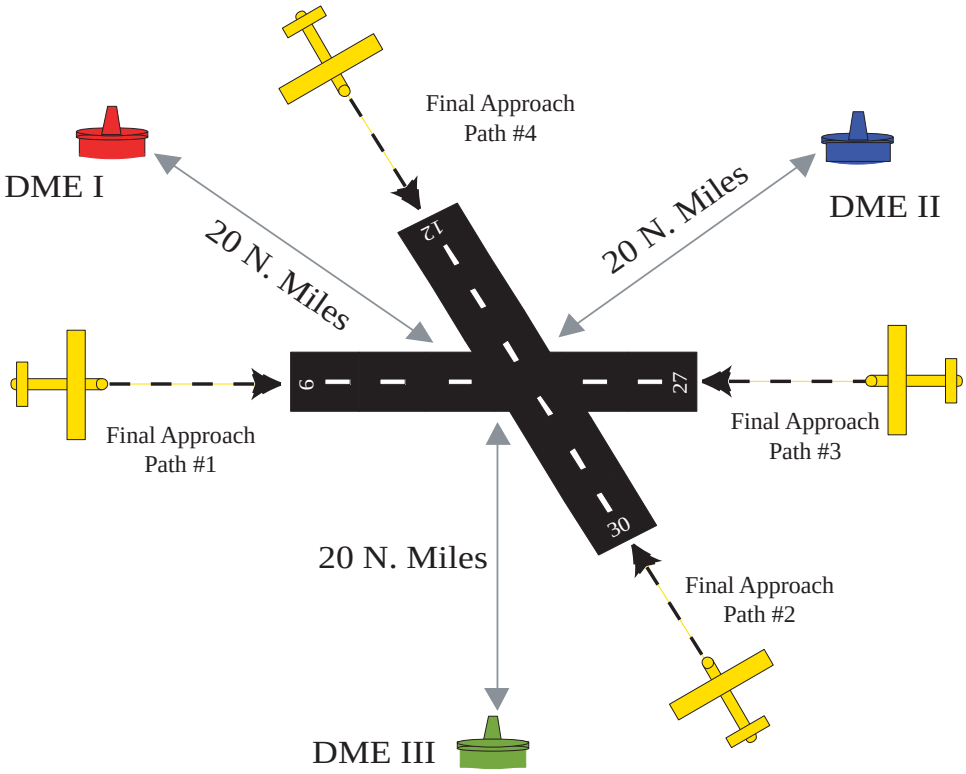

Figure 7.1: Schematic of a Triple DME Coverage Scenario at a Hypothetical Airport.

consider the case shown in Figure 7.1. In this case an airport is located in the middle of an equilateral triangle formed by three DME transponders. The transponders are 20 nautical miles from the center of the airport and are used for position fixing. Position fixing errors are the result of range measurement errors being mapped into the position domain. If, for the moment, it is assumed that all the errors in the DME range measurement are due to wide-band noise only, then a measure of the "goodness" of the position solution would be the Horizontal Dilution Of Precision (HDOP). HDOP is a measure of the degree to which measurement errors (in this case, wide-band noise) map into the position estimate. Mathematically, HDOP is the square root of the trace of the matrix $\left(H_k^T H_k\right)^{-1}$ given in Equation 6.3. It is effectively a number which, when multiplied by the magnitude of the measurement noise, yields the magnitude of the horizontal position error.

Figure 7.2 shows the HDOP for the case where three DMEs are used for position fixing. What is clear from Figure 7.2 is that, except in the case where a user is located immediately adjacent to a DME transponder, the accuracy of the position solution is relatively insensitive to location. While the position accuracy provided by a three DME geometry is best when the user is located at the center of the triangle, users located elsewhere will still have relatively small positioning errors. This can be demonstrated by the simple quantitative analysis that follows. The error model developed in Chapter 3 (page 72) and repeated in Table 6.1 of Chapter 6 (page 195) lists the DME range measurement noise as 0.004 nautical miles or 7.4 meters. Figure 7.2 shows that HDOP values for triple DME coverage range from 1.2 to 2.0. This means that position fixing accuracies between 9 and 15 meters can be achieved. In reality, correlated DME range biases on the order 0.17 nautical miles significantly degrade the position accuracy. The more important message from Figure 7.2, however, is qualitative; position fixing accuracy in the vicinity of an airport with triple DME coverage is relatively insensitive to user location. As shown in Figure 7.1, the practical implication of this is that there can be multiple final approach paths to an airport with triple DME coverage.

While triple DME coverage is superior, it is not always required. In many cases, double DME coverage is sufficient. In the double coverage case, however, the accuracy is dependent on the path flown and the user's location relative to the DME transponders being used. This is clearly demonstrated in Figure 7.3 which shows the HDOP for the position fixing problem when only two DMEs are used. The in-track errors become large as the aircraft approaches the imaginary line connecting the two DMEs.

Inflation of in-track error can be mitigated by appropriately choosing the location of the DME transponders relative to the final approach path and the airport. Figure 7.4 shows how two DMEs might be arranged in the vicinity of an airport to provide double DME coverage with acceptable position accuracy all the way to the airport. This is achieved by moving the DMEs (and hence, the imaginary line connecting the two DMEs) away from the airport by some distance, H. It may appear that such an arrangement limits the number of runways to which instrument approaches may be flown (e.g., Runway 09 only in Figure 7.4). This is not necessarily the case,

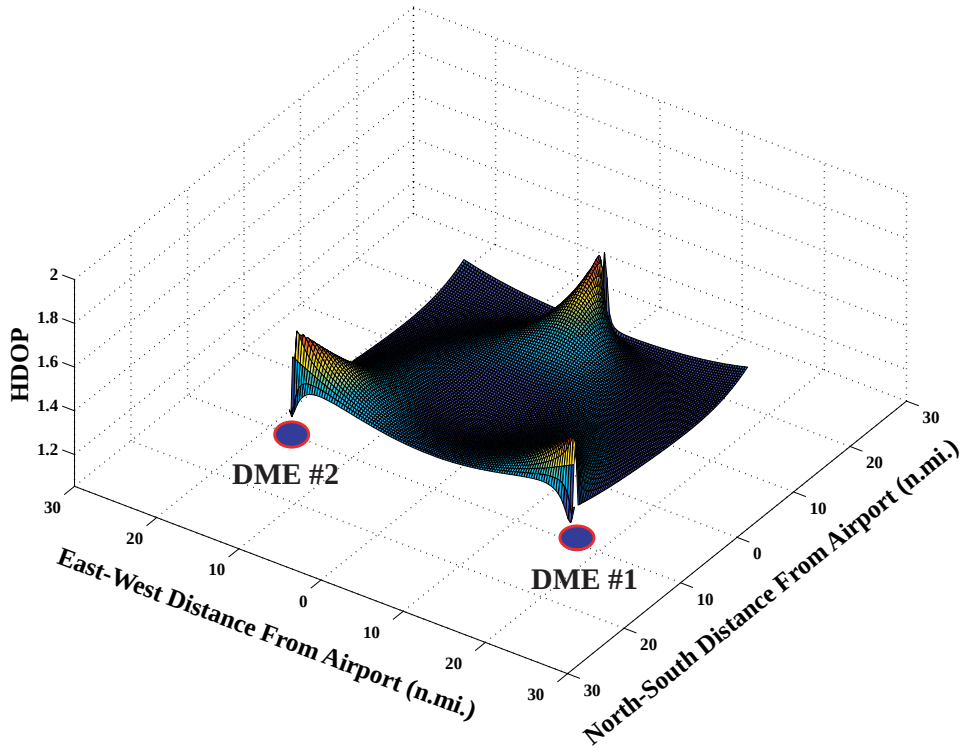

Figure 7.2: Dilution of Precision for 3 DME Position Fixing.

however, especially when considering the fact that these DMEs will be used as part of a navigation system to support non-precision approaches. Such approaches do not have to be straight-in approaches and thus an aircraft intending to land on Runway 12, for example, would approach the airport by initially flying in-line with Runway 09. When it is in the vicinity of the airport and has the runway environment in sight (i.e., it is within the dashed circle shown in Figure 7.4), it can alter course to land on Runway 12. This would be similar to the "circle-to-land" instrument approach procedures in current use.

7.2 Navigator Performance Studies

This section discusses the results of a series of simulation studies that were conducted to assess the performance of the DME-aided dead reckoning navigator. These

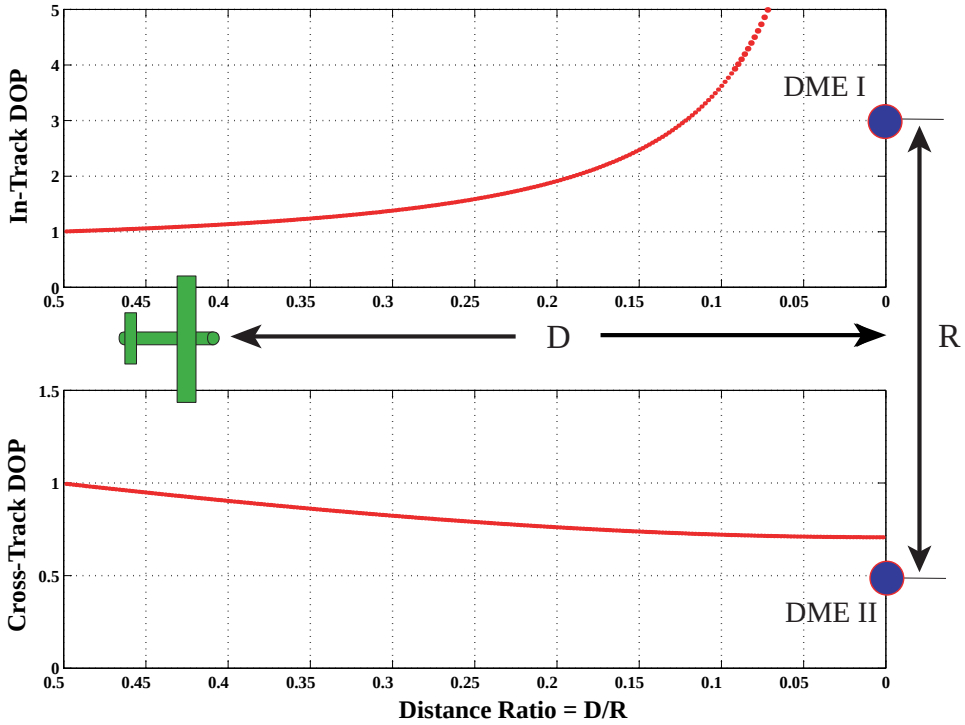

Figure 7.3: Dilution of Precision for 2 DME Position Fixing.

simulation studies considered the performance of the backup navigator in the vicinity of an airport with double DME coverage. These results can be viewed as a limiting case or "worst-case" scenario because the performance of the navigator in the vicinity of an airport with triple DME coverage will be better.

The trajectory for these simulations assumes that an aircraft is approaching an airport where coverage from two DMEs is available. The configuration of the approach track and the DME geometry is shown in Figure 7.5. Earth's surface is modeled in accordance with the WGS-84 reference ellipsoid [58] and the simulation begins 50 nautical miles out at an altitude of 6000 feet. The aircraft is flying wings level and descending at a constant rate such that it is at an altitude of 800 feet by the time it is 2 nautical miles away from the airport. At this point the aircraft stops descending and flies at a constant altitude until it reaches the airport.

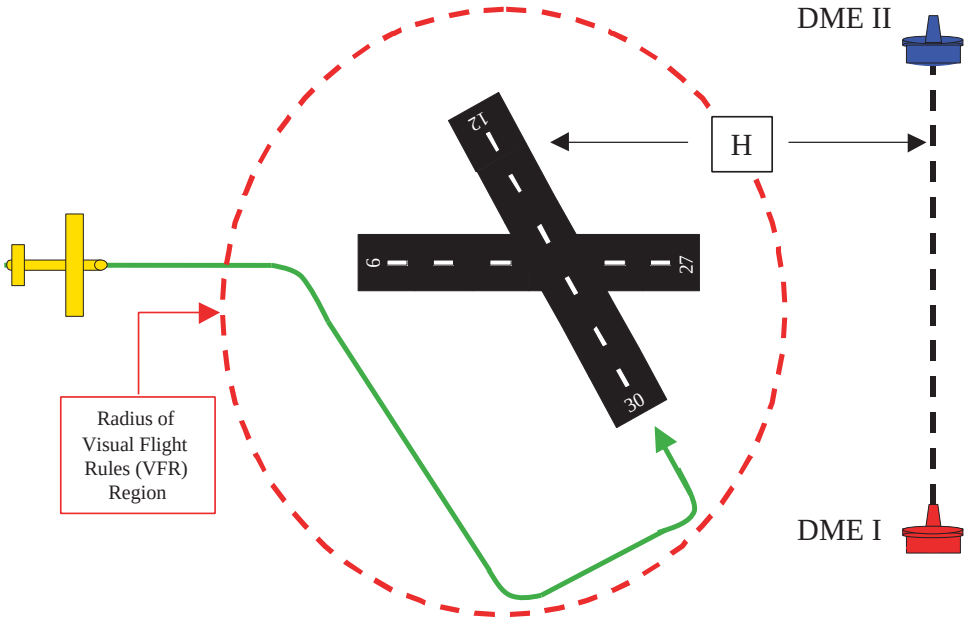

Figure 7.4: Schematic of a Double DME Coverage Scenario at a Hypothetical Airport.

The tool used for the simulation studies is a covariance analysis which uses the dynamic and measurement models developed in Chapter 6. Given the initial state error covariance matrix, P_0, it is then propagated forward in time by solving the Algebraic Riccati Equation as discussed in Chapter 6 on page 195. The initial conditions and results for the various case studies will now be discussed in detail separately.

7.2.1 Performance of the Full-Order System

As noted earlier, the weak observability of some of the navigation states required that a practical and realizable DME-aided dead reckoning navigator be based on a reduced-order estimator. Before a reduced order estimator can be accepted for navigation, however, one important aspect of this estimator must be quantified. That is, will the states that have been ignored in the reduced-order estimator cause a divergence in the position solution? The reduced-order estimator effectively ignored the unobservable states of the full-order system and assumed that all position errors are due to wind and initial position errors. So, another way to look at the question

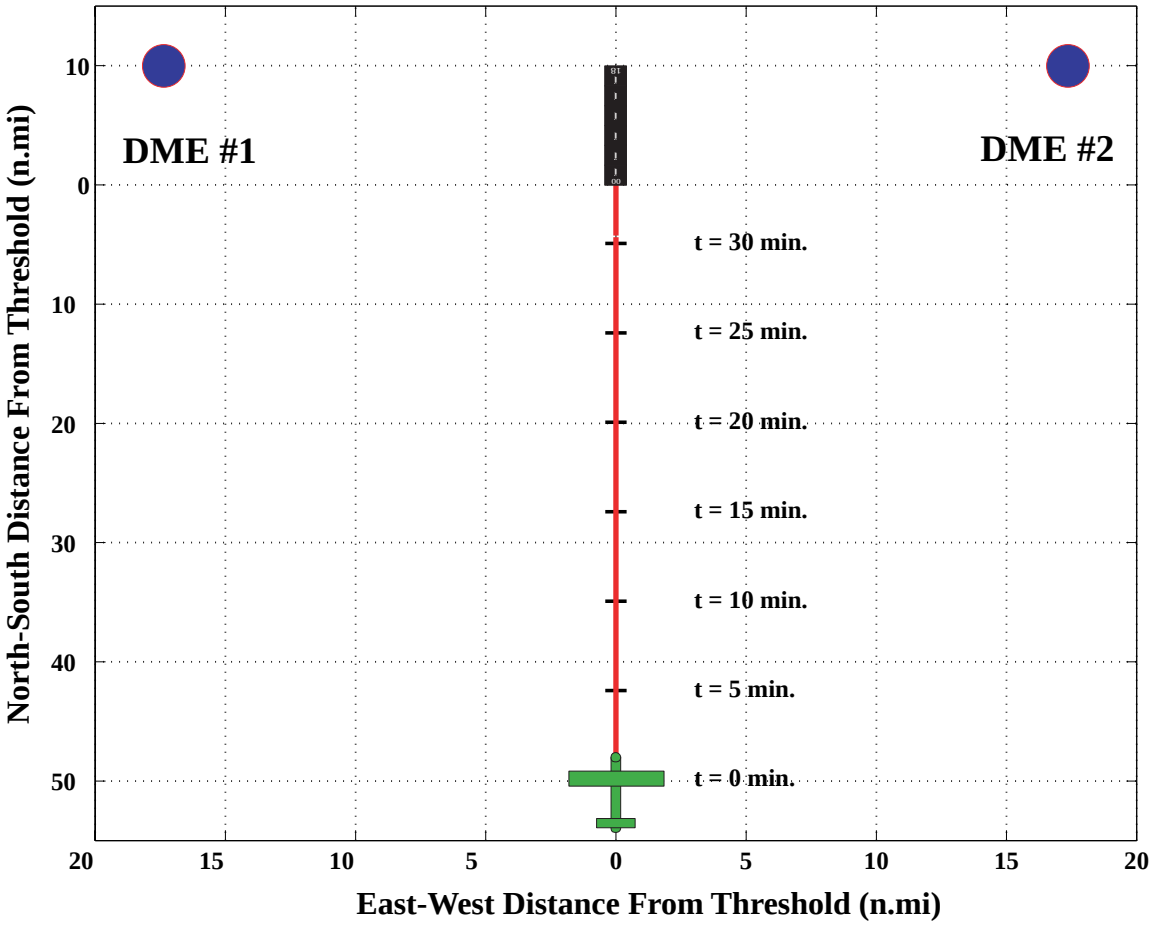

Figure 7.5: Simulation Ground Track and DME Geometry.

posed above is as follows: Will the unobservable states in the full-order system cause a divergence in the position solution?

To answer this question, a simulation using the trajectory described above was performed. The simulation assumes that the aircraft in question is a General Aviation aircraft (i.e., a Group E aircraft in Table 1.1) flying with an initial airspeed, V, of 90 knots, initial heading, ψ, of true north and vertical speed, $\dot{h}$, of 166 ft/min. These initial conditions and the initial state error covariance matrix, P_0, are as given in Table 7.1.

Variable	Variable Name	Initial Value
V	Air Speed	90 knots (46.3 m/s)
ψ	Heading	0° (True North)
$\dot{h}$	Vertical Speed	166 ft/min
P_0	North-South Position Error Variance (P_{11})	$(2\text{ m})^2$
	East-West Position Error Variance (P_{22})	$(2\text{ m})^2$
	Altitude Error Variance (P_{33})	$(5\text{ m})^2$
	North-South Wind Error Variance (P_{44})	$(5\text{ m/s})^2$
	East-West Wind Error Variance (P_{55})	$(5\text{ m/s})^2$
	Heading Error Variance (P_{66})	$(2.5°)^2$
	Air Speed Error Variance (P_{77})	$(5\text{ knots})^2 = (2.6\text{ m/s})^2$
	DME #1 Range Error Bias (P_{88})	$(0.17\text{ N.M})^2 = (317\text{ m})^2$
	DME #2 Range Error Bias (P_{99})	$(0.17\text{ N.M})^2 = (317\text{ m})^2$

Table 7.1: Initial Conditions for Simulation Assessing the Performance of the Full-Order System.

The DME range measurements were obtained intermittently at 15 second intervals. That is, DME #1 is interrogated first, followed by 15 seconds of coasting on dead reckoning alone, followed by an interrogation of DME # 2, followed by 15 seconds of coasting, and so on.

The initial conditions on north-south position, east-west position and altitude are obtained by assuming that right before the start of the simulation, GPS was available and was used to initialize the navigation state vector. These initial position errors are consistent with the accuracy for GPS/WAAS given as part of the GPS error model described in Chapter 3 (page 72). The remaining entries of P_0 have been discussed earlier and are also obtained from the error models discussed in Chapter 3.

The result of this analysis is shown in Figure 7.6. The blue line in Figure 7.6 shows the 1-σ covariance bound for the north-south and east-west position errors. The most important thing to note from this figure is that the position error remains bounded. This leads to the conclusion that the unobservable states do not cause a divergence in position estimates. However, they do cause a degradation in the system performance. This is because errors in the states that have been ignored will be lumped into wind and position error estimates. Because these errors are never

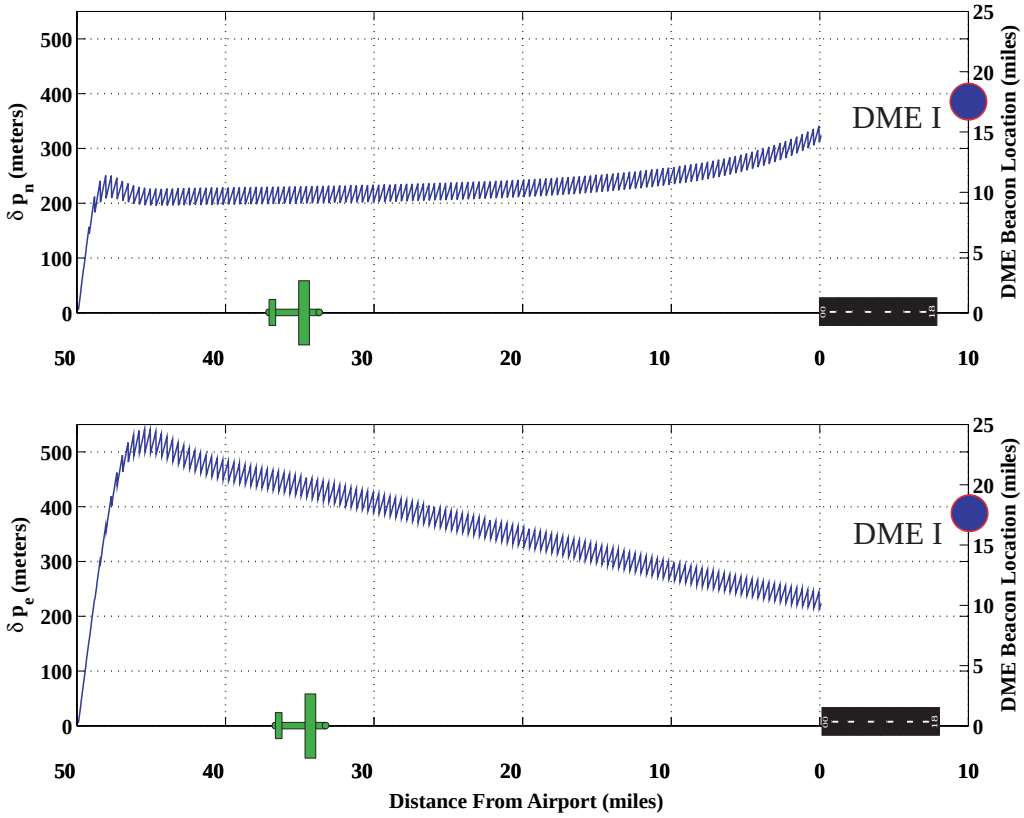

Figure 7.6: Covariance Analysis Results for the Full-Order System.

estimated and thus not compensated for, they will lead to a noisy or "jittery" position solution at the measurement updates. If these errors are small enough, the jitter in the position solution will not be excessive and will hence be acceptable.

The other important fact to note is that the position errors are primarily governed by the relative geometry between the user and DMEs. The cross-track (east-west) position errors decrease steadily as the aircraft approaches the airport while the in-track (north-south) position errors increase. This is consistent with the DOP analysis shown in Figure 7.3.

7.2.2 Comparison of DME Updating Methods

The objective of the analysis discussed in this section is to show that the method in which the DME range measurements are blended into the total navigation solution also affects the position accuracy. As discussed in earlier chapters, the method proposed for the backup navigator is one where a single DME receiver is used to obtain range measurements from two separate DME transponders alternately. Range measurements are obtained at 15 second intervals in accordance with the DME interrogation schedule shown in Figure 2.10 on page 31. In the discussion that follows, this method will be referred to as the "intermittent" or "1-DME-Receiver" method.

For comparison purposes, two other ways for blending the DME range measurements with the dead reckoning position solution are considered. The first one is to continually and simultaneously obtain range measurements from two separate DME transponders. In most cases DME saturation concerns make this type of DME ranging impractical. However, because of their low interrogation rates, scanning DMEs can be used in this manner without saturating the ground transponders. Accordingly, in the discussion that follows this will simply be called the "scanning" method. It should be noted that in this scheme, the dead reckoning system is not required because lateral position is observable from the two DME range measurements. However, even though combining dead reckoning would not be *required*, it would be *desirable* because it would aid in filtering the jitter or noise in the position solution derived by the DME position fixing alone. Thus, in the simulation studies described below, dead reckoning was combined with the scanning DME systems.

The second method for blending DME range measurements uses two separate non-scanning DME receivers to obtain simultaneous range measurements at regular intervals. The range measurements are spaced out in time at regular intervals in order to mitigate saturation concerns. Thus, a dead reckoning system is required to be part of the system to allow coasting between the simultaneous range measurements. In what follows, this is called the "simultaneous" or "2-DME-Receiver" system.

To evaluate the effect of these various DME interrogation schemes, the simulation discussed in the previous section when analyzing the full-order system was repeated. The initial conditions for this simulation were identical to those given in Table 7.1.

The results for this simulation are shown in Figure 7.7. As would be expected,

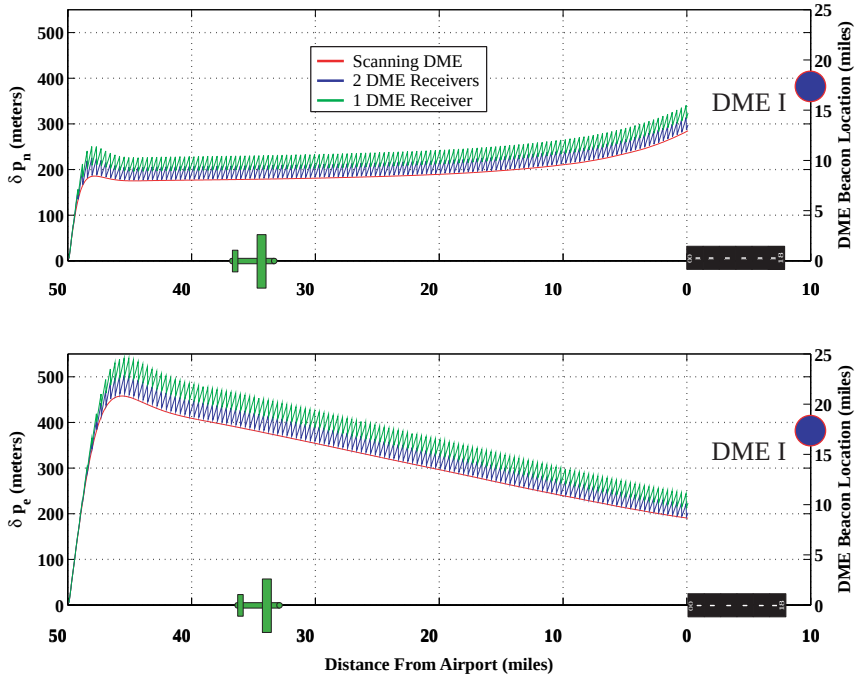

Figure 7.7: Comparison of Scanning, 1-DME Receiver and 2-DME Receiver Systems.

the scanning DME method gives the most accurate solution. This is because the navigator does not have to deal with position drift between measurement updates. Next in performance is the simultaneous or 2-DME-Receiver method. This is followed by the intermittent or 1-DME-Receiver method. The maximum difference in position (i.e, position errors) between the scanning and 2-DME-Receiver method is seen to be on average 25 meters. On the other hand, the maximum difference in position between the scanning and intermittent method is on average 50 meters.

Figure 7.8 on page 213 is a close-up of the position errors for the scanning versus intermittent systems as a function of time. The black line represents the scanning case which can be viewed as the best performance case. The red line shows the intermittent case when the time between measurement updates is set to 15 seconds. At each measurement update, the position error is reduced but does not become as small as the scanning case. However, the error remains bounded. Similarly, Figure 7.9

is a close-up of the position errors for the scanning versus simultaneous as a function of time. Once again, the black line represents the best performance case. The red line shows the simultaneous case when the time between DME range measurements is set at 15 seconds. It is seen that the navigator's performance is slightly degraded when compared to the scanning case. Furthermore, what can be seen from this figure is that the position error grows between measurement updates but resets (or "snaps back") to the level of the scanning case at each measurement update. Thus, at 15 second intervals a single measurement allows bounding of the position error growth such that it does not drift far away from the best performance line. In addition, traces are shown for updates spaced out 30 and 60 seconds apart. What is clear from these additional traces is that as the time between measurement updates is increased, a single measurement is not sufficient to reset the position errors back to the best performance line.

It is also interesting to note that, the simultaneous or 2-DME receiver case at 30 second measurement update intervals has comparable performance to the intermittent or 1-DME receiver case where the measurement update interval is 15 seconds. Essentially, going from the 2- to 1-DME-Receiver has a similar effect as spacing out the measurement updates in time.

The basic difference between the 1- versus 2-DME case can be understood better by looking at position error ellipses. Figure 7.10 shows the error ellipses that result for the DME aided navigator. These error ellipses were generated from the simulation described earlier and for which the trajectory is shown in Figure 7.5. Error ellipses were generated for the times between 27 and 30 minutes. Figure 7.5 shows a representative 1.6 km portion for this simulated flight. The sub-plot on the left in Figure 7.10 shows the error ellipses for the 1-DME-Receiver system while the sub-plot on the right is for the 2-DME-Receiver system. For clarity and to avoid overlap of the ellipses, the dimensions of the error ellipses in Figure 7.10 have been reduced by a factor of 2.5.

In both the left and right sub-plots in Figure 7.10, the error ellipses are seen to grow between measurement updates. As would be expected, for the simultaneous range update case, the dimensions of the error ellipse shrink uniformly in all directions at the measurement update. This is indicative of the fact that all the information needed

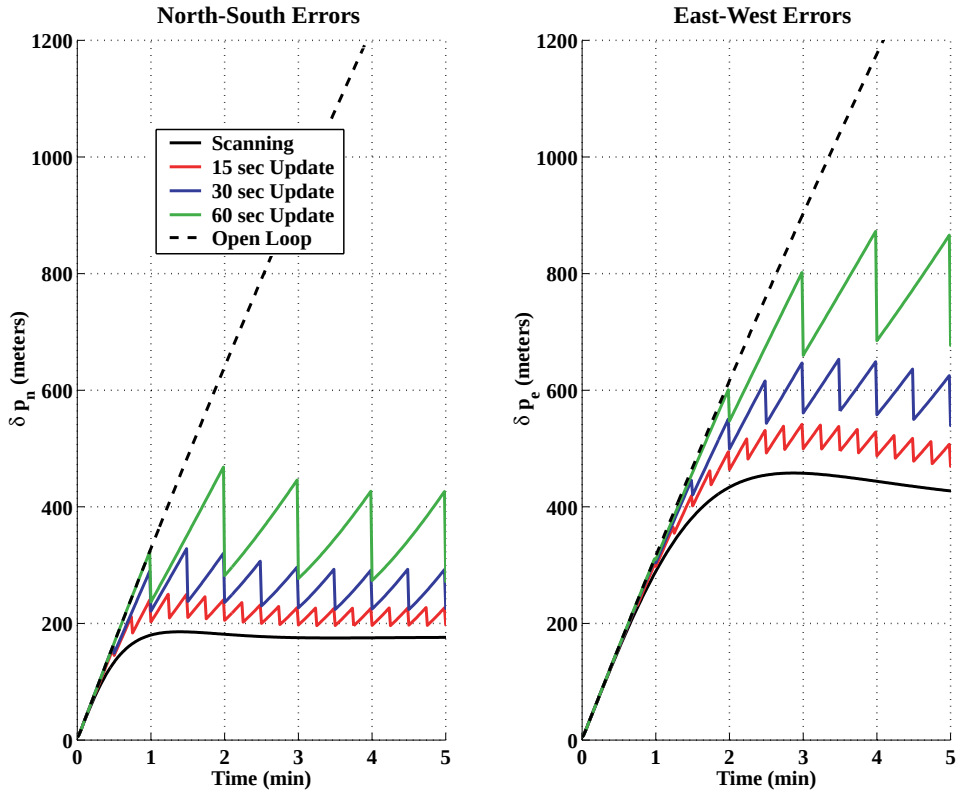

Figure 7.8: Comparison of a 1-DME Receiver versus a Scanning DME Receiver System.

to construct the navigation states (or compute the error in the states) is available from these simultaneous range measurements. The situation is different when a 1-DME-Receiver system is being used. In this case, only one range measurement is available at each measurement update. The error ellipse shrinking only occurs in the direction from which the range measurement is obtained. Another way to view this is that only partial state information is available from one range measurement. Therefore, the error ellipse can only be reduced in one direction. However, there is still a "check"on the growth of the position errors when mechanizing the navigator using intermittent range measurements.

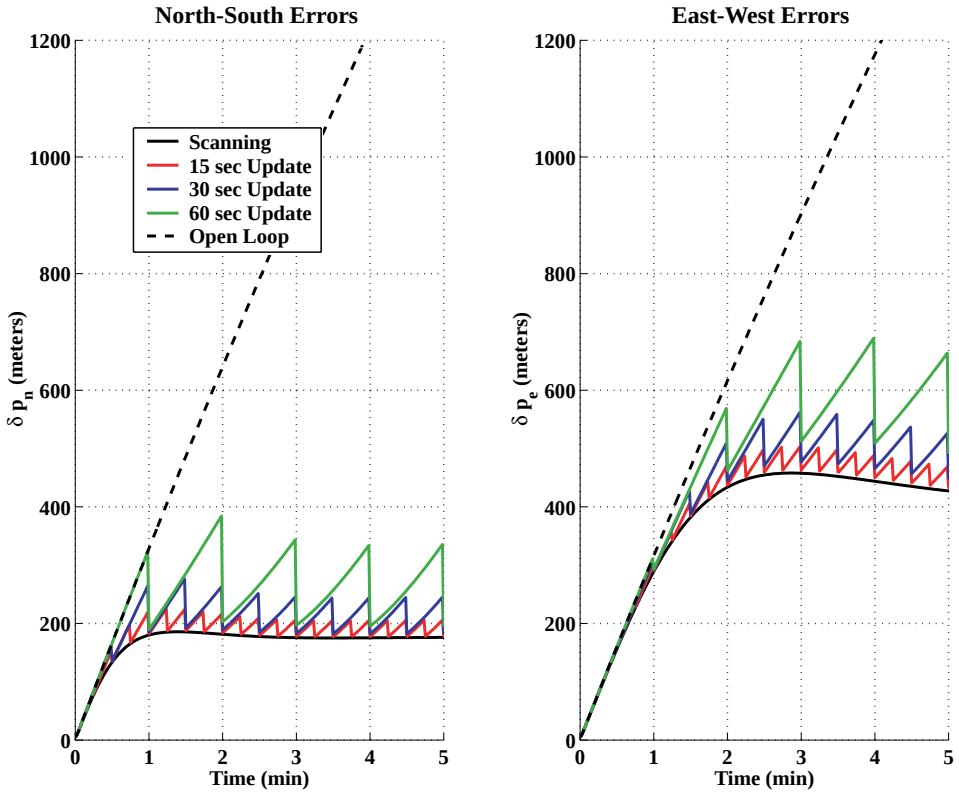

Figure 7.9: Comparison of a 2-DME Receiver versus a Scanning DME Receiver System.

7.2.3 Effect of Measurement Update Interval

It has been demonstrated that intermittent position fixing at 15 second intervals results in a position solution with bounded errors. The shape of the error ellipses for the intermittent position fixing case shown in Figure 7.10, however, raises one question. That is, if the time between measurement updates is allowed to get large, will there be a case where the intermittent updating scheme will fail to keep the error ellipse in "check"?

A partial answer to this question was provided in Figure 7.8 which shows the navigator's performance with DME update intervals as large as 60 seconds. To answer

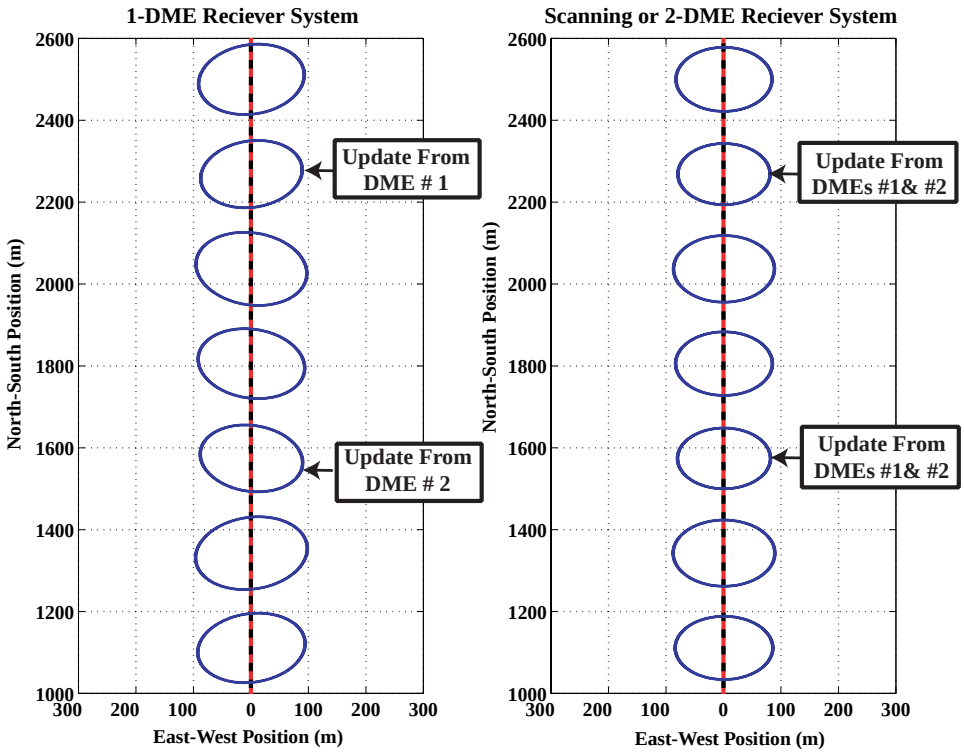

Figure 7.10: Position Error Ellipses for DME-Aided Dead Reckoning Navigator (For Clarity, Ellipse Dimensions have been Scaled Down by a Factor of 2.5).

this question completely, the same simulation study was repeated but with measurement update intervals as large as 120 seconds. A summary of this simulation study is shown in Figure 7.11. This figure shows that the covariance is kept in check for all update cases. However, for the longer update times, the initial transient results in error covariances that are very large and beyond the 0.5 nautical mile limit (or 926 meters) and will require a long period for the errors to be reduced down to an acceptable level.

7.3 Experimental Setup and Results

Experimental validation of the DME-aided dead reckoning navigator algorithm was conducted on post-processed flight test data collected using a Beechcraft QueenAir,

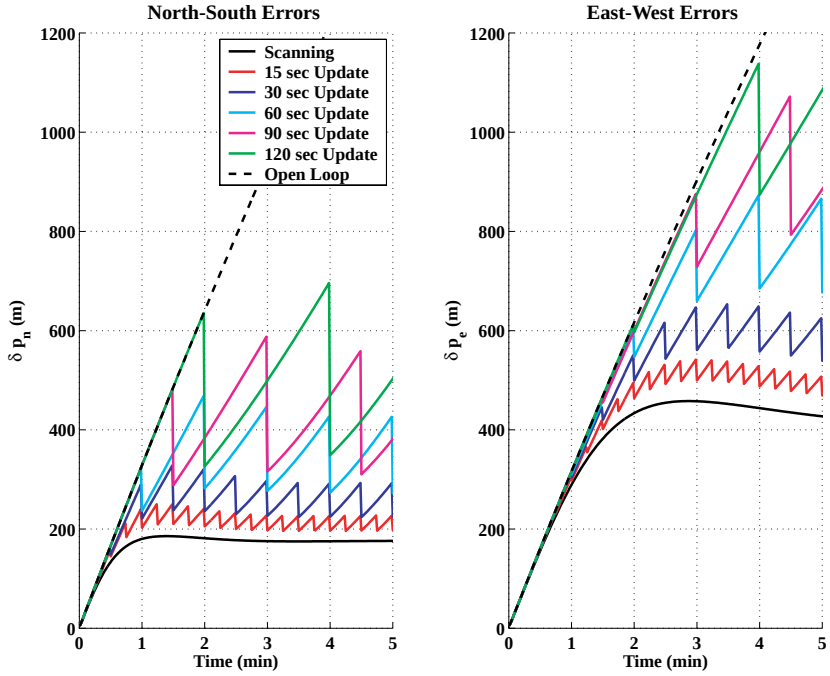

Figure 7.11: Growth of Error Covariances for DME-Aided Dead Reckoning Navigator.

a twin engine General Aviation aircraft. From start to finish, the test lasted 30 minutes and the trajectory flown during this test is shown in Figure 7.12. The flight trajectory consisted of a series of 360° turns followed by a straight-in approach to runway 25L at Livermore airport in Livermore, CA.

The aircraft was equipped with the sensor suite described in Section 4.11.1 (Page 130) of Chapter 4. Heading was derived using the AHRS algorithm described in Chapter 4, Section 4.12 which relied on angular rate outputs from a low-performance FOG aided by accelerometers and magnetometers. A very accurate record of the aircraft's trajectory was captured using GPS augmented by the Stanford University Wide Area Augmentation System (WAAS) prototype. As noted earlier in this chapter and also in Chapter 3, the accuracy of this system is 2 meters in the horizontal direction and 5 meters in the vertical direction [22].

In addition to the equipment described on page 130, a low cost DME transceiver

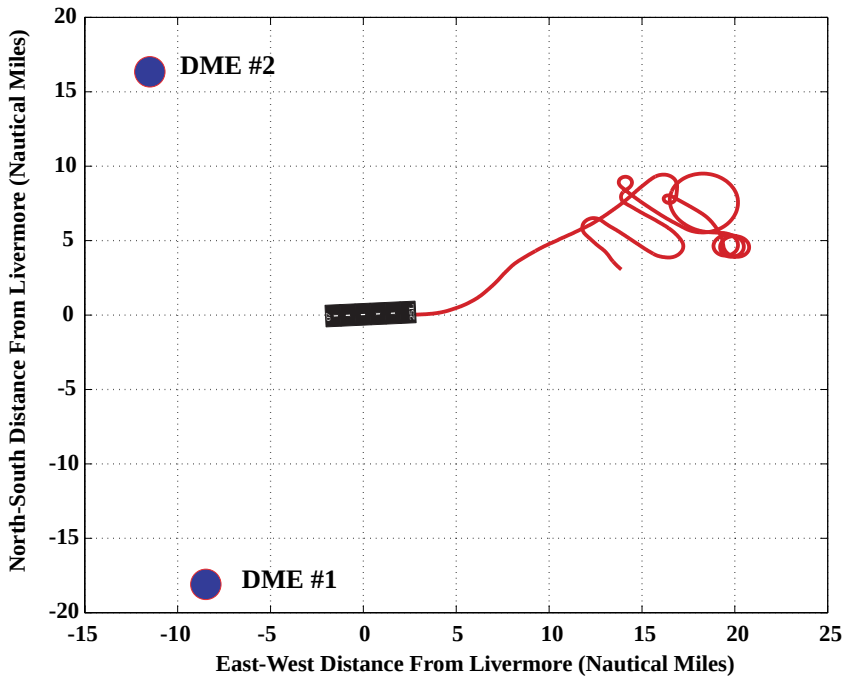

Figure 7.12: Test Aircraft's Ground Track in Relation to Livermore Airport and the Hypothetical DME Transponders. (Runway 25L Not to Scale)

(Bendix-King/Allied Signal KN-64) was also part of the equipment suite. However, since part of the study was to determine the effect of DME geometry on the navigation solution, in the results that follow, the DME range measurements were simulated. Given the position coordinates of the simulated DME transponders, the accurate record of aircraft position recorded by GPS/WAAS was used to back-out the error-free DME ranges that would have been observed. The generated range measurements were then corrupted using DME range error models documented in Chapter 3. In accordance with the simplified DME loading analysis contained in Chapter 3, DME scanning frequency was limited to once every 15 seconds.

Figures 7.13, 7.14 and 7.15 document the results of this flight test. Figure 7.13 is a close up of the aircraft's trajectory around a point located 16 miles east and 6 miles north of Livermore airport. This is the aircraft's trajectory for approximately

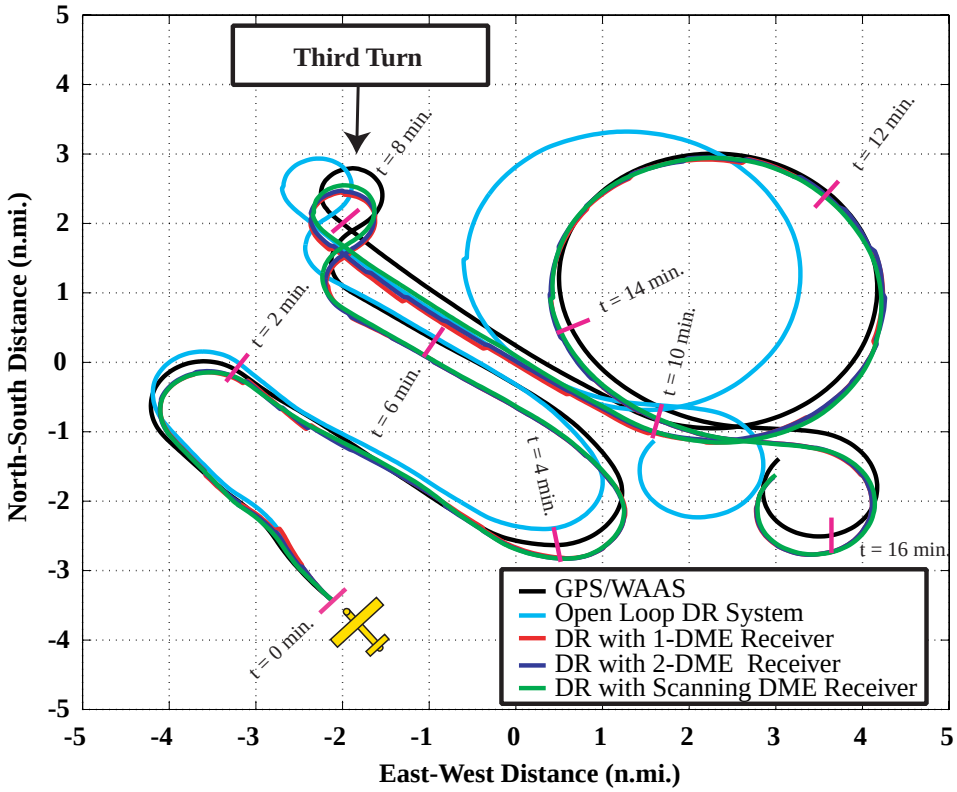

Figure 7.13: Comparison of Position Solutions for various Navigators. Center of Figure is 16 miles east and 6 miles north of Livermore Airport.

the first 15 minutes of the flight. The different color traces correspond to the position solutions generated by GPS and the various mechanizations of the backup navigator. The black line is the position solution generated from GPS augmented by Stanford University's WAAS prototype. This trajectory was used as the "truth reference" against which all the other solutions are compared.

The cyan line is the position solution generated by the open loop dead reckoning system. It can be seen that the open loop dead reckoning position solution is diverging from the GPS/WAAS solution as the aircraft travels forward in time. This divergence is seen more clearly in Figure 7.14 which shows the position errors for the various navigators as a function of time. The open loop dead reckoning solution is seen to have developed an error in excess of the 1/2 nautical mile before the end of the 15

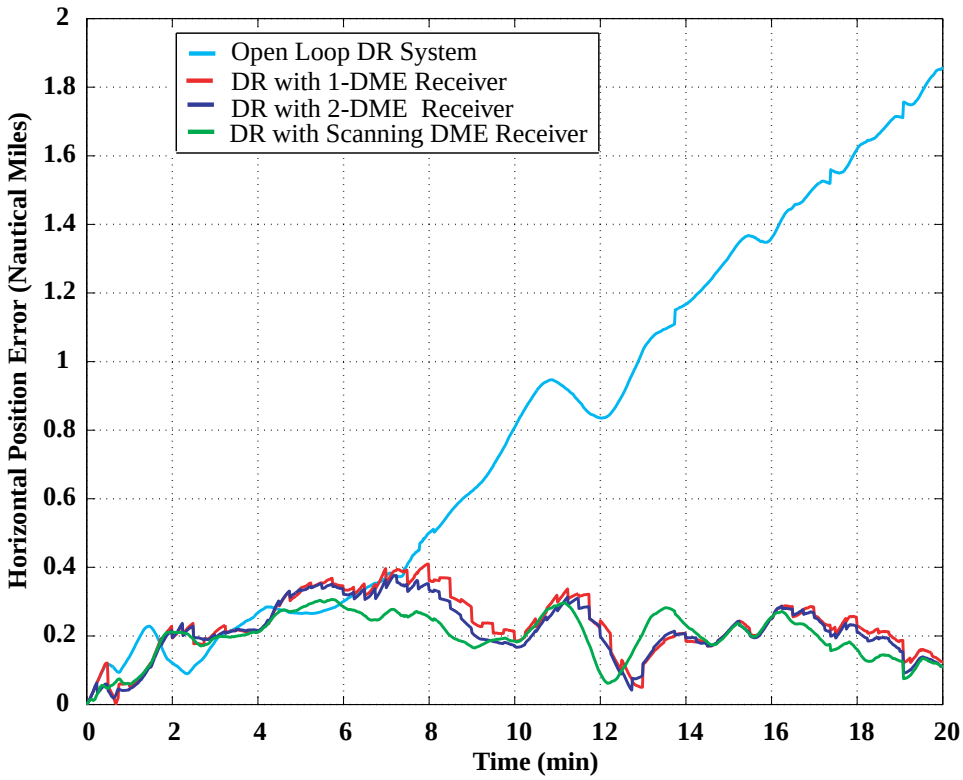

Figure 7.14: Comparison of Position Error for various Dead-Reckoning Navigators.

minute period. Figure 7.14 includes the performance of the open loop system for another five minutes beyond the trajectory shown in Figure 7.13. As expected, the performance of the open-loop system continues to deteriorate.

The red line in Figures 7.13 and 7.14 corresponds to the position solution generated by a DME aided dead reckoning system which was equipped with only one DME receiver. Thus, this system obtained intermittent position fixes from the two DMEs at 15 second intervals. That is, a range measurement is obtained from DME #1 followed by a coasting phase followed by another range measurement from DME #2. This pattern is repeated for the duration of the flight. The blue line corresponds to the position solution generated by an aided dead reckoning system equipped with two DME receivers. The navigator obtains simultaneous range measurements from *both* DMEs #1 and #2 at 15 second intervals. Finally, the green trace corresponds

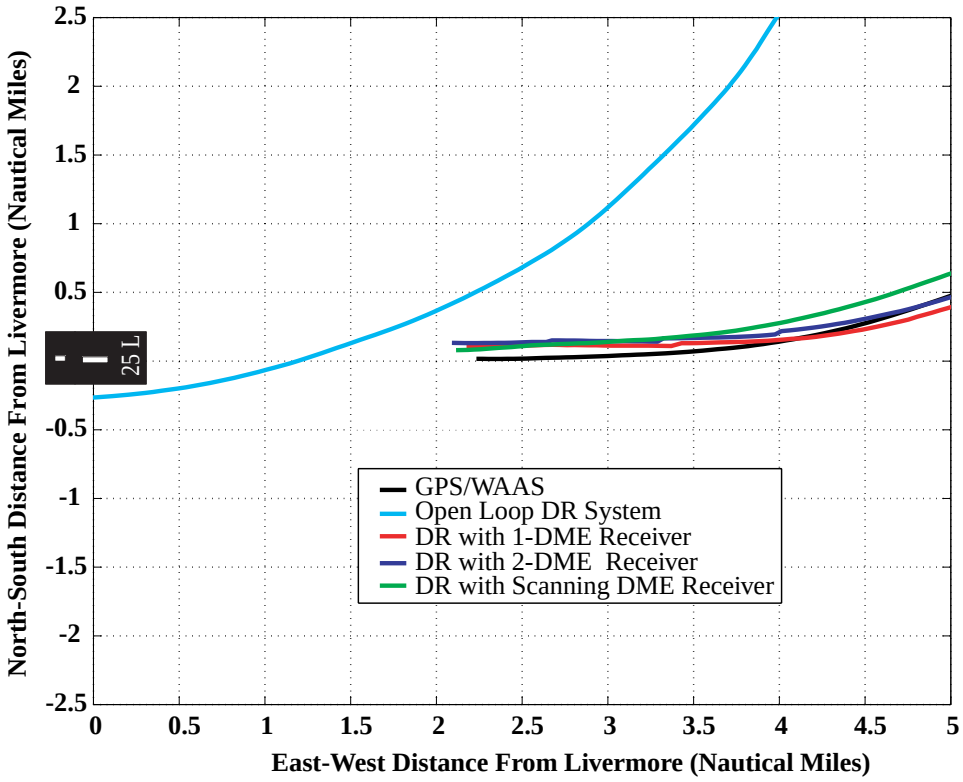

Figure 7.15: Position Solution of the Various DME-Aided Dead Reckoning Navigators in the Vicinity of Livermore Airport. (Runway 25L Not to Scale)

to the solution generated by an aided dead reckoning navigator equipped with a scanning DME. In this case, the navigator is supplied with two, simultaneous range measurements from both DMEs every second.

From Figure 7.13, it is seen that all three DME aided navigators have performances that are similar. For example, at the third turn (which is marked as such) in Figure 7.13, it is seen that all three DME aided systems exhibit similar position errors. This similar characteristic is even clearer to see in Figure 7.14. They all have a position solution that is biased in the same direction relative to the true position. However, the solution never drifts far away from the GPS/WAAS (or "true") position solution. This error is due to biases in the DME range measurements. Inspection of the trajectories at other points along the flight confirms this in that the same general

characteristic can be seen. This observation leads to two conclusions. Firstly, the accuracy of the position solution of the DME aided dead reckoning system is primarily governed by the DME range measurement accuracy. Secondly, although the position solution generated by the DME aided dead reckoning navigator is biased, the errors are bounded.

The fact that the open loop dead reckoning solution drifts while the DME aided solution does not has important practical implications that are shown in Figure 7.15. This figure shows the position solution close to the Livermore airport 28 minutes after commencement of navigation using the backup system. From this figure it can be seen that by the time the open loop dead reckoning solution computes a position solution indicating that the airplane is right above the airport, the other systems indicate a position that is still 2 miles east and on the final approach course. Thus, a pilot relying on an open loop system would have descended to the minimum descent altitude before it was safe to do so because the navigator would be indicating that the airplane was farther down the approach path than it really is.

In closing, the position error plot shown in Figure 7.14 provides a means for comparing the performance of the DME aided dead reckoning navigator with other proposed backup navigation systems such as LORAN and VORs. LORAN is a hyperbolic navigation system that has a nominal accuracy of 0.25 nautical miles [41]. Its performance, therefore, is *on par* with the DME aided dead reckoning navigator. An advantage the aided dead reckoning navigator has over LORAN is the fact that it would be a system applicable to all users whereas LORAN is hardly used by aircraft in Categories A through C of Table 1.1 on page 6. Furthermore, Table 1.1 shows that the equipment required to mechanize a DME-aided dead reckoning navigation system is generally found on these aircraft.

VORs on the other hand, have an accuracy that is dependent on the distance between the user and the VOR transmitter. To see this clearly, consider the fashion in which VORs are currently used to fly instrument approaches. Suppose the DMEs shown in Figure 7.12 were collocated with VORs that were used to guide the aircraft to the runway. An aircraft would use the VORs to execute an instrument approach in a fashion similar to that shown in Figure 2.1 on page 16 in Chapter 2. That is, the airplane would initially fly to one of the two VORs shown in Figure 7.12. Then, it

would track a specified VOR radial to the airport. Assuming a nominal VOR angular measurement error of between 1 and 5 degrees, the cross-track position error by the time the aircraft was at Livermore would be between 0.35 and 1.7 nautical miles. VOR does not provide in-track position information which has to be deduced using other means. Thus, the total position error would be in excess of the 0.5 nautical miles maximum position error that the backup navigation system must achieve. From the foregoing discussion one concludes that a NAS architecture based on retaining a skeletal network of VORs only is highly unlikely.

Chapter 8

Summary and Closing Remarks

8.1 Conclusions

The work in this thesis demonstrated that a GPS backup navigation system can be constructed from the fusion of low-performance inertial, air data and magnetic sensors. This system is capable of providing navigation services in the vicinity of airports that are served by DME. The navigation services provided by this system can be on the same level of accuracy as the currently used navigation systems such as LORAN and VOR. If much of the aircraft fleet was equipped with such a system, it would allow the FAA to begin de-commissioning a large number of existing radio-navigation aids while retaining only a small subset. In summary, the key points of the research contained in this thesis are:

1. A dead reckoning navigator based on the fusion of low-performance sensors aided by a skeletal network of DME transponders appears to be the most logical candidate for a backup navigation system for GPS.

2. An important component of any dead reckoning navigator aimed at users in Groups C through E of Table 1.1 is an inexpensive AHRS. A method of constructing and mechanizing an AHRS that uses low-performance sensors was discussed in detail in Chapter 4. An AHRS mechanized in the same manner as those discussed in Chapter 4 will likely become standard equipment on these aircraft. In this case, providing a backup navigation capability would most likely be a matter of software and wiring changes because most of the sensors required for such a system are part of newer aircraft in these groups.

3. Dead reckoning systems based on low-performance sensors cannot provide the accuracy required in aviation applications. Inertial navigation systems that are mechanized in the traditional manner using low performance inertial sensors have very large position drifts and cannot be relied on to give the navigation performance required of a backup navigation system. As noted in Chapter 3, the term "low-performance" means any INS which has performance worse than that of a tactical grade INS. The error growth rate of dead reckoning navigation systems based on low-performance sensors is not as rapid as that of the inertial navigators mechanized using the same quality sensors. The primary error sources for heading and speed dead reckoning where the speed measurement comes from air data sensors is the stochastic nature of the wind field.

4. Construction of a successful low-cost backup navigation system must be based on the combination of dead reckoning using heading and velocity measurements combined with intermittent position fixing. The errors caused by the wind field measurements are kept in check by the intermittent position fixes obtained from DME based triangulation. Ultimately, the accuracy of this navigator is controlled by the accuracy of the DME position fixes. In turn, as was shown in Chapters 3, Chapter 6 and Appendix D, the accuracy of position fixes is controlled by the quality of the DME receiver and the geometry of the ground based DME transponders. With the appropriate DME geometry a position accuracy better than 0.5 nautical miles (3000 ft) can be easily achieved.

5. If the entire Group C through E aircraft fleet that desired a GPS backup navigation system was equipped with the magnetometer-air speed navigator aided with intermittent DME updates, and there was a sparse DME network suitably located, the FAA could de-commission all NDBs and VORs and reduce the number of DMEs maintained from approximately 1000 to 400. Since a significant part of the $84 Million NAS radio-navigation infrastructure upkeep cost is devoted to VORs, the resultant savings would be significant. Even though an additional cost savings would be realized by de-commissioning LORAN, there are advantages to considering a future NAS architecture where LORAN is retained alongside a skeletal network of DMEs. In such a NAS architecture, the

DME based navigator would be the backup providing coverage for all users in terminal areas while LORAN would be relied on by Group D and E users for enroute navigation.

8.2 Future Research

While the basic system as described and demonstrated in this thesis will perform acceptably, its performance can be enhanced through further refinement of some of the concepts and algorithms used. Therefore, in what follows, these improvements and other research that can be the outgrowth of this work will be discussed.

8.2.1 Surveillance Radars and Data-Links

Inertial navigation or heading and speed dead reckoning alone cannot provide a navigation system that will meet the performance requirements laid out in Chapter 1. An external source of intermittent position is required to make such a system work. One of the limitations of the DME based system is the fact that DME is an active system with finite capacity. To mitigate the potential of DME saturation, DME range measurements were limited to once every 15 seconds. The range measurements obtained every 15 seconds were partial position fixes. Thus, to keep the position error growth of the dead reckoning system in check, a *history* of position fixes is required. If DME position fixes cannot be obtained at the 15 second interval, the resulting position solution degrades. This is also why a classical inertial navigator based on low-performance sensors could not be used with intermittent DME position fixing; a 15 second partial position fix does not provide sufficient information to allow updating the 15 element state vector of an inertial navigator.

One possible solution to this problem is to use primary and secondary surveillance radars. These radars are part of the NAS and will remain part of the terminal environment even after GPS becomes the primary means of navigation. These radars are normally installed at primary airports in a given terminal area. Radars of this sort are used in the current NAS for traffic separation. This means that these radars are capable of determining the position with an acceptable accuracy in the terminal

area. They are also capable of determining the position of an aircraft at a rate which is greater than the once every 30 seconds that is achievable by DME position fixing. In an alternate architecture of the backup navigation system, surveillance radars will be used for position fixing in lieu of DMEs. The radars are located on the ground and the navigation processor for the backup system is located in the airplane. Thus, to make this system work there must be a means of relaying the position fixes determined by the radars up to the aircraft. This can be achieved by using a data link such as ADS-B, which is currently projected to include an uplink of radar traffic.

Data links can also help to enhance the performance of the navigator in another way. With architecture of the backup navigator presented in this thesis, the factor that limited the system accuracy was the stochastic nature of the wind field. Currently, there is considerable work underway to construct accurate wind models. There is also considerable effort underway to devise ways of monitoring current wind conditions. If an accurate estimate of current wind information is available–determined either by accurate models or real-time measurements–the information can be relayed up to an aircraft via a data-link. This wind information can then be used by the dead reckoning navigator to generate an accurate position solution.

8.2.2 Novel Sensing and Sensor Fusion Concepts

Systems based on low cost solid state sensor technology are poised to bring enhanced operational capabilities to low-end users in the world of aviation. These capabilities are expected to increase safety in aviation sectors such as General and Business aviation. They are also expected to increase operational flexibility to all low-end users including UAVs. The Highway-In-The-Sky (HITS) concept reported in [12] and [6] is an example of an enhanced operational capability enabled by the low-cost AHRS technology discussed in Chapter 4.

GPS was a crucial component of the low cost systems discussed in Chapter 4. In the absence of GPS, making systems based on low cost sensors work involved augmenting the system either with speed information, knowledge of the platform dynamics or resorting to the use of expensive sensors. There are practical application, however, where GPS is not going to be available and the above mentioned augmentation methods will fail. For example, [71] discusses that head-trackers–devices used to

determine the attitude of a pilots head–will be required to make the (HITS) concept work in helicopters. Other practical applications that require attitude determination systems that do not rely on GPS are navigation of highly maneuverable/acrobatic UAVs or navigation in urban and indoor environments.

These applications will require novel sensor fusion concepts or new sensing technologies that will give GPS-like ranging information. In the area of new sensing and positioning methods, the challenge will be to explore what new technologies in sensing and communication can be exploited to serve as navigation sensors.

Appendix A

Inertial Navigation Error Equation

A.1 Introduction

The Inertial Navigation System (INS) equations which describe the time rate of change of velocity, position and attitude are non-linear. These equations are normally linearized when used in an estimator which blends the outputs of an INS with another sensor. The linearized equations are also used in covariance analyses to assess the performance of an INS as a function of sensor quality. These linearized equations are called the INS error equations and will be derived in this appendix.

A.2 INS Differential Equations

The INS equations are just a restatement of Newton's second law. That is, the time rate of change of velocity in an inertial frame of reference is equal to the product of mass and acceleration. They are a set of coupled differential equations describing the time rate of change of velocity, position and attitude. A detailed derivation of these equations can be found in texts such as [65] and [68] and will not be repeated here.

The differential equation describing the time rate of change of velocity in the locally level navigation frame (expressed in North, East, Down coordinates), is given by:

$$\dot{\vec{v}}^{\,n} = \overset{b\rightarrow n}{C}\,\vec{f}^{\,b} - (2\vec{\Omega}_e^n + \vec{\rho}^{\,n}) \times \vec{v}^{\,n} + \vec{g}^{\,n}. \tag{A.1}$$

The superscript "n" above the velocity vector, $\vec{v}$, indicates that the vector is being

expressed in the locally level navigation frame. The vector $\vec{f}^{\,b}$ is the specific force measurement generated by a triad of accelerometers fixed in the body frame of a vehicle. The superscript "b" indicates that this vector is expressed in the body frame. $\overset{b\to n}{C}$ is a direction cosine matrix that transforms the specific force vector from the body frame to the navigation frame. It is a function of the vehicle's attitude and, therefore, couples the velocity equations to the attitude equations. The vector $\vec{g}^{\,n}$ is the familiar gravitational acceleration vector expressed in the navigation frame. $\vec{\Omega}_e^n$ and $\vec{\rho}^{\,n}$ are Earth's rotation rate and the vehicle's transports rate vectors respectively expressed in the navigation frame.

The position channel differential equation is simply:

$$\dot{\vec{p}}^{\,n} = \overset{n\to g}{C}\ \vec{v}^{\,n}. \tag{A.2}$$

The vector $\vec{p}^{\,n}$ is the position vector expressed in geodetic coordinates (i.e., latitude, longitude and altitude). $\overset{n\to g}{C}$ is a transformation matrix that maps velocity expressed in North, East, Down coordinates into geodetic coordinates (i.e., latitude rate, longitude rate and altitude rate) and is given by:

$$\overset{n\to g}{C} = \begin{bmatrix} \frac{1}{(R_{NS}-h)} & 0 & 0 \\ 0 & \frac{1}{(R_{EW}-h)\cos(\Lambda)} & 0 \\ 0 & 0 & 1 \end{bmatrix}. \tag{A.3}$$

In developing these equations an ellipsoid Earth model is assumed. Thus, the north-south and east-west radii of Earth's curvature will not be the same. The variable R_{NS} is the radius of curvature in the north-south direction and is given by the following [65]:

$$R_{NS} = R_0(1 + f(3\sin^2(\Lambda) - 2)). \tag{A.4}$$

The variable R_{EW} is Earth's radius of curvature in the north-south direction given by:

$$R_{EW} = R_0(1 + f\sin^2(\Lambda)). \tag{A.5}$$

The variable f in the above equations is the flattening of Earth. The variable R_0 is the equatorial radius of Earth. The values for these variables are obtained from [58]

and are:

$$\begin{aligned} f &= 1/298.257223563 \\ R_0 &= 6378137.0 \text{ metres.} \end{aligned}$$

The direction cosine matrix, $\overset{b\to n}{C}$, must be known accurately to perform the velocity integrations. Computing $\overset{b\to n}{C}$ is the attitude determination problem. The direction cosine matrix is a function of the attitude quaternion and can be expressed as:

$$\overset{n\to b}{C}(\mathbf{q}) = \begin{bmatrix} 1-2({q_2}^2+{q_3}^2) & 2(q_1q_2+q_3q_0) & 2(q_1q_3-q_2q_0) \\ 2(q_1q_2-q_3q_0) & 1-2({q_1}^2+{q_3}^2) & 2(q_2q_3+q_0q_1) \\ 2(q_1q_3+q_2q_0) & 2(q_2q_3-q_1q_0) & 1-2({q_1}^2+{q_2}^2) \end{bmatrix}. \tag{A.6}$$

The time rate of change of the attitude quaternion is given by the following relation:

$$\dot{\mathbf{q}} = \frac{1}{2}\Omega\mathbf{q}. \tag{A.7}$$

The matrix Ω is a skew symmetric matrix given by:

$$\Omega = \begin{bmatrix} 0 & -p & -q & -r \\ p & 0 & r & -q \\ q & -r & 0 & p \\ r & q & -p & 0 \end{bmatrix}. \tag{A.8}$$

The variables p, q and r represent the angular rate output from the three orthogonal rate gyros. More specifically, p is the output of the rate gyro with its sensing axis aligned with the roll axis. Similarly, q is the pitch axis rate gyro output and r is the yaw axis gyro output.

A.3 INS Error Equations

INS error equations are derived by using a perturbation analysis. The three navigation error state vectors of interest are position errors ($\delta\vec{p}$), velocity errors ($\delta\vec{v}$) and attitude errors ($\delta\vec{\epsilon}$).

In the analysis that follows, the attitude errors are represented as small rotation of the about the NED coordinates. The variables $\delta\psi$, $\delta\theta$ and $\delta\phi$ are used represent these attitude errors. Thus, the attitude error vector $\delta\vec{\epsilon}$ is written as follows:

$$\delta\vec{\epsilon} = \begin{bmatrix} \delta\psi \\ \delta\theta \\ \delta\phi \end{bmatrix}. \tag{A.9}$$

In addition to the navigation errors, sensor error states can be included. The sensor error states are the accelerometer and gyro bias vectors denoted as $\delta\vec{f}$ and $\delta\vec{\omega}$, respectively. Once all the states of interest are defined, the overall INS error state vector, $\delta\vec{x}$, becomes a vector composed of the navigation error statesm $\delta\vec{p}$, $\delta\vec{v}$ and $\delta\vec{\epsilon}$, augmented by the sensor error states, $\delta\vec{f}$ and $\delta\vec{\omega}$. In vector notation, this INS error state vector is written as:

$$\delta\vec{x} = \begin{bmatrix} \delta\vec{p} \\ \delta\vec{v} \\ \delta\vec{\epsilon} \\ \delta\vec{f} \\ \delta\vec{\omega} \end{bmatrix}. \tag{A.10}$$

When expanded, this INS state vector can be written as:

$$\delta\vec{x} = \begin{bmatrix} \delta\Lambda \\ \delta\lambda \\ \delta h \\ \delta V_N \\ \delta V_E \\ \delta V_D \\ \delta\psi \\ \delta\theta \\ \delta\phi \\ \delta f_{sp_x} \\ \delta f_{sp_y} \\ \delta f_{sp_z} \\ \delta\omega_x \\ \delta\omega_y \\ \delta\omega_z \end{bmatrix} \tag{A.11}$$

The equations developed in the following sections will be expressed in terms of this state vector. The final objective of this analysis is to get a model for the error dynamics of an INS in the standard state-space form that can be written as follows:

$$\delta\dot{\vec{x}}_{INS} = F_{INS}\delta\vec{x}_{INS} + \Gamma_{INS}\vec{w}. \tag{A.12}$$

The matrix F_{INS} is a partitioned matrix of the following form:

$$F(t) = \begin{bmatrix} P2P & V2P & A2P & S2P & G2P \\ P2V & V2V & A2V & S2V & G2V \\ P2A & V2A & A2A & S2A & G2A \\ P2S & V2S & A2S & S2S & G2S \\ P2G & V2G & A2G & S2G & G2G \end{bmatrix} \tag{A.13}$$

where P, V, A, S, G stand for position, velocity, attitude, specific force and gyro (or angular rate) respectively. The notation P2P means "position to position," V2P

means "velocity to position," and so on. The entries of this matrix are obtained by linearization of the ,velocity and attitude equations.

A.3.1 Linearization of the Position Equation

The position error variables are latitude error ($\delta\Lambda$), longitude error ($\delta\lambda$) and altitude error (δh). The governing differential equations for the first two of these states (i.e., latitude rate, $\dot{\Lambda}$, and longitude rate, $\dot{\lambda}$) are given by:

$$\dot{\Lambda} = \frac{V_N}{(R_{NS} - h)} \tag{A.14}$$

and

$$\dot{\lambda} = \frac{V_E}{(R_{EW} - h)\cos(\Lambda)} \tag{A.15}$$

Altitude rate is simply the velocity in the down direction. That is:

$$\dot{h} = V_D. \tag{A.16}$$

A perturbation of these equations leads to the linearized position channel equations below:

$$\delta\dot{\Lambda} = \frac{\delta V_N}{(R_{NS} - h)} - \frac{V_N \delta h}{(R_{NS} - h)^2}. \tag{A.17}$$

$$\delta\dot{\lambda} = \frac{\delta V_E}{(R_{EW} - h)\cos(\Lambda)} - \frac{V_E \delta h}{(R_{EW} - h)^2 \cos(\Lambda)} + \frac{V_E \sin(\Lambda)\delta\Lambda}{(R_{EW} - h)\cos^2(\Lambda)}. \tag{A.18}$$

$$\delta\dot{h} = \delta V_D. \tag{A.19}$$

A.3.2 Linearization of the Velocity Equation

A perturbation of the velocity equation leads to:

$$\delta\dot{\vec{v}} = \delta\overset{b\to n}{C}\,\vec{f} - \overset{b\to n}{C}\,\delta\vec{f} - (2\delta\vec{\Omega}_e + \delta\vec{\rho}) \times \vec{v} - (2\vec{\Omega}_e + \vec{\rho}) \times \delta\vec{v} + \delta\vec{g}. \tag{A.20}$$

Each of the terms in the perturbation equation above will be discussed separately.

The $\overset{b\to n}{\delta C}\ \vec{f}$ Term

The first term in Equation A.20 is a perturbation of the direction cosine matrix. As shown in [32], this perturbation can be written as:

$$\overset{n\to b}{C} = \begin{bmatrix} 1 & \delta\psi & -\delta\theta \\ -\delta\psi & 1 & \delta\phi \\ \delta\theta & -\delta\phi & 1 \end{bmatrix} \tag{A.21}$$

which can be written in more compact form as

$$\overset{n\to b}{C} = I_{3\times 3} - [\delta\vec{\epsilon}]^{\times}. \tag{A.22}$$

Thus, the first term in Equation A.20 is written as:

$$\overset{b\to n}{\delta C}\ \vec{f} = \vec{f} - [\vec{f}_{sp}]^{\times}\delta\vec{\epsilon}. \tag{A.23}$$

The $\overset{b\to n}{C}\ \delta\vec{f}$ Term

The second term in Equation A.20 is self explanatory.

The $(2\delta\vec{\Omega}_e + \delta\vec{\rho}) \times \vec{v}$ Term

The third term involves perturbation of Earth's rotation rate, $\vec{\Omega}_e$, and transport rate, $\vec{\rho}$, vectors. Writing $\vec{\Omega}_e$ in NED coordinates:

$$\vec{\Omega}_e = \Omega_e \begin{bmatrix} \cos(\Lambda) \\ 0 \\ -\sin(\Lambda) \end{bmatrix} \tag{A.24}$$

Perturbation of this equations leads to:

$$\delta\vec{\Omega}_e = -\Omega_e \begin{bmatrix} \sin(\Lambda) \\ 0 \\ \cos(\Lambda) \end{bmatrix} \delta\Lambda \tag{A.25}$$

The transport rate vector is expressed in NED coordinates as:

$$\vec{\rho} = \begin{bmatrix} \dot{\lambda}\cos(\Lambda) \\ -\dot{\Lambda} \\ -\dot{\lambda}\sin(\Lambda) \end{bmatrix} \tag{A.26}$$

Perturbation of $\vec{\rho}$ leads to:

$$\delta\vec{\rho} = \begin{bmatrix} \frac{\delta V_E}{(R_{EW}-h)} - \frac{V_E \delta h}{(R_{EW}-h)^2} \\ -\frac{\delta V_N}{(R_{NS}-h)} + \frac{V_N \delta h}{(R_{NS}-h)^2} \\ -\frac{\delta V_E \tan(\Lambda)}{(R_{EW}-h)} + \frac{V_E \tan(\Lambda)\delta h}{(R_{EW}-h)^2} - \frac{V_E \sec^2(\Lambda)}{(R_{EW}-h)}\delta\Lambda \end{bmatrix} \tag{A.27}$$

Combining the perturbation of twice Earth's rotation rate vector with perturbation of the transport rate vector leads to:

$$2\delta\Omega_e + \delta\vec{\rho} = \begin{bmatrix} -2\Omega_e \sin(\Lambda)\delta\Lambda + \frac{\delta V_E}{(R_{EW}-h)} - \frac{V_E \delta h}{(R_{EW}-h)^2} \\ -\frac{\delta V_N}{(R_{NS}-h)} + \frac{V_N \delta h}{(R_{NS}-h)^2} \\ -2\Omega_e \cos(\Lambda)\delta\Lambda - \frac{\delta V_E \tan(\Lambda)}{(R_{EW}-h)} + \frac{V_E \delta h \tan(\Lambda)}{(R_{EW}-h)^2} - \frac{V_E \sec^2(\Lambda)}{(R_{EW}-h)}\delta\Lambda \end{bmatrix} \tag{A.28}$$

Carrying out the cross product of this term with $\vec{v}$ indicated in Equation A.20 leads to contributions to the $P2V$ and $V2V$ matrices.

The $(2\vec{\Omega}_e + \vec{\rho}) \times \delta\vec{v}$ Term

Perturbation of the fourth term in Equation A.20 is straight forward. Carrying out the perturbation and the associated cross product, leads to a contribution to the $V2V$.

The $\delta\vec{g}$ Term

Perturbation of the last term requires knowledge of the $\vec{g}$ field. A simple model for $\vec{g}$ in NED coordinates is given in [68] and can be written as follows:

$$\vec{g} = \begin{bmatrix} 0 \\ 0 \\ g_0 \frac{{R_0}^2}{(R_0-h)^2} \end{bmatrix} \tag{A.29}$$

The variable g_0 is the magnitude of the local gravitational acceleration which is latitude dependent. R_0 is the equatorial radius of Earth defined in [58] and is equal to 6378.137 km. Expanding the third term in the above equation using the binomial theorem, leads to:

$$g_0 \frac{{R_0}^2}{(R_0-h)^2} = g_0(1 + 2\frac{h}{R} + H.O.T) \tag{A.30}$$

where H.O.T stands for Higher Order Terms. Perturbation of this expanded form while ignoring higher order terms leads to:

$$\delta\vec{g} = \begin{bmatrix} 0 \\ 0 \\ 2g_0 \frac{\delta h}{R_0} \end{bmatrix} \tag{A.31}$$

A.3.3 Linearization of the Attitude Equations

The details behind linearization of the attitude equation will not be discussed here. The interested reader is referred to a thorough derivation in [32]. All that will be given here is a summary of the governing equations. Accordingly, if a state vector, δz, which is the attitude error vector augmented by the gyro biases is defined, then this vector is given by:

$$\delta\vec{z} = \begin{bmatrix} \delta\vec{\epsilon} \\ \delta\vec{\omega} \end{bmatrix}. \tag{A.32}$$

The dynamics for this state vector are given by the following equation:

$$\delta\dot{\vec{z}} = A\delta\vec{z} + B\vec{w}. \tag{A.33}$$

The A matrix above is defined as:

$$A = \begin{bmatrix} -[\overset{b\to n}{\omega}]^{\times} & I_{3\times 3} \\ 0_{3\times 3} & 0_{3\times 3} \end{bmatrix}. \tag{A.34}$$

The B matrix is given by:

$$B = \begin{bmatrix} -I_{3\times 3} & 0 \\ 0_{3\times 3} & I_{3\times 3} \end{bmatrix}. \tag{A.35}$$

The vector, $\vec{w}$, is the driving noise matrix which is composed of the sampling wide band noise, $\vec{n}_{gyro}$, on the rate gyros and the process noise that drives the the gyro biases, $\vec{w}_{bias}$. As such, this vector becomes:

$$\vec{w} = \begin{bmatrix} \vec{n}_{gyro} \\ \vec{w}_{bias} \end{bmatrix} \tag{A.36}$$

The quantity $\vec{n}_{gyro}$ is a quantity that can be measured directly. Determining $\vec{w}_{bias}$, however, requires knowledge of the gyro error characteristics. This requires developing a model for the gyro bias, $\delta\vec{\omega}$. For example, these biases can be modeled as a combination of a null-shift and a time varying component. For a certain class of gyros the time varying bias is modeled as a first order Gauss-Markov process. In this case, $\vec{w}_{bias}$ is now completely specified because its power spectral density will be known as it is a function of the variance and time constant of the Gauss-Markov process. Modeling the gyro biases in this way gives the following dynamic model:

$$\delta\dot{\vec{\omega}} = \begin{bmatrix} \delta\dot{\omega}_x \\ \delta\dot{\omega}_y \\ \delta\dot{\omega}_z \end{bmatrix} = \begin{bmatrix} -\frac{1}{\tau_{gyro}} & 0 & 0 \\ 0 & -\frac{1}{\tau_{gyro}} & 0 \\ 0 & 0 & -\frac{1}{\tau_{gyro}} \end{bmatrix} \begin{bmatrix} \delta\omega_x \\ \delta\omega_y \\ \delta\omega_z \end{bmatrix} + \vec{w}_{bias} \tag{A.37}$$

A similar argument can be carried out for models of the accelerometer biases. This completes derivation of the INS error equations.

Appendix B

Angle Random Walk

B.1 Introduction

In inertial navigation systems the output from a triad of rate gyros are integrated to yield the attitude quaternion or Euler angles. The error in the computed attitude grows as a function of time if the rate gyros have a null shift (bias) that has not been estimated and accounted for. Estimating of the null shift can be accomplished in real time using an estimator. This aspect of attitude determination was discussed in detail in Chapter 4. It was also noted in Chapter 4 that sensor noise contributes to the drift in the Euler angle estimates. In this appendix, a relationship for the the error growth rate in the Euler angle domain as a function of sensor noise is derived. In discrete time systems, this error is a function of sampling rate. The relationship between sampling rate and error growth rate will be derived.

B.2 Discrete Integration

The process of determining Euler angles is an integration process where the angular rate output from rate gyros is sent through an integrator to yield Euler angles. Let us assume that we are only looking at the pitch channel. If a system at rest is postulated, the input to the integrator will be wide-band noise. So the discrete time integration of this wide-band noise process leads to the pitch angle, θ, as a function of time given as follows:

$$\theta_{k+1} = \theta_k + \dot{\theta}_k \Delta t. \tag{B.1}$$

If this integration is carried out for n steps, the pitch angle estimate at the end of the n steps will be given by:

$$\theta_n = \left(\dot{\theta}_1 + \dot{\theta}_2 + \dot{\theta}_3 + \cdots + \dot{\theta}_{n-1}\right)\Delta t. \tag{B.2}$$

Squaring the estimate of θ at n time steps yields:

$${\theta_n}^2 = \left(\dot{\theta}_1^2 + \dot{\theta}_2^2 + \dot{\theta}_3^2 + \cdots + \dot{\theta}_{n-1}^2 + 2\dot{\theta}_1\dot{\theta}_2 + 2\dot{\theta}_1\dot{\theta}_3 + \cdots\right)\Delta t^2. \tag{B.3}$$

The variance ${\sigma_\theta}^2$ of the angle estimate is given by:

$$\begin{aligned} {\sigma_{\theta_n}}^2 &= \mathcal{E}\left[{\theta_n}^2\right] && \text{(B.4)}\\ &= \left(\mathcal{E}\left[\dot{\theta}_1^2\right] + \mathcal{E}\left[\dot{\theta}_2^2\right] + \cdots + \mathcal{E}\left[2\dot{\theta}_1\dot{\theta}_2\right] + \mathcal{E}\left[2\dot{\theta}_1\dot{\theta}_3\right] + \cdots\right)\Delta t^2. && \text{(B.5)} \end{aligned}$$

Since $\dot{\theta}$ is assumed to be an uncorrelated process, the expectation of the cross terms are zero. Furthermore, the expectation of $\dot{\theta}$ is nothing more than the standard deviation of the sensor noise. From this, the following is obtained:

$$\begin{aligned} {\sigma_{\theta_n}}^2 &= n\mathcal{E}\left[\dot{\theta}_2^2\right]\Delta t^2 && \text{(B.6)}\\ &= n{\sigma_{\dot{\theta}}}^2\Delta t^2 && \text{(B.7)} \end{aligned}$$

To express this in terms of sampling frequency, f_s, and duration of integration, T, it is noted that the sampling frequency is given by:

$$f_s = \frac{1}{\Delta t} \tag{B.8}$$

and that the duration of integration is given by:

$$T = n\Delta t. \tag{B.9}$$

Substituting this into the expression for ${\sigma_{\theta_n}}^2$ and taking square roots to get standard deviations leads to:

$$\sigma_{\theta_n} = \sigma_{\dot{\theta}}\sqrt{\frac{T}{f_s}} \tag{B.10}$$

From this result it can be seen that errors due to random walk are functions of both duration of integration and sampling frequency. The expression for the standard deviation of the random walk process collapses into a classical Brownian motion when the sampling frequency, f_s, goes to infinity. To show this, one notes that Equation B.2 can be written as a Riemann sum in the following manner:

$$\theta(t) = \sum_{k=1}^{N} \dot{\theta}_k \Delta t \tag{B.11}$$

When Δt becomes diminishingly small (i.e., f_s tends to infinity), the Riemann sum becomes an integral. From here on, the derivation continues as shown in [18] and reduces to the classical Brownian motion.

Appendix C

The Allan Variance

C.1 Introduction

The Allan variance can be viewed as the time domain equivalent of the power spectrum. Instead of power as a function of frequency it gives power as a function of averaging time. In this appendix the basic method of computing the Allan variance from a given batch of data will be presented. Without proof, the relationship between Allan variance and Power Spectral Density (PSD) will be given. Finally, some illustrative examples that show how error models can be constructed from Allan variance charts will be presented.

C.2 Computing the Allan Variance

Construction of an Allan variance chart begins by collecting data from the sensor we wish to model. The data will be a time series. That is, the collected data will be a vector of sensor output as a function of time. Given this sensor data, the methodology outlined below is used to generate the Allan variance. The procedure below and the results generated by it are given without any mathematical support. For the interested reader, a more thorough and theoretical treatment can be found in [67] and [59] which are based on the original work of D. W. Allan contained in [5].

Let us assume that the time series is a record of rate gyro outputs, $\omega(t)$ (in volts or deg/sec), as a function of time. Let us say that the data was sampled at a rate of f_s Hertz and recorded for T seconds. The total number of data points recorded is,

therefore, $N = f_s T$. Construction of an Allan variance chart using this data is done as follows:

1. Define a vector of averaging times, τ_{av}, as:

$$\tau_{av} = \left[\text{ 1 sec}, \quad \text{2 sec}, \quad \cdots \ , \quad \tfrac{T}{2} \text{ sec} \ \right]. \tag{C.1}$$

2. For each τ_{av}, divide the entire data record into $M = T/\tau_{av}$ clusters.

3. For each k^{th} cluster, compute the time average of ω. That is:

$$\bar{\omega}(k) = \frac{1}{\tau_{av}} \int_{t_k}^{t_k + \tau_{av}} \omega(t) dt \tag{C.2}$$

   For discrete data, use the discrete equivalent of the above expression which is:

$$\bar{\omega}(t) = \frac{1}{L} \sum_{i=1}^{L} \omega_i, \text{ where } L = f_s \tau_{av} \text{ and } k = 1, 2, 3, \cdots M \tag{C.3}$$

4. Use these cluster averages to form an new variable called the Allan variance (σ^2) which is defined as:

$$\sigma^2(\tau_{av}) = \frac{1}{2} \mathcal{E} \left[\bar{\omega}(k+1) - \bar{\omega}(k) \right]. \tag{C.4}$$

5. On a log-log scale, plot $\sigma(\tau_{av})$ versus τ_{av}. This is the Allan variance chart.

C.3 Identifying Error Mechanisms

It can be shown that the Allan variance is related to the PSD of the gyro output noise by the following equation [67].

$$\sigma^2(\tau_{av}) = \frac{4}{\pi \tau_{av}} \int_0^{\infty} S_\omega \left(\frac{u}{\pi T} \right) \frac{\sin^4(u)}{u^2} du \tag{C.5}$$

Using this and equations for the PSD of standard error mechanisms (i.e., wide band noise, flicker noise, quantization noise, etc.) we can derive expressions for the respective Allan variances. For example, let us consider sampling noise which is white and corrupts an otherwise "clean" angular rate output, ω, from a rate gyro. The autocorrelation function, $R(\tau)$, for this process is defined in terms of the Dirac Delta function, $\delta(\eta - \tau)$, and is given by the following:

$$R(\tau) = \mathcal{E}\{\omega(\eta)\omega(\tau)\} = Q^2\delta(\eta - \tau). \tag{C.6}$$

Q is a constant which is equal to the PSD for this white noise process. It has a magnitude equal to the noise amplitude and is normally given in units of deg/hr/$\sqrt{Hz}$ or deg/sec/$\sqrt{Hz}$. Substituting this into Equation C.5 and evaluating the integral gives:

$$\begin{aligned}
\sigma^2(\tau_{av}) &= \frac{4}{\pi\tau_{av}}\int_0^\infty Q^2\frac{\sin^4(u)}{u^2}du \\
&= \frac{4Q^2}{\pi\tau_{av}}\int_0^\infty \frac{\sin^4(u)}{u^2}du \\
&= \frac{4Q^2}{\pi\tau_{av}}\frac{\pi}{4} \\
&= \frac{Q^2}{\tau_{av}}
\end{aligned} \tag{C.7}$$

On a log-log plot, this will appear as a line with a slope of $-\frac{1}{2}$. It should be noted that the value of Q is the so-called *Angle Random Walk Parameter* (which should not be confused with *Rate Random Walk* which will be discussed later) given on rate integrating gyro specification sheets. On gyro specification sheets, however, this number is given in units of deg/$\sqrt{hr}$. This specification can be viewed as the expected *angular* random walk error when simply integrating the rate output. On the Allan variance chart, if $\sigma(\tau_{av})$ is given in units of deg/hr, Q can be picked off by looking at the point where $\tau_{av} = 1$. That is:

$$\begin{aligned}
\log_{10}(\sigma(\tau_{av})) &= \log(Q) - \log(\sqrt{1}) \\
&= \log(Q) \quad \text{when } \tau = 1.
\end{aligned} \tag{C.8}$$

Error Mechanism	Allan Variance Slope
Wide-Band Noise	$-\frac{1}{2}$
Exponentially Correlated Noise (First Order Gauss-Markov Process)	$+\frac{1}{2}$
Rate Random Walk	$+\frac{1}{2}$
Linear Rate Ramp	$+1$
Quantization Noise	-1
Sinusoidal Input	$+1$
Flicker Noise	0

Table C.1: Summary of Standard Error Sources and their Respective Allan Variance Slopes

If one performs a similar analysis with other error mechanisms, the results summarized in Table C.1 are obtained.

C.3.1 A Practical Example

In this section we will demonstrate using simulated data how the Allan variance works. It is shown how wide band noise, exponentially correlated noise and a ramp instability will manifest them selves on an Allan variance chart.

To demonstrate the behavior of wide band noise on an Allan variance chart, a simulated time series of a zero mean process corrupted by wide band noise is generated. A sampling frequency of 1 Hz and a noise amplitude of 0.05 deg/sec (which corresponds to a 0.05 deg/sec/$\sqrt{Hz}$ PSD) is selected. This noise amplitude is selected because it is consistent with a typical low cost rate gyro such as the Systron Donner Horizon. The length of the time series is 3 hours. This corresponds to 108,000 data points and the largest time constant for which the Allan variance is computed is 5400 seconds (1.5 hours). The cyan colored trace in Figure C.1 shows the Allan variance for this process. Note the characteristic -1/2 slope. Consistent with Equation C.8, the magnitude of the Allan variance at τ_{av} of 1 seconds is approximately equal to the power spectral density of the noise at the 1 Hz sampling rate.

The next error type to be explored is a rate random walk. This type of error

results from the integration of wide band noise. In the case of a rate gyro, this error manifests itself as a rate error that grows in an unbounded fashion. Although it is not a realistic error mechanism for a sensor, it is a good approximation of other realistic errors that will be examined later. To explore the effect of a rate random walk, a white noise sequence is passed through an integrator. The resulting time series is sampled at 1 Hz for 3 hours. The Allan variance for this sequence is shown as the blue trace in Figure C.1. The characteristic of this error mechanism is the +1/2 slope.

The next error type that will be examined is a ramp error. For a solid state rate gyro, a rate ramp would manifest itself as an angular rate output that grows linearly with time when the gyro is static. To demonstrate the effect of a rate ramp on the Allan variance, a simulated time series of a rate gyro output is generated. The output is corrupted by a rate ramp. The rate ramp selected grows at the rate of 1 deg/sec/hr. The time series is sampled at 1 Hz for 3 hours. The green trace in Figure C.1 is the Allan variance for this rate ramp and it clearly shows the characteristic slope of +1 for this process.

A very common type of output error seen in low cost rate gyros is that of an exponentially correlated noise or a Gauss-Markov process. This error mechanism is the output of a low pass filter where the input is a wide band noise. This is a realistic model for error mechanisms because it is a stochastic process with a finite variance. To demonstrate the effect of an exponentially correlated process on an Allan Variance plot, a simulated time series of a gyro output corrupted by this error mechanism is generated. The exponentially correlated process has a time constant of 1000 seconds and a variance of 0.05 deg/sec. The red trace on Figure C.1 shows the Allan variance for this error mechanism. A characteristic identifier for this error mechanism is the +1/2 slope.

When all of the previous error models are combined, they appear as the red trace on Figure C.2. For comparison purposes, a gyro output that is corrupted by errors in the form of wide band noise and an exponentially correlated process (with a time constant of 1000 seconds) only is plotted. It is the a blue line on Figure C.2 and is shown here because it is a common error model used in the performance analysis of inertial navigation systems.

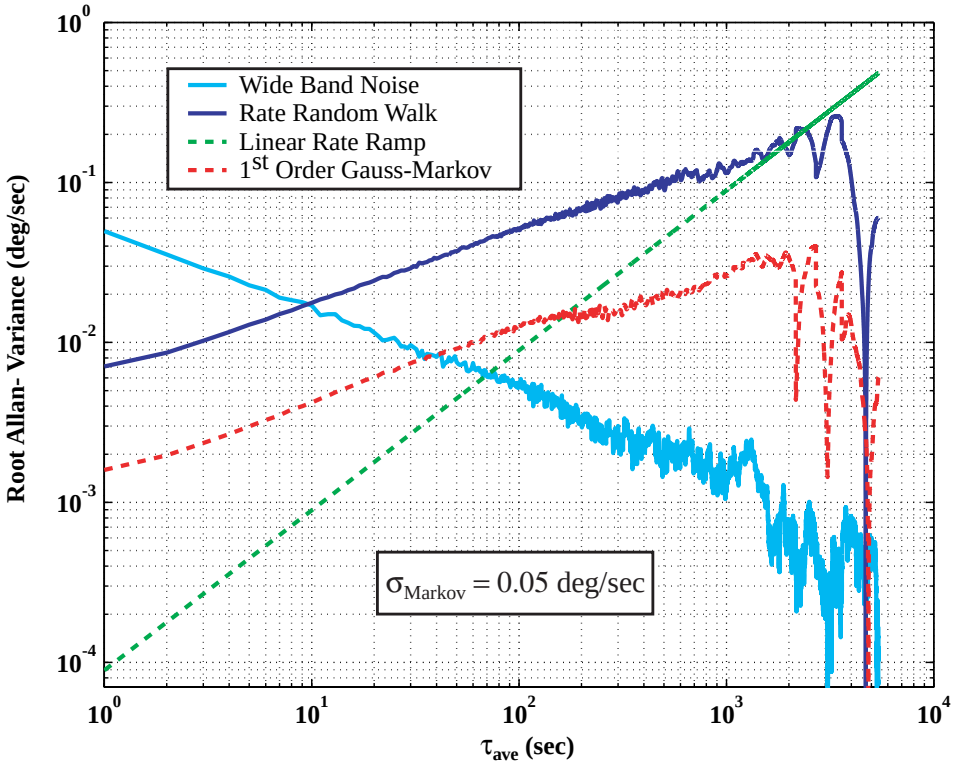

Figure C.1: Allan Variance for Various Error Mechanisms.

In closing, the relationship between the standard deviation of a first order Gauss-Markov process and its Allan variance chart should be noted. Figure C.3 is a schematic of an Allan variance chart for two separate first order Gauss-Markov processes. These two processes are referred to as time-series "A" and "B" in Figure C.3. They both have the same amount of wide-band noise but different Gauss-Markov components. For their respective Gauss-Markov components, they have the same time constant, τ, but different standard deviations. The standard deviation of "A" is larger than the standard deviation of "B." It can be seen that the effect of a larger standard deviation is to move the low-point of the Allan variance chart to the left towards smaller τ_{av} values.

In light of Figure C.3, we can better understand the error model for the Systron Donner "Horizon" rate gyro developed in Chapter 3. The model developed for this

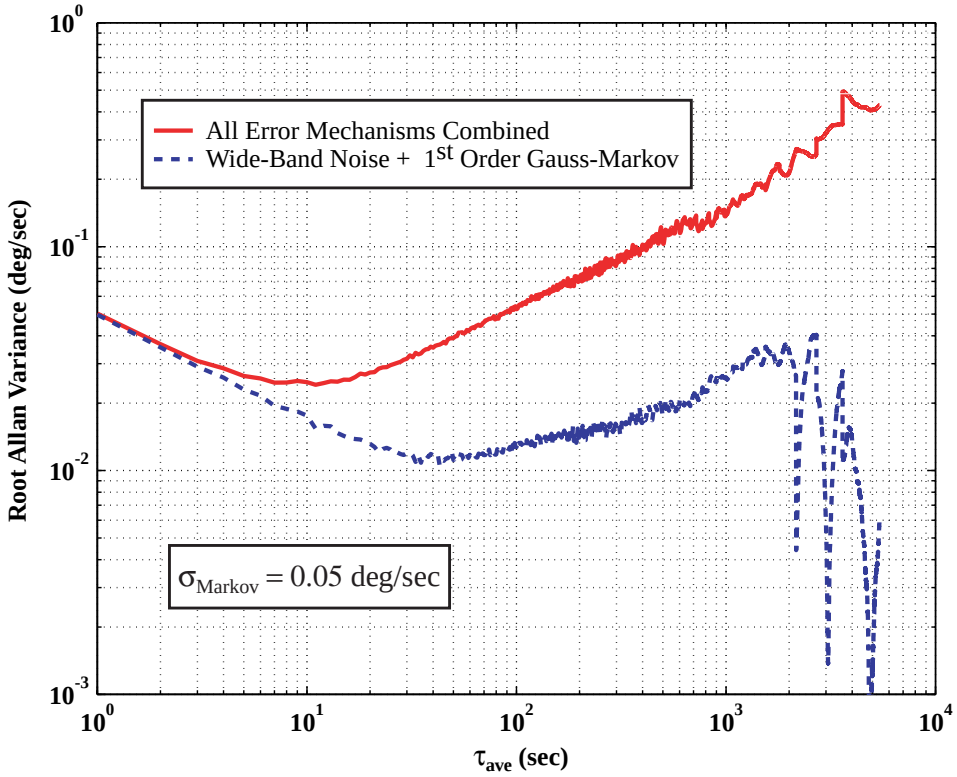

Figure C.2: Allan Variance for a Hypothetical Rate Gyro.

gyro (and subsequently used in Chapter 4) was based on a standard deviation 0.05 deg/sec for the Gauss-Markov component of the output error. The value of 0.05 deg/sec was the result of increasing the standard deviation of 0.01 deg/sec (due to purely stochastic causes) to account for temperature effects.

Figure C.4 shows the Allan variance for a simulated Systron Donner "Horizon" output where 0.01 deg/sec was used for the standard deviation of the Gauss-Markov component of the output error. It is seen that this Allan variance chart matches more closely the experimentally developed Allan variance chart shown in Figure 3.2 on page 44. This quantitatively shows the benefit of compensating for temperature effects; temperature compensation will increase the performance of the Systron Donner "Horizon" rate gyro.

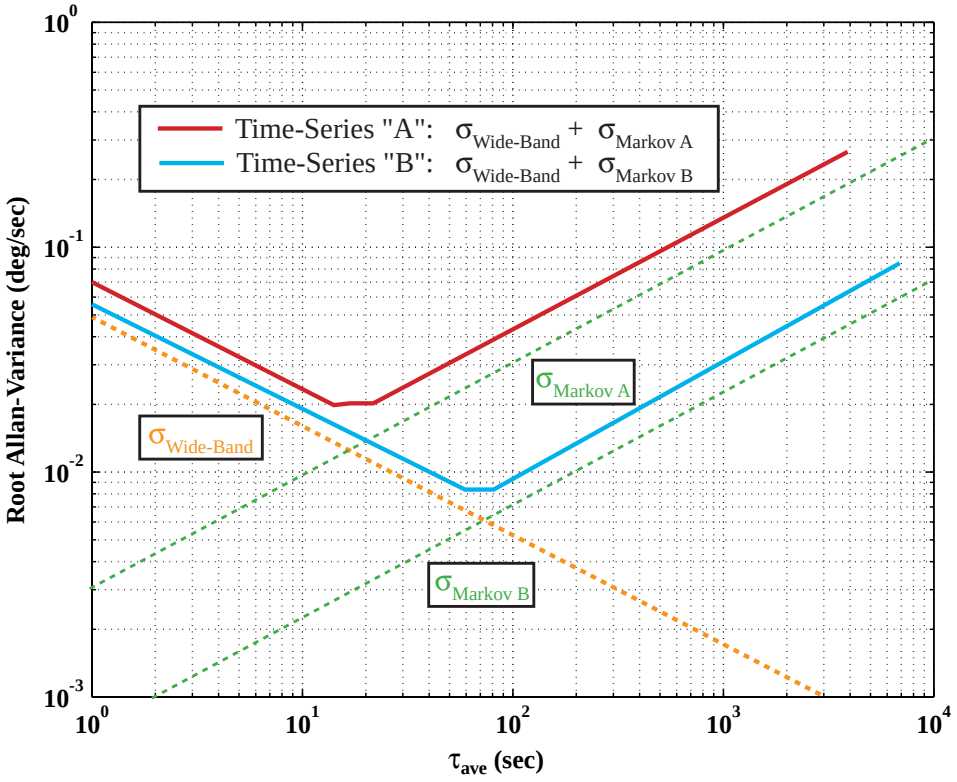

Figure C.3: Effect of Standard Deviation Magnitude on the Allan Variance Chart for a Hypothetical Rate Gyro.

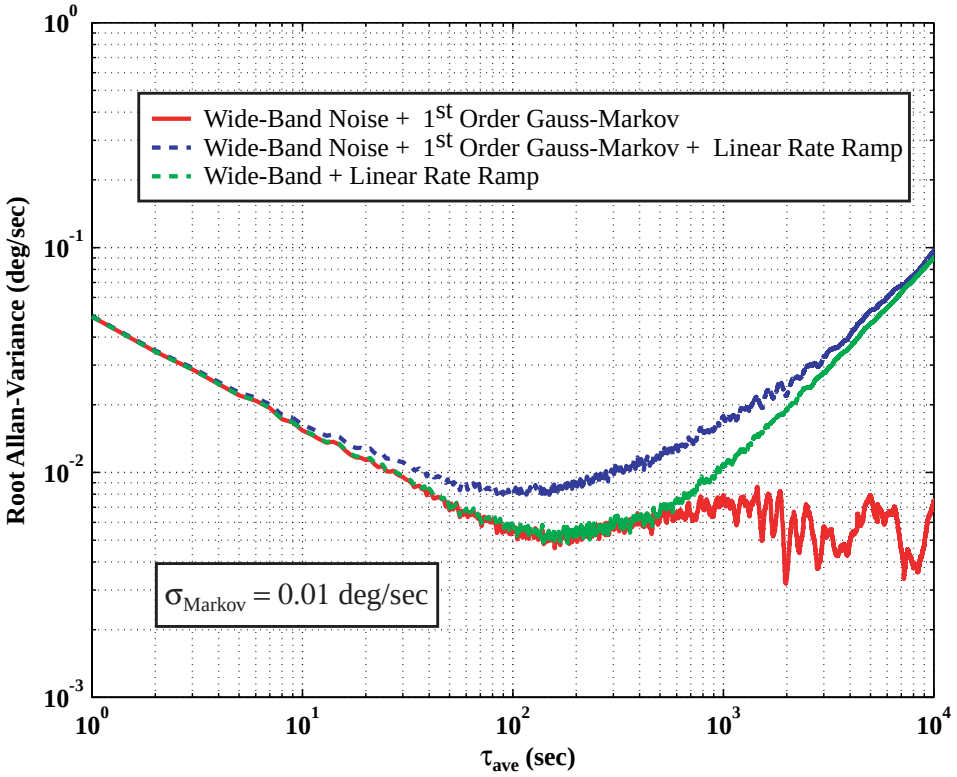

Figure C.4: Allan Variance for a Simulated Systron Donner "Horizon" Rate Gyro.

Appendix D

Position Fixing

D.1 Introduction

This appendix discusses the basics of position fixing. This discussion will begin by presenting the fundamental idea behind three basic position fixing methods; namely ρ-ρ, θ-θ, and ρ-θ position fixing. From the mathematical formulation of these problems, it will be seen that the position fixing equations are non-linear. The ρ-ρ position fixing problem will then be used as an example to demonstrate how to linearize and solve position fixing problems. Finally, an illustrative example comparing the accuracy of the three position fixing methods will be presented. From this example, it will be shown that, in the context of this thesis, ρ-ρ position fixing is superior to the to ρ-θ and θ-θ position fixing.

D.2 Basics of Position Fixing

When navigating on Earth's surface, it is possible to determine one's position by measuring the range or bearing to three distinct points at known geographical locations. The required range measurements can be obtained from systems such as GPS or DMEs while bearing measurements can be obtained from VORs or NDBs. The process of determining a user's position in this manner is called position fixing.

Mathematically, the position fixing problem is nothing more than solving three, coupled and non-linear equations for three unknowns. The three unknowns are the

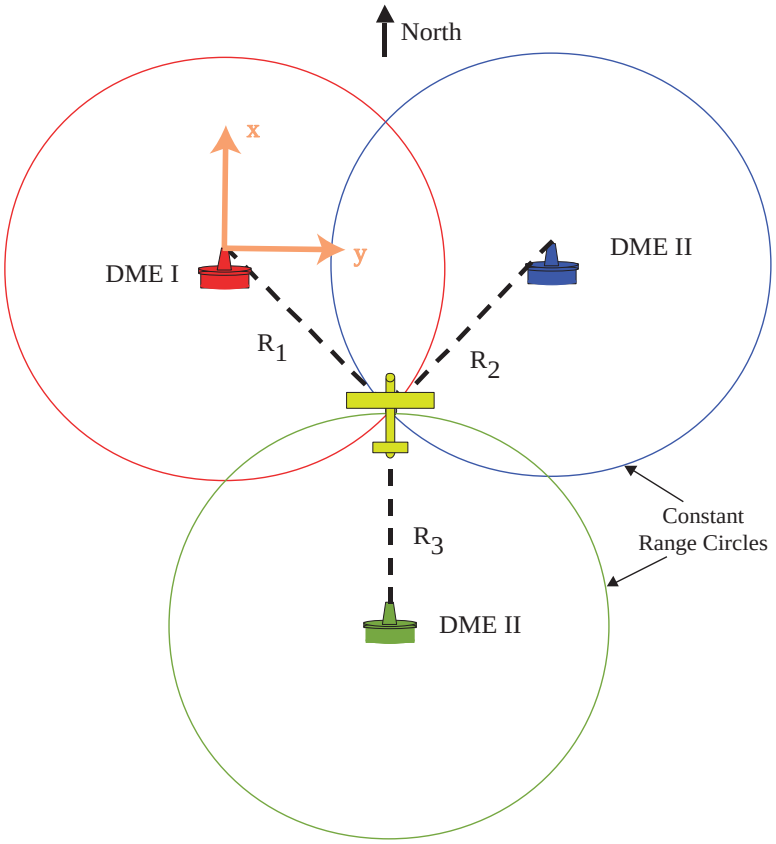

Figure D.1: Basics of ρ-ρ Position Fixing.

coordinates of the user's position. In most instances, position fixing is used to determine a user's lateral or horizontal position on the surface of Earth. In this case, the number of unknowns solved for is reduced from three to two. The known inputs into these coupled non-linear equations are multiple range, bearing or range and bearing measurements. When the inputs are multiple range measurements, the problem is called a ρ-ρ position fixing problem. When the inputs are bearing measurements, the problem is said to be a θ-θ problem. When the inputs are both range and bearing measurements, the problem is a ρ-θ problem.

Figure D.1 shows the basic idea behind ρ-ρ position fixing. In Figure D.1 a user is located at a position defined by the unknown coordinates, x, y, and z, where three separate DME range measurements are available. If, in the most general case, n

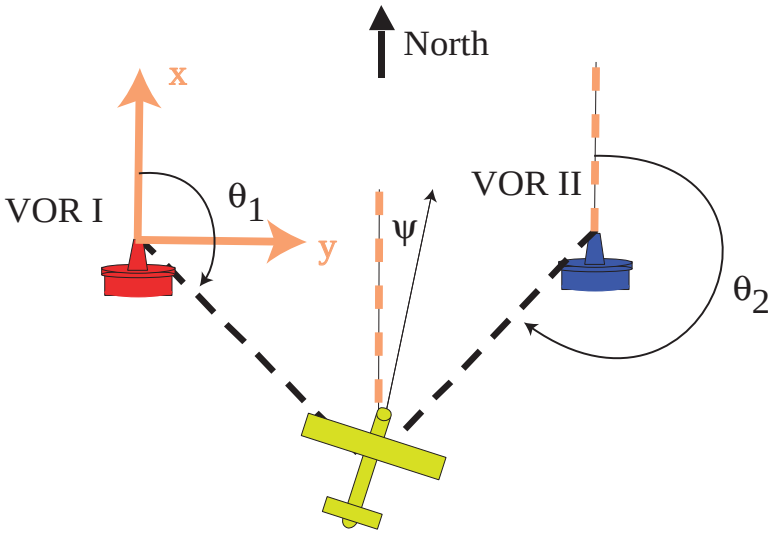

Figure D.2: Basics of θ-θ Position Fixing.

range measurements are available, the system of equations that is solved for this ρ-ρ position fixing problem is given by:

$$\begin{array}{rcccccc} {R_1}^2 & = & (x-x_1)^2 & + & (y-y_1)^2 & + & (z-z_1)^2 \\ {R_2}^2 & = & (x-x_2)^2 & + & (y-y_2)^2 & + & (z-z_2)^2 \\ {R_3}^2 & = & (x-x_3)^2 & + & (y-y_3)^2 & + & (z-z_3)^2 \\ \vdots & = & \vdots & + & \vdots & + & \vdots \\ {R_n}^2 & = & (x-x_n)^2 & + & (y-y_n)^2 & + & (z-z_n)^2. \end{array} \tag{D.1}$$

The variables x_i, y_i and z_i are the known coordinates of the i^{th} DME. If lateral position coordinates x and y are the only unknowns being solved for, the system of equations becomes:

$$\begin{array}{rcccc} {R_1}^2 & = & (x-x_1)^2 & + & (y-y_1)^2 \\ {R_2}^2 & = & (x-x_2)^2 & + & (y-y_2)^2 \\ {R_3}^2 & = & (x-x_3)^2 & + & (y-y_3)^2 \\ \vdots & = & \vdots & + & \vdots \\ {R_n}^2 & = & (x-x_n)^2 & + & (y-y_n)^2. \end{array} \tag{D.2}$$

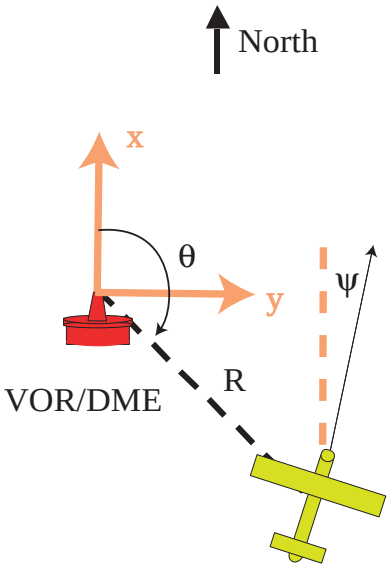

Figure D.3: Basics of ρ-θ Position Fixing.

Figure D.2 shows the basics of the θ-θ position fixing problem. In Figure D.2, it is assumed that (without loss of generality) VORs are being used to generate the bearing measurements. If the user's lateral position coordinates are the only unknowns being solved for, then, as shown in Figure D.2, only two bearing measurements are required. In this instance, the system of equations to be solved is:

$$\begin{aligned} \theta_1 &= \tan^{-1}\left(\tfrac{x-x_1}{y-y_1}\right) \\ \theta_2 &= \tan^{-1}\left(\tfrac{x-x_2}{y-y_2}\right). \end{aligned} \tag{D.3}$$

As shown in Figure D.2, ψ is the aircraft's heading with respect to true north, θ_i is the i^{th} bearing measurement and x_i and y_i are the position coordinates of the i^{th} VOR (which generates the i^{th} bearing measurement).

Finally, Figure D.3 shows the basic idea behind the ρ-θ position fixing. In Figure D.3, it is assumed that the bearing and range measurements are generated by a collocated VOR and DME. For the ρ-θ position fixing problem shown in Figure D.3,

the system of equations that is solved has the following form:

$$\begin{aligned} R^2 &= (x - x_1)^2 + (y - y_1)^2 \\ \theta &= \tan^{-1}\left(\frac{y - y_1}{x - x_1}\right). \end{aligned} \tag{D.4}$$

D.3 Solving the Position Fixing Equations

A practical and simple solution to the ρ-ρ position fixing problem is based on a linearization of the fundamental position fixing relation given in Equations D.1 and Equation D.2. Only the ρ-ρ case is discussed here, because the method of solving the θ-θ and the ρ-θ problems is fundamentally the same.

Considering the case where the only unknowns are the lateral position coordinates, Equation D.2 can be linearized by perturbing it about some initial estimated position given by coordinates $\hat{x}$ and $\hat{y}$. That is,

$$\delta R_i = \frac{\partial R_i}{\partial x}\delta x + \frac{\partial R_i}{\partial y}\delta y. \tag{D.5}$$

R_i is the i^{th} range measurement. The quantity δx is the difference between $\hat{x}$ and x. That is, it is the error in the initial estimate of x. Similarly, δy is the error in the initial estimate of y and is defined to be the difference between $\hat{y}$ and y. Thus, using the above notation, a perturbation to linearize Equation D.1 leads to the following matrix equation:

$$\begin{bmatrix} \delta R_1 \\ \delta R_2 \end{bmatrix} = \begin{bmatrix} \frac{(\hat{x}-x_1)}{\hat{R}_1} & \frac{(\hat{y}-y_1)}{\hat{R}_1} \\ \frac{(\hat{x}-x_2)}{\hat{R}_2} & \frac{(\hat{y}-y_2)}{\hat{R}_2} \\ \frac{(\hat{x}-x_3)}{\hat{R}_3} & \frac{(\hat{y}-y_3)}{\hat{R}_3} \end{bmatrix} \begin{bmatrix} \delta x \\ \delta y \end{bmatrix} \tag{D.6}$$

The notation δR_i is used to represent the difference $\hat{R}_i - R_i$ where $\hat{R}_i$ is the estimate of R_i. This is a computed value which is a function of $\hat{x}$, $\hat{y}$, x_i and y_i given by the following:

$$\hat{R}_i^2 = (\hat{x} - x_i)^2 + (\hat{y} - y_i)^2. \tag{D.7}$$

Using matrix notation, Equation D.6 can be written in a more compact form as

follows:

$$\delta\vec{r} = H\delta\vec{p}. \tag{D.8}$$

The vector $\delta\vec{r}$ is the difference between the measured and estimated range to the two DME transmitters, H is the measurement geometry matrix and $\delta\vec{p}$ is a vector of the position errors. Given an estimate of one's initial position $\hat{\vec{p}}^{(-)} = [\hat{x}\,\hat{y}]^T$, a simple algorithm for determining position using this linearized equation can be implemented as follows:

1. Compute H using $\hat{\vec{p}}^{(-)}$.
2. Compute $H^\dagger$, the pseudo-inverse of H. That is, $H^\dagger = [H^T H]^{-1} H^T$
3. $\delta\vec{p} = \alpha H^\dagger \delta\vec{r}$. The factor α is a tuning parameter or gain that can be adjusted to control stability and convergence speed of the algorithm.
4. $\hat{\vec{p}}^{(+)} = \hat{\vec{p}}^{(-)} + \delta\vec{p}$.
5. Return to Step (2), replace $\hat{\vec{p}}^{(+)}$ in lieu of $\hat{\vec{p}}^{(-)}$ and repeat until the solution converges.

D.4 Position Fixing Error Ellipses

One method for comparing the performance of the various position fixing schemes entails generating error ellipses. To understand the meaning of error ellipses, consider the ρ-ρ position fixing problem based on DME range measurements. Let us assume that the only error corrupting the DME range measurements is stochastic wide band noise. Since the measurement error is stochastic, it is reasonable to assume that the resulting position errors will also be stochastic. This is indeed the case, and an error ellipse is nothing more than the 1-σ (or 1-standard deviation) bound for the position errors. It is a graphical representation of how wide-band noise on the range measurement maps into position errors. In a more general sense, it is a graphical depiction of how navigation (or position fixing) sensor errors map into position errors. The interested reader will find a more precise mathematical definition of error ellipses in [19] and [49].

Generating error ellipses requires linearizing the position fixing equations because the dimensions of the error ellipse are functions of the measurement geometry matrix,

H, and the variance of the wide band noise corrupting the DME range measurements, σ_r^2. More precisely, consider a user at a position defined by the position vector, $\vec{p}$, given by:

$$\vec{p} = \begin{bmatrix} x \\ y \end{bmatrix}. \tag{D.9}$$

The variables x and y are the lateral coordinates of $\vec{p}$. The estimated position vector, $\hat{\vec{p}}$, is the position solution computed by using DME range measurements that are corrupted by stochastic sensor error. Thus, the position error vector, $\delta\vec{p}$, is equal to the difference $\vec{p} - \hat{\vec{p}}$. The position error covariance matrix, P, which is defined as

$$P = \mathcal{E}\{\delta\vec{p}\,\delta\vec{p}^{T}\}, \tag{D.10}$$

is a measure of the spatial scatter in the estimated (or computed) position solution around the vicinity of the actual position, $\vec{p}$. The position error covariance matrix, P, is computed using the following expression.

$$P = {\sigma_r}^2 \left(H^T H\right)^{-1} H^T. \tag{D.11}$$

The error ellipses are related to the position error covariance matrix, P because the major and minor axes of the error ellipse are equal to the square root of the eigenvalues of P^{-1}. Furthermore, the orientation of the orthogonal major and minor axes of the ellipse are defined by the eigenvectors of P^{-1}. Once the magnitude and orientation of the major and minor axes are identified, the error ellipse can be sketched easily.

The procedure for generating error ellipses for the other two position fixing methods is the same. That is, it requires linearizing the governing system of equations in order to generate the measurement geometry matrix, H. Then, using the variance of the measurement noise, the position error covariance matrix, P, is constructed. Computing the eigenvalues and eigenvectors of the inverse of the position error covariance matrix, P^{-1}, yields all the information needed to construct the error ellipse.

D.5 An Illustrative Example

The following is an example adapted from [64] and will be used to demonstrate how error ellipses can be used to evaluate the performance of the various position fixing schemes. In the context of this thesis, the objective of this example is to illustrate that ρ-ρ position fixing is superior to both ρ-θ and θ-θ position fixing. Thus, it is the justification for the choice of a future National Airspace System architecture that retains a skeletal network of DMEs in lieu of a skeletal network of VORs or NDBs.

The problem setup is shown in Figure D.4. The objective of the problem is to generate the best estimate of the aircraft's location via position fixing. The range and bearing information needed for position fixing comes from the pair of collocated VOR/DME transmitters shown in Figure D.4. The VOR and DME transmitters labeled A are located at (North, East) = $(8.6, -1.5)$ n.mi. while the transmitter pair labeled B is at $(7.6, 14.9)$ n.mi. Furthermore, as depicted in Figure D.4, the following VOR/DME (ρ and θ) measurements are made by the user in the airplane:

1. From Transmitter A - VOR Bearing is 187° and DME distance is 13.9 n.mi.

2. From Transmitter B - VOR Bearing is 226°, DME distance 24.7 n.mi.

The range and bearing measurements are corrupted by wide band noise. In Chapter 3 a DME range measurement error model was developed. This model gave the standard deviation of the wide-band noise on the DME range measurement, σ_{rw}, to be 0.004 n.mi. The standard deviation on the correlated noise, σ_{wr}, was given as 0.17 n.mi. To be conservative, the DME range measurement noise standard deviation that to be used in this analysis will be 0.17 n.mi. Furthermore, in accordance with discussions in [15], [33] and [49], the standard deviation of the VOR bearing measurement noise is taken to be 1 degree.

In this instance, there are five options for the position fixing. The options available are:

1. ρ-ρ position fixing

2. θ-θ position fixing

3. ρ-θ position fixing using Transmitter pair A.

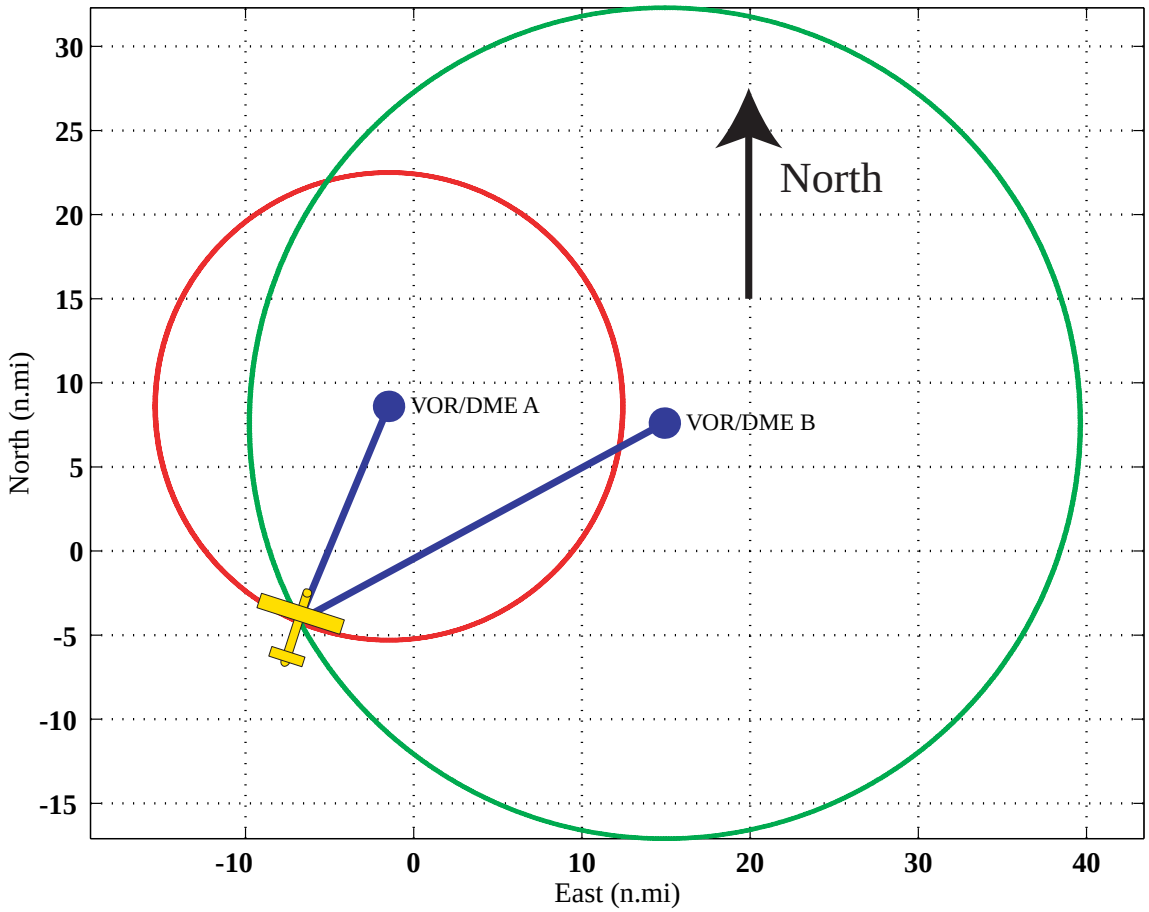

Figure D.4: DME Range Circles.

4. ρ-θ position fixing using Transmitter pair B.

5. Weighted Least Squares (WLS) using all four measurements.

Just by looking at Figure D.4, an initial, but accurate guess of the user location can be made. Using this location and the procedure outlined in the previous section, error ellipses for the five schemes of position fixing can be made. Figure D.5 shows the error ellipses for all five cases. Table D.1 lists the dimensions of the major and minor axes of the various methods.

As can be seen form Figure D.5 and Table D.1, using all four measurements in a

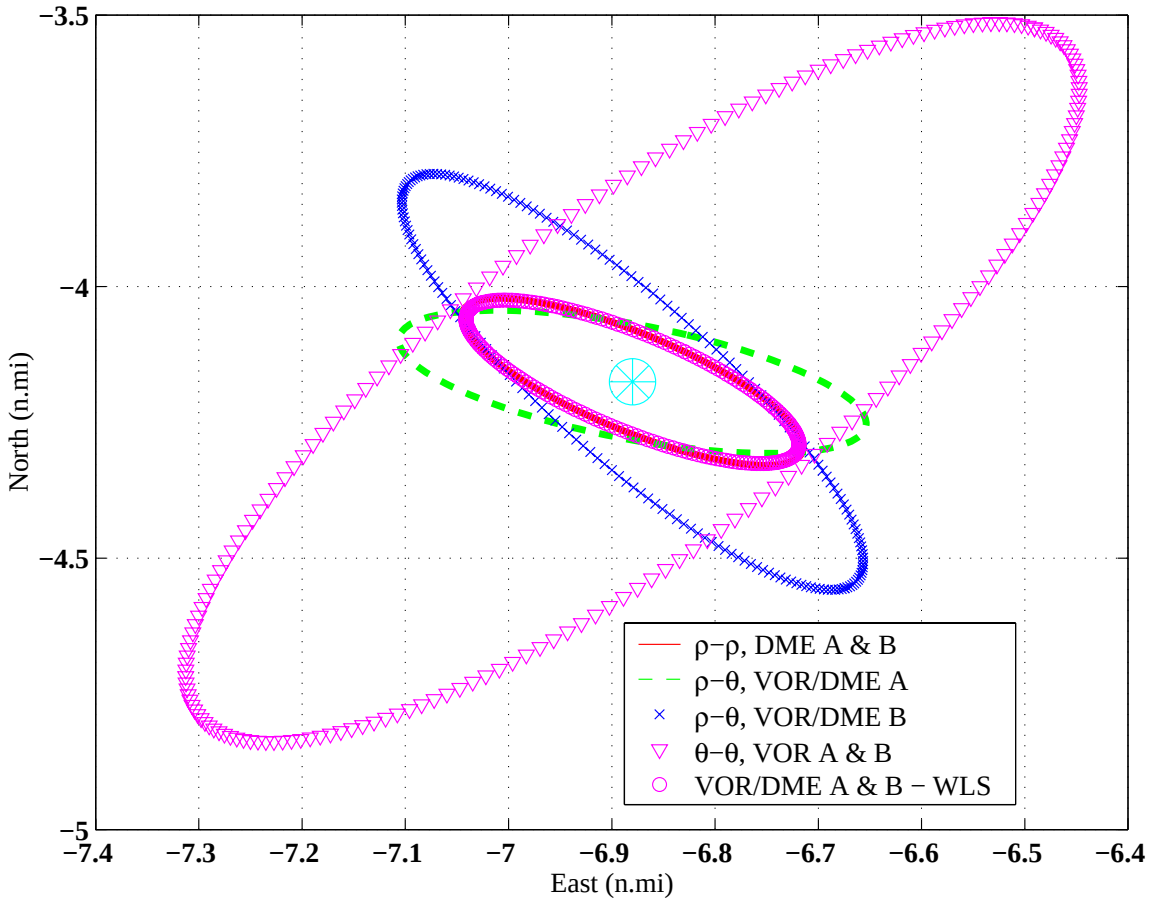

Figure D.5: Error Ellipses for the Various Methods of Position Fixing.

weighted least squares solution yields the best result (i.e., the smallest error ellipse). However, the accuracy of this position solution is comparable to the ρ-ρ position fixing using the two DME range measurements only. Thus, it is seen that including bearing measurements does not appreciably improve the position solution generated by ρ-ρ position fixing. So, the optimum solution (i.e., one that achieves maximum accuracy with fewer measurements) is to use the two DME range measurements only.

In closing it is noted that, in Chapters 1 and 2 of this thesis, it was proposed that retaining a skeletal network of DMEs in lieu of VORs would result in a cost savings for NAS infrastructure maintenance. This illustrative example showed that another

Method	Minor Axis (n.mi)	Major Axis (n.mi)
$\rho - \rho$ DME A and B	0.0750	0.2131
$\rho - \theta$ VOR/DME A	0.1003	0.2419
$\rho - \theta$ VOR/DME B	0.0998	0.4321
$\theta - \theta$ VOR A and B	0.2198	0.7598
Weighted Least Squares (WLS)	0.0749	0.2075

Table D.1: Error Ellipse Dimensions.

added benefit of retaining DMEs is increased accuracy in the resultant position fixing solution.

Bibliography

[1] Eric C. Abbott. *Land-Vehicle Navigation Systems: An Examination of the Influence of Individual Navigation Aids on System Performance*. PhD thesis, Stanford University, Stanford, California 94305, March 1997.

[2] Federal Aviation Administration. *GPS Transistion Plan*. FAA, Washington, D.C, 1998.

[3] Federal Aviation Adminstration. *Airman's Information Manual*. U.S. Department of Transportation, Washington, D.C., 2000.

[4] Federal Aviation Adminstration. *Title 14 CFR, Part 23: Airworthiness Standards: Normal, Utility, Acrobatic, and Commuter Category Airplanes*. Department of Transportation, Washington, D.C., 2000.

[5] D. W. Allan. Statistics of Atomic Frequency Standards. *Proceedings of the IEEE*, 54(2):221–230, February 1966.

[6] Keith W. Alter. *GPS 3-D Cockpit Displays: Sensors, Algorithms, and Flight Testing*. PhD thesis, Stanford University, Stanford, California 94305, December 2001.

[7] Vidal Askenazi, Terry Moore, and et. al. The Use of Airborne Differential GPS to Detect Coordinate and Calibration Errors in DME Navigation Aids. In *Proceedings of the Institute of Navigation ION-GPS, Salt Lake City, UT, ION-GPS 1994*, pages 965 – 972. ION, 1994.

[8] General Aviation Manufacturers Association. *1999 General Aviation Statistical Handbook*. General Aviation Manufacturers Association, Washington, D.C., 1999.

[9] I.Y. Bar-Itzhack and M. Idan. Recursive Attitude Determination from Vector Observations: Euler Angle Estimation. *AIAA Journal of Guidance Control and Navigation*, 10(2):152 – 157, March - April 1987.

[10] I.Y. Bar-Itzhack and Y. Oshman. Attitude Determination from Vector Observations: Quaternion Estimation. *IEEE Transactions on Aerospace Electronic Systems*, 21(1):128 – 135, January 1985.

[11] I.Y. Bar-Itzhack and J. Reiner. Estimation of Rodrigues Parameters from Vector Observations. *IEEE Transaction on Aerospace Electronic Systems*, 32(2):578 – 585, April 1996.

[12] Andrew K. Barrows. *GPS 3-D Cockpit Displays: Sensors, Algorithms, and Flight Testing*. PhD thesis, Stanford University, Stanford, California 94305, May 2000.

[13] C.E. Barton. Revision of International Geomagnetic Reference Field Release. *EOS Transactions*, 77(16), April 1996.

[14] Zeev Berman and J. D. Powell. The Role of Dead Reckoning and Inertial Sensors in Future General Aviation Navigation. In *Proceedings of the IEEE Position Location and Navigation Symposium, PLANS 1998*, pages 510 – 517. IEEE, 1998.

[15] John C. Bobick. *Improved Navigation by Combining VOR/DME Information with Air or Inertial Data*. PhD thesis, Stanford University, Stanford, California 94305, December 1972.

[16] Nathaniel Bowditch. *The American Practical Navigator*. Defense Mapping Agency, Hydrographic/Topographic Center, Bethesda, Maryland, USA, 1995.

[17] Michael S. Braasch. Current Developments in Signal Modeling of the Precision Distance Measuring Equipment. Master's thesis, Ohio University, Athens, Ohio, November 1989.

[18] Robert Grover Brown and Patrick Y.C. Hwang. *Introduction to Random Signals and Applied Kalman Filtering*. J. Wiley, New York, New York, 2^{nd} edition, 1992.

[19] Arthur E. Bryson and Yu-Chi Ho. *Applied Optimal Control*. Hemisphere Publishing Corp., 1975.

[20] Heinz Buell and Leonid Oleinik. The AN/ASN-128B: An Integrated Doppler/GPS Navigation System for Helicopters. *Navigation: Journal of the Institute of Navigation*, 45(3):173 – 182, 1998.

[21] Michael J. Caruso. Application of Magnetic Sensors for Low Cost Compass Systems. In *Proceedings of the IEEE Position Location and Navigation Symposium, PLANS 2000*, pages 177 – 184. IEEE, 2000.

[22] Tim Cashin, Donna Kraus, and Bryant Elrod. New WAAS Test Results with the NSTB. *ION Global Positioning System: Selected Papers on Satellite Based Augmentation Systems (SBASs)*, 6:435 – 455, 1999.

[23] Clark E. Cohen. *Attitude Determination Using GPS*. PhD thesis, Stanford University, Stanford, California 94305, December 1992.

[24] Glenn Colby, Michel Smith, and et. al. Test Results of the Joint FAA/DOD Investigation of GPS Interference. *Air Traffic Control Quarterly*, 4:5 – 76, October 1996.

[25] RTCA Special Committee-159. *Minimum Operation Performance Standards for Airborne Equipment Using Global Positioning System-Wide Area Augmentation System*. RTCA, Washington, D.C., 1998.

[26] The Boeing Company. *777-200 Operations Manual*. The Boeing Company, 1994.

[27] T. M. Corrigan. *GPS Risk Assessement Study*. The John Hopkins University, Applied Physics Laboratory, 1999.

[28] G. Creamer. Spacecraft Attitude Determination Using Gyros and Quaternion Measurements. *The Journal of Astronautical Sciences*, 44(3):357 – 371, July - September 1996.

[29] J. R. Crowe. Federal Radionavigation Plan–Pie in the Sky for Civil Aviation? In *Proceedings of the IEEE Position Location and Navigation Symposium, PLANS 1998*, pages 115 – 122. IEEE, 1998.

[30] Gabriel H. Elkaim. *System Identification for Precision Control of a GPS-Autonomous Catamaran*. PhD thesis, Stanford University, Stanford, California 94305, August 2001.

[31] Per Enge, Eric Swanson, and et. al. Terrerstrial Raionavigation Technologies. *Navigation*, 42(1):61 – 108, Spring 1995.

[32] Jay A. Farrell and Matthew Barth. *The Global Positioning System and Inertial Navigation*. McGraw Hill, New York, New York, 1999.

[33] B. Forssell. *Radionavigation Systems*. Prentice Hall, New York, New York, 1991.

[34] Gene F. Franklin, J. David. Powell, and Michael L. Workman. *Digital Control of Dynamic Systems*. Addison Wesley, Menlo Park,CA, 1994.

[35] Bernard Friedland. *Control System Design: An Introduction to State Space Methods*. McGraw-Hill, New York, New York, 1986.

[36] D. Gebre-Egziabher, G. H. Elkaim, J. D. Powell, and B. W. Parkinson. A Gyro-Free, Quaternion Based Attitude Determination System Suitable for Implementation Using Low-Cost Sensors. In *Proceedings of the IEEE Position Location and Navigation Symposium, PLANS 2000*, pages 185 – 192. IEEE, 2000.

[37] D. Gebre-Egziabher, G. H. Elkaim, J. D. Powell, and B. W. Parkinson. A Non-Linear, Optimal Two-Step Estimation Algorithm for Calibrating Solid-State Strapdown Magnetometers. In *Proceedings of the Eighth International Conference on Integrated Navigation Systems, St. Petersburg Russia, May 2001*. IEEE, 2001.

[38] D. Gebre-Egziabher, R. C. Hayward, and J. D. Powell. GPS-Based Attitude and Guidance Displays for General Aviation. In *Proceedings of the IEEE Emerging Technologies and Factory Automation Symposium, Kauai, HI*. IEEE, 1996.

[39] D. Gebre-Egziabher, R. C. Hayward, and J. D. Powell. A Low Cost GPS/Inertial Attitude Heading Reference System (AHRS) for General Aviation Applications. In *Proceedings of the IEEE Position Location and Navigation Symposium, PLANS 1998*, pages 518 – 525. IEEE, 1998.

[40] Arthur Gelb. *Applied Optimal Estimation*. The MIT Press, Cambridge, Massachusetts, 1974.

[41] United States Coast Guard. *LORAN-C User Handbook*. U.S. Government Printing Office, Washington, D.C., 1992.

[42] Gordon Thomas Haupt. *Development and Experimental Verification of A Nonlinear Data Reduction Algorithm for Gravity Probe B Relativity Mission*. PhD thesis, Stanford University, Stanford, California 94305, March 1996.

[43] R. C. Hayward, D. Gebre-Egziabher, M. Schwall, J. D. Powell, and J. Wilson. Inertially Aided GPS Based Attitude Heading Reference System (AHRS) for General Aviation Aircraft. In *Proceedings of the Institute of Navigation ION-GPS Conference*, pages 1415 – 1424. ION, 1997.

[44] R. C. Hayward, A. Marchick, and J. D. Powell. Two Antenna GPS Attitude and Integer Ambiguity Resolution for Aircraft Applications. In *Proceedings of the Institute of Navigation National Technical Meeting ION-NTM, San Diego, CA, ION-NTM 1999*. ION, 1999.

[45] J. B. Hewson. *A History of the Practice of Navigation*. Brown, Son and Ferguson, LTD., Glasgow, United Kingdom, 1951.

[46] Alfred Hine. *Magnetic Compasses and Magnetometers*. Adam Hilger LTD., London, U.K., 1968.

[47] ICAO. *International Standards and Recommended Practices–Aeronautical Telecommunications, Annex 10 to the Convention on International Civil Aviation*. ICAO, 1985.

[48] J. N. Juang. *Applied System Identification*. Prentice Hall, NJ, 1994.

[49] Myron Kayton and Walter R. Fried. *Avionics Navigation Systems*. John Wiley and Sons, Inc, New York, New York, 2^{nd} edition, 1997.

[50] R. J. Kelly. System Considerations for the New DME/P International Standard. *IEEE Transactions on Aerospace Electronic Systems*, 20(1):2 – 24, January 1984.

[51] Jack B. Kuipers. *Quaternions and Rotation Sequences*. Princeton University Press, Princeton, New Jersey, 1999.

[52] Anthony Lawrence. *Modern Inertial Technology: Navigation, Guidance and Control*. Springer Verlag, New York, New York, 1998.

[53] Litton. *LN-200 Fiber Optic Inertial Measurement Unit Specification Sheet*. Litton Guidance and Control Systems, Woodland Hills, CA, 1998.

[54] Lennart Ljung. *Sytem Identification: Theory for the User*. Prentice Hall, Englewood Cliffs, New Jersey, 1987.

[55] Kelly Markin. *Development and Performance Assessment of Alternative Navigation Architectures*. The MITRE Corporation, McLean, VA, 2000.

[56] Richard Von Mises. *Theory of Flight*. Dover, New York, New York, 1959.

[57] Paul Y. Montgomery. *Carrier Differential GPS As A Sensor for Automatic Control*. PhD thesis, Stanford University, Stanford, California 94305, June 1996.

[58] National Imagery and Mapping Agency, Bethesda, MD. *United States Department of Defense, World Geodetic System 1984, Its Definition and Relationships With Local Geodetic Systems, Third Edition*, 1997.

[59] Lawrence C. Ng and Darryll J. Pines. Characterization of Ring Laser Gyro Performance Using the Allan-Variance Method. *AIAA Journal of Guidance Control and Navigation*, 20(1):211–213, July - August 1984.

[60] Aircraft Owners and Pilots Association. *AOPA's 1999 Aviation Fact Card*. Aircraft Owners and Pilots Association, Fredrick, MD., 1999.

[61] Bradford W. Parkinson and James J. Spilker Jr. *Global Positioning System: Theory and Applications*, volume 1 and 2. AIAA, Washington D.C., 1996.

[62] Boris S. Pervan. *Navigation Integrity for Aircraft Precision Landing Using the Global Positioning System*. PhD thesis, Stanford University, Stanford, California 94305, March 1996.

[63] J. David Powell. A Proposal to Study GPS-Based Attitude and Velocity Estimation for General Aviation. Technical Report AERO34-94, Department of Aeronautics and Astronautics, Stanford University, Stanford, CA, 94305, March 1994.

[64] J. David Powell. *Unpublished Class Notes for AA272B: Introduction to Radio and Inertial Navigation*. Stanford University, Stanford, CA, 1998.

[65] Geroge M. Siouris. *Aerospace Avionics Systems: A Modern Synthesis*. Academic Press, Inc., San Diego, CA, 1993.

[66] Scott I. Snyder. *Integration of Satellite Navigation Systems (GPS) with Inertial Navigation Systems*. Honeywell, Minneapolis, MN, 1997.

[67] M. M. Tehrani. Ring Laser Gyro Data Analysis with Cluster Sampling Technique. *Proceedings of SPIE*, 412(2):207–220, 1983.

[68] D. H. Titterton and J. L. Weston. *Strapdown Inertial Navigation Technology*. Peter Peregrinus,Ltd., London, England, 1997.

[69] U.S. Department Of Transportation. *United States Standards for Terminal Instrument Procedures (TERPS)*. FAA, Washington, D.C, 3^{rd} edition, 1976.

[70] Grace Wahba. Problem 65-1 (Solution). *SIAM, Review*, 8:384 – 386, 1966.

[71] J. R. Wilson. A Real-World Look at Synthetic Vision. *AIAA Aerospace America*, 38(10):24 – 30, October 2000.